Modelling mercury oxidation and radiative heat transfer in oxy-coal environments

Alastair Greenman Clements

Submitted in accordance with the requirements for the degree of
Doctor of Philosophy

The University of Leeds

Energy Technology & Innovation Initiative

School of Chemical and Process Engineering

February 2016

The candidate confirms that the work submitted is his own, except where work which has formed part of jointly authored publications has been included. The contribution of the candidate and the other authors to this work has been explicitly indicated below. The candidate confirms that appropriate credit has been given within the thesis where reference has been made to the work of others.

The work in Chapter 5 of this thesis has been based on the following publication:

A. G. Clements, R. Porter, A. Pranzitelli, and M. Pourkashanian, "Evaluation of FSK models for radiative heat transfer under oxyfuel conditions," *Journal of Quantitative Spectroscopy and Radiative Transfer*, vol. 151, pp. 67 – 75, 2015.

In this publication the candidate was responsible for developing new test cases for the radiation models, as well as implementing the narrow band models and updating the existing FSK model code base, which was developed by Dr. R. Porter. Supervision was provided by Dr. A. Pranzitelli and Prof. M. Pourkashanian.

Acknowledgements

I would like to acknowledge the excellent support and guidance provided to me by all of my PhD supervisors during this work: Dr. Kevin Hughes, Prof. Lin Ma, Prof. Bill Gale, Prof. Derek Ingham and Prof. Mohamed Pourkashanian, all of whom have my deepest gratitude in providing me this opportunity to further my studies. I would also like to acknowledge my colleagues at the Universities of Leeds and Sheffield, especially Dr. Alessandro Pranzitelli and Dr. Sandy Black for their support and tutelage during my doctorate studies. Finally, I would also like to thank my family for their support during my work, especially my wife Katie, who provided endless encouragement when it was all too often required.

The funding for the work contained in this thesis was received from the European Commission Seventh Framework Programme for Reliable and Efficient Combustion of Oxygen/Coal/Recycled Flue Gas Mixtures (RELCOM), which is gratefully acknowledged, along with the useful discussions and assistance from many members of the consortium.

Abstract

There is a growing need for secure, flexible and inexpensive energy across the world, however there is also a need to simultaneously curb emissions of greenhouse gasses and toxic pollutants. Fossil fuel combustion is expected to meet a significant portion the world's growing energy demand, however CO_2 emissions need to be mitigated to avoid potentially catastrophic effects caused by global warming. Carbon capture and storage (CCS) technologies have been developed to permit the use of fossil fuel combustion in a future with strict controls over greenhouse gas emissions. CCS technologies are still yet to be deployed at large industrial scales, and it is necessary to reduce the efficiency overheads associated with CCS before the technology is economically feasible. Computational modelling can play a significant role in designing and optimising CCS technologies for power generation due to its flexibility and comparatively low costs.

The work in this thesis develops and validates models for predicting mercury oxidation and thermal radiation under oxyfuel combustion conditions, which is a promising CCS technology that is competitively placed for large-scale implementation. The oxidation of mercury is a key chemical process in mitigating emissions of the toxic metal, and predicting the principal oxidation pathways will improve the design of control technologies. Thermal radiation, which is the most significant mode of heat transfer at combustion temperatures, is a very important physical mechanism for predicting many properties of combustion, such as gas temperatures, chemical reaction rates and heat fluxes, and thermal radiation models must accurately account for changes in the combustion environment. The models developed and validated in this thesis provide new approaches to predict mercury oxidation and thermal radiation under oxyfuel conditions. The results and conclusions from this work offer clear guidance on methods to model thermal radiation in oxyfuel conditions, and provide new insight on the mercury oxidation mechanism.

Contents

List of Figures

List of Tables

1 Introduction

The benefits associated with the use of coal as a fuel for power and heat generation are clear; the commodity is inexpensive, can be easily stored and is available throughout the world, making coal a secure and reliable energy supply. Despite these benefits, there are just as many widely-acknowledged drawbacks to the utilisation of coal, specifically the high emissions of toxic and hazardous pollutants alongside climate forcing species such as CO_2. If the benefits of coal combustion are to be realised in the future, when global energy demand is expected to continue to increase rapidly, advances in the abatement of these harmful emissions must be achieved. The advancement of carbon capture and storage (CCS) technologies, where CO_2 emissions are mostly removed from the combustion process, is necessary if fossil fuels are to be included in a sustainable future energy mix.

Coal combustion serves as the main source of anthropogenic mercury pollution [1, 2], and these emissions must also be curbed in order to reduce the environmental impact of its combustion. Mercury and its compounds are of particular concern as they can be highly toxic to humans, affecting the renal, cardiovascular and nervous systems [3–5], as well as causing corrosive damage to aluminium alloys [6], which may cause operational concerns for certain CCS technologies. It is necessary to predict the behaviour of mercury under different firing conditions in the development of adequate control technologies, however the chemistry of mercury is not well understood [7]. This uncertainty in the behaviour of mercury is exacerbated when combined with CCS technologies that will significantly change the combustion environment.

The aim of this thesis is the development and validation of a model for thermal radiation and a chemical kinetic model to predict mercury speciation for coal combustion under oxyfuel conditions. The oxyfuel process introduces high concentrations of CO_2, with potentially higher H_2O concentrations as well, into the combustion environment. The elevated concentrations of these gaseous species can significantly alter heat transfer and chemical kinetics. Thermal radiation is the most significant mode of heat transfer at combustion temperatures [8] and is significantly affected by the combustion environment, particularly the concentrations of CO_2 and H_2O. Accurate accounting of thermal radiation will improve predictions of pollutant emissions, such as mercury, that are estimated using models that are based on chemical kinetics, which are sensitive to local gas temperatures.

This chapter discusses the motivation for this research. Section 1.1 describes the motivation and the strategies for CCS, focussing on the importance of an accurate chemical kinetic model for mercury speciation under oxy-coal flue gas conditions. Section 1.2 outlines the environmental concerns for mercury; the driving force behind the current regulations for limiting mercury emissions, and the reason why further regulatory work is likely in the near future. Considerations relating to the challenges of modelling oxy-coal combustion are discussed in Section 1.3, highlighting the necessity of an accurate radiation model to predict gas temperatures and heat fluxes. A full outline of this thesis is provided in Section 1.4.

1.1 CCS and oxy-coal combustion

The atmospheric concentration of carbon dioxide (CO_2) is recognised as the greatest concern for anthropogenically forced climate change through the greenhouse effect [9]. The greenhouse effect is caused by radiative absorption of solar and terrestrial heat by atmospheric gasses, trapping the energy within the atmosphere and raising the global ambient temperature [10]. A rise of 2 K above pre-industrial climate temperatures by 2050 has been recognised as being too drastic for the planet to adapt and cope with [11], and a global effort is under-way to prevent this rise coming to fruition. There has been a steady increase in atmospheric CO_2 levels reported since 1958, see Figure 1.1, which has been attributed to anthropogenic activity [9]. Current forecasts indicate that it is necessary to reduce global CO_2 emissions to 50% of the 1990 emission levels, with developed countries reducing their emissions to 80%-95% below the 1990 emission levels, to prevent the 2 K rise in ambient temperature before 2050 [12].

There are numerous proposed strategies for reducing CO_2 emissions, including efficiency savings and switching from fossil fuel combustion to low-carbon energy sources, such as renewable or nuclear fission power, however it is widely accepted that no single technology will solve the energy trilemma of providing affordable, secure and environmentally friendly electricity [14]. CCS is an emerging technology aimed at reducing CO_2 emissions from existing sources, such as fossil fuel power stations, permitting their use in a future with strict controls over greenhouse gas emissions. Unlike the other competing low-carbon technologies, fossil fuel power generation provides the flexibility needed to follow energy demand; a quality that secures

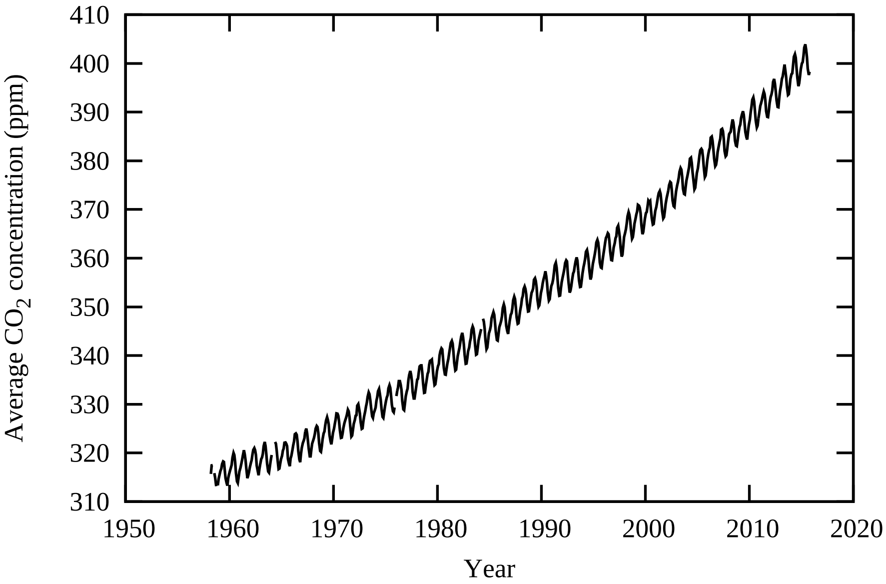

Figure 1.1: The rise in atmospheric concentration of CO_2 from 1958 to 2015. Data acquired from [13].

their relevance for the future, and emphasises the necessity of CCS technology to reduce global CO_2 emissions.

The premise of CCS technology involves the isolation of CO_2 from the combustion flue gas with subsequent transportation and long-term storage [14]. Small and medium scale CCS projects have proved that the capture and storage of CO_2 is a feasible prospect [15, 16], however large scale demonstration projects have been slow to begin their development. The deployment of CCS for power stations imposes new capital costs in the construction of the capture and transport technology, as well as further operational costs associated with separating and compressing the CO_2 from the flue gas, resulting in a lower plant efficiency. While there are various competing technologies for isolating CO_2 from the flue gas, all of the approaches impose a parasitic load on the system, and it is a significant and necessary challenge to reduce these efficiency penalties before widespread adoption of CCS is feasible.

Following capture, CO_2 will need to be compressed into its dense phase for efficient transport. Future pipelines are expected to require CO_2 to be compressed above its critical pressure of 7.38 MPa before transport to storage sites [17], illustrated in the phase diagram for CO_2 in Figure 1.2. This compression is necessary to increase the transport efficiency, reduce the possibility of two-phase flow and to prepare the CO_2 for stor-

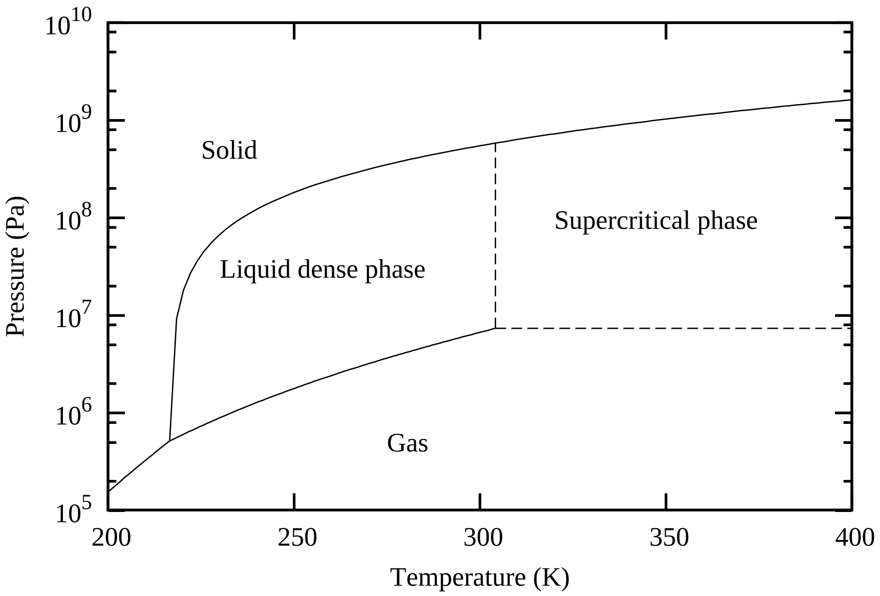

Figure 1.2: Phase diagram for CO_2. Transport will occur in the liquid dense or supercritical phase, requiring substantial compression. Data obtained from [19].

age. Ideally, heat exchangers composed of aluminium alloys are used to achieve this compression [18], however trace amounts of mercury in the CO_2 stream will affect the applicability of aluminium alloys as the liquid metal will corrode the heat exchangers, increasing the operational cost of the plant by forcing the use of less cost-effective materials. The likely concentrations of mercury in the CO_2 stream is dependent on the CO_2 capture strategy. The various technologies that have been proposed for CO_2 capture from industrial power stations can be broadly grouped into three categories; post-combustion capture, pre-combustion capture and oxyfuel combustion.

Post-combustion CO_2 capture involves using a sorbent to strip CO_2 from the flue gas. The sorbent is then regenerated in a separate chamber where pure CO_2 is released and collected for transport. Some CO_2 sorbents that have been studied include aqueous amine solutions, most commonly studied as monoethanolamine (MEA), solid sorbents such as CaO, and ionic liquids [20]. Amine-based solvents have been utilised for decades to strip CO_2 from flue gasses for use in enhanced oil recovery, and so it is a well proven concept [21]. Post-combustion strategies benefit from being an “end of pipe” control method, making them relatively easy to retrofit onto existing systems. This modular nature of the post-combustion capture unit has allowed the methods to be applied to a partial slipstream of flue gas from industrial facilities, which resulted in early pilot scale projects being easily demonstrated on existing stations [22].

The operating costs associated with post-combustion capture arise from replacing spent sorbent and alternating the conditions of the sorbent between CO_2 capture and release [20]. Post-combustion capture facilities are also quite large, requiring extra capital costs to secure a suitable site, which might not be possible for all retrofit cases. Mercury is not a specific concern to post-combustion capture as it will not generally react with the sorbents; elemental mercury (Hg^0) does not absorb into MEA solutions [23], and it also will not react with CaO under its carbonation conditions, which are at temperatures over 900 K [20]. The overall concerns regarding mercury release under post-combustion capture regimes are the same as with traditional coal-fired stations.

Pre-combustion CO_2 capture strategies utilise partial combustion of fuel in oxygen to generate a synthetic gas mixture of mostly carbon monoxide, hydrogen gas and steam, called syngas. These syngas mixtures are already used in integrated gasification combined cycle (IGCC) plants for high efficiency and low emission electricity production. For pre-combustion capture, the syngas mixture can be converted to CO_2 and higher levels of H_2 through the water-gas shift reaction [24],

$$CO + H_2O \longrightarrow CO_2 + H_2 \tag{R 1.1}$$

This gas preparation is performed under elevated pressures, facilitating the removal of CO_2 using more economical absorbents than used under post-combustion capture. The higher pressures also reduce the additional compression required after liberating the CO_2 for transport. Another benefit of this process is the flexibility of H_2 as a clean chemical energy source for applications outside of electricity generation, namely transport and heating [25].

The major disadvantage of pre-combustion capture is that it is unsuitable for retrofitting to existing power stations, making the technology infeasible in the short-to-medium term. However, due to the flexibility of H_2 as an alternative fuel in other industries, and the relatively low efficiency penalty imposed by the process, pre-combustion CO_2 capture is recognised as a potential long-term solution for CO_2 emission mitigation [26]. As with the other fuel-derived pollutants, mercury can be removed from the syngas mixture prior to the generation of H_2, typically using sorbents, such as activated carbon beds, however mercury is still a potential concern [27].

The remaining CO_2 capture technology that is potentially applicable for industrial power stations is oxyfuel combustion, which is the focus of this work. Under oxyfuel combustion, the fuel is fired in a mixture of oxygen, which is typically above 95% purity, and recycled flue gas, which will contain mostly CO_2. The recycled flue gas dilutes the oxygen in order to control the combustion temperature and stabilise the flame, providing a significant avenue of control over the combustion process. The resulting flue gas from the oxyfuel process is composed entirely from the products of combustion, without significant dilution from incompressible gasses, most notably nitrogen, that make it difficult to separate CO_2 from the flue gas of typical air-fired combustion. By compressing and processing the resulting flue gas from oxyfuel combustion it is possible to efficiently remove the water and water-soluble pollutants, effectively purifying the CO_2 in the flue gas for storage [28–30].

Similarly to post-combustion capture, oxyfuel technology can be retrofitted to existing plants, making the strategy viable in the intermediate term. An oxyfuel station can still operate under air-fired conditions, retaining flexibility if the oxygen supply is cut or under scenarios where satisfying the energy demand is prioritised over emission mitigation. Oxyfuel combustion also produces less SO_x and NO_x pollutants per energy unit when compared with air-firing, resulting in the strategy becoming an overall more attractive plant design for reducing polluting emissions [31–33]. Sour gas compression technology, which can be used to compress the effluent CO_2, has also been shown to push NO_x and SO_x equilibria towards NO_2 and SO_3 respectively, which are both highly soluble in the condensed water as nitric and sulphuric acids [30, 34]. These acidic compounds can also mitigate mercury emissions [29, 30], which makes the oxyfuel process a highly attractive approach for clean coal combustion. Additionally, with the unique control over oxygen concentrations, it is also possible to introduce additional fuel flexibility under oxyfuel conditions [35].

The overriding cost associated with oxyfuel combustion is the supply of oxygen [20]. Pure oxygen is also required for pre-combustion capture and some strategies of post-combustion, but not on the scale that will be required for the oxyfuel process. Currently the only technology available that can provide an adequate supply of oxygen is through cryogenic separation of air, however potentially more energy efficient membrane and chemical looping technologies are emerging [36, 37]. Some technical-economic studies on CCS technologies have identified oxyfuel combustion to be the most cost-effective strategy for coal combustion [38]. Other studies focussing on the full-chain life-cycle suggest that oxy-coal has more potential than other CCS methods, including natural gas CCS, in reducing greenhouse gas effects [39]. However, due to the different stages of development for the various strategies, comparisons like this should be considered tentatively [40].

The significantly altered combustion environment for the oxyfuel process provides challenges in optimisation. Empirical methods that have been built on decades of experience of operating conventional combustion facilities are no longer valid, and new methods must be developed to overcome shortfalls in experience. Mercury chemistry is not well understood on a fundamental basis [7, 41], and it is uncertain how an oxyfuel combustion environment will affect emissions or adsorption onto fly-ash. The oxyfuel process can also be significantly controlled through the manipulation of the recycle scheme and oxygen enrichment, and modelling strategies that can predict these impacts will be crucial in reducing the economic penalty of adopting the capture technology.

1.2 Mercury toxicity and pollution

Understanding the chemistry and behaviour of mercury is important for both environmental and engineering concerns associated with coal combustion. Mercury (Hg) is present in coal with an average quantity of 0.1 (±0.01) $\mathrm{ppm_w}$ [42], which is released entirely during combustion. Throughout history, mercury has been utilised by several industries, such as gold mining and chemical processes, as well as in the manufacture of numerous goods, including measuring instruments, cosmetics, batteries, lamps, fungicides and vaccine preservatives [5, 43, 44]. In modern times, increasing regulations and improving technologies are reducing the intentional use of mercury in most areas [44].

Current global trends show a decrease in the atmospheric concentration of mercury, which has been attributed to the belated consequence of reduced mercury use [45]. Despite this recent decline, the current atmospheric levels are still much higher than during pre-anthropogenic times, and further attention is being paid towards minimising mercury pollution from unintentional sources, such as the emissions from waste incineration and fossil fuel combustion, to tackle global mercury pollution. Gaseous $\mathrm{Hg^0}$ is inert and exhibits low water solubility, which results in $\mathrm{Hg^0}$ having a long atmospheric lifetime that is estimated between 4.5-18 months [46]. $\mathrm{Hg^0}$ can be transported across continental boundaries while it is in the atmosphere for this extended time, earning mercury the moniker as a ‘global pollutant’. An estimated 40% of the mercury deposited in European countries originates from a source outside of the continent [47]. Mercury is deposited in the oxidised form, mercuric mercury ($\mathrm{Hg^{2+}}$), which leads to the formation of highly toxic monomethyl mercury (MMHg) through natural biological and chemical processes [48, 49]. The atmospheric oxidation of $\mathrm{Hg^0}$ to the

Hg^{2+} form, the process that determines the atmospheric lifetime of Hg^0, is still subject to significant uncertainties [7].

In addition to MMHg, the inorganic forms of mercury, both Hg^0 and Hg^{2+}, also exhibit toxicological effects [50]. Hg^0 is effectively absorbed through the lungs in its gaseous phase, but not through ingestion due to its low water solubility [51]. As a monatomic gas, mercury vapour can diffuse into cells and cross the blood-brain barrier and the placenta, potentially causing serious neurological damage and harming foetal development [52]. In contrast to Hg^0, water soluble Hg^{2+} compounds are absorbed via the gastrointestinal tract, but cannot cross the blood-brain barrier or affect the nervous system [5]. Instead, Hg^{2+} accumulates in the kidneys, causing tissue necrosis that results in renal failure [50]. Poisoning from Hg^0 also exhibits damage to the renal system, indicating that Hg^0 is oxidised within the body to form Hg^{2+} [5]. The principle route for inorganic mercury poisoning is from inhaling elemental mercury vapour from dental amalgam fillings or occupational hazards [50, 53], and is not linked to the atmospheric levels influenced by emissions, as the concentrations are too low [54].

The formation of MMHg that results from mercury emissions is of particular concern due to its effective bioaccumulation, magnifying the low atmospheric concentrations to harmful levels [55]. The principle production pathway of MMHg is through the methylation of Hg^{2+} via sulphur reducing bacteria in anoxic estuarine sediments, where it is then released into the aquatic food web [56]. Once introduced into the food web, MMHg is efficiently retained to such a high degree that the ratio of MMHg to total Hg rises from 10% in the water column, to over 90% within the fish species that dwell there [57]. The principle route for exposure of MMHg to humans is by consuming fish following this accumulation, particularly the consumption of long-lived predatory fish such as sharks and swordfish [58].

Following the consumption of contaminated food, MMHg is efficiently absorbed through the gastrointestinal tract into the bloodstream [52]. Like Hg^0, MMHg can pass through the blood-brain barrier and the placenta [59, 60]. MMHg forms complexes with cysteine amino acids, mitigating its transport into cells and across these protective barriers [52, 61]. Symptoms of MMHg poisoning include a reduction in muscle coordination and sensory loss due to its attack on the nervous system, while acute poisoning can cause comas and death [5, 62]. Due to its transport across the placenta, MMHg is a concern for foetal neurological development, however studies have produced mixed conclusions over the effects of prenatal MMHg exposure [63, 64]. In addition to the neurological toxicity of MMHg, studies have also identified a link between MMHg levels and cardiovascular diseases, but haven't yet identified any specific mechanisms of toxicity [65]. Mercury toxicity from bioaccumulated MMHg has recently been identified to be causing significant ecological harm, where animal populations are being reduced due to consuming tainted aquatic life [66].

The bioaccumulation of MMHg and the global transport of Hg^0 result in a system where sparse and low level emissions can cause discernible health effects to the global human population, emphasising the need of strict control over mercury pollution. In 2005 the European Union (EU) launched their mercury strategy to reduce global mercury emissions [67]. The EU have passed regulations to limit mercury exports [68], and mercury emissions from waste incineration [69]. Some countries, such as Germany [70] and the USA [71], have already passed regulations to limit mercury emissions from power stations in particular. Mercury emission regulations for coal combustion systems, the largest anthropogenic source of mercury to the atmosphere, have been slow to be implemented due to the low mercury concentrations in the flue gas, reducing the applicability of control measures. In January 2013, more than 140 nations signed up to a set of legally binding measures to curb mercury pollution at the UN's INC5 meeting, which includes steps to reduce emissions form power stations [72]. Coal combustion can no longer be ignored in the context of global mercury reduction, and emerging regulations are motivating a need for the practical understanding of mercury in post-coal combustion flue gas. Through the development of an accurate and validated model it will be possible to predict the behaviour of mercury, and ultimately make confident decisions to control emissions at a minimal cost.

1.3 Modelling of oxy-coal combustion

Mathematical modelling allows for low-cost exploration of parameters that may affect a physical process. Even pilot scale combustion systems can be expensive and time-consuming to construct and run, and the scale-up from pilot-scale to full-scale implementation is a non-linear process that can often yield unexpected results. Through modelling practices it is possible to investigate how manipulating one parameter of the system will influence its operation. With application to oxy-coal combustion, it should be possible to predict how changing the combustion environment will affect the performance of a utility boiler, and optimise the combustion process. For a retrofit oxyfuel coal combustion facility it is important to predict the required flue gas recycling scheme and coal feed rate to achieve the same operating conditions that were present under air-fired combustion to adhere to the original boiler specifications. On a new-build oxyfuel system it will be advantageous to optimise specific operating conditions to maximise the economic performance of the plant by improving the boiler combustion efficiency and flexibility.

Computational fluid dynamics (CFD) is a technique used to model flows, whereby the principle fluid is treated as a continuum and the arising equations based on mass and energy conservation are solved across a discretised space. Various sub-models can be incorporated into CFD solutions, allowing the method to be applied to several engineering domains, such as aerodynamics, architectural design and modelling combustion processes. Solutions derived from CFD can influence engineering design decisions, experiment parameters, and can also be integrated into more wide-reaching process models to optimise large-scale complex systems such as an entire power station [73–75].

Modelling the coal combustion process is complex as it involves the consideration of three-dimensional two-phase fluid dynamics, turbulent mixing, fuel evaporation, radiative and convective heat transfer, and chemical kinetics [8]. While each phenomena in isolation may lead to intuitive conclusions, the complex coupling of each physical and chemical mechanism makes it necessary to use a comprehensive tool. Sub-models for each of these considerations should be accurate for the problem being investigated, otherwise the resulting solution is unlikely to represent the physical case. Approximate methods are often required for the sub-models included for combustion to provide solutions with realistic resources, however these approximations need to be assessed against appropriate test cases to ensure the validity of the assumptions that are involved.

The higher concentrations of CO_2 and H_2O in oxy-coal derived flue gas are known to exhibit strong spectral dependence for radiative heat absorption and emission. As thermal radiation is the most significant mode of energy transfer at combustion temperatures, inaccuracies in the absorption of participating species will significantly affect gas temperature and heat flux predictions [76, 77]. Correct prediction of combustion temperatures is crucial in modelling pollutant formation, gas residence times and material corrosion, while the surface heat flux represents one of the key optimisation parameters of the boiler, and will directly affect the predicted efficiency of a combustion system. Furthermore, the design of the oxyfuel recycle regime will directly control the concentrations of CO_2 and H_2O in the combustion environment, and it will be necessary to correctly account for the impact of these species on the thermal radiation transport to correctly predict the optimal recycle scheme. For these reasons, the development of accurate radiation models for oxyfuel environments has been repeatedly highlighted as a priority for accurate prediction of the combustion process [78–80].

1.4 Outline of thesis

The work in this thesis outlines the development and validation of a mercury kinetic model and thermal radiation model for oxyfuel combustion. A review of current literature is contained in Chapters 2 and 3. Studies that have focused on the behaviour of mercury in oxidising conditions are discussed in Chapter 2, with a review on how chemical kinetics can be predicted, and which techniques can be used to determine the necessary parameters to run a predictive model. An evaluation of CFD sub-models for predicting coal combustion, with a specific focus on radiative heat transfer, is discussed in Chapter 3.

Chapter 4 contains a thermodynamic and kinetic investigation into mercury oxidation under flue gas conditions, analysing how changes in the combustion environment may affect the oxidation chemistry of mercury. A validation study for non-grey radiation models that are applicable to CFD for oxy-coal combustion is conducted in Chapter 5, where recommendations for future modelling of oxyfuel combustion systems are made. Chapter 6 extends the model validation work in Chapter 5 to coal combustion systems, evaluating the impact of other modelling assumptions on radiative heat transfer. The final chapter, Chapter 7, summarises the conclusions of this thesis, and makes suggestions for future work.

2 Mercury oxidation

Previous studies on mercury oxidation are mostly motivated by the heavy metal's toxicity to humans; either predicting how Hg^{2+} is formed in the atmosphere to estimate deposition, or how mercury oxidises under various flue gas conditions in order to mitigate emissions from processes such as waste incineration and coal combustion. Under oxy-coal derived flue gas conditions, the environment is composed mostly of CO_2, and due to the flue gas recycle, there can be elevated concentrations of HCl, NO_x and SO_x pollutants when compared to the conditions of conventionally fired combustion systems. The NO:NO_2 and SO_2:SO_3 ratios can all be significantly different from conventional coal-derived flue gas due to the higher residence times and elevated O_2 concentrations. It is important to understand the elementary steps involved in mercury oxidation to allow accurate predictions under the unfamiliar conditions of oxyfuel combustion.

This chapter discusses the existing work on mercury oxidation chemistry and modelling. Section 2.1 covers various studies that focus on the possible pathways and mechanisms for mercury oxidation. The influence of combustion conditions and flue gas composition, particularly NO_x and SO_x concentrations, have on the oxidation of mercury is reviewed in this section. Chemical kinetic modelling, and its application to mercury oxidation, is covered in Section 2.2, where different proposed rate coefficients are compared and discussed. A summary of the discussion in this chapter is provided in Section 2.3, where the aim of this research in relation to the greater body of work is declared.

2.1 Mercury oxidation chemistry

Understanding the pathways of mercury oxidation, how Hg^{2+} is formed from Hg^0 emissions, is important for controlling mercury concentrations in the outlet of the flue gas train. Elemental mercury is difficult to capture because it is relatively inert and exhibits low water solubility. In contrast, mercuric compounds, particularly the mercuric halides, show appreciable solubility in water and can be captured by existing air pollution control devices (APCDs), such as wet flue gas desulphurisation (WFGD) chambers [81, 82]. Under an oxy-coal scheme, it may be possible to significantly reduce mercury concentrations in the flue gas by recycling the flue gas after the WFGD scrubbers, but only if mercury has been oxidised [33]. If the bulk of the mercury emissions are still in their elemental state after the WFGD, recycling the flue gas will reduce the concentration of reactive halogen species, which will serve to reduce the mercury oxidation efficiency, demonstrating the need to have a good understanding on mercury's chemistry prior to the design of the flue gas recycle scheme.

The formation of the mercuric halides is a significant process because these species are unusually stable for mercury compounds. Mercuric halides have a first bond dissociation enthalpy above 250 kJ mol^{-1}, far higher than other mercuric compounds [83], so are the only Hg^{2+} species that are likely to form under flue gas conditions. The thermodynamic stability of Hg^0 at temperatures above 800 K results in all mercury compounds readily decomposing during combustion, making Hg^0 the dominant mercury species in the flue gas at the exit of the furnace [84, 85]. The formation of the mercuric halides in the cooler sections of the flue gas train is dependent on the halogen concentrations arising from the parent coal for oxidising all of the mercury that leaves the furnace.

The relative quantities of the halogen species in the majority of coals follows the trend $Cl>F\gg Br>I$ [86], although some Eastern European coals contain greater bromine concentrations than chlorine [87]. Both chlorine and fluorine usually represent greater than 50 ppm$_w$ in coal, and bromine and iodine species tend to represent less than 10 ppm$_w$ [86]. In certain "salt coals" there can be much higher chlorine levels, sometimes making up greater than 10000 ppm$_w$ of coal [87, 88]. It is possible to notice a weak correlation between coal chlorine levels and Hg^0 concentration at the stack exit of power stations, shown in Figure 2.1, indicating that a high chlorine content in the feed coal promotes mercury oxidation [89]. The chlorine content of coal has also shown good selectivity in artificial neural network models for predicting mercury pollutant emissions [90], demonstrating a strong empirical correlation. Despite this pattern, there are wide variations in mercury oxidation found across different power plants that can not simply be attributed to the coal-chlorine content. Studies on industrial power stations have shown that mercury oxidation can vary between 5% and 95% of the total mercury [89, 91, 92]. There is a need for a better understanding of how mercury reacts in the flue gas before it is possible to predict mercury oxidation rates under standard air-fired processes, let alone under oxyfuel combustion conditions.

Due to the relative abundance of chlorine within most coals, the majority of flue

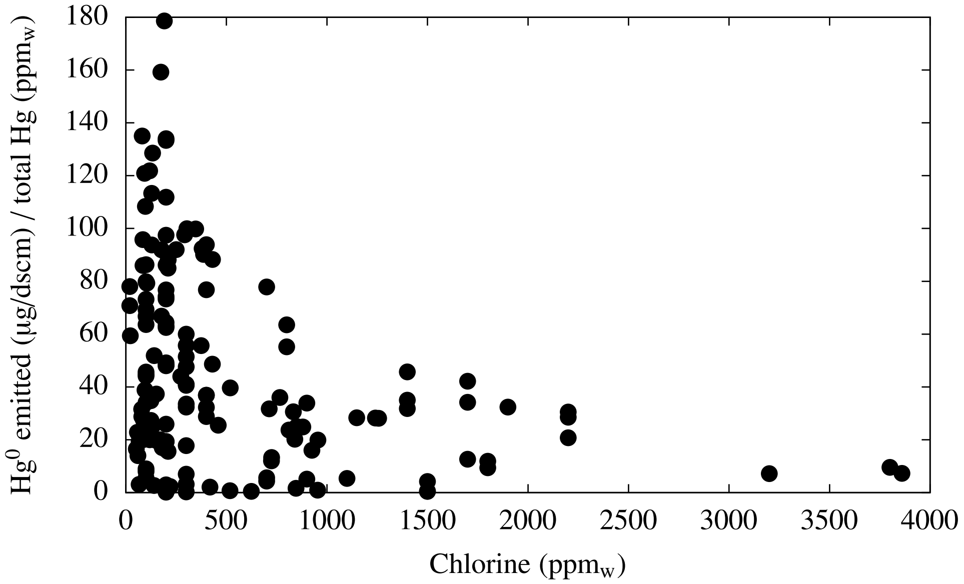

Figure 2.1: Correlation between Hg^0 emissions and HCl coal content. The Hg^0 levels are presented as a ratio between vapour concentration of unrecoverable Hg^0 and mass fraction of Hg in the feed coal in order to compare data from different power stations that are equipped with various APCDs, coal loading and feed coal rank. Data adapted from [89].

gas mercury oxidation studies have focussed on $HgCl_2$ formation [93–95]. Fluorine is usually dismissed as the halogen forms the strongly bound HF at high temperatures, which is unlikely to dissociate or react with mercury in the gaseous phase [96]. Mercury-bromine reactions have been subject to increasing study due to the high mercury oxidation efficiencies that are achievable [97]. Despite these results, bromine concentrations in most coals are too low to affect mercury oxidation during the residence times of the flue gas train. Due to its oxidation efficiency, bromine activated carbons and $CaBr_2$ injection have been proposed as a means of controlling mercury emissions [98, 99]. Iodine levels are too low to be considered as a significant oxidising agent for mercury under flue gas conditions, so mercury-iodine interactions in post-coal combustion flue gas have only been studied as a form of mercury emission control technology [100–102]. The work covered in this chapter will focus on mercury-chlorine and mercury-bromine interactions due to their potential significance in coal-derived flue gas.

Predictions that were only based upon gas-phase interactions between mercury and the halogen species have been unsuccessful in estimating mercury oxidation rates across different experimental conditions [103]. Studies have suggested that gas-phase reactions between mercury and chlorine are too slow to account for the high levels of oxidation measured in field studies [97], further motivating a search for a different class of mechanisms. Many reactions are catalysed by solid surfaces, and mercury is known to adsorb onto surfaces, where it can stabilise solid-phase molecules such as $(HgCl)_n$, HgO, $HgSO_4$ and $(HgSO_4 \cdot 2\,HgO)$ [104, 105]. These solid-phase compounds are able to form on the walls of the flue gas chambers and potentially react with the fairly abundant HCl species to form $HgCl_2$ [95]. The rates of these surface catalysed oxidation pathways are limited by the thermal stability of the solid-phase intermediates and the surface availability [103]. Both the rates and the elementary steps involved in these mechanisms still need to be specified before they can be applied in models.

In addition to the gas-phase oxidation process, mercury also adsorbs onto fly-ash particles, where it is referred to as particulate bound mercury (Hg_P), and can be captured by particulate control devices such as electrostatic precipitators (ESPs) or fabric filters (FFs) [33, 82, 106]. Both oxidised and elemental mercury adsorb onto ash particles at different rates, reiterating the importance of understanding how mercury oxidises to predict Hg^0, Hg^{2+} and Hg_P distributions. The surfaces of fly-ash particles can also catalyse mercury oxidation by the halogen species [107]. The interactions between fly-ash particles and Hg^0 is complex and not well defined, however the most industry proven method to control mercury emissions, the use of an activated carbon sorbent, mimics the behaviour of native organic fly-ash in the flue gas.

The proposed mercury oxidation pathways can be generalised into these three categories: gas-phase homogeneous reactions, surface catalysed mechanisms and fly-ash interactions. It is unclear how much each pathway contributes to the final speciation of mercury. This section identifies key work behind these potential oxidation schemes for mercury, and how they may alter under an oxy-coal flue gas environment. Subsection 2.1.4 provides a summary for the mercury oxidation mechanisms.

2.1.1 Homogeneous oxidation

The formation of the mercuric halides through gas-phase interactions requires the intermediate monohalide species, which further reacts through a second oxidation phase. This process is illustrated for mercuric chloride formation in Reactions (R 2.1) to

(R 2.8) [93],

$$\mathrm{Hg + Cl + M \rightleftharpoons HgCl + M} \quad \text{(R 2.1)}$$

$$\mathrm{Hg + Cl_2 \rightleftharpoons HgCl + Cl} \quad \text{(R 2.2)}$$

$$\mathrm{Hg + HCl \rightleftharpoons HgCl + H} \quad \text{(R 2.3)}$$

$$\mathrm{Hg + HOCl \rightleftharpoons HgCl + OH} \quad \text{(R 2.4)}$$

$$\mathrm{HgCl + Cl + M \rightleftharpoons HgCl_2 + M} \quad \text{(R 2.5)}$$

$$\mathrm{HgCl + Cl_2 \rightleftharpoons HgCl_2 + Cl} \quad \text{(R 2.6)}$$

$$\mathrm{HgCl + HCl \rightleftharpoons HgCl_2 + H} \quad \text{(R 2.7)}$$

$$\mathrm{HgCl + HOCl \rightleftharpoons HgCl_2 + OH} \quad \text{(R 2.8)}$$

A direct reaction with the halogen molecule is not usually considered due to a high energy barrier associated with the insertion reaction [108]. From the reactions that produce the monohalide species, only the reaction with the atomic halogen species, Reaction (R 2.1), can proceed at an appreciable rate; the other routes, Reactions (R 2.2) to (R 2.4), are prevented by highly endothermic reaction enthalpies [109], and these routes will be more prevalent in the destruction of the monohalide species, reducing mercury back to its elemental form.

The second phase of oxidation is faster due to the increased stability of the mercuric halide, and could feasibly proceed by reacting with molecular halogen species, as in Reactions (R 2.6) and (R 2.8). The reaction between the monohalide and the halogen acid, Reaction (R 2.7), is still not thermodynamically viable under flue gas conditions [110]. The role of the atomic halogen radical in the second stage of oxidation is more complicated due to the competing destruction of the monohalide species in the reverse direction of Reaction (R 2.2), while the reaction with molecular chlorine, Reaction (R 2.6), provides a route to form mercuric halide while liberating reactive chlorine radicals from the diatomic chlorine molecule.

Following the above mechanism, the mercury oxidation rate in most coal-derived flue gas conditions is limited by the availability of atomic chlorine (Cl) for Reaction (R 2.1), as chlorine is usually the only significant halogen present in coal. Atomic chlorine radicals in the flue gas are produced through reactions with oxygen radical species, namely the O and OH radicals, illustrated in the following reactions [111]

$$\mathrm{HCl + O \rightleftharpoons Cl + OH} \quad \text{(R 2.9)}$$

$$\mathrm{HCl + OH \rightleftharpoons Cl + H_2O} \quad \text{(R 2.10)}$$

Suriyawong [112] demonstrated experimentally that an increase in oxygen species concentrations increases mercury oxidation rates, and also that no Hg^{2+} species were produced in a reaction mixture void of oxygen species. Further results of the experiments by Suriyawong [112] indicated that H_2O had an inhibitory effect on mercury oxidation, postulating that a rise in OH radicals served to destabilise the monohalide through the reverse direction of Reaction (R 2.4), contrary to the promotive effects of Reaction (R 2.10). These results highlight the sensitivity of mercury chlorination on the availability of Cl radicals and the stability of HgCl, which are both heavily influenced by the combustion environment. During oxyfuel combustion it is likely that these two oxygen radical species will be present in higher concentrations than conventionally-fired combustion, with the OH radical being increasingly important under wet flue gas recycle schemes.

A significant sink for the Cl radical concentration is the formation of molecular chlorine (Cl_2) through the recombination reaction,

$$\mathrm{Cl + Cl + M \rightleftharpoons Cl_2 + M} \tag{R 2.11}$$

The sensitivity of mercury oxidation with respect to Reaction (R 2.11) depends on the rate of the reaction between HgCl and Cl_2, Reaction (R 2.6). If Reaction (R 2.6) is fast, Reaction (R 2.11) will promote mercury oxidation by forming Cl_2 to react through Reaction (R 2.6), which also releases further Cl radicals to oxidise Hg^0. If Reaction (R 2.6) is slow, mercury oxidation becomes solely reliant on the Cl radical concentration, and the overall oxidation efficiency is reduced by Reaction (R 2.11).

The Cl, O and OH radicals exhibit reactive chemistry with several other species in the flue gas, including NO and SO_2. It has been suggested that increased concentrations of NO could reduce mercury oxidation rates by consuming O, OH and Cl radicals through the following reactions [112, 113],

$$\mathrm{NO + O + M \rightleftharpoons NO_2 + M} \tag{R 2.12}$$

$$\mathrm{NO + OH + M \rightleftharpoons HONO + M} \tag{R 2.13}$$

$$\mathrm{HONO + Cl \rightleftharpoons HCl + NO_2} \tag{R 2.14}$$

Halogen radicals can also react directly with NO to form the nitrosyl halide compounds, which can promote the formation of the less reactive halogen molecule or acid species [111, 114, 115], illustrated below for nitrosyl chloride (ONCl),

$$\mathrm{NO + Cl + M \rightleftharpoons ONCl} \tag{R 2.15}$$

$$\mathrm{ONCl + Cl \rightleftharpoons NO + Cl_2} \tag{R 2.16}$$

$$\mathrm{ONCl + H \rightleftharpoons NO + HCl} \tag{R 2.17}$$

The net effect of Reactions (R 2.15), (R 2.16) and (R 2.17) is to remove the reactive halogen species from the gas mixture, thus preventing mercury oxidation from initiating. The formation of the nitrosyl halides, Reaction (R 2.15), is particularly influential as NO is a much more competitive reactant for halogen radicals over Hg^0, which is due to the far higher stability of nitrosyl halides over the mercurous monohalide species, and the abundance of NO over Hg^0 in the flue gas. The nitrosyl halides may further influence mercury oxidation through direct interactions with mercury species, such as in the reactions

$$\mathrm{Hg + NOCl \rightleftharpoons HgCl + NO} \tag{R 2.18}$$

$$\mathrm{HgCl + NOCl \rightleftharpoons HgCl_2 + NO} \tag{R 2.19}$$

however these reactions have not been studied before. As the nitrosyl halide species are relatively stable, it is unlikely that Reaction (R 2.18) will promote mercury oxidation, and will probably serve to destabilise the monohalide species through the reverse direction and reduce the overall oxidation rate. Reaction (R 2.19) could promote mercury oxidation, however this pathway would probably proceed slowly as both of the reactant species are expected to be in very low concentrations.

Increased concentrations of NO have been shown to reduce mercury oxidation in some bench-scale experiments [112], however separate bench-scale experiments have found very little influence of NO on mercury oxidation [97, 116, 117]. The variation in these results may be down to the significantly different gas compositions between the two experiments; Suriyawong [112] used a simulated gas mixture with 10% (vol) O_2 concentration, where the other bench-scale experiments were conducted on the flue gas from a methane combustion flame with less than 2% (vol) O_2 concentration [97, 116, 117]. These latter measurements that were undertaken on combustion flue gas, where no significant sensitivity of the mercury oxidation ratio was found with regards to the NO concentration, was unable to operate a baseline case without any NO interference due to the production of thermal NO_x, and therefore it is possible that the influence was already saturated at these levels as the rate limiting step of nitrosyl halide formation is likely to be the atomic halogen concentration, and not the NO concentration.

The comparison between an air-fired and oxyfuel conditions by Preciado et al. [117] showed increased oxidation efficiency under the oxyfuel combustion environment, however the oxyfuel conditions contained significantly lower nitrogen species, which would result in lower thermal NO_x production. While the sensitivity of mercury oxidation to the NO concentration was tested for air-fired environments, where the minimum concentration of NO was prescribed by thermal NO_x production at 30 ppm_v, this sensitivity test was omitted from the oxyfuel tests, and therefore it is uncertain if the changes in oxidation efficiency is associated with the oxyfuel environment or the absence of NO. During coal combustion, nitrogen in the fuel is the primary source for NO_x pollutant formation, and therefore cannot be significantly reduced in oxy-coal combustion, and the conclusions from the study by Preciado et al. [117] may not be transferable to an oxy-coal environment. Measurements in oxy-coal flue gas have not shown such a significant improvement in the ratio of oxidised mercury [116, 118, 119], although it is not possible to isolate the homogeneous mechanism in these measurements of a real coal flame.

Understanding the influence of sulphur species on mercury oxidation has often been afflicted with the effect of SO_2 over a bias in mercury detection tests. Small amounts of Cl_2, potentially formed from HCl, can produce a large bias in Hg^{2+} recordings in the standard Ontario Hydro method, where hypochlorite ions, ClO^-, oxidise mercury in the conditioning train [120]. Through the addition of SO_2, this bias is mitigated, and mercury oxidation is shown to decrease. Further studies, using sodium thiosulphate (Na_2SO_3) to remove ClO^- ions, have shown that SO_2 has a minimal effect on mercury oxidation [97, 116, 117, 121], however a bench-scale experiment by Smith et al. [122] found that SO_2 oxidised mercury in the absence of HCl, and demonstrated increased oxidation when combined with low concentrations of HCl, although mercury oxidation was somewhat mitigated at higher HCl concentrations. As only elemental mercury was measured in the study by Smith et al. [122], with oxidised mercury inferred from the difference between inlet and outlet concentrations, it is possible that the non-elemental mercury species could be $HgSO_{4(s)}$ formed on the surfaces of the reactor, and not be associated with gas-phase reactions. Measurements of mercury oxidation in an oxy-coal flame, with simulated flue gas recycle with an elevated concentration of SO_2, H_2O and NO in the combustion medium, showed elevated mercury oxidation compared to environments without additional pollutants.

Sulphur species are known to influence additional oxidation reactions in combustion environments as they will react with available radicals [123, 124]. The availability of O and OH radicals will affect the dissociation of HCl into reactive species, however these radical species will also react with sulphur compounds, which will further react to essentially catalyse the recombination of molecules, much like the way ONCl catalyses the recombination of Cl_2 and HCl in Reactions (R 2.15) to (R 2.17).

Bromine species are much more efficient than chlorine at oxidising mercury. Even with modest concentrations of 50 ppm_v HBr in the gas mixture, mercury oxidation rates are several times greater than under similar conditions with 100 ppm_v HCl [97, 125]. Bromine reactions with mercury are believed to be analogous to chlorine, and follow much the same pathway as presented by Reactions (R 2.1) to (R 2.8) [126, 127]. Unlike chlorine, bromine species are not dominated by the halogen acid at high temperatures, but have a reasonably high concentration of atomic bromine (Br), which accelerates the otherwise limiting step of atomic recombination, Reaction (R 2.1) [126]. While measurements of mercury oxidation by bromine species demonstrated greater efficiency in oxyfuel conditions compared to air-fired results [117], these measurements are subject to the same uncertainties concerning the interaction between NO and the atomic halogen as with chlorine oxidation, and these trends have not been demonstrated in real oxy-coal flames [116]. Native bromine concentrations in coal derived flue gas are often found to be less than 1 ppm_v, so without control procedures to provide higher bromine concentrations, chlorine chemistry is still expected to be the dominant oxidising agent for mercury [97, 128, 129].

An alternative proposed gas-phase pathway for mercury oxidation involves the halite radical species, illustrated for the chlorate radical (ClO) in Reactions (R 2.20) and (R 2.21),

$$\mathrm{Hg} + \mathrm{ClO} \rightleftharpoons \mathrm{HgO} + \mathrm{Cl} \qquad \text{(R 2.20)}$$

$$\mathrm{HgO} + \mathrm{HCl} \rightleftharpoons \mathrm{HgCl} + \mathrm{OH} \qquad \text{(R 2.21)}$$

This mechanism avoids the dependency on atomic chlorine by producing HgO, which reacts with the far more abundant HCl species [130], however this mechanism was developed using thermodynamic data that has since been shown to be in wide disagreement with theoretically calculated values. More recent calculations suggest the value for the enthalpy of formation for HgO is less than 17 kJ mol^{-1} [83, 131], and not the experimentally determined value of 268(±63) kJ mol^{-1} [132]. Recalculating the reaction enthalpies for Reaction (R 2.20) (and similarly for the BrO species) reveals that this pathway is endothermic, and so the mechanism is unlikely to contribute to mercury oxidation [133, 134].

Alternative products with halite radicals are the XHgO species, where X refers to any halogen atom [133, 135]. The conformers HgOX and HgXO have been determined to be bound only by shallow van der Waals forces, and so are not stable [136]. The possible pathways for the XHgO species are shown in Reactions (R 2.22) to (R 2.26),

$$\mathrm{Hg} + \mathrm{XO} \longrightarrow \mathrm{XHgO} \tag{R 2.22}$$

$$\mathrm{Hg} + \mathrm{XO} \longrightarrow \mathrm{HgX} + \mathrm{O} \tag{R 2.23}$$

$$\mathrm{Hg} + \mathrm{XO} \longrightarrow \mathrm{HgO} + \mathrm{X} \tag{R 2.24}$$

$$\mathrm{HgY} + \mathrm{XO} \longrightarrow \mathrm{YHgO} + \mathrm{X} \tag{R 2.25}$$

$$\mathrm{HgO} + \mathrm{XO} \longrightarrow \mathrm{XHgO} + \mathrm{O} \tag{R 2.26}$$

The direct formation of the XHgO species via the insertion reaction, Reaction (R 2.22), is suspected to have a high energy barrier of around 167 kJ mol^{-1}, so the reaction rate should make this pathway insignificant [137]. Alternative pathways of formation are via intermediates created in Reaction (R 2.23) and (R 2.24), which then react via Reaction (R 2.25) or (R 2.26), but these initial reactions are endothermic to a similar degree to the energy barrier of Reaction (R 2.22) [133], making these pathways even less likely.

Despite the absence of any apparently feasible formation pathway, experimental results have confirmed the oxidising potential of the halite radicals. An experiment by Raofie and Ariya [138] confirmed the existence of BrHgO as a product of BrO radicals and Hg^0. Additional species of HgBr and HgO were also detected in the experiment, however all of the products were formed in the condensed phase, and it is unclear whether they could be produced through gas-phase interactions. A separate experiment found that gas-phase Hg^0 decay was accelerated when atomic Cl radicals were exposed to oxygen, suggesting that ClO radicals were forming and efficiently oxidising elemental mercury [139]. Experiments purposefully utilising ClO to oxidise mercury have found high oxidation efficiencies [140], however the products that are formed through these reactions are still unclear, as well as the mechanisms that the species follow.

In addition to the XHgO products, mercuric hypohalites (XOHgY, where X and Y are halogen atoms), can be formed from halite interactions, and have been suggested as stable, strongly bound species [136]. The FHgOF species has been determined to exist experimentally, but in conditions that are far removed from practical circumstances [141]. The halite species offer a significant uncertainty over mercury oxidation mechanisms. The current state of knowledge is not sufficient to include these interactions in any model, as there are no definite reaction mechanisms or well-characterised products, but it is important to be aware that the complete mechanism of potential oxidation pathways is incomplete.

In the gas-phase homogeneous interaction between mercury and halogen species, oxidation of Hg^0 occurs mainly through the Reactions (R 2.1) to (R 2.8). Under coal-derived flue gas conditions, mercury oxidation is reliant on atomic chlorine concentrations, which could be severely limited due to its reactive chemistry with other flue gas components. If the feed coal has a significant bromine content, it is likely that mercury will effectively oxidise, allowing the toxic pollutant to be captured through WFGD chambers, but this is not likely for the majority of coals. Under oxy-fuel combustion it is uncertain whether mercury oxidation will be promoted or mitigated, and further studies on key mercury oxidation reactions are required.

2.1.2 Surface catalysed oxidation

Several experimental studies have noted accelerated mercury oxidation rates on uncoated surfaces [104, 142, 143]. Mercury can adsorb onto surfaces where solid-phase compounds can form, accelerating mercury oxidation. A proposed global reaction mechanism for this process is shown in Reactions (R 2.27) and (R 2.28) [95],

$$\mathrm{Hg_{(g)} + SO_{2(g)} + O_{2(g)} \longrightarrow HgSO_{4(ads)}} \tag{R 2.27}$$

$$\mathrm{HgSO_{4(ads)} + 2\,HCl_{(g)} \longrightarrow HgCl_{2(g)} + H_2SO_{4(l)}} \tag{R 2.28}$$

The solid-phase intermediate formed in this reaction is mercuric sulphate, $HgSO_4$, which is the most thermodynamically stable species that is likely at lower temperatures [144]. This process is expected to be fast, but highly sensitive to the surface temperature, only occurring between 420 K and 670 K [105]. Elementary reactions for this scheme have not been proposed, but studies at a pilot plant have indicated that mercury oxidation is accelerated within this temperature range [103].

An expected intermediate of Reaction (R 2.27) would be HgO, which is also produced in the absence of SO_2 [105]. Further interactions between adsorbed oxygen species and SO_2 could complete the formation of $HgSO_4$ to react with HCl, however this scheme entails a lot of speculation over how stable intermediates may form, and further studies into these pathways are required.

Experiments have shown that $HgSO_4$ formation is fast given the right conditions, but elementary mechanisms have not been suggested. The effect of changing the combustion environment on this pathway is unknown due to the complex nature of surface-catalysed reactions, however experiments suggest that the surface temperature and SO_2 concentration are the only dominant factors for the rate of this reaction scheme, and as SO_2 is expected to be in excess under both air-firing and oxyfuel conditions, this mechanism may not demonstrate any dependence on changes in the combustion environment.

2.1.3 Heterogeneous oxidation with fly-ash

Mercury interacts with fly-ash in the flue-gas train to form Hg_P. The ratio between total Hg and Hg_P varies between 0% to up to 43% across different coal-fired power stations [89]. Fly-ash is made up of both inorganic and organic matter. The inorganic phases of fly-ash are mostly composed of silicates and metal oxides derived from the minerals of the parent coal. The majority of the inorganic fly-ash is unaffected by changing from air-fired to oxy-fired conditions [145]. The organic fly-ash matter, often referred to as unburned carbon (UBC), is mostly composed of char derived from the fuel, however a significant portion of the total surface area of organic matter is derived from sub-micron soot particles. Emissions of particulate matter are restricted by regulations, and fly-ash is often captured via ESP and FF control devices, facilitating the capture of Hg_P from the flue gas. Mercury can be controlled by increasing the adsorbed Hg_P species in the flue gas, however this may affect the saleability of the fly-ash product, often consumed as a ballast in cement production. Additionally, surface mechanisms, as described above in Subsection 2.1.2, are equally possible on fly-ash surfaces, and will influence the oxidation efficiency of the process.

Trace metals are known to interact with the inorganic components of fly-ash, adsorbing at temperatures above their vapour dew point [146]. In isolation, mercury adsorption on inorganic fly-ash is not significant [147–149], however experiments by Smith et al. [122] have shown that Hg^0 levels are reduced when inorganic particle loading is combined with HCl. Additional studies have identified that HCl will adsorb onto fly-ash, where it can then readily react with Hg^0 [150, 151]. Further studies are required to elucidate the specific mechanisms and rates between mercury and inorganic fly-ash so they can be effectively included in predictive models.

Mercury shows a far greater affinity to adsorption onto the organic component of fly-ash [152, 153]. Injection of carbon-based sorbents have been proven to reduce mercury emissions by up to 80% [154]. Despite the success of activated carbons in capturing mercury, the mechanism by which they work, and its applicability to native organic fly-ash, is still uncertain. Mercury adsorption is usually promoted by cooler temperatures, suggesting a physisorption mechanism [153], however this temperature relationship is more likely to be a consequence of the thermodynamic and kinetic properties of mercury [155]. Furthermore, flue gas composition, particularly the concentrations of SO_2, H_2O and acid gasses such as HCl and NO_2, have been shown to impact the rate of adsorption, suggesting a chemisorption mechanism [118, 149, 156–160]. Experimental studies have identified significant amounts of chemisorbed mercury species on activated carbons, suggesting that mercury can effectively oxidise on the carbon surface and chemically bind onto a graphene edge site of organic particles [100, 161, 162].

Theoretical studies suggest that protonation occurs at carbon edge sites to form a carbenium ion [163]. This activated site will oxidise and adsorb mercury, where it could react with adsorbed Cl or HCl to form $HgCl_2$, or remain combined to the char particle [107]. The acidic gasses NO_2 and HCl, as well as H_2SO_4 in small quantities, promote the creation of the carbenium active sites, improving mercury adsorption rates, whilst SO_2 competes with Hg^0 for oxidation and mitigates Hg_P formation [107, 118]. The variations in these flue gas species will have an influence on how much mercury is adsorbed onto native fly-ash under oxy-coal flue gas conditions.

Native organic fly-ash is usually avoided because it arises from inefficiencies of combustion. The UBC is also considered a contaminant of the fly-ash, rendering it useless to the concrete industry, the major consumer of coal-derived fly-ash, heavily affecting its sale value [164, 165]. Efficiencies in boiler design can greatly reduce UBC in the fly-ash, however this is often avoided to reduce NO_x emissions [166]. The conditions under oxy-coal combustion are radically different, and these efficiencies may be readopted depending on whether it is necessary to control NO_x concentrations. Additionally, soot formation is often reduced under oxy-coal combustion, which will greatly reduce the surface area of native organic fly-ash matter [167, 168].

Under oxy-coal combustion there will be different levels of UBC, HCl, SO_x and NO_x; all depending on boiler designs and the flue gas recycle scheme. All of these species have a varying level of influence over the fate of Hg_P, and the potential to oxidise mercury on the particle surface. Mechanisms for the adsorption and oxidation of Hg^0 on graphene edge sites have been suggested, however the availability of these sites on native coal-derived UBC is uncertain. There is a significant challenge in predicting how mercury will behave with native UBC under oxy-fired conditions.

2.1.4 Summary of oxidation pathways

Mercury oxidation is complex, without any clear dominant pathway. Homogeneous gas-phase reactions and surface mechanisms involving fly-ash particles and chamber walls have been considered to predict mercury's chemistry. When considering the differences between air-fired to oxy-fired coal combustion environments, all of the potential pathways could be affected.

In the homogeneous gas-phase mechanisms, the modifications in the gaseous species and their concentrations could greatly affect how mercury oxidation chemistry behaves. Potential increases in atomic Cl arising from higher oxygen concentrations could increase oxidation levels, while increased H_2O could have the opposite affect. There are still uncertainties over how halite species may react and the efficacy of the halogen atomic recombination reaction over mercury oxidation.

Surface catalysed oxidation reactions require further studies into how mercury adsorbs onto available sites, along with the kinetics of the reaction mechanisms, before it can be reliably modelled. This process is unlikely to be affected by changing the combustion environment for oxy-coal due to the overriding reliance on temperature and surface availability, however without a fundamental explanation for this phenomena it is not possible to accurately predict how oxyfuel conditions may change this mechanism.

The mechanism for mercury adsorption onto fly-ash can be related to the most proven method of emission mitigation – activated carbon injection. The formation of SO_x, NO_x and organic fly-ash particles under oxy-fuel conditions will affect the applicability of these mechanisms. The sulphur species in the flue gas compete with mercury on organic adsorption sites, reducing Hg_P and preventing the removal of mercury from the flue gas stream. Other species, such as NO_2 and HCl, serve to enhance the number of active sites on the fly-ash, and so could serve to improve mercury adsorption.

This section has covered the proposed pathways for the formation of removable mercury species, namely Hg^{2+} and Hg_P. These pathways are likely to occur at different rates between air-fired and oxy-fired conditions, but in a complicated and currently unpredictable manor. The focus of this thesis is to elucidate uncertainties associated with mercury oxidation via homogeneous gas-phase reactions in an oxyfuel flue gas environment. It is important to appreciate how both Hg^0 and Hg^{2+} interact outside of the gas-phase oxidation pathway in order to make inferences from practical applications, however the remaining focus of this thesis will be solely on homogeneous interactions.

2.2 Chemical kinetic modelling

Mercury species do not reach equilibrium under flue gas conditions, and oxidation is subject to kinetic limitations [94]. Equilibrium calculations based on thermodynamic values predict complete mercury oxidation at the conditions when the flue gas is released from the stack, which is not shown in experimental results or field studies [169]. The reaction kinetics of mercury oxidation need to be understood for accurate predictions of mercury speciation.

Kinetic studies focus on the macroscopic properties of a chemical reaction; the reaction mechanism and the rate coefficient. The mechanism specifies the elementary steps involved in a reaction, and the rate coefficients for those elementary reactions indicate how rapidly they influence the concentrations of the species involved. Various mechanisms for mercury oxidation were covered in Section 2.1, however the rates of the proposed reactions were not discussed in detail.

This section will discuss kinetic rates for mercury oxidation, and identify areas of uncertainty associated with these determined values. Kinetic rate laws and the equations used to model rate coefficients are discussed in Subsection 2.2.1, identifying the parameters that need to be determined for each reaction prior to the undertaking of kinetic modelling. The different methods employed to infer kinetic rates, both experimental and theoretical, are discussed in Subsection 2.2.2. Subsection 2.2.3 covers previous work on mercury chemical kinetic models and proposed rates.

2.2.1 Kinetic rates

The evolution of a species' concentration across time is determined by the reactions that consume and produce it. The rate of a reaction, how fast the reaction alters the concentration of its products and reactants, is proportional to the concentration of the reacting species that are involved. For an isolated general reaction, as in Reaction (R 2.29), this is illustrated by Equation (2.1),

$$x\mathrm{A} + y\mathrm{B} \longrightarrow \mathrm{C} \tag{R 2.29}$$

$$\frac{\mathrm{d[C]}}{\mathrm{d}t} \propto [\mathrm{A}]^m[\mathrm{B}]^n \tag{2.1}$$

The powers that each concentration is raised to, m and n, are usually set to be equal to the stoichiometry of the reactants, which are represented by x and y respectively in Equation (2.1). Through formulating the rate of a reaction it is possible to predict the progress of a chemically reactive system by integrating Equation (2.1) for all of the relevant reactions across time.

The constant of proportionality in Equation (2.1) is often referred to as the rate coefficient, represented as k. The rate coefficient has long been known to change with temperature [170]. This temperature dependence of the rate coefficient is often modelled using the Arrhenius equation,

$$k(T) = A \exp\left(-\frac{E_a}{RT}\right) \tag{2.2}$$

where k is the rate coefficient, A is the pre-exponential factor, E_a is the activation energy, R is the universal gas constant and T represents the temperature. The Arrhenius equation requires two parameters to be defined for each reaction; the activation energy and the pre-exponential factor.

In elementary reactions, the activation energy represents the energy barrier that has to be overcome in order for the reactants to successfully form the product. In the Arrhenius equation, the term '$\exp(-\frac{E_a}{RT})$' represents the proportion of the gas mixture that is excited with this activation energy, as defined by the Maxwell-Boltzman distribution. The activation energy therefore defines the temperature dependence of the rate coefficient in the Arrhenius equation.

The pre-exponential factor in the Arrhenius equation represents the frequency of potentially reacting collisions. In the classical Arrhenius equation this value is a constant, however experimental data over a wide temperature range often illustrates a noticeable curvature away from the Arrhenius equation [171]. To get a better empirical fit over a wide temperature range, the modified Arrhenius equation is often used,

$$k(T) = A \left(\frac{T}{T_{ref}}\right)^n \exp\left(-\frac{E_a}{RT}\right) \tag{2.3}$$

where T_{ref} is a reference temperature, usually set to 1 K, and n is an additional parameter. In Equation (2.3) a further temperature dependence is applied to the pre-exponential term to capture the observed behaviour.

The proposed mechanisms for mercury oxidation involve three-body recombination reactions, such as Reactions (R 2.1) and (R 2.5). A general three-body recombination reaction is expressed as

$$\mathrm{A + B + M \rightleftharpoons AB + M} \tag{R 2.30}$$

where A and B are reactants, AB is the product and M represents any molecule in the gas mixture. A three-body recombination reaction in the form of Reaction (R 2.30) is not elementary. At its most basic level this reaction proceeds via the steps (R 2.31) to (R 2.33),

$$\mathrm{A + B \longrightarrow AB^*} \tag{R 2.31}$$

$$\mathrm{AB^* \longrightarrow A + B} \tag{R 2.32}$$

$$\mathrm{AB^* + M \longrightarrow AB + M} \tag{R 2.33}$$

The three-body reaction initiates by forming an excited complex from an initial collision between the reactants, Reaction (R 2.31). This step occurs as the kinetic energy involved in the collision between the reactants does not have an alternative outlet. This complex, $\mathrm{AB^*}$, will either dissociate through Reaction (R 2.32), or stabilise through dissipating the excess energy upon further collisions with an arbitrary third body particle, M in Reaction (R 2.33).

Assuming the excited complex is in steady state, the overall rate coefficient of a three-body recombination reaction is given by [172]

$$k_{R\,2.30} = \frac{k_{R\,2.31} k_{R\,2.33} [\mathrm{M}]}{k_{R\,2.32} + k_{R\,2.33} [\mathrm{M}]} \tag{2.4}$$

where k represents the rate coefficient for the subscripted reaction. In the low and high pressure limits, where $[\mathrm{M}] \to 0$ and $[\mathrm{M}] \to \infty$ respectively, k_{obs} can be approximated by the following equations

$$k_{R\,2.30,0} = \frac{k_{R\,2.31} k_{R\,2.33} [\mathrm{M}]}{k_{R\,2.32}} \tag{2.5}$$

$$k_{R\,2.30,\infty} = k_{R\,2.31} \tag{2.6}$$

where $k_{R\,2.30,0}$ is the rate coefficient in the low pressure limit, and $k_{R\,2.30,\infty}$ is the rate coefficient in the high pressure limit. This relationship results in a fall-off region, where the rate becomes second-order in the high pressure limit. The position of this fall-off with regards to pressure is dependent upon the lifetime of the intermediate $\mathrm{AB^*}$. For large atoms, such as Hg, which will exert considerable London dispersion forces, this regression to second-order kinetics is very unlikely at atmospheric pressures [173], and the reactions of mercury oxidation are expected to exhibit a linear dependence on pressure.

In the deactivation of the excited complex, Reaction (R 2.33), energy is dissipated through an arbitrary molecule in the gas mixture. As the temperature of the gas mixture increases, the amount of energy that can be dissipated through the average molecular collision will reduce, which will make the intermediate liable to dissociate before the molecule can stabilise. This process will reduce the rate of the overall reaction at higher temperatures and produce a negative temperature dependence. In the Arrhenius equation this is modelled by a negative activation energy.

The efficiency of the third-body molecule at absorbing the excess energy held by the excited complex also affects the overall rate coefficient. Molecules such as SF_6 and CO_2 show greater third-body efficiencies than N_2 or Ar [174–176]. The rate constant for the atomic chlorine recombination reaction, Reaction (R 2.11), has been shown to be between two and four times greater in a CO_2 atmosphere than when N_2 is the bath gas [115, 177, 178]. Observed rate coefficients for the mercury recombination reaction with atomic chlorine, Reaction (R 2.1), have been shown to differ by more than an order of magnitude when changing the bath gas molecule from He to N_2 [139]. This third-body efficiency highlights another uncertainty when applying values derived from air-fired chemistry to predict oxy-fired chemical speciation. When deriving the parameters for the modified Arrhenius equation it is important to be mindful of these dependencies on temperature, pressure and bath gas.

2.2.2 Determination of kinetic rate coefficients

Both theoretical and experimental methods exist for determining the rate coefficients of chemical reactions. Theoretical techniques make use of the fundamental properties of atomic structures to predict how products are formed. The experimental methods include either direct or indirect concentration measurements to infer the decay or production rate of a species. Regardless of the method, there is substantial uncertainty associated with applying the determined rate coefficients to predict the chemical progress of a system [7].

The transition state theory (TST) and Rice-Ramsperger-Kassel-Markus (RRKM) methods are usually employed to predict bimolecular and unimolecular reaction rates respectively. Both methods utilise fundamental properties of the reactants in order to predict the energy requirement and the development of the reaction, which are determined from quantum chemical calculations. This process becomes increasingly difficult as the complexity of the reactants increases. Reaction steps that involve large atoms, such as mercury, demand specifically sophisticated approaches to describe the interactions within the electron cloud, as well as accounting for special relativistic effects for inner-core electrons that will have a velocity comparable to the speed of light [179]. The additional complexities introduced when studying heavy elements such as mercury exacerbate uncertainties in theoretically derived rate coefficients [7].

Rate coefficients can be experimentally determined through indirect measurement against a reference reaction, or through direct time-dependent measurements of species' concentrations. Indirect measurements using the relative rate method have been conducted for mercury reactions [143]. The relative rate method involves benchmarking the target reaction against a reference reaction with a known and well characterised rate coefficient. Both the reference and target reactions are required to consume the same unstable reactant species and the final gas mixture is analysed using a technique such as mass spectrometry. The relative concentration in the product species of the two reactions is then used to infer the kinetic rate. Any reactant decay to form alternative products in the gas mixture can be dismissed due to the direct measurement of the product species for the target reaction.

The immediate issue regarding the relative rate method is that the derived rates can only be as accurate as the rate coefficient for the reference reaction. This issue is often mitigated by calculating the rate against several reference reactions. An additional drawback of this technique is that it is a static system. It is difficult to isolate strictly gas-phase reactions in this system, exacerbated in mercury studies as Hg^0 shows a high propensity for surface-catalysed oxidation. Experiments using the relative rate method have utilised halocarbon wax to mitigate mercury-surface interactions [143], however the melting point of the wax would make this approach impossible for flue gas conditions.

The direct measurement of the reaction rate coefficient involves evaluating the rate of change in the concentration of the reactive specie against time. The flash photolysis method for direct rate measurement has been used for mercury reactions [139, 180–182]. Flash photolysis uses a photon source to produce a reactive radical species from a stable mixture of reactants and precursors. The photolysis pulse acts as a starting point for the reaction, whereby the excitation elevates the precursors internal energy to a position that will cause the molecule to dissociate. The eventual decay of the reactant species can be measured through techniques such as laser induced fluorescence (LIF) or absorption spectroscopy. The delay between the photolysis pulse and the detection scheme can be altered to provide a profile of the measured concentration of the tested specie across time.

The flash photolysis method can operate under slow-flow conditions, regenerating the analysed sample between measurements, thus bypassing one of the limitations of the relative rate method. This method can only be applied where at least one of the reactants can be produced from a stable species through laser photolysis, and where the reactants can be monitored via LIF or absorption spectroscopy without interference. It must also be possible to isolate the reactions being studied; any impurities or secondary chemistry could greatly affect the reported values.

2.2.3 Mercury kinetic rates

There are numerous theoretical [93, 94, 109, 113, 114, 137, 183–193] and experimental [139, 143, 180–182, 194–196] studies on the kinetics of mercury oxidation by bromine and chlorine species. Mercury-chlorine reactions have been studied in more detail than their bromine counterparts due to the greater abundance of chlorine species in coal derived flue gas. There is less motivation for studying bromine reactions under combustion conditions as the native concentrations of bromine species are far too low to oxidise mercury. Motivation for studying bromine reactions has increased due to its potential role as an additive to control mercury emissions [197], however some European coals contain a high bromine content that could potentially influence mercury in the native flue gas [87].

Chemical kinetics on mercury-chlorine reactions are usually focussed on the mechanism proposed by Widmer et al. [93], illustrated in Reactions (R 2.1) to (R 2.8) in Subsection 2.1.1. Under this reaction scheme, the recombination of mercury and chlorine atoms, Reaction (R 2.1), is often identified as the rate limiting step due to the scarcity of atomic chlorine, and as a result, this reaction has received the most attention. The Arrhenius plot in Figure 2.2 illustrates the wide variation in the reported rate constants for this key reaction.

The disagreement in reported rate coefficients is owed in some part to the different approaches in measuring and calculating the rate coefficient, as well as the uncertainties in deriving kinetics rates that were outlined in Subsection 2.2.2. Experiments by Donohoue [139] provide the most thorough study on the atomic mercury-chlorine recombination reaction, however the investigation was conducted under ambient temperatures, which reduces the confidence in applying the reported rate coefficient to combustion conditions. The experimental rate coefficients reported by Taylor et al. [180] that were conducted at elevated temperatures are often rejected as the calculated reverse rates are implausibly high, suggesting the presence of secondary chemistry that influenced the experiment [198]. The scale of the difference in the measurements of Donohoue [139] and Taylor et al. [180], for a relatively similar experimental approach, demonstrates the difficulty in accurately measuring reaction kinetics.

One particularly noteworthy rate coefficient in Figure 2.2 is the recent theoretical rate calculated by Krishnakumar and Helble [192], the only published rate that suggests a positive activation energy. This rate serves to illustrate the sensitivity over

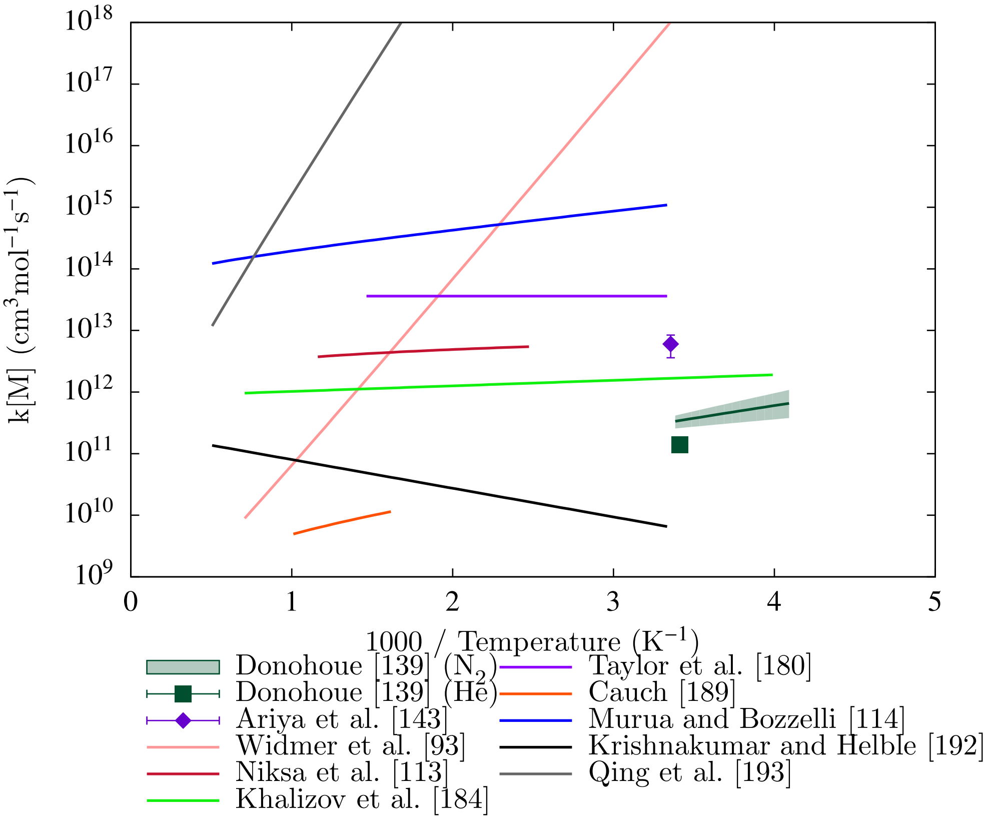

Figure 2.2: Arrhenius plot for Hg + Cl + M $\rightleftharpoons$ HgCl + M rates at atmospheric pressure.

the calculated rate coefficient with regards to the selected basis set and calculation method. An alternative rate coefficient calculated by Krishnakumar and Helble [192] for the same reaction, but derived with a different method and alternative basis set, varied by as much as eight orders of magnitude at low temperatures.

Due to the bias discovered in the Ontario Hydro method, models that were validated against early bench-scale data have been called into question [121]. Previous modelling results, such the results by Fry et al. [199], Niksa et al. [113] and Murua and Bozzelli [114], demonstrated very good approximations of the experimental data, which have since been shown to be invalid. A more recent modelling study conducted by Gharebaghi et al. [198] that combined published rate coefficients achieved good qualitative agreement with bench-scale experimental data by Cauch et al. [121], however the model was unable to show quantitative agreement with the measurements, and exaggerated the influence of temperature over the final mercury oxidation ratio.

Less focus has been applied to mercury-bromine interactions due to the reduced

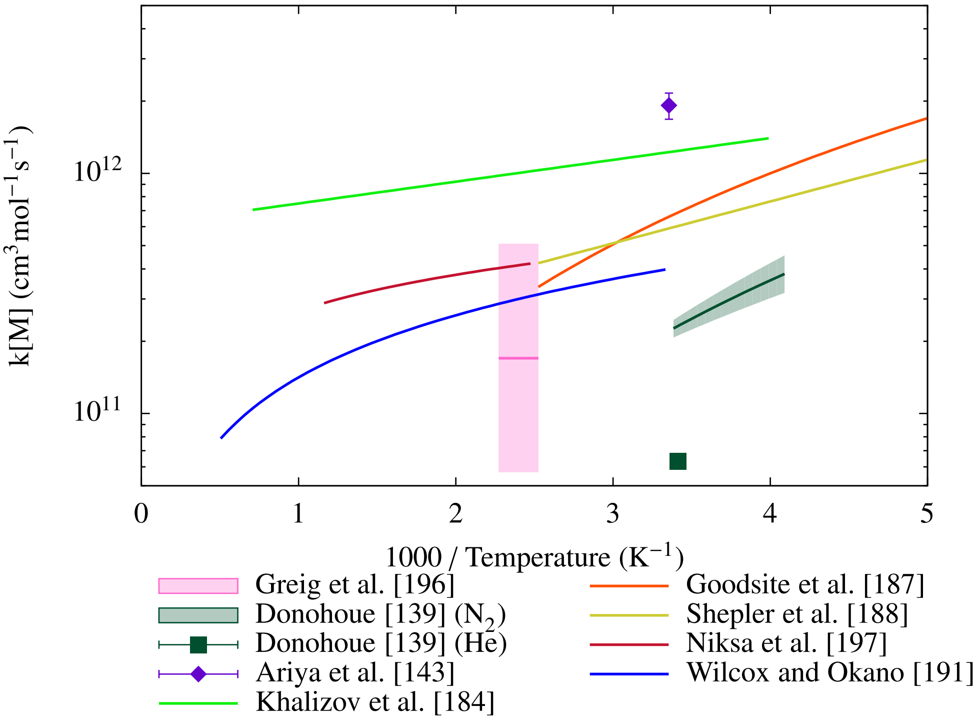

Figure 2.3: Arrhenius plot for $Hg + Br + M \rightleftharpoons HgBr + M$ rates at atmospheric pressure.

concentrations of bromine species in coal-derived flue gas. As with chlorine, the majority of studies on the rate coefficients for bromination have focused on the atomic mercury-bromine recombination reaction. The Arrhenius plot in Figure 2.3 shows much better agreement between the published rates than for the analogous reaction with atomic chlorine. The rates illustrated in Figure 2.3 are all a lot slower than the atomic mercury-chlorine recombination reaction, however, the efficiency of bromine to oxidise mercury is attributed to the far higher proportion of bromine present as atomic bromine under flue gas conditions [126].

Models predicting mercury oxidation rates by bromine have shown good agreement in limited cases, but not across different operating conditions [126, 127, 200]. Unlike mercury oxidation by chlorine species, the atomic recombination reaction is not limited by the concentration of gaseous bromine atoms. Only a few theoretical studies have been published on the remaining reactions between mercury and bromine species [191, 197, 201], leading to considerable uncertainty regarding the full reaction mechanism.

There is a need for further experiments for rate coefficients for key mercury oxidation reactions under combustion conditions. Models incorporating published rate coefficients have been ineffective in being validated against different operational conditions, however the inherent uncertainties in the derived rate parameters offer significant interpretation in the combined result of hundreds of coupled kinetic rates.

2.3 Summary

Under coal-derived flue gas conditions mercury will be oxidised by halogen species and will chemically bind onto activated carbon sites in the native organic fly-ash. Inorganic fly-ash and the chamber walls of the flue gas train could also facilitate the oxidation of mercury. The influence of these complex interactions over the final speciation of mercury, and how they alter under oxy-coal conditions, is highly uncertain. Studies that have focussed on gas-phase reaction kinetics between mercury and the halogens using currently available rate coefficients have been unsatisfactory in being validated against different operational conditions.

It is not clear if homogeneous oxidation of mercury species is relevant for flue gas conditions [105]. The development of a kinetic mechanism that can approximate measured values across operational parameters, such as reactor temperatures and residence times, will offer insight as to whether gas-phase mercury oxidation is plausible with the currently developed mechanisms. Further work is also required to better elucidate the role of gas-phase pollutants such as NO and SO_2 on the oxidation chemistry of mercury.

The work in this thesis aims to improve the understanding of mercury oxidation under oxyfuel conditions through the application of gaseous chemical kinetic models. The study in Chapter 4 takes heed of the uncertainty in kinetic parameters and applies modelling strategies to identify how the combustion environment influences the kinetic scheme of mercury and halogen species, and aims to demonstrate whether current mercury kinetic mechanisms are capable of explaining experimentally determined behaviours. The modelling approach is also used to discuss the relevance of NO and SO_2 on the oxidation chemistry, which will add to the understanding of the potential benefits of different recycle schemes on pollutant controls.

3 CFD modelling for oxy-coal combustion

It is necessary to obtain a detailed representation of gas temperatures and residence times of real combustion systems to predict the performance criteria and pollutant emissions in practical cases. CFD has been applied as a tool to predict the complex behaviour of a wide variety of fluid flows, including coal combustion systems at small laboratory scales [202–204], pilot and demonstration scales [205–216] and large industrial scales [217–219]. CFD employs fundamental laws of energy and mass exchange to calculate the behaviour of fluid flows, allowing the prediction of complicated emergent behaviours from the underlying physical properties of the system. Applying CFD to coal combustion requires the inclusion of sub-models to account for turbulence, combustion chemistry, radiative heat transfer, and multiphase treatment for the interaction between solid fuel particles and the combustion environment. It is often necessary to simplify the numerical representations of physical phenomena within these models so that they can be applied to problems of practical interest, and the inherent assumptions in these simplifications need to be reviewed and validated to gain confidence in the resulting predictions.

Modelling the oxyfuel process is challenging due to the relatively unfamiliar combustion environment, which requires additional confidence in the model solutions to compensate for the lack of experimental experience, particularly at large scales, where there is not enough data available to develop empirical models. Furthermore, the variable combustion environment serves as an additional operating parameter, as the process can vary according to the inlet gas compositions and flue gas recycling scheme. The combustion process will change significantly due to the oxygen enrichment, which can vary between different inlet registers, or due to whether the flue gas is dried, cooled or cleaned prior to its recycle. Clearly, being able to predict the influence of these operating parameters would be beneficial in the optimisation of the oxyfuel combustion process, and will control gas temperatures, combustion efficiency, heat flux and pollutant formation. Traditional modelling capabilities have assumed an air-fired combustion environment [220], and it is necessary to develop models that are less dependent on the combustion environment that can be applied to a wide range of potential oxyfuel conditions.

The high CO_2 concentration within an oxyfuel environment can have a significant impact on the combustion chemistry and radiation heat transfer [79]. Unlike N_2, CO_2 chemically reacts with fuel and intermediate species, as well as absorbing and emitting radiative energy. Due to the complexity of combustion chemistry and radiation, CFD calculations require either heavily simplified models, which enforce relatively sweeping assumptions about the combustion environment, or empirical models that will not translate to a novel environment. The physical properties of CO_2, such as density, viscosity and heat capacity, also vary from those of N_2 and will affect the combustion process [79], however these properties are not usually predefined in calculation methods, and current approaches in CFD calculations are expected to provide adequate predictions of how these properties will affect the combustion process.

Thermal radiation is the most significant mode of heat transfer at the high temperatures found in combustion systems [8]. Radiative energy is absorbed and emitted by participating gas molecules, such as CO, CO_2 and H_2O, which will be present at different concentrations under oxyfuel conditions. Suspended particles also participate in radiative transfer, with solid-phase fuel, char, fly-ash and soot particles exhibiting very strong radiative absorption, emission and scattering [8]. The higher concentrations of the participating gas species in an oxyfuel environment will increase the amount of radiation that is emitted and absorbed by the combustion medium, which will have a direct impact on the gas temperatures, particle heating rates and heat flux to the furnace walls [221]. Accurate predictions of radiative heat transfer are vital in calculating the overall heat flux in combustion systems, which governs the efficiency of coal-fired boilers, as well as surface temperatures that govern the corrosion rates of the furnace materials; two very important, and often counteracting, quantities in defining the optimal combustion regime. Reviews of modelling oxyfuel have repeatedly identified accurate consideration of radiative heat transfer as being a high priority for improving CFD predictions of oxyfuel combustion environments [78–80].

This chapter reviews methods for predicting coal combustion using CFD calculations, with a specific focus on methods that can be used to predict radiative heat transfer. Section 3.1 discusses radiation transfer within a participating medium, focussing on methods used for CFD calculations and how they translate to an oxy-coal environment. Further models for predicting coal combustion using CFD, including the modelling of turbulent flow and coal combustion phenomena, are reviewed in Section 3.3. The discussions in this chapter are summarised in Section 3.4, including an outline of how the research in this thesis develops current approaches for modelling coal combustion using CFD.

3.1 Radiation transfer in a participating medium

Radiation describes energy that is transported as massless particles known as photons, which behave as a wave propagated by the electromagnetic force. Any molecule at a temperature above absolute zero will emit radiative energy, which will be at a specific wavelength that corresponds to the rovibronic state associated with how the energy was stored within the molecule. Radiation can be absorbed at the same wavelengths that it can be emitted from, as a transition between internal energy states can occur in both directions, and can also be scattered through interactions with particles and surfaces, changing the direction of propagation for the energy transfer. Radiation often travels long distances before it is absorbed, enabling energy to be transferred between localised heat sources and distant surfaces. This long distance transfer becomes more significant as the combustion facility increases in size [8, 222].

The transport of radiation energy across a path through a participating medium is described by the radiation transfer equation (RTE). The directional monochromatic RTE at radiative equilibrium, where emission and absorption occur at the same rate, and with a unity index of refraction, is given as [223]

$$\frac{\mathrm{d}I_\eta\left(\hat{\mathbf{r}},\hat{\mathbf{s}}\right)}{\mathrm{d}\hat{\mathbf{s}}} = \kappa_\eta I_{b\eta}\left(\hat{\mathbf{r}}\right) - \left(\kappa_\eta + \sigma_\eta\right) I_\eta\left(\hat{\mathbf{r}},\hat{\mathbf{s}}\right) + \frac{\sigma_\eta}{4\pi}\int_{4\pi}\Phi_\eta\left(\hat{\mathbf{s}},\hat{\mathbf{s}'}\right) I_\eta\left(\hat{\mathbf{r}},\hat{\mathbf{s}'}\right)\mathrm{d}\Omega \tag{3.1}$$

where η denotes wavenumber ($\eta = 1/\lambda$ where λ is wavelength), $I_\eta\left(\hat{\mathbf{r}},\hat{\mathbf{s}}\right)$ is the spectral radiative intensity at location $\hat{\mathbf{r}}$ travelling in direction $\hat{\mathbf{s}}$, $I_{b\eta}\left(\hat{\mathbf{r}}\right)$ is the Planck function evaluated at the temperature at position $\hat{\mathbf{r}}$, κ_η is the spectral absorption coefficient, σ_η is the spectral scattering coefficient, Φ_η is the scattering phase function and Ω denotes solid angle. The assumption of radiative equilibrium is often valid for combustion applications as the time-scales of radiative transfer, proportional to the speed of light within the medium, are far smaller than processes that govern the quantities in the RTE. Equation (3.1) describes the change in monochromatic radiation across a single ray, where the three terms on the right hand side represent radiative emission, attenuation from absorption and out-scattering, and augmentation from in-scattering respectively. The RTE is subject to the following boundary condition, assuming diffusely reflecting opaque walls, [223]

$$I_{w\eta}\,(\hat{\mathbf{r}}_w) = \epsilon_w I_{b\eta}(\hat{\mathbf{r}}_w) + \frac{1-\epsilon_w}{\pi} \int_{\hat{\mathbf{s}}\cdot\hat{\mathbf{n}}<0} I_\eta(\hat{\mathbf{r}},\hat{\mathbf{s}})|\hat{\mathbf{s}}\cdot\hat{\mathbf{n}}|\,\mathrm{d}\Omega \tag{3.2}$$

where I_w is the intensity leaving the wall surface, ϵ_w is the emissivity of the wall, $\hat{\mathbf{n}}$ is the inward facing wall normal and $\hat{\mathbf{r}}_w$ is a position on the wall surface. The RTE represents an integro-differential equation that is defined across three spatial and two angular dimensions, which can not be solved analytically in most practical situations, and therefore must be solved with approximate methods.

The Planck function, which is denoted by $I_{b\eta}$ in the above equations, describes the monochromatic emission of intensity from a black-body, which is defined as an idealised object that absorbs all incident radiation. The Planck function describes the spectral distribution of emission at a given temperature, and is given as [223]

$$I_{b\eta}(T) = 2hc^2\eta^3 \frac{1}{\exp\left(hc\eta/(k_{\mathrm{B}}T)\right) - 1} \tag{3.3}$$

where T is the temperature of the black-body object, h is the Planck's constant, c is the speed of light in the medium and k_{B} is the Boltzmann constant. The spectrally integrated form of the Planck function can be evaluated as [223]

$$I_b(T) = \int_0^\infty I_{b\eta}(T)\,\mathrm{d}\eta = \frac{2\pi^4 k_{\mathrm{B}}^4}{15h^3c^2}T^4 = \frac{\sigma_{\mathrm{SB}}}{\pi}T^4 \tag{3.4}$$

where σ_{SB} is the Stefan-Boltzmann constant. Equation (3.4) demonstrates the origin of the fourth-power relationship between temperature and radiative emission, which is the reason why radiation quickly becomes the most significant thermal transfer mode at high temperatures. The Planck function evaluated at three temperatures, 1500 K, 2000 K and 2500 K, is shown in Figure 3.1, which illustrates how the spectrally integrated emissive power increases with temperature, as well as the spectral range that is relevant to these temperatures.

The radiative intensity field is coupled to the energy solution in CFD calculations through the radiation source term in the energy equation, accounting for the energy exchange between the radiation field and the fluid enthalpy, and the radiative heat flux, where radiative energy is exchanged with the boundaries of the medium. The radiation source term is the divergence of radiative heat flux through a medium, and

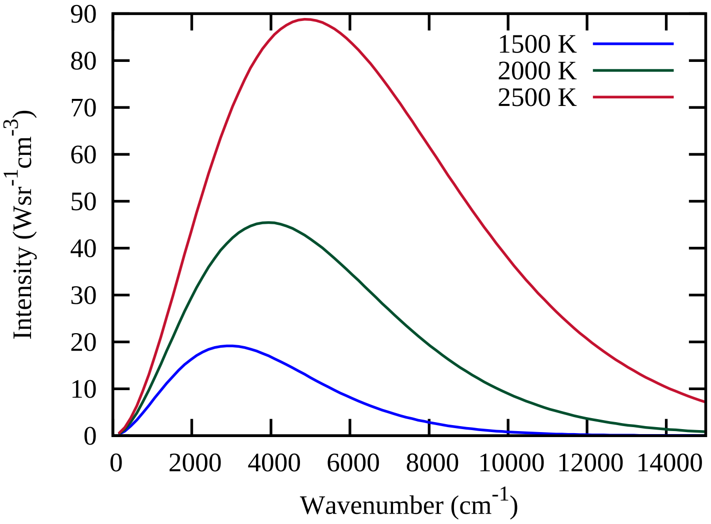

Figure 3.1: The Planck function, Equation (3.3), evaluated at two different temperatures.

can be expressed as the net change in intensity across a volume,

$$\nabla \cdot \mathbf{q}_{\mathrm{R}} (\hat{\mathbf{r}}) = \int_0^{\infty} \kappa_\eta \left(4\pi I_{b\eta} (\hat{\mathbf{r}}) - \int_{4\pi} I_\eta (\hat{\mathbf{r}}, \hat{\mathbf{s}}) \, \mathrm{d}\Omega \right) \mathrm{d}\eta \tag{3.5}$$

where $\mathbf{q}_{\mathrm{R}}$ is the radiative heat flux at a position in the domain. The radiation source term is important in calculating the temperature field, which has a significant impact on gas velocities and chemical kinetics. The radiative contribution to the total heat flux at a surface can be calculated as the complement of Equation (3.2) in terms of the amount of energy absorbed and emitted at the boundary;

$$\mathbf{q}_{\mathrm{R}} (\hat{\mathbf{r}}_w) \cdot \hat{\mathbf{n}} = \int_0^{\infty} \epsilon_w \left(\int_{\hat{\mathbf{s}} \cdot \hat{\mathbf{n}} < 0} I_\eta (\hat{\mathbf{r}}, \hat{\mathbf{s}}) |\hat{\mathbf{s}} \cdot \hat{\mathbf{n}}| \, \mathrm{d}\Omega \right) - \epsilon_w \pi I_{b\eta} (\hat{\mathbf{r}}_w) \, \mathrm{d}\eta \tag{3.6}$$

where, again, $\hat{\mathbf{n}}$ is the inward surface normal and $\hat{\mathbf{r}}_w$ is a position on the surface. The majority of the heat flux during combustion arises from radiative transfer to the walls, and so the accurate calculation of this quantity will have a significant influence over the calculated heat transfer for the system being modelled.

To evaluate the spectrally integrated quantities of interest, Equations (3.5) and (3.6), the RTE needs to be solved for numerous discrete intervals across the spectral dimension to accurately resolve the radiative intensity. A direct approach to solving radiative

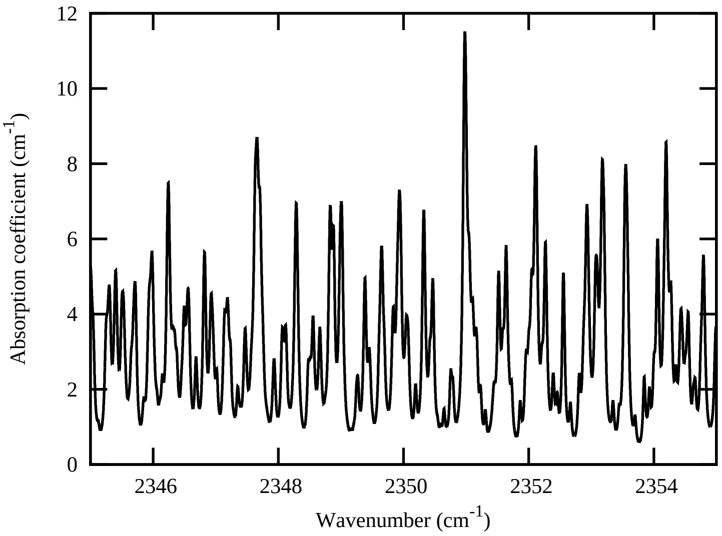

Figure 3.2: The absorption coefficient of CO_2 over a small band of the electromagnetic spectrum at a temperature of 1500 K. The absorption coefficient was calculated from the HITEMP2010 database [224].

transfer, the line-by-line (LBL) method, requires solving the RTE for over 10^5 spectral intervals, due mostly to the erratic variation of the absorption coefficient across the spectral dimension. The absorption coefficient for CO_2 across a narrow band of the spectrum is shown in Figure 3.2, illustrating how the coefficient changes rapidly for small changes in the spectral dimension; note that the horizontal axis in Figure 3.2 is only 10 cm^{-1}, compared to 15000 cm^{-1} in Figure 3.1. It is necessary to model the absorption coefficient to calculate the spectrally integrated values with reasonable resources, which requires assumptions that may reduce the accuracy of the predictions, and therefore require validation.

This section reviews approximate methods for solving the RTE to predict the radiative intensity field and methods to model spectral radiation transfer. Popular methods that are often used for CFD calculations to evaluate the radiative intensity across spatial and angular dimensions are discussed in Subsection 3.1.1. Models that are used to simplify the evaluation of spectrally integrated quantities are reviewed in Subsection 3.1.2, focussing on methods that are applicable to CFD solutions of oxyfuel combustion.

3.1.1 Solving the radiation transfer equation

The monochromatic radiative intensity field is defined across three spatial and two angular dimensions, resulting in the requirement of approximate methods to solve its transfer for most practical applications. There have been numerous developments of methods to solve radiative transfer problems, and this subsection discusses some of the most popular methods that have been applied to CFD calculations, focussing on their suitability for oxycoal conditions.

3.1.1.1 Method of spherical harmonics

In the method of spherical harmonics, widely referred to as the P_{N} method or the differential approximation, the radiative intensity field, $I_\eta(\hat{\mathbf{r}}, \hat{\mathbf{s}})$, that is defined across position $\hat{\mathbf{r}}$ and direction $\hat{\mathbf{s}}$, is recast in terms of a two-dimensional Fourier series as [225]

$$I_\eta(\hat{\mathbf{r}}, \hat{\mathbf{s}}) = \sum_{l=0}^{\infty} \sum_{m=-l}^{l} I_l^m(\hat{\mathbf{r}}) \, Y_l^m(\hat{\mathbf{s}}) \tag{3.7}$$

where $I_l^m(\hat{\mathbf{r}})$ are position-dependent coefficients and $Y_l^m(\hat{\mathbf{s}})$ are spherical harmonics, which are predetermined coefficients based on direction, and that satisfy Laplace's equation in spherical coordinates. The truncation of the infinite series in Equation (3.7) to $l = N$ gives rise to the order of the P_{N} method. Modification of the RTE to describe the transfer of the terms in Equation (3.7) results in a series of coupled partial differential equations for the unknowns $I_l^m(\hat{\mathbf{r}})$. Recent developments in the spherical harmonics method has reduced the number of partial differential equations to $N(N+1)/2$, where N is the order of the method [225, 226].

The most widely used order for the spherical harmonics method is the P_1 method, which maintains the series for $l = 0$ and $l = 1$. The P_1 method has been widely used within CFD calculations due to its simplicity, as the RTE can be reduced to a single scalar transport equation [223]. The extension of the P_{N} method to higher orders is a non-trivial task, however recent developments have applied a general implementation of the method to CFD codes, with results up to the P_7 method [225–230]. Even-ordered methods are known to be less accurate than the lower odd-ordered method, and are therefore never used [8].

It is not possible to directly satisfy the boundary condition for the RTE, as shown in Equation (3.2), using the spherical harmonics method as the intensity is no longer represented on a directional basis. Instead, the boundary condition is often satisfied only in an integral sense, resulting in the so-called Marshak's or Mark's boundary conditions, the latter of which is seldom used as it is difficult or impossible to apply to complex geometries [223]. Additionally, the P_{N} method has been shown to perform poorly in optically thin media or in regions where the radiative transfer is highly anisotropic, such as at the boundaries of the domain or in highly scattering regions [8, 231], although higher orders, such as the P_3 method, can somewhat overcome this. The method is most suitable to optically thick media [232], where the radiative field is dominated from isotropic emission within the domain, and anisotropic emission from the boundaries is absorbed over a relatively short path-length [225]. Some extensions to the method, such as the modified differential approximation [233] or improved differential approximation [234], have been developed to account for this shortfall of the P_{N} method by calculating the radiation arising from the boundaries and the medium separately. However, as suspended particles are often treated with spectrally constant radiative properties, there are no transparent windows in a coal combustion medium and these methods cannot be used.

One of the most important quantities in the optimisation of the combustion process is the heat flux to the boiler walls. The calculation of the radiative heat at the boundaries can be highly anisotropic, and the P_{N} method does not faithfully represent the boundary intensities. As the majority of the heat transfer through the furnace walls is derived from radiative heat, the P_{N} method is ill-suited for the prediction of heat flux, and thus will be unsuitable for the optimisation of the oxyfuel process, however as a coal combustion medium is optically thick, the P_{N} method will be suitable for calculating gas temperatures in the furnace, which is likely to compensate for small inaccuracies at the boundaries. Furthermore, as a spectral solution method, the spherical harmonics method is likely to provide faster convergence over the more widely used finite difference methods [225].

3.1.1.2 Discrete transfer method

The discrete transfer method (DTM), developed by Lockwood and Shah [235], solves the integral form of the RTE, which is presented for the path between two nodal points, positioned at points $\hat{\mathbf{r}}_n$ and $\hat{\mathbf{r}}_{n+1}$, as

$$I_\eta\left(\hat{\mathbf{r}}_{n+1}, \hat{\mathbf{s}}\right) = I_\eta\left(\hat{\mathbf{r}}_n, \hat{\mathbf{s}}\right)\tau_{n\to n+1} + S_\eta\left(1 - \tau_{n\to n+1}\right) \tag{3.8}$$

where S_η is the radiative source function and $\tau_{n\rightarrow n+1}$ is the transmissivity across the path between the two nodal points, defined as

$$\tau_{n\rightarrow n+1} = \exp[\int_{n}^{n+1} -\beta \,\mathrm{d}s] \tag{3.9}$$

where $\int_{n}^{n+1} \mathrm{d}s$ denotes integration across the path $|\hat{\mathbf{r}}_{n+1} - \hat{\mathbf{r}}_n|$ and β $(= \kappa + \sigma)$ is the extinction coefficient of the medium. The radiative source function is given as

$$S_\eta = (1-\omega)\, I_{b\eta,n+1/2} + \frac{\omega}{4\pi}\int_{4\pi} I\left(\hat{\mathbf{s}}'\right)\Phi_\eta\left(\hat{\mathbf{s}},\hat{\mathbf{s}'}\right)\mathrm{d}\Omega \tag{3.10}$$

where ω $(= \sigma/\beta)$ is the single scattering albedo. The integral on the right hand side of Equation (3.10) is approximated for an isotropic phase function ($\Phi_\eta\left(\hat{\mathbf{s}},\hat{\mathbf{s}'}\right) = 1$) as [236]

$$\int_{4\pi} I\left(\hat{\mathbf{s}}'\right)\mathrm{d}\Omega \approx \frac{4\pi\sum_i \bar{I}\left(\hat{\mathbf{s}}_i\right)\delta\Omega_i}{\sum_i \delta\Omega_i} \tag{3.11}$$

where $\bar{I}\left(\hat{\mathbf{s}}_i\right)$ is the mean intensity between $I_\eta\left(\hat{\mathbf{r}}_n, \hat{\mathbf{s}}_i\right)$ and $I_\eta\left(\hat{\mathbf{r}}_{n+1}, \hat{\mathbf{s}}_i\right)$ and $\delta\Omega$ denotes discrete intervals across the solid angle. Scattering is rarely implemented when the DTM is applied to CFD calculations. The boundary condition in Equation (3.2) is used directly in the DTM.

The method traces rays from control surfaces through the domain, solving the integral equation across the path of the rays. The amount of radiation that is absorbed and emitted by the control volumes as the ray is being traced are accounted for, and the radiative source term is calculated based on the net intensity through the volume. The rays originate from the boundaries of the domain, where the originating intensity can be obtained from Equation (3.2). In the case of reflecting walls or a scattering medium, the solution procedure is iterative. A numerical quadrature of the solid angle is used to determine the number and direction of the rays.

The DTM is a relatively straightforward representation of the physical phenomena of radiative transfer, and can easily be extended to higher accuracy by increasing the number of rays that are traced. The DTM method is the only widely used approach that solves the integral form of the RTE directly. The main drawback of the DTM is that the method has been shown to require significantly larger computational time than other solution methods, without any noticeable gain in accuracy [237, 238], however it should be mentioned that the memory overhead of the method can be significantly lower than other methods.

3.1.1.3 Discrete ordinates and finite volume methods

The discrete ordinates (DO) method and the finite volume method (FVM) are two of the most popular methods for calculating radiative transfer through a participating medium. The DO method solves the positional dependence of the RTE using a finite volume approach, and employs a quadrature scheme to solve the angular integrations, so that they are approximated by a weighted sum [239],

$$\int_{4\pi} I\left(\hat{\mathbf{r}}, \hat{\mathbf{s}}\right) \mathrm{d}\Omega \approx \sum_{i=1}^{n} w_i I\left(\hat{\mathbf{r}}, \hat{\mathbf{s}}_i\right) \tag{3.12}$$

where n represents the number of directions in the quadrature and w_i is the weight associated with direction $\hat{\mathbf{s}}_i$. This approach assumes that the radiation intensity is constant within each ordinate in the quadrature set used to describe the solid angle, and becomes exact as the number of ordinates approaches infinity. This ability to extend the method relatively easily for increased accuracy, traded against the computational expense of calculating additional ordinates, has made the method very popular. Furthermore, as the radiation intensity is calculated on a directional basis, it is more accurate than the P_{N} method for calculating radiative heat transfer at the boundaries of the domain.

Drawbacks to the DO method include the tendency to predict false scattering effects, where spatial discretisation errors induce a smearing of the radiative propagation, and ray affects, where propagation becomes biased into the direction of singular ordinates, and the transport of radiation across angular intervals is lost. Both of these effects can be mitigated by increasing the spatial and angular discretisations respectively, however these effects are known to cancel each other out when both are under-resolved, which will lead to false conclusions when only one discretisation is refined [240, 241].

The DO method does not conserve scattered energy unless the phase function is integrated exactly using the quadrature scheme [242]. Methods to renormalise the phase function to ensure that the in-scattering and out-scattering terms are balanced have been suggested [243, 244], however these methods invariably introduce additional false scattering or require a significantly high number of quadrature points to adequately resolve the phase function, and so the DO method is realistically restricted to isotropic scattering in CFD calculations [245]. The use of isotropic phase functions will introduce significant errors in complex geometries, however in symmetric cases, the anisotropic factors will often cancel out, and thereby reduce the reliance on complex phase functions [246].

The FVM is an extension of the DO method, whereby the angular discretisation is described by non-overlapping finite angles, and the method is a finite volume method both in space and direction [247]. The method can be fully conservative as analytical integrations over the control angles can be achieved, however in practice, highly irregular scattering phase directions still require large numbers of control volumes to be described faithfully, which is often prohibitive. The main benefit of the FVM approach is that it is more readily expanded, as the discretisation in the polar and azimuthal angles are explicitly provided, and the method is more amenable to more complex computation meshes with arbitrary control volume geometries.

Both the DO method and the FVM require iterative solution procedures in cases with scattering media or non-black walls, which requires the storage of nodal intensity values for each direction in the quadrature method. As the number of directions required in either method often exceeds fifty for modest angular discretisations, the memory requirement is significant, and can become a limiting factor in case sizes. This requirement is also scaled linearly with each spectral interval, so for a S_8 quadrature for five spectral intervals, the DO approach requires the memory storage of 400 intensity values for each control volume in the domain, which is far higher than any memory storage requirements of any other typical CFD sub-model. These two methods are also known to converge slowly in optically thick media, such as coal combustion conditions. In some cases it may be necessary to follow a solution procedure that first employs the P_1 method to achieve a reasonable temperature distribution quickly, followed by a FVM approach for the more accurate solution of the radiative intensity field.

3.1.1.4 Monte Carlo ray tracing method

The Monte Carlo ray tracing method solves the integral form of the RTE in the same fashion as the DTM, however the ray trace is governed by random sampling [223]. The initial position of the ray and its wavenumber is determined stochastically, as well as any directional scattering the ray may encounter as it is traced. The ray is typically traced until its intensity diminishes to insignificance, reflecting off any non-black walls as it is traced. As the number of rays reaches infinity, the solution converges to an exact result.

The main drawback is that the Monte Carlo method takes a large number of rays to reach a stable solution, which is not generally feasible in coupled CFD calculations. Furthermore, the ray tracing approach is not well-suited to the grid partitioning method that is usually used to distribute CFD calculations across multi-node architectures, as the rays will need to frequently cross these boundaries. However, as mentioned with the DTM, the ray tracing approach has a very small memory overhead, and it is possible to apply high resolution spectral information to the solution to achieve accurate benchmark solutions in complex geometries. It is also possible to estimate the error in benchmark solutions with the Monte Carlo method by analysing the statistical variance.

3.1.1.5 Zonal method

The zonal method decomposes the problem of interest into reasonably coarse volumes and surfaces, referred to as zones, where the radiative properties are considered uniform [248, 249]. The radiative exchange between these zones is calculated based on the evaluation of ‘exchange areas’, which describe the net proportional transfer between each zone. The calculation of these areas is an expensive task, particularly for complex geometries [250], and is dependent upon the optical properties of a participating medium. Due to this computational expense, it is necessary to use a reasonably coarse grid to define the zones, which can lead to inaccurate representations of the problem.

As the radiative properties of a medium vary relatively coarsely compared to the fluid properties, it is not necessary to refine the grid in the zonal model to the degree that is necessary for CFD predictions. This is especially the case for near wall treatment for fluid flow, which requires a very high spatial resolution that is wholly unnecessary for calculating radiative heat transfer where the optical properties of the fluid are unlikely to change through the boundary layer. It is necessary to take advantage of this property to employ the zonal method to CFD calculations by using two different grids [251], however the coupling between two different discretisation methods for the radiative transfer and fluid flow is not simple, and could possibly lead to interpolation errors.

3.1.2 Modelling radiative properties

The calculation of spectral radiative heat transfer is computationally difficult due to the large variability of the spectral absorption coefficient. Each spectral interval used to evaluate the radiative intensity typically requires an additional RTE solution, thereby linearly scaling the resources required for the calculation. There have been numerous developments in spectral models to reduce the computational burden of evaluating the total radiative intensity, effectively reducing the number spectral intervals to be

Database	Molecule	No. of lines
HITRAN2012 [252]	CH_4	468,013
HITEMP2010 [224]	H_2O	114,241,164
	CO_2	11,193,608
	CO	113,631
CDSD-4000 [253]	CO_2	628,324,454

Table 3.1: Details of LBL databases for combustion gasses.

reduced from an order of over 10^5 to typically less than 10, allowing the accurate accounting of radiative transfer in a participating medium to be coupled with fluid flow calculations. This subsection reviews models that can be used for modelling spectral radiative transfer under oxyfuel conditions, and identifies methods that are suitable for CFD calculations.

3.1.2.1 The line-by-line method

The line-by-line (LBL) method is the most exhaustive approach to modelling spectral radiation. The method calculates radiative intensity at a very high spectral resolution, using an absorption coefficient calculated from high resolution spectroscopic databases that describe individual molecular energy transitions. The spectral databases are often generated from ab initio calculations, but are also combined with experimentally measured transmission lines. A list of recently published spectroscopic databases is shown in Table 3.1, detailing the number of spectral transitions that are described for molecules that are of interest to combustion in each database. These spectroscopic data are used in numerous fields, such as astrophysics, meteorology and lab-scale spectroscopy, as well as studying radiative heat transfer in combustion.

The databases store line intensities, S, that represent the total absorption coefficient attributable to a single energy transition,

$$S \equiv \int_0^\infty \kappa_\eta \, \mathrm{d}\eta \tag{3.13}$$

The line intensities are stored at a reference temperature, usually 296 K, and need to be scaled to temperatures of interest [224];

$$S(T) = S(T_0) \frac{Q(T_0)}{Q(T)} \frac{\exp(-c_2 E_l/T)}{\exp(-c_2 E_l/T_0)} \frac{1 - \exp(-c_2 \eta_0/T)}{1 - \exp(-c_2 \eta_0/T_0)} \tag{3.14}$$

where T_0 is the reference temperature, $Q(T)$ is the total internal partition sum at temperature T, c_2 is the second radiation constant ($c_2 = hc/k_\text{B} \approx 0.01439$ m K), η_0 is the line centre and E_l is the energy related to the lower-state of the transition. The line centre η_0 in the above equation must also be corrected for pressure induced shifts, and is calculated from the provided vacuum wavenumber η_{vac} as

$$\eta_0 = \eta_{vac} + \delta_s p \tag{3.15}$$

where δ_s is the air-pressure-induced line shift and p is the total pressure. The quantities of the above equations; $S(T_0)$, E_l, η_{vac} and δ_s, are all provided as part of the spectroscopic databases. The total internal partition sum $Q(T)$, which represents a summation of all possible rovibronic energy transitions at a given temperature, is usually supplied separately for easier evaluation.

The distribution of a single line intensity across wavenumbers is caused by the probabilistic nature of quantum mechanics, known as natural broadening, as well as collisional and Doppler broadening. The natural and collisional broadening result in the same Lorentz line profile, which describes the monochromatic absorption coefficient κ_η that arises from the line S in isolation as [254]

$$\kappa_\eta = \frac{S}{\pi} \frac{\gamma_l}{(\eta_0 - \eta)^2 + \gamma_l^2} \tag{3.16}$$

where γ_l is the Lorentz line half-width at half-maximum and η_0 is the centre of the line intensity. The line-width γ_l depends the gaseous mixture, and is defined in the databases as the combination of self-broadening, $\gamma_{l,self}$, and air-broadening, $\gamma_{l,air}$, as well as a temperature exponent n, and is calculated as [254]

$$\gamma_l = \left(x\gamma_{l,self} + (1 - x)\gamma_{l,air}\right) \frac{p}{p_0} \left(\frac{T_0}{T}\right)^n \tag{3.17}$$

where x is the mole fraction of the participating species, p_0 is a reference pressure and T_0 is a reference temperature, usually set to 1 atm and 296 K respectively.

Doppler broadening is caused by shifts in the observed spectrum due to relative motion of the emitting body. The absorption coefficient caused by Doppler broadening is calculated as [223]

$$\kappa_\eta = \frac{S}{\gamma_d} \sqrt{\frac{\ln 2}{\pi}} \exp\left[-(\ln 2)\left(\frac{\eta_0 - \eta}{\gamma_d}\right)^2\right] \tag{3.18}$$

where γ_d is the Doppler line half-width, which is given by [223]

$$\gamma_d = \frac{\eta_0}{c_0} \sqrt{\frac{2k_{\mathrm{B}}T}{m_a} \ln 2} \tag{3.19}$$

where m_a is the mass of the molecule and c_0 is the speed of light in a vacuum.

The combination of both Lorentz and Doppler broadening leads to a Voigt line profile, where the absorption coefficient due to both effects is evaluated as [223]

$$\kappa_\eta = \frac{S\gamma_l}{\pi^{3/2}} \int_{-\infty}^{+\infty} \frac{\exp(-x^2)}{\left(\eta - \eta_0 - \frac{x\gamma_d}{\sqrt{\ln 2}}\right)^2 + \gamma_l^2} \, \mathrm{d}x \tag{3.20}$$

where

$$x = v\sqrt{\frac{m_a}{2k_{\mathrm{B}}T}} \tag{3.21}$$

and where v is the relative velocity of the molecule. As there is no closed-form solution to Equation (3.20), the profile is often approximated using the Humlíček [255] algorithm. Doppler broadening is often negligible with respect to Lorentz broadening at temperatures below 2000 K, and so it is often suitable to use Equation 3.16 to describe the line shape [223, 256]. The total absorption coefficient at a specific wavenumber is evaluated by accumulating the individual contributions from all of the overlapping spectral lines.

While the LBL method provides a very detailed representation of the physical phenomena concerned in radiative transfer, the method's obvious downside is that the method requires such enormous resources that it is impractical in most cases. The LBL method requires a significant number discrete intervals of the absorption coefficient to describe the part of the spectrum of interest, ranging between 10^5 to 10^7 values for the absorption coefficient [256, 257], with the calculation of the absorption coefficient itself being very time consuming, involving accumulating the integration of around 10^8 line intensities. The storage of all these spectral intervals and radiation lines also requires vast amounts of memory, which makes any problem with variations in the absorption coefficient very difficult to calculate. However, the method introduces very few approximations, which results in very good agreement with high-resolution experimental measurements [256, 258, 259]. Due to this good agreement and a lack of approximations, the method is also widely used in the development of benchmark data for validating other models in cases where experimental data isn't available [257, 260]. The LBL method is also integral in the development of the more time-efficient models discussed below, where the results of the LBL method are used to produce parameters on a different spectral resolution.

3.1.2.2 Statistical narrow band model

The statistical narrow band (SNB) model is a narrow band model that shows very good agreement with experimental measurements [259, 261] and LBL calculations [260, 262–265]. The model assumes that absorption lines across a narrow band are randomly spaced and have a random distribution of strengths. Under this approximation, the band-averaged transmissivity across a path between $\hat{\mathbf{r}}_n$ and $\hat{\mathbf{r}}_{n+1}$, $\bar{\tau}_{n \to n+1}$, can be expressed as [266]

$$\bar{\tau}_{n \to n+1} = \exp\left[-\frac{\bar{W}_{n \to n+1}}{\bar{\delta}}\right] \tag{3.22}$$

where $\bar{\delta}$ is the average line spacing and $\bar{W}_{s \to s'}$ is the arithmetic mean of the equivalent line width, $W_{s \to s'}$. The equivalent line width between two positions describes the fraction of incoming radiation that is absorbed across the path, and is defined for a single absorption line as

$$W_{n \to n+1} = \int_{-\infty}^{+\infty} 1 - \exp\left(-\kappa_\eta |\hat{\mathbf{r}} \to \hat{\mathbf{r}}_{n+1}|\right) \mathrm{d}\eta \tag{3.23}$$

where κ_η in the above equation represents the absorption coefficient for a single line transition. There are several statistical models that describe a probability distribution for the line strengths across the narrow band, however the Malkmus [267] SNB model has shown particularly good agreement with LBL calculations and experiments [259–261, 264, 268]. The Malkmus [267] model applies an exponential-tailed S^{-1} probability distribution for the line strengths and assumes a Lorentz line shape, approximating the mean transmissivity across a narrow band as

$$\bar{\tau}_{s \to s'} = \exp\left[-\frac{2\bar{\gamma}_l}{\bar{\delta}}\left(\sqrt{1 + \frac{\bar{k}\bar{\delta}xp|s \to s'|}{\bar{\gamma}_l}} - 1\right)\right] \tag{3.24}$$

where $\bar{\gamma}_l$ is the mean spectral line Lorentz half-width, $\bar{k}$ is the mean intensity-to-spacing ratio, x is the mole fraction of absorbing species and p is the total pressure of the medium. The SNB parameters are usually derived from LBL spectral databases [262, 263]. The transmissivity of a mixture of absorbing species, such as CO_2 and H_2O, is often calculated under the assumption that the absorption lines of the gasses are statistically independent, and can therefore be calculated as the product of single-specie transmissivities,

$$\bar{\tau}_{s\rightarrow s',mix} \approx \prod_{i}^{N_s} \bar{\tau}_{s\rightarrow s',i} \tag{3.25}$$

where N_s is the number of participating species.

The Curtis-Godson approximation [269] is often applied with the SNB model for non-isothermal or non-homogeneous media [261, 270–272]. Under this approximation the transmissivity is calculated as an equivalent homogeneous path, using path-averaged band parameters in Equation (3.24), which is valid if it is assumed that the spectral dependence of the band parameters can be removed from the dependence on local properties, known as the scaling approximation. The Curtis-Godson approximation has been shown to be accurate for most cases without significant pressure gradients across the path [260, 273].

The SNB model requires the solution of the RTE for greater than 100 bands, which is generally prohibitive for CFD calculations. A further drawback of the SNB model is that the method describes the optical properties of the medium as a path-dependent quantity; the gas transmissivity. As such, the method cannot be applied to general RTE solution methods, and must be applied with methods that resolve the integral form of the RTE, such as the DTM. This drawback of the SNB method also means that the model is ill-suited for scattering media [274] or for cases with reflecting walls without introducing considerable effort [275]. Furthermore, due to the resolution of band-averaged quantities, it is necessary to also calculate additional terms in the radiative transfer to accommodate correlation terms across spectral intervals [270], further increasing the computational demand of the method. Despite these difficulties, in cases with black walls and a non-scattering medium, the SNB method can produce very accurate results that can be used in the absence of LBL solutions for benchmarking global models [265].

3.1.2.3 Correlated-k method

The correlated-k (CK) method is an alternative narrow band model for optical gas properties that has also shown good agreement with LBL calculations [274, 276–278]. Unlike the SNB model, the CK method resolves the gas absorption directly, and is therefore applicable to general RTE solution methods. The CK method replaces the absorption coefficient within a narrow band with a reordered k-distribution, which is a smooth function that can be integrated efficiently.

Under the assumption that only the absorption coefficient varies significantly across a narrow band, a k-distribution, $f(\underline{\phi}, k)$, is generated by accumulating the frequency that the absorption coefficient takes the same value [279],

$$f(\underline{\phi}, k) = \frac{1}{\Delta\eta} \int_{\Delta\eta} \delta(k - \kappa_\eta(\eta, \underline{\phi}))\,\mathrm{d}\eta \tag{3.26}$$

where $\underline{\phi}$ is a vector containing the local variables that affect the absorption coefficient, namely temperature, pressure and the mole fractions of participating species, and δ is the Dirac delta function. The k-distribution itself represents the fraction of the narrow band where the absorption coefficient is equal to the parameter k, thereby grouping the spectral regions of similar absorption, which can be solved with identical RTE solutions, assuming that only κ_η varies across the narrow band. The cumulative k-distribution, which is denoted as $g(\underline{\phi}, k)$, is defined as [279]

$$g(\underline{\phi}, k) = \int_0^k f(\underline{\phi}, k')\,\mathrm{d}k' \tag{3.27}$$

where the cumulative distribution represents the fraction of the narrow band where the absorption coefficient is less than k, and is a smooth monotonically increasing function that is bound between 0 and 1. Integration of the inverse function of Equation (3.27), which is denoted as $k(\underline{\phi}, g)$, between 0 and 1 is equivalent to integrating the absorption coefficient across all wavenumbers within the narrow band; however due to the smooth variation in the k-g distribution, this integration can be done using very few points and an accurate numerical quadrature scheme. In addition to evaluating the k-g distribution from line-by-line data, as shown above, it is also possible to calculate $g(\underline{\phi}, k)$ from SNB parameters [280], resulting in the so-called statistical narrow-band-based correlated-k (SNB-CK) method.

Neglecting scattering, the RTE for the narrow band k method that describes the transfer of band-averaged intensity across g-space, $\bar{I}_{g\Delta\eta}$, in a homogeneous medium is expressed as [279]

$$\frac{\mathrm{d}I_{g,n}\left(\hat{\mathbf{r}}, \hat{\mathbf{s}}\right)}{\mathrm{d}\hat{\mathbf{s}}} = k_n(\underline{\phi}, g)\left(I_{b\eta,n} - \bar{I}_{g,n}\left(\hat{\mathbf{r}}, \hat{\mathbf{s}}\right)\right) \tag{3.28}$$

where $I_{g,n}$ is the radiative intensity in g-space of the narrow band n, $k_n(\underline{\phi}, g)$ is the k-g distribution for the narrow band and $I_{b\eta,n}$ is the Planck function evaluated at the centre of band n. Following the calculation of the intensity field in g-space using Equation (3.28), the spectrally integrated intensity can be calculated from the band-averaged intensity, which is often evaluated using an efficient Gauss quadrature scheme,

$$I = \sum_{n}^{N_{bands}} \Delta_{\eta,n} \bar{I}_{\Delta\eta} = \sum_{n}^{N_{bands}} \Delta_{\eta,n} \int_0^1 I_{g,n} \,\mathrm{d}g \approx \sum_{n}^{N_{bands}} \Delta_{\eta,n} \sum_{i}^{N_q} w_i I_{g_i,n} \tag{3.29}$$

where N_{bands} is the number of spectral bands, $\Delta_{\eta,n}$ is the width of band n, N_q is the number of quadrature points used for integration, which is typically less than seven points [263, 281], w_i is the quadrature weight associated with point i, and $I_{g_i,n}$ is the intensity in g-space associated with the quadrature abscissa point i in band n. The number of bands required for the CK method is often less than the SNB method, however a separate RTE evaluation is required for each quadrature point in each band, so the total number of RTEs required are often similar.

The k-distribution of a gas mixture can be assembled from the single-specie k-distributions under the same approximation introduced for the SNB model in Equation (3.25), where absorption lines are assumed to be statistically uncorrelated. Applying this approximation to k-g distributions results in the mixing scheme by Modest and Riazzi [282], whereby the mixture cumulative k-distribution of two species can be calculated as

$$g_{mix}(\underline{\phi}, k_{mix}) = \int_0^1 g_2(\underline{\phi}, k_{mix} - k_1(\underline{\phi}, g_1)) \,\mathrm{d}g_1 \tag{3.30}$$

The reordering operation in the narrow band k method is not consistent between thermodynamic states, and so the groupings within two different k-distributions often represent separate absorption lines, and therefore should not interact. If the absorption coefficient is assumed to be correlated within the narrow bands between the two states, where variations in the absorption coefficient can be mapped independently from the spectral quantity, it can be shown that the cumulative k-distributions are equivalent, and the method is valid [279]. This correlated assumption often breaks down in cases with significant gradients in temperature, where ‘hot lines’, which are insignificant at low temperatures, are grouped with lines that are less sensitive to temperature [283]. Similarly, under conditions where relative species concentrations vary significantly, absorption lines from one gas specie will be grouped similarly to separate lines arising from a different specie in the absence of the former [284]. These effects can be mitigated in the narrow band correlated-k method through an optimal choice in banding, however they cannot be eradicated. Both of these conditions are likely under combustion conditions, and in particular oxyfuel combustion, and the assumptions should be validated.

3.1.2.4 Wide band models

Wide band models approximate the radiative transfer arising from wide spectral features, such as entire rotational-vibrational bands in the spectrum, which are comprised of several overlapping individual lines. One of the most widely used wide-band model is the exponential wide band model [285], which, like the SNB method, describes integral properties of radiative transfer, and is therefore unsuitable for scattering media or non-black walls. While wide band models have been used to develop parameters for global models [220, 286], they are inherently less accurate than narrow-band models, while also being less efficient and applicable than global methods, and are therefore rarely used in CFD calculations.

3.1.2.5 Weighted sum of grey gasses model

The weighted sum of grey gasses (WSGG) method was originally developed for the zonal method to represent the total emission from an inhomogeneous zone, but has also been shown to be a valid representation of the medium to use with the general formulation of the directional RTE, Equation (3.1) [287]. The WSGG method has shown great popularity for CFD calculations [77, 217, 218, 288], particularly its grey formulation, as it is computationally cheap. The effective emissivity of a medium in the WSGG method is represented by the weighted contribution from fictitious grey gasses

$$\epsilon = \sum_{j=0}^{J} a_j \left[1 - \exp\left(-\kappa_j p s\right)\right] \tag{3.31}$$

where ϵ is the total emissivity of the medium, J is the number of grey gases, which is typically less than five, a_j is the weighting of grey gas j, κ_j is the absorption coefficient of grey gas j, p is the partial pressure of participating species, usually just CO_2 and H_2O for combustion environments, and s is the path length for the emission. The gas for $j = 0$ is often reserved for a transparent gas with $\kappa_j = 0$ to account for spectral windows in the absorption coefficient. The weights and absorption coefficients for the grey gasses are calculated by fitting the parameters to Equation (3.31) using tabulated values of gas emissivity, which are often calculated for a range of gas compositions, pressures, temperatures and beam lengths using more expensive models. The weights, a_j, and the absorption coefficients, κ_j, can be defined as a function of local values, but neither are allowed to depend on the beam length, while all other optical quantities are assumed to be grey, i.e. spectrally constant.

The emission and absorption of the grey gasses are treated independently in the non-grey WSGG method, and the RTE in a non-scattering medium for each fictitious gas is represented as [287]

$$\frac{\mathrm{d}I_j}{\mathrm{d}\hat{\mathbf{s}}} = a_j\kappa_j I_b - \kappa_j I_j \tag{3.32}$$

where I_j is the intensity of grey gas j. The boundary condition for the non-grey WSGG method, assuming diffusively reflecting walls, is given as

$$I_{w,j}\left(\hat{\mathbf{r}}_w\right) = a_j\epsilon_w I_b(\hat{\mathbf{r}}_w) + \frac{1-\epsilon_w}{\pi}\int_{\hat{\mathbf{s}}\cdot\hat{\mathbf{n}}<0} I_j(\hat{\mathbf{r}},\hat{\mathbf{s}})|\hat{\mathbf{s}}\cdot\hat{\mathbf{n}}|\,\mathrm{d}\Omega \tag{3.33}$$

where $I_{w,j}$ is the radiation intensity for gas j leaving from the boundary. The total radiation intensity is then approximated as an accumulation of the grey gas intensities [287],

$$\int_0^\infty I_\eta\,\mathrm{d}\eta \approx \sum_{j=0}^{J} I_j \tag{3.34}$$

The number of RTEs that are required to calculate the total intensity is the same as the number grey gasses that are used, including the transparent gas, which can usually be less than five, and is therefore a significant computational reduction from most band-models.

Simplifications are often applied to the WSGG model to reduce the medium to a representative grey gas, and therefore reduce the number of RTE calculations to one. An effective grey absorption coefficient is calculated from the total gas emissivity, which is evaluated from Equation (3.31). The beam length in Equation (3.31) is taken as a mean beam length of the domain, which is often estimated from the geometric relation [223]

$$s = \frac{3.6V}{A} \tag{3.35}$$

where A is the internal surface area of the domain and V is the volume of the medium. The same length is then used to convert the total gas emissivity to an effective grey absorption coefficient by rearranging Equation (3.31),

$$\kappa_e = -\frac{\ln\left(1-\epsilon\right)}{s} \tag{3.36}$$

While this step has no physical meaning, removing the spectral dimension from Equations (3.1), (3.5) and (3.6) greatly simplifies the calculations for modelling thermal radiation, and still achieves acceptable results in most cases. The calculation of the beam length used in Equations (3.31) and (3.36) is known to influence the resulting calculations [289, 290], however there is no clear guidance for selecting the correct value beyond the simple relation shown in Equation (3.35), and therefore highlights an issue with the generalisability of the method.

As the model parameters are fitted to specific environments, the WSGG model cannot be freely applied to novel environments, such as oxycoal combustion, and will be incapable of capturing the affect the combustion environment has on radiative heat transfer. Recently, several new sets of coefficients have been published for oxyfuel conditions [286, 291–294], as well as refinements to parameters for air-fired combustion [295, 296], which vary significantly in their development and implementation. From the new parameter sets for oxyfuel combustion, only the coefficient values suggested by Kangwanpongpan et al. [292] and Bordbar et al. [294] are based on LBL calculations of emissivity, using the HITEMP2010 database [224]. The parameter sets from Johansson et al. [291] and Krishnamoorthy [293] were developed from emissivity values calculated by SNB models that were based on earlier spectral databases, which may introduce inaccuracies at high temperatures [263, 297]. The values from Yin et al. [286] were calculated from emissivity predictions from the exponential wide band model in a similar way that was used by Smith et al. [220] to develop the parameters that are widely used for air combustion, but share the same limitations with the SNB developed parameters, in that high-temperature radiative properties may be inaccurately accounted for.

The developments of the WSGG method from Johansson et al. [291], which is also used for the parameters developed by Kangwanpongpan et al. [292] and Bordbar et al. [294], fitted the values of a_j and κ_j to variable ratios of H_2O and CO_2 to improve the parameter fittings for a wide range of potential oxyfuel environments. While both studies were concerned with the grey WSGG implementation, the dependence of the weighting function on the local gas composition provides an uncertainty in the treatment of the boundary condition for the non-grey WSGG, Equation (3.33), where the weighting function needs to be evaluated at the wall. This uncertainty is replicated when accounting for the radiative emission from suspended particles, which is discussed in Section 3.2.

Despite its popularity, several studies have demonstrated that the WSGG and grey WSGG models are often inaccurate under combustion conditions [274, 298, 299]. The chief attraction of the WSGG model has been that it is computationally cheap to calculate, however with the increased concentrations of participating gaseous species under oxyfuel conditions, it is important to develop and validate more accurate models to achieve acceptable results that can be used in predictive modelling.

3.1.2.6 Spectral line-based WSGG model

The sepctral line-based weighted sum of gray gasses (SLW) method can be considered a general WSGG model, where the grey gas absorption coefficients and emissivity weighting factors are evaluated directly from spectral data. The method itself centres around the definition of the absorption-line blackbody distribution function (ALBDF) [300],

$$F(C_{abs}, T_b, \underline{\phi}) = \frac{\pi}{\sigma_{\mathrm{SB}} T_b^4} \int_{\eta : C_\eta(\underline{\phi}) \leq C_{abs}} I_{b\eta}(T_b)\,\mathrm{d}\eta \tag{3.37}$$

where F is the ALBDF, C_{abs} is a specified absorption cross-section, C_η is a spectral absorption cross-section calculated from a high-resolution spectral database, T_b is the emission source temperature, $I_{b\eta}$ is the Planck function and $\underline{\phi}$ is a vector of variables that alter the absorption cross section, such as the species concentration, total pressure and gas temperature, which may be different to the temperature T_b. The absorption cross section is essentially the absorption coefficient of a gas per unit particle. The ALBDF represents the fraction of emission power that is produced by absorption cross-sections that are less than C_{abs}, much like the g-functions introduced in the CK model, Equation (3.27). The fraction of power that is emitted between discrete intervals of the absorption cross-section, C_j and C_{j-1}, can be calculated from the ALBDF as [301]

$$a_j = F(C_j, T_b, \underline{\phi}) - F(C_{j-1}, T_b, \underline{\phi}) \tag{3.38}$$

where a_j is equivalent to the emissivity weighting factors introduced in Equation (3.32) for the WSGG method. The corresponding absorption coefficient, κ_j, can be evaluated as a representative value for the cross section interval, often calculated from the geometric mean of the discrete values [301],

$$\kappa_j = N\sqrt{C_j C_{j-1}} \tag{3.39}$$

where N is the molar or molecular density of the participating gas species, depending on the units of C. The discrete values for C_j are often logarithmically spaced between predetermined values for C_{min} and C_{max}. A transparent gas is also usually employed so that $\kappa_0 = 0$ and $a_0 = F(C_{min}, T_b, \underline{\phi})$.

The total radiation intensity is calculated in the SLW method by integrating across the absorption cross sections, thereby calculating the total intensity as a function of grouped absorption cross sections, which is analogous to the CK method, but applied to the entire spectrum. The calculation of radiative intensity and the integration across cross sections is done in the same way as the non-grey WSGG, solving the RTE in

Equation (3.32), subject to the boundary condition in Eqiation (3.33), with total intensity calculated from the cross-section intervals using Equation (3.34).

It is necessary to calculate the ALBDF for gas mixtures from the single-specie ALBDFs due to the computational expense of otherwise having to evaluate the function from LBL data for all potential mixtures. The identified methods for calculating the mixture ALBDF are the direct spectral integration, convolution, superposition and multiplicative methods [302].

Under the direct spectral integration scheme, the RTE is modified to account for the grey gasses of all species [301], and for a non-scattering case is given by

$$\frac{\mathrm{d}I_{j_1,j_2,\cdots,j_{N_s}}}{\mathrm{d}\hat{\mathbf{s}}} = \kappa_{j_1,j_2,\cdots,j_{N_s}} \left(a_{j_1,j_2,\cdots,j_{N_s}} I_b - I_{j_1,j_2,\cdots,j_{N_s}} \right) \tag{3.40}$$

where N_s is the total number of participating gas species in the mixture. By assuming that the species' absorption spectra are statistically uncorrelated, the emissivity weights are calculated as the products of the individual species' weights [301],

$$a_{j_1,j_2,\cdots,j_{N_s}} = \prod_{i}^{N_s} a_{j_i} = F_i(C_{j_i}, T_b, \underline{\phi}) - F_i(C_{j_i-1}, T_b, \underline{\phi}) \tag{3.41}$$

and the absorption coefficient is calculated as the sum of the components' absorption,

$$\kappa_{j_1,j_2,\cdots,j_{N_s}} = \sum_{i}^{N_s} N_i C_{j_i} \tag{3.42}$$

The total intensity is then solved by summing across the various discrete cross-sections;

$$I = \sum_{j_0}^{J} \sum_{j_1}^{J} \cdots \sum_{j_{N_s}}^{J} I_{j_1,j_2,\cdots,j_{N_s}} \tag{3.43}$$

The direct spectral integration method requires solving J^{N_s} RTEs, which can quickly become a significant overhead, negating the advantage of using a global model to solve the radiative transfer; therefore making the direct spectral integration method unsuitable for CFD calculations.

The convolution approach simplifies the direct integration method by assuming the ratio between participating species is spatially constant throughout the domain. Under the convolution approach the ALBDF function for a mixture is calculated as [302]

$$F(C_{mix}) = \int \cdots \int F_1\left(\frac{C - (1 - r_2)C_2 - \cdots - (1 - r_{N_s})C_{N_s}}{r_2 \cdots r_{N_s}}\right) \times \mathrm{d}F_2(C_2)\cdots \mathrm{d}F_{N_s}(C_{N_s}) \quad (3.44)$$

where

$$r_i = \frac{N_i}{\sum_k^i N_k} \quad (3.45)$$

where N_i is the molar density of species i. The absorption coefficient for the mixture can be calculated as

$$\kappa_{mix} = C_{mix}\sum_i^{N_s} N_i \quad (3.46)$$

The convolution method successfully reduces the number of RTE evaluations required to model radiative energy transfer through a gas mixture, however the assumption of spatially constant molar ratios is too restrictive for the method to be applied to practical problems of oxyfuel combustion.

Within the superposition and multiplicative approach the effective ALBDF is calculated for an individual component of a mixture as [302]

$$F_{CX_i}(C) = F(C/X_i) \quad (3.47)$$

where X_i is the mole fraction of component i. Under the superposition approach, it is assumed that the spectra of the participating species do not overlap significantly and the ALBDF of a mixture is calculated from the component parts [302],

$$F(C_{mix}) = (1 - N_s) + \sum_i^{N_s} F\left(\frac{C}{X_i}\right) \quad (3.48)$$

Alternatively, the absorption cross-sections between participating species could be assumed to be statistically uncorrelated, and the ALBDF can be approximated by applying the multiplication rule for the probability of uncorrelated events [302],

$$F(C_{mix}) = \prod_i^{N_s} F\left(\frac{C}{X_i}\right) \quad (3.49)$$

Both of these methods are applicable for CFD calculations, however these methods make assumptions for the entire spectrum that are unlikely to be true, and can therefore introduce significant errors.

As with the banded models, approximations need to be made to apply the SLW method to non-isothermal or non-homogeneous media. Using the scaled approximation, where it is assumed that spectral variations in the absorption cross-section can be separated from changes induced from the local thermodynamic state, results in the so-called SLW reference approach, which assumes that the absorption coefficient is scaled between thermodynamic states [303]. Under this approach, the local absorption cross-sections, $C_{loc,j}$, are evaluated based on the implicit relation

$$F(C_j, T_0, \underline{\phi}_0) = F(C_{loc,j}, T_0, \underline{\phi}) \tag{3.50}$$

where C_j are the predetermined absorption cross sections, T_0 is a reference temperature, $\underline{\phi}_0$ is a reference thermodynamic state and $\underline{\phi}$ is the local thermodynamic state. Under this scaled assumption it is presumed that the cross sections $C_{loc,j}$ and C_j represent the same spectral location. The absorption coefficient for a position within the domain is then evaluated from the local cross-sections. The reference temperature T_0 and reference state $\underline{\phi}_0$ are calculated as volume-weighted averages over the domain [303].

The weighting factors, a_j, in non-isothermal media using the SLW reference approach are calculated using the predetermined cross-sections, with T_b set to the local temperature, to correctly account for the local emission, and using the fixed reference state $\underline{\phi}_0$,

$$a_j = F(C_j, T, \underline{\phi}_0) - F(C_{j-1}, T, \underline{\phi}_0) \tag{3.51}$$

The fixed reference state and cross-section is used so that all the emission from within the domain is associated with the same spectral intervals. Alternatively, the weights can be calculated from the local cross-sections evaluated from Equation (3.50) and the local state [304],

$$a_j = F(C_{loc,j}, T, \underline{\phi}) - F(C_{loc,j-1}, T, \underline{\phi}) \tag{3.52}$$

These two methods of calculating the weighting factors represent the only significant difference between the SLW method and the absorption distribution function (ADF) method [305]. The latter formulation of the emission weights, Equation (3.52), depends on the local gas composition, and therefore is not compatible with the boundary condition for the SLW method, as the weighting can not be evaluated at the walls, or from suspended particles, without further developments.

An extension to the SLW method is the SLW-1 method, where the number of RTEs is reduced to represent a transparent gas and a single grey gas [306, 307]. Under this simplification, the absorption coefficient and emissivity weighting for the grey gas can be fitted to emissivity calculations using the SLW method at a high resolution. The SLW-1 method is a promising approach to modelling gas radiative properties, achieving good agreement with more expensive methods while requiring minimal computational resources [307].

The SLW method overcomes a major limitation of the traditional WSGG method as the model is not associated with any particular predefined gas composition. The addition of a transparent gas is also beneficial for representing participating gas species, as gaseous molecules are transparent for large portions of the spectrum [308], however it is unclear whether this will be significant in the presence of suspended particles, which are often treated with spectrally constant radiative properties. The SLW method often requires greater than ten spectral intervals to achieve good accuracy [309], which will require significant, if not prohibitory, computational resources to be applied to CFD calculations. The SLW-1 method provides an alternative approach with a minimal computational requirement, but will need to be validated against potential oxycoal environments to be employed with confidence.

3.1.2.7 Full spectrum k-distribution methods

When applying the k-distribution method, as described in Subsubsection 3.1.2.3, to the entire spectrum, the black-body emission cannot be assumed to be constant, and the full-spectrum k-distributions are weighted by the Planck function [284],

$$f(\underline{\phi}, T, k) = \frac{1}{I_b(T)} \int_0^\infty I_{b\eta}(T, \eta) \delta \left(k - \kappa(\underline{\phi}) \right) \mathrm{d}\eta \tag{3.53}$$

where $f(\underline{\phi}, T, k)$ is the full-spectrum k-distribution, $\underline{\phi}$ is a vector containing the local conditions that alter the absorption coefficient (temperature, pressure and gas composition), I_b is the total black-body intensity, $I_{b\eta}$ is the Planck function and δ is the Dirac delta function. The first step towards developing the RTE for the full-spectrum k-distribution (FSK) methods involves multiplying Equation (3.1) by $\delta \left(k - \kappa(\underline{\phi}_0) \right)$ and integrating over all wavenumbers,

$$\frac{\mathrm{d}I_k(\hat{\mathbf{r}}, \hat{\mathbf{s}})}{\mathrm{d}\hat{\mathbf{s}}} = k f(\underline{\phi}_0, T, k) I_b(T) - (k + \sigma) I_k(\hat{\mathbf{r}}, \hat{\mathbf{s}}) + \frac{\sigma}{4\pi} \int_{4\pi} \Phi\left(\hat{\mathbf{s}}, \hat{\mathbf{s}'}\right) I_k\left(\hat{\mathbf{r}}, \hat{\mathbf{s}'}\right) \mathrm{d}\Omega \tag{3.54}$$

where $I_k = \int_0^\infty I_\eta \delta\left(k - \kappa(\underline{\phi}_0)\right) \mathrm{d}\eta$, which represents the intensity from all lines where the absorption coefficient is equal to k, and the spectral dependence on scattering quantities have been dropped, and they are assumed to be grey. Essentially, the RTE in Equation (3.54) represents a single solution for each spectral location where κ_η assumes the same value k. The boundary condition for Equation (3.54) is given as

$$I_{wk}\left(\hat{\mathbf{r}}_w\right) = \epsilon_w f(\underline{\phi}_0, T_w, k) I_b(T_w) + \frac{1-\epsilon_w}{\pi} \int_{\hat{\mathbf{s}}\cdot\hat{\mathbf{n}}<0} I_k(\hat{\mathbf{r}}, \hat{\mathbf{s}}) |\hat{\mathbf{s}} \cdot \hat{\mathbf{n}}| \, \mathrm{d}\Omega \tag{3.55}$$

where T_w is the temperature of the boundary. To transform the RTE into smoothly-varying g-space, Equations (3.54) and (3.55) are divided by the Planck-weighted k-distribution evaluated at a reference temperature [279];

$$\begin{aligned} \frac{\mathrm{d}I_g\left(\hat{\mathbf{r}}, \hat{\mathbf{s}}\right)}{\mathrm{d}\hat{\mathbf{s}}} = k(\underline{\phi}_0, T, g_0) a(T, T_0, g_0) I_b(T) - \left(k(\underline{\phi}_0, T, g_0) + \sigma\right) I_g\left(\hat{\mathbf{r}}, \hat{\mathbf{s}}\right) + \\ \frac{\sigma}{4\pi} \int_{4\pi} \Phi\left(\hat{\mathbf{s}}, \hat{\mathbf{s}'}\right) I_g\left(\hat{\mathbf{r}}, \hat{\mathbf{s}'}\right) \mathrm{d}\Omega \end{aligned} \tag{3.56}$$

where

$$I_g = \frac{I_k}{f(\underline{\phi}_0, T_0, k)} \tag{3.57}$$

$$g(\underline{\phi}, T, k) = \int_0^k f(\underline{\phi}, T, k') \, \mathrm{d}k' \tag{3.58}$$

$$a(T, T_0, g_0) = \frac{f(\underline{\phi}_0, T, k)}{f(\underline{\phi}_0, T_0, k)} = \frac{\mathrm{d}g(\underline{\phi}_0, T, k)}{\mathrm{d}g(\underline{\phi}_0, T_0, k)} \tag{3.59}$$

and where $k(\underline{\phi}_0, T, g_0)$ is the inverse function of Equation (3.58). The boundary condition in g-space is given as

$$I_{wg}\left(\hat{\mathbf{r}}_w\right) = \epsilon_w a(T_w, T_0, g_0) I_b(T_w) + \frac{1-\epsilon_w}{\pi} \int_{\hat{\mathbf{s}}\cdot\hat{\mathbf{n}}<0} I_g(\hat{\mathbf{r}}, \hat{\mathbf{s}}) |\hat{\mathbf{s}} \cdot \hat{\mathbf{n}}| \, \mathrm{d}\Omega \tag{3.60}$$

Finally, the total intensity can be calculated by integrating across all values of k, which is equivalent to the integration across g-space between 0 and 1, and can be achieved using an efficient Gauss quadrature scheme,

$$\int_0^\infty I_\eta \, \mathrm{d}\eta = \int_0^\infty I_k \, \mathrm{d}k = \int_0^1 I_g \, \mathrm{d}g \approx \sum_i^{N_q} w_i I_{g,i} \tag{3.61}$$

where the number of quadrature points, N_q, can be less than ten for the entire spectrum [76, 229, 310, 311]. While the development of the FSK is similar to the SLW method, far fewer spectral intervals are required due to this efficient integration, where the SLW method can be interpreted as taking a trapezoidal integration scheme for the total intensity, albeit with a different spectral variable [223, 305].

While the above derivation for the FSK method is exact, it is limited to a homogeneous medium, where $\underline{\phi}_0$ is constant across the domain. As discussed for all the previous models, the FSK method is required to adopt an approximation so that the absorption coefficient at the local thermodynamic state can be related to the reference state $\underline{\phi}_0$, allowing for the different g-space dimensions between the states to be accounted for without the spectral information. The two identified methods are the correlated and scaled assumptions [279].

An absorption coefficient that is correlated between two states, $\underline{\phi}$ and $\underline{\phi}_0$, can be defined as

$$\kappa_\eta(\underline{\phi}) = k^*(\underline{\phi}, \kappa_\eta(\underline{\phi}_0)) \tag{3.62}$$

where k^* is a function such that identical values of $\kappa_\eta(\underline{\phi}_0)$ are mapped to identical values of $\kappa_\eta(\underline{\phi})$, so that the general shape of the absorption coefficient is maintained. Under this restriction it can be shown that the cumulative function g is identical for two states [279],

$$g(T, \underline{\phi}_0, k) = g(T, \underline{\phi}, k^*) \tag{3.63}$$

so that k and k^* can be inverted to represent the same g-space. Furthermore, under the correlated assumption, the effect of varying the temperature used for the Planck function weighting in the full-spectrum k-distributions, results only in a stretch in g-space, which can be accounted for by evaluating k^* at the reference temperature. Following the introduction of these relations and employing the correlated approximation, the RTE for the full-spectrum correlated k-distribution (FSCK) method is given as

$$\begin{aligned}\frac{\mathrm{d}I_g\left(\hat{\mathbf{r}},\hat{\mathbf{s}}\right)}{\mathrm{d}\hat{\mathbf{s}}} = k^*(\underline{\phi}, T_0, g_0)a(T, T_0, g_0)I_b(T) - \\ \left(k^*(\underline{\phi}, T_0, g_0) + \sigma\right) I_g\left(\hat{\mathbf{r}},\hat{\mathbf{s}}\right) + \\ \frac{\sigma}{4\pi}\int_{4\pi} \Phi\left(\hat{\mathbf{s}},\hat{\mathbf{s}'}\right) I_g\left(\hat{\mathbf{r}},\hat{\mathbf{s}'}\right)\mathrm{d}\Omega\end{aligned} \tag{3.64}$$

where g_0 represents g-space at T_0 and $\underline{\phi}_0$.

Alternatively to the correlated approach, the absorption coefficient can be assumed to be scaled, where a scaled absorption coefficient can be decomposed into a function of the spectral quantity and a scalar function between thermodynamic states,

$$\kappa_\eta(\underline{\phi}) = \kappa_\eta(\underline{\phi}_0)u(\underline{\phi}, \underline{\phi}_0) \tag{3.65}$$

where u is the scaling function. While the scaled approximation is a more restrictive assumption, it offers further freedom in the selection of u to improve the representation of true absorption coefficients that are neither scaled nor correlated. A sensible choice in the selection of u revolves around solving u so that the emissivity of a representative path is maintained using the implicit relation [279]

$$\int_0^1 \exp\left[-k^*(\underline{\phi}, T_0, g)s\right] \mathrm{d}g = \int_0^1 \exp\left[-k(\underline{\phi}_0, T_0, g_0)u(\underline{\phi}, \underline{\phi}_0)s\right] \mathrm{d}g_0 \tag{3.66}$$

where s is a specified path length, which can be taken as the mean beam length specified by Equation (3.35). The above relation can be evaluated efficiently using a Newton-Raphson scheme, and there is a negligible difference in computational cost between a scaled and correlated assumption [279]. The RTE for the full-spectrum scaled k-distribution (FSSK) method can now be written as

$$\begin{aligned} \frac{\mathrm{d}I_g\left(\hat{\mathbf{r}}, \hat{\mathbf{s}}\right)}{\mathrm{d}\hat{\mathbf{s}}} = k(\underline{\phi}_0, T_0, g_0)u(\underline{\phi}, \underline{\phi}_0)a(T, T_0, g_0)I_b(T) - \\ \left(k(\underline{\phi}_0, T_0, g_0)u(\underline{\phi}, \underline{\phi}_0) + \sigma\right) I_g\left(\hat{\mathbf{r}}, \hat{\mathbf{s}}\right) + \\ \frac{\sigma}{4\pi}\int_{4\pi} \Phi\left(\hat{\mathbf{s}}, \hat{\mathbf{s}}'\right) I_g\left(\hat{\mathbf{r}}, \hat{\mathbf{s}}'\right) \mathrm{d}\Omega \end{aligned} \tag{3.67}$$

Within both of the FSK methods, it is important to select the correct reference state and temperature, as the methods are only going to be theoretically exact under these conditions. It is recommended that the gas composition and total pressure of the reference state is calculated from a volume average, while the temperature in the reference state and the reference temperature T_0 is calculated based on a Planck mean temperature through the implicit relation [284]

$$\kappa_{\mathrm{PL}}(\underline{\phi}_0)T_0^4 = \frac{1}{V}\int_V \kappa_{\mathrm{PL}}(\underline{\phi})T^4 \,\mathrm{d}V \tag{3.68}$$

where κ_{PL} is the Planck mean absorption coefficient ($\kappa_{\mathrm{PL}} = \int_0^\infty \kappa_\eta I_{b\eta} \,\mathrm{d}\eta / I_b$).

While the full-spectrum k-distributions can be calculated from the spectral absorption coefficient using Equation (3.53), it is often more computationally efficient to calculate the distributions from pre-calculated narrow band k-distributions with a negligible loss in accuracy [282]. The full-spectrum k-distributions can be assembled from the narrow-band distributions as

$$f(\underline{\phi}, T, k) = \sum_{n}^{N_{bands}} \frac{\int_{\Delta\eta} I_{b\eta}(T)\,\mathrm{d}\eta}{I_b(T)} f_n(\underline{\phi}, k) \tag{3.69}$$

where N_{bands} is the number of bands, $\Delta\eta$ is the width of the band and $f_n(\underline{\phi}, k)$ is the narrow band k-distribution for band n. This approach allows for the full-spectrum k-distribution for a gas mixture to be assembled from the narrow band k-distributions for that mixture, which can be accurately calculated from single-specie k-distributions using the mixing scheme by Modest and Riazzi [282]. Assembling the k-distributions using this method every time the RTE is solved is still too cumbersome for CFD calculations, and therefore it is necessary to tabulate the full-spectrum k-distributions for given thermodynamic states, alongside emissivity weights, and linearly interpolate to the local conditions. This approach achieves high computational efficiency without any significant loss of accuracy [279].

The FSSK and FSCK method have both been previously applied to CFD calculations [76, 210, 312], as well as being validated against benchmark LBL and narrow band results for combustion conditions [229, 299, 311, 313]. The studies identify the FSK models as being highly promising for predicting spectral radiative transfer, however the methods still need to be validated against a range of oxyfuel conditions, and there are no clear studies to identify the optimum number of quadrature points that are necessary for combustion conditions.

3.2 Particle radiation

Suspended particles, such as soot, coal, char and ash particles, contribute significantly to radiative heat transfer through a participating medium [314–320]. Coal, char and soot particles often demonstrate significant absorption and emission [310, 319–321], while ash particles are highly scattering [322]. The temperatures of char particles can often be significantly higher than the surrounding gas due to exothermic reactions at the particle surface [323], which will also significantly increase the radiative emission of the particulate phase.

Under oxyfuel conditions, higher oxygen concentrations could increase the particle surface temperatures due to char combustion [324], however, in oxygen depleted regions, endothermic H_2O and CO_2 gasification reactions, as well as decreased O_2 diffusivity through CO_2, could have the opposite effect [325–327], localising the emission sources to the oxygen rich regions. Particle heating rates due to radiation are likely to be increased under oxyfuel conditions as there will be a greater amount of radiative energy emitted from the gas phase, however the convective heating rates will be lower due to the potentially lower gas velocities and the higher heat capacity of CO_2, affecting the temperature difference between the particle and the gas phase.

This section discusses methods to determine the radiative properties for suspended particles. The interaction between electromagnetic radiation and suspended particles is discussed in Subsection 3.2.1, and values for the parameters that define this interaction are discussed in Subsection 3.2.2.

3.2.1 Particle radiation interaction

The interaction between a suspended particle and the propagation of an electromagnetic wave can be described based on the complex index of refraction of the particle, $m = n - ki$, and the ratio between the particle's projected length and the wavelength of incoming radiation, which for a spherical particle with radius r is calculated as $x = 2\pi r\eta$. The two components of the index of refraction, n and k, represent the fractional speed of electromagnetic radiation through the medium, compared against a vacuum, and the absorptivity of the material respectively. The radiative properties of suspended particles are often referred to in terms of their absorption cross section, C_{abs}, scattering cross section, C_{sca}, and total extinction cross-section C_{ext} $(= C_{abs} + C_{sca})$, or by their non-dimensionalised equivalent efficiency quantities $Q_{ase} = C_{ase}/\pi r^2$, where the subscript *ase* is either *abs*, *sca* or *ext*.

The equivalent absorption and scattering coefficients for suspended particles within a volume are calculated from the accumulated cross sections [223],

$$\kappa_{\mathrm{P}} = \int_0^\infty f(r) C_{abs} \, \mathrm{d}r \tag{3.70}$$

$$\sigma_{\mathrm{P}} = \int_0^\infty f(r) C_{sca} \, \mathrm{d}r \tag{3.71}$$

where κ_{P} and σ_{P} are the effective absorption and scattering coefficients respectively, and $f(r)$ is the number density of particles within the volume with radius r. The amount of radiative energy that is emitted from the dispersed particle phase is calculated in a similar fashion, however the emission is weighted by the Planck function at the particle temperature;

$$E_{\mathrm{P},\eta} = \int_0^\infty f(r) C_{abs} I_{b\eta}(T_{\mathrm{P}}) \, \mathrm{d}r \tag{3.72}$$

where T_{P} is the particle temperature. Finally, the scattering phase function, which describes the direction of radiative scattering, is calculated in the same way, but is weighted by the scattering cross section [223]

$$\Phi_{\mathrm{P}}\left(\hat{\mathbf{s}}, \hat{\mathbf{s}'}\right) = \frac{1}{\sigma_{\mathrm{P}}} \int_0^\infty f(r) C_{sca} \Phi\left(\hat{\mathbf{s}}, \hat{\mathbf{s}'}\right) \mathrm{d}r \tag{3.73}$$

where Φ_{P} is the effective phase function and Φ is the phase function for individual particles. The RTE defined in Equation (3.1) can be modified to incorporate particulate effects as

$$\begin{aligned} \frac{\mathrm{d}I_\eta(\hat{\mathbf{r}}, \hat{\mathbf{s}})}{\mathrm{d}\hat{\mathbf{s}}} = \kappa_\eta I_{b\eta}(\hat{\mathbf{r}}) + E_{\mathrm{P},\eta} - \left(\kappa_\eta + \kappa_{\mathrm{P}} + \sigma_{\mathrm{P}}\right) I_\eta(\hat{\mathbf{r}}, \hat{\mathbf{s}}) + \\ \frac{\sigma_{\mathrm{P}}}{4\pi} \int_{4\pi} \Phi_{\mathrm{P}}\left(\hat{\mathbf{s}}, \hat{\mathbf{s}'}\right) I_\eta\left(\hat{\mathbf{r}}, \hat{\mathbf{s}'}\right) \mathrm{d}\Omega \end{aligned} \tag{3.74}$$

where only scattering from the particle-phase has been included for brevity.

In the limiting case for small particles relative to the radiation wavelength, where $x \ll 1$, which is generally the case for soot particles and molecular gas particles, the scattering and extinction efficiencies can be evaluated through the Rayleigh scattering theory as [223]

$$Q_{sca} = \frac{8}{3} \left| \frac{m^2 - 1}{m^2 + 2} \right| x^4 \tag{3.75}$$

$$Q_{ext} = -4\Im \left\{ \frac{m^2 - 1}{m^2 + 2} \right\} x \approx Q_{abs} \tag{3.76}$$

where $\Im$ denotes the imaginary component of the bracketed complex number. As $x \ll 1$, it can be seen that the absorption efficiency for small particles is significantly higher than the scattering efficiency, and therefore scattering from the gas phase and soot particles is often neglected, as in the RTE shown in Equation (3.74). Due to the linear dependence of the extinction efficiency on the size parameter, it is possible to derive the absorption coefficient for small spherical particles from Equation (3.76) and the volume fraction of particles, f_v, as [223]

$$\kappa_\eta = -4\Im \left\{ \frac{m^2 - 1}{m^2 + 2} \right\} 6\pi f_v \eta \tag{3.77}$$

This equation provides a relation for the absorption coefficient for soot particles based on the local volume fraction and the particle's index of refraction, which has been measured for various soot particles derived from hydrocarbon flames [328–331], however the optical properties of coal-derived soot have not been measured, which may be significantly different to most other fuels due to their soot particle's very different precursor species and formation mechanisms, but may also vary significantly between coal ranks [332].

When the size parameter x is comparable to unity, which is the case for coal, char and ash particles, the interaction between radiative energy and suspended particles becomes more complex, and the particles can show appreciable scattering as well as absorption. Radiative scattering describes the alteration of the direction of transfer, and refers to the accumulated interactions of refraction within the particle, reflection from the particle surface and diffraction caused by distortions in the electromagnetic field that affect the wave propagation away from the particle. Mie theory has often been applied to describe these phenomena [223].

Mie theory describes an analytical solution to Maxwell's macroscopic electromagnetic wave equations in spherical coordinates [333]. The intensity of radiation scattered in direction Θ from an unpolarised electromagnetic wave is defined in terms of the intensity magnitude of two perpendicularly linearly polarised waves [223],

$$\frac{I_{sca}(\Theta)}{I_{in}} = \frac{1}{2}\frac{|S_1(x,m,\Theta)| + |S_2(x,m,\Theta)|}{x^2} \tag{3.78}$$

where $I_{sca}(\Theta)$ is the intensity scattered into the direction Θ, I_{in} is the incoming radiation intensity, S_1 and S_2 are complex amplitude functions for two perpendicularly polarised electromagnetic waves, and as above, x and m are the size parameter and complex index of refraction for the particle respectively. The complex functions S_1 and S_2 are given as an infinite series [223],

$$S_1(x,m,\Theta) = \sum_{n=1}^{\infty} \frac{2n+1}{n(n+1)} \left[a_n(m,x)\pi_n(\cos\Theta) + b_n(m,x)\tau_n(\cos\Theta)\right] \tag{3.79}$$

$$S_2(x,m,\Theta) = \sum_{n=1}^{\infty} \frac{2n+1}{n(n+1)} \left[b_n(m,x)\pi_n(\cos\Theta) + a_n(m,x)\tau_n(\cos\Theta)\right] \tag{3.80}$$

where a_n and b_n are known as the Mie scattering coefficients, which are related to Ricatti-Bessel functions, and π_n and τ_n are related to Legendre polynomials.

The extinction and scattering efficiencies for a particle can be evaluated directly from the Mie scattering coefficients as [223]

$$Q_{sca} = \frac{2}{x^2} \sum_{n=1}^{\infty} (2n+1)(|a_n|^2 + |b_n|^2) \tag{3.81}$$

$$Q_{ext} = \frac{2}{x^2} \sum_{n=1}^{\infty} (2n+1)\Re\{a_n + b_n\} \tag{3.82}$$

where $\Re$ denotes the real part of the bracketed complex number. The absorption efficiency can be calculated as the difference between the extinction and scattering efficiencies. The extinction, scattering and absorption efficiencies for a constant refractive index that is typical for bituminous coal particles, taken from Mengüç and Viskanta [334], are plotted against the size parameter x in Figure 3.3. A clear observation from this figure is that the efficiency values often exceed unity, which demonstrates that particles with the given size parameter influence the electromagnetic wave far beyond their respective projected area, owing to the phenomena of diffraction [333]. The efficiencies plotted in Figure 3.3 demonstrate notably non-grey behaviour in terms of x. This non-grey behaviour, however, is often smoothed out when the average efficiency values are calculated across a size distribution of particles, and grey values are often employed in CFD calculations. The use of grey particle properties is also often mandated by the use of global models to describe the spectral radiation of the gas-phase, however the use of non-grey particle values may overestimate the solid-phase participation [335], and this assumption should be validated.

The scattering phase function, $\Phi_{\mathrm{P}}\left(\hat{\mathbf{s}}, \hat{\mathbf{s}'}\right)$ in Equation (3.74), is a normalised function that describes the direction of scattering, and can be defined for a spherical particle from Equation (3.78) as [223]

$$\Phi\left(\hat{\mathbf{s}}, \hat{\mathbf{s}'}\right) = \frac{1}{2} \frac{|S_1(x, m, \hat{\mathbf{s}} \cdot \hat{\mathbf{s}'})| + |S_2(x, m, \hat{\mathbf{s}} \cdot \hat{\mathbf{s}'})|}{x^2 Q_{sca}} \tag{3.83}$$

The calculated phase function for two particles, one representative of coal and the other of fly-ash, are shown in Figure 3.4. These phase functions demonstrate highly anisotropic scattering, with a significant forward-scattering peak, as well as a backward scattering peak for the ash particle. Scattering efficiencies calculated through Mie theory should not be used with an isotropic phase function as this would greatly overestimate the directional scattering [336], however direct application of the phase function defined by Equation (3.83) within the RTE solution methods discussed in Subsection 3.1.1 requires an exceptionally high angular resolution, which is often im-

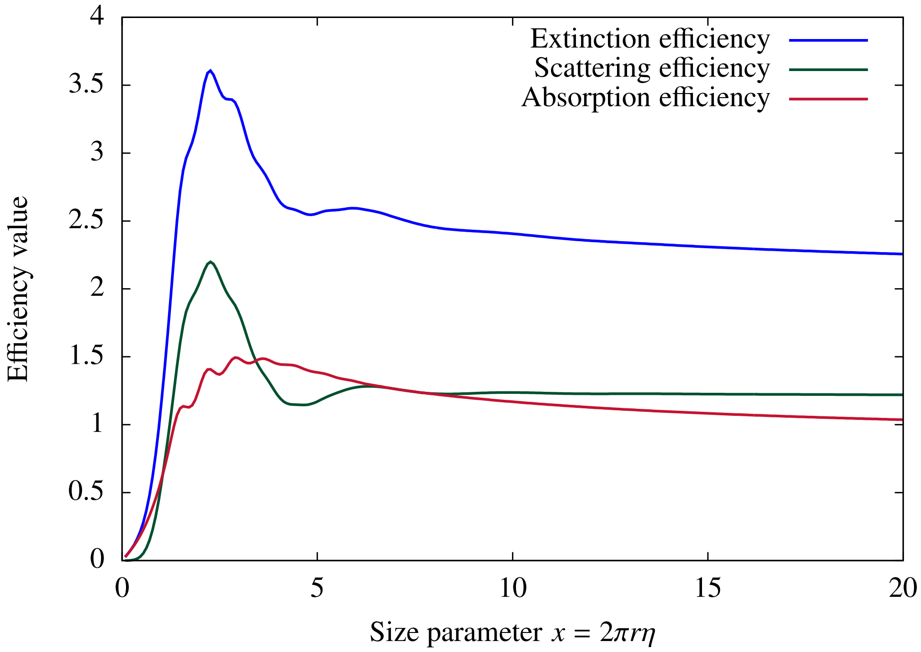

Figure 3.3: Mie theory calculated values for particle extinction, scattering and absorption efficiencies for constant $m = 1.85 - 0.22i$ and variable x.

practical.

Simplified phase functions are often used based on the asymmetry factor, which is defined as [223]

$$g = \frac{1}{4\pi}\int_{4\pi} \Phi\left(\hat{\mathbf{s}}, \hat{\mathbf{s}}'\right)\cos\left(\hat{\mathbf{s}}\cdot\hat{\mathbf{s}}'\right)\mathrm{d}\Omega \tag{3.84}$$

where g is the asymmetry factor, and varies between -1 for pure backward scattering, 0 for isotropic scattering and +1 for pure forward scattering, and can be directly calculated from the Mie scattering coefficients. A widely used simplified phase function is the Henyey-Greenstein function, which can be written as [338]

$$\Phi_{\text{HG}}\left(\hat{\mathbf{s}}, \hat{\mathbf{s}}'\right) = \frac{1 - g^2}{\left[1 + g^2 - 2g(\hat{\mathbf{s}}\cdot\hat{\mathbf{s}}')\right]^{\frac{3}{2}}} \tag{3.85}$$

While the Henyey-Greenstein function is a reasonable approximation to the phase function, it still requires a far higher angular resolution than is practical in most CFD applications [245].

The delta-Eddington approximate phase function separates the forward scattering

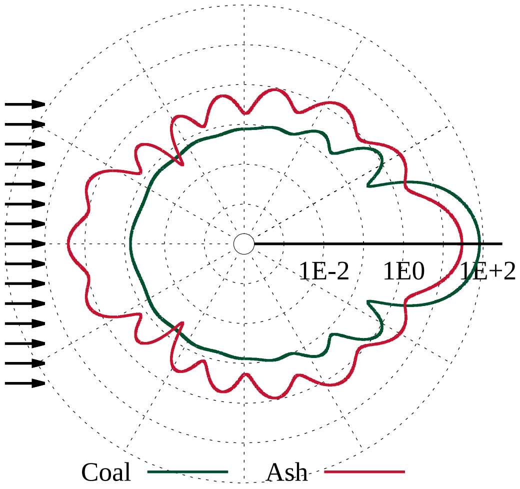

Figure 3.4: Scattering phase functions for particles calculated from Mie theory. Size parameter $x = 10$. Arrows indicate the direction of the radiation field. Char parameters are taken from Manickavasagam and Mengüç [337] and ash parameters are taken from Goodwin and Mitchner [316] for a wavelength of 2 µm.

peak from the directional scattering [339],

$$\Phi_{\delta-Edd}\left(\hat{\mathbf{s}}, \hat{\mathbf{s}}'\right) = 2f\delta(1 - \hat{\mathbf{s}} \cdot \hat{\mathbf{s}}') + (1 - f)(1 + 3g'\hat{\mathbf{s}} \cdot \hat{\mathbf{s}}') \tag{3.86}$$

where f is the fractional scattering in the forward direction, g' is the asymmetry factor of the truncated phase function and δ is the Dirac delta function. In order to maintain the same overall asymmetry factor for the phase function and satisfy the second moment of the Henyey-Greenstein function, f and g' are defined as [339]

$$f = g^2 \tag{3.87}$$

$$g' = \frac{g}{g+1} \tag{3.88}$$

where g is the asymmetry factor of the true phase function. The main drawback of the delta-Eddington phase function is that at high asymmetry factors, where $g > 1/2$, the function returns negative values for the backward directions, which is physically invalid. Furthermore, it is not generally feasible to employ anything other than a simple isotropic phase function, and it is necessary to employ a so-called ‘zero-order’ delta-Eddington phase function [223],

$$\Phi_{\delta-Edd-0}\left(\hat{\mathbf{s}}, \hat{\mathbf{s}'}\right) = g\delta(1 - \hat{\mathbf{s}} \cdot \hat{\mathbf{s}'}) + (1 - g) \tag{3.89}$$

where the asymmetry factor is used to represent the forward scattering direction. By treating the forward scattering as transmission, it is simpler to represent this phase function with an isotropic function and modifying the scattering efficiency so that $Q^*_{sca} = (1 - g)Q_{sca}$, where Q^*_{sca} is the corrected scattering efficiency [231, 245].

The above discussions have focussed on the interaction between radiative transfer and idealised spherical particles. This treatment is usually upheld under the assumption that a polydispersion of randomly oriented near-spherical particles will behave similarly as a polydispersion of equivalent spherical particles, which is often a valid approximation [8, 340]. More computationally expensive methods, such as the T-matrix method [341, 342], are able to calculate the radiative properties for arbitrarily shaped particles, but have not been applied to coal particles. Calculations for spherical and area-equivalent non-spherical particles generally agree with respect to forward-scattering, but disagree at other angles [333], however it is not possible to accurately account for this anisotropic scattering within CFD calculations, and so the approximation of spherical particles is a reasonable and somewhat necessary assumption.

3.2.2 Optical properties of coal particles

The simplest and most widely adopted method for modelling the optical properties of suspended particles is to assume a constant particle absorption and scattering efficiency. The absorption efficiency of char particles is often taken to be around 0.9 following reasonable agreement to FT-IR measurements [343, 344]. There is less clear evidence for a suitable value for the emissivity of fly-ash, however it is often modelled with a lower value [345].

Some studies have incorporated Mie theory calculations to derive the radiative properties for suspended particles [320], however there is a need to define a suitable complex index of refraction m. The complex index of refraction is known to vary across the spectral dimension, among coal rank and during burnout [322, 337, 346]. Furthermore, the index of refraction for fly-ash particles can be highly sensitive to the mineral composition of the fly-ash, which can be sensitive to the combustion environment [322].

From the different mineral compositions incorporated in fly-ash, Fe chemistry has been shown to have a significant impact on the resulting radiative properties of the particle [322]. Within a fly-ash particle, the Fe is mostly distributed into hematite (Fe_2O_3), which is practically transparent at the infra-red section of the spectrum, and magnetite (Fe_3O_4), which is opaque [316]. These stark differences in the optical properties of these minerals highlight the importance of having the correct indices of refraction for the coal and ash particles being studied, however very few studies have measured these quantities, and therefore there are only a narrow range of indices to call upon.

The spectrally variable measurements of the refractive index for fly-ash by Goodwin and Mitchner [322] are often used in studies [320, 336, 347–349], however the wide variability between coals offers considerable uncertainty in their application to practical combustion systems. The optical constants for coal and char particles often show reduced sensitivity between coal types and measured values for various coal ranks across the spectral dimension are available [328, 334, 337, 346].

3.3 Modelling coal combustion

In addition to the accurate modelling of thermal radiation, the modelling of the coal combustion process requires adequate representation of turbulent fluid flow and combustion chemistry. This section reviews methods for calculating turbulent reacting flows with a dispersed combusting particle phase, highlighting areas of the standard modelling approach that may introduce inaccuracies in the modelling of oxy-coal combustion. The focus on the work in this thesis is attributed to the development and validation of thermal radiation models, and so the discussion in this section is mostly limited to standard modelling approaches for coal combustion.

3.3.1 Modelling turbulent flows

Many practical engineering flows are turbulent, particularly in combustion where the increased mixing introduced through the breakup of turbulent structures is used to improve the combustion performance. Turbulent flows are characterised as being chaotic, three-dimensional, unsteady, swirled and dissipative, where turbulent structures known as eddies break down into increasingly smaller structures until viscous forces within the fluid transform the contained kinetic energy into heat. The Navier-Stokes equations for turbulent flows describe the evolution of the fluid dynamics by assuming the flow is a continuum.

The length- and time-scales of turbulent structures vary significantly in practical flows. The largest eddies are dependent upon the characteristic lengths of the geometry being studied, where these structures will then transfer energy into increasingly smaller eddies until the dissipative force arising from the molecular viscosity of the fluid is large compared to the inertial force of the eddy, and the kinetic energy is dissipated into heat. These small dissipative scales can be several orders of magnitude smaller than the largest scales, both in terms of length- and time-scales. Calculations that directly solve the Navier-Stokes equations and resolve all of these scales are referred to as direct numerical simulations (DNSs), however these computations require enormous resources, and practical cases require models to describe the behaviour of turbulent flows.

The methods of modelling turbulent fluid flows can be grouped into two approaches; Reynolds averaged Navier Stokes (RANS) methods and large eddy simulations (LESs). The most popular and time-effective approach is associated with applying RANS models, whereby the solution is solved for temporally averaged quantities, and models are used to describe the full range of turbulent scales. Alternatively, LES approaches spatially filter the instantaneous flow, whereby geometry-dependent large-scale eddies are resolved, with smaller eddies, ideally self-similar structures dominated by viscous dissipation, are modelled. These two approaches are now discussed.

3.3.1.1 Reynolds averaged Navier-Stokes equations

In contrast to the instantaneous flow field, the distribution of time-averaged quantities vary smoothly in space and are relatively well behaved. By taking the Favre average, which is the density weighted average across time, of the Navier-Stokes equations it is possible to derive a new set of governing equations that are more readily solved. The first step is the assumption that the Reynolds decomposition can be applied to each scalar, such that its instantaneous value, ϕ, can be described as the composition of both the Favre averaged, $\tilde{\phi}$, and the fluctuating contribution, ϕ', such as

$$\phi(t) = \tilde{\phi} + \phi'(t) \tag{3.90}$$

Applying this operation to the Navier-Stokes equations for continuity and momentum, and applying the relation that $\tilde{\phi'} = 0$, results in additional unclosed terms in the underlying equations, known as the Reynolds stresses.

One of the widely used approaches to modelling the Reynolds stresses involves introducing the Boussinesq hypothesis to relate the unclosed terms to an effective eddy viscosity, and there are a range of models that have been applied to represent the turbulent viscosity, with the most popular methods being the k-ϵ and k-ω models, which introduce a further two transport equations. One of the main drawbacks to the eddy viscosity methods is that all turbulence is treated as isotropic, which could be an inaccurate assumption in cases with dominant anisotropic turbulence, such as in cases with highly swirling flows, which is common in combustion. Alternatively, Reynolds stress models have been developed which introduce additional transport equations for each of the Reynolds stress terms, however the additional equations also require further constants to close specific terms.

RANS calculations are often sensitive to the choice of turbulence model, although the Reynolds stress model is often shown to be more accurate than eddy viscosity models for swirled combusting flows [350–352]. However, the range of available models alludes to one of the weaknesses of the RANS approach; as all the turbulent structures are being modelled, including the largest geometry-dependent scales, the accuracy of the model is somewhat dependent upon the flow conditions and geometry being studied.

3.3.1.2 Large eddy simulations

In contrast to RANS calculations, the LES method solves the instantaneous Navier-Stokes equation, which has been spatially filtered. The filtering operation allows for the more coarser energy containing eddies to be directly simulated, while the smaller eddies, which are assumed to be self-similar isotropic structures, are modelled. While a range of filters have been suggested in the literature, it is most common to imply the Schumann filter [353], whereby the filter length is identical to the cell size. As simulations are often computationally restricted to the number of cells in the domain, it is necessary to pursue the smallest possible filter size permissible, which is realised by this choice of implicit filter.

Applying the filter to the Navier-Stokes equations results in unclosed terms analogous to the Reynolds stress terms in RANS calculations. However, unlike RANS calculations, only the sub-filter scales need to be modelled, with the large geometry dependent scales being simulated without any further approximations. Very fine spatial scales are required in order to ensure that only the geometry independent structures are modelled, which often imposes a far higher spatial dependency than is required in RANS calculations. Furthermore, LES calculations require the full resolution of specific turbulent structures, which means that the modelled domain must be fully three-dimensional and unsteady.

LES has been successfully applied to model coal combustion in air-fired and oxy-fuel conditions [203, 210, 213, 214, 216, 354–356]. Studies comparing RANS predictions to LES results often show improvement in agreement with measured data using the LES approach [73, 216]. However qualitative trends are often similar to RANS approaches, suggesting that the results are almost equally sensitive to the other sub-models that are used to predict combustion.

3.3.1.3 Particle motion and heat transfer

Simulating multiple phase flows introduces additional complexity, as the physical properties of different phases vary significantly. For coal combustion, the density of solid-phase coal particles is significantly higher than the density of the combustion environment, and it is necessary to separate the phases. As coal particles occupy a small volume fraction in pulverised fuel combustion systems, modelling approaches will often track the particles in a Lagrangian frame without accounting for the volume of the particles within the fluid, and treat the mass and energy transfer as source terms in the relevant equations. When particle-particle interactions and particle feedback on the fluid is significant, it is necessary to consider alternative Eulerian multiphase models, however this approach introduces further challenges associated with accurately modelling the inter-phase exchange rates [357], and the Lagrangian method is often preferred in coal combustion systems.

In Lagrangian tracking, the motion of the discrete particle phase is modelled by treatment of the forces acting on the particle [357]. The change in a particle's velocity is calculated using the drag and gravitational forces for particles as

$$\frac{\mathrm{d}\hat{\mathbf{v}}_{\mathrm{P}}}{\mathrm{d}t} = F_D\left(\hat{\mathbf{v}} - \hat{\mathbf{v}}_{\mathrm{P}}\right) + \frac{\hat{\mathbf{g}}\left(\rho_{\mathrm{P}} - \rho\right)}{\rho_{\mathrm{P}}} \tag{3.91}$$

where $\hat{\mathbf{v}}_{\mathrm{P}}$ is the velocity of the particle, $\hat{\mathbf{v}}$ is the velocity of the fluid, F_D is the drag force, $\hat{\mathbf{g}}$ is the gravity force vector, ρ_{P} is the density of the particle and ρ is the density of the fluid. The drag force is calculated in turbulent flows from as[207]

$$F_D = \frac{3}{4}\frac{\mu C_D Re}{\rho_{\mathrm{P}} d_{\mathrm{P}}^2} \tag{3.92}$$

where μ is the dynamic viscosity of the fluid, d_{P} is the particle diameter, C_D is the drag coefficient for the particle and Re is the Reynolds number of the particle, which is calculated as

$$Re = \frac{\rho d_{\mathrm{P}}\left|\hat{\mathbf{v}}_{\mathrm{P}} - \hat{\mathbf{v}}\right|}{\mu} \tag{3.93}$$

The drag coefficient, C_D is often calculated using correlations assuming spherical particles, however correlations based on non-spherical particles are also used for solid fuel combustion [218]. Additional forces, such as the thermophoretic and Brownian forces, can be included as additional terms on the right hand side of Equation (3.91), however the two forces that are shown are often dominant for pulverised fuel particles, which are usually greater than 1 μm in diameter.

The heat transfer towards a particle, assuming that the particle is at a constant internal temperature, is described by the following equation [218]

$$m_{\mathrm{P}} C_{\mathrm{P}} \frac{\mathrm{d}T_{\mathrm{P}}}{\mathrm{d}t} = h A_{\mathrm{P}} (T_{\infty} - T_p) + f_h \frac{\mathrm{d}m_p}{\mathrm{d}t} H + Q_{abs} \sigma_{\mathrm{SB}} A_{\mathrm{P}} (T_{rad}^4 - T_{\mathrm{P}}^4) \tag{3.94}$$

where m_{P}, C_{P}, T_{P} and A_{P} is the mass, specific heat, temperature and external surface area of the particle respectively, h is the heat transfer coefficient, which describes convective and conductive heat transfer, Q_{abs} is the absorption efficiency of the particle, σ_{SB} is the Stefan-Boltzmann constant and T_{rad} is the radiation temperature, which is defined by the local incident radiation intensity,

$$T_{rad} = \left(\frac{\int_{4\pi} I \, \mathrm{d}\Omega}{4\sigma_{\mathrm{SB}}} \right)^{\frac{1}{4}} \tag{3.95}$$

The heat transfer coefficient h is often calculated from correlations based on a spherical particle shape, such as the Ranz and Marshall [358] method.

The above description of particle motion and heat transfer requires correlations and assumptions for the derivation of the drag and heat transfer coefficients, as well as assumptions on the particle being spherical and thermally thin. Furthermore, the equations require terms for the instantaneous velocity, density, temperature and incident radiation for the fluid phase, which are values that are not necessarily available for either RANS or LES calculations. Models are often used to describe the instantaneous or subgrid velocity fluctuations by incorporating a stochastic perturbation of the particle's velocity, such as the discrete random walk model for RANS [359] or the Bini and Jones [360] method for LES. However, the unresolved temperature, incident radiation or species composition is often neglected. These fields are crucial in calculating the heat transfer to the particle and the progression of combustion, and neglecting the instantaneous values may induce significant errors. This is particularly the case in RANS calculations, as the time-averaged quantities for fields such as O_2 concentration could potentially vary considerably from instantaneous values.

3.3.2 Coal combustion

Coal combustion is usually described by a succession of sequential processes. The first of these processes is the evaporation of the particle's inherent moisture as the particle heats up and dries. Drying is followed by the evolution of volatiles during the devolatilisation process, where the coal particle undergoes thermal decomposition, releasing light combustible gasses and tars that undergo combustion in the gas phase, liberating a significant proportion of the particle's heating value. After the particle is left with only the solid residual components of the fuel, comprising of the fixed char and non-combustible ash, the solid carbon undergoes heterogeneous oxidation to conclude the combustion process. The ash that is left following the complete combustion of the fuel is usually considered as inert, however the particles will still influence fluid momentum and heat transfer.

Drying, devolatilisation and char combustion are usually modelled sequentially, where the preceding step inhibits the following process; drying prevents the particle from reaching temperatures of devolatilisation, and the volatile flame inhibits the diffusion of oxidising species for char combustion. However it is noted that one-mode combustion may be prevalent under oxyfuel conditions, where devolatilisation and char oxidation occur simultaneously, due to the increased concentration of CO_2 and H_2O [361].

The devolatilisation and char combustion steps are complex chemical processes that are important to the overall behaviour of the combustion process, and must be modelled using approximate methods. This subsection will now review methods to model the devolatilisation and char combustion of coal particles. The formation of soot particles in the coal flame can also be significant in the overall heat transfer due to the particulate material's interaction with thermal radiation, and so methods to predict soot formation in coal flames is also discussed in this subsection.

3.3.2.1 Devolatilisation

The coal devolatilisation process occurs when light gasses and tars evolve from the thermal decomposition of the coal particle. The process is often modelled using empirical models, such as the single rate model [362] or two competing rates model [363], or semi-empirical network models such as the FLASHCHAIN [364], functional group (FG) [365], functional group devolatilisation-vaporisation-cross-linking (FG-DVC) [366] and chemical percolation devolatilisation (CPD) [367] models. The volatile matter itself is often modelled as an empirically defined species that is consistent with the proximate and ultimate analyses of the coal, and assumes a standard state enthalpy that is consistent with the calorific analysis of the fuel.

The single rate model approximates the devolatilisation process as a kinetic rate characterised with an Arrhenius expression,

$$\frac{\mathrm{d}m_p}{\mathrm{d}t} = -m_v A \exp\left(-\frac{E_a}{RT_p}\right) \tag{3.96}$$

where m_v is the mass of volatiles in the particle, R is the universal gas constant, T_p is the particle temperature, and A and E_a are empirical parameters fitted to measurements. The measurements for the empirical fitting are often taken from experiments such as thermogravimetric analysis or drop-tube furnace combustion, which measure the change in particle mass as a coal sample proceeds through the devolatilisation process [368, 369]. In the absence of experimental measurements it is also common to fit the empirical parameters to results from the network models mentioned above [203, 218].

The single rate model offers a straightforward mechanism to relate volatile mass release to the particle's temperature, however the devolatilisation process is more complicated than can be captured with a single rate, and so more complex empirical models have been developed. The Kobayashi model [363] applies two competing kinetic rates to model the devolatilisation process; one rate defines the volatile at a low heating rate, while a second rate represents high temperature pyrolysis. The volatile yield from the Kobayashi model is calculated as

$$\frac{\mathrm{d}m_p}{\mathrm{d}t} = -m_c \int_0^t (\alpha_1 k_1 + \alpha_2 k_2) \exp\left(\int_0^t (k_1 + k_2)\,\mathrm{d}t\right) \mathrm{d}t \tag{3.97}$$

where m_c is the mass of residual char, k_1 and k_2 are kinetic rates, usually expressed in terms of Arrhenius expressions, and α_1 and α_2 are the associated weights. The weights α_1 and α_2 are traditionally referred to as mass stoichiometric coefficients, with the α_1 corresponding to the volatile yield measured in the proximate analysis and α_2 is chosen to produce the high temperature volatile yield, however as the model is empirical in nature, both of these parameters are sometimes chosen to achieve a better fit to measured data.

The semi-empirical network models for coal devolatilisation use structural information of the investigated fuel, which is either ^{13}C NMR data in the case of the FLASH-CHAIN or CPD models, or detailed analysis of functional groups in the FG-DVC model, in order to predict devolatilisation rates from global kinetic mechanisms of the

	INY		UMZ		G#5		TSH	
	meas.	calc.	meas.	calc.	meas.	calc.	meas.	calc.
P_0	0.8	0.61	0.85	0.69	0.62	0.50	0.09	0.59
$\sigma + 1$	5.5	5.3	4.6	4.9	4.6	5.0	2.3	4.2
MW_{cl}	419	320	348	266	448	380	400	255
MW_{δ}	29.2	30.2	25.7	26.8	45.1	36.6	41.9	19.6

Table 3.2: Measured and calculated parameters of the CPD model for some South African coals. The measurements are from the study by Hattingh et al. [371], and the calculated parameters are evaluated from the correlations by Genetti et al. [370].

thermal decomposition. As these detailed measurements of the coal structure are seldom available for fuels, these parameters are often estimated using a correlation based on a library of coals, such as the correlations for the CPD model developed by Genetti et al. [370]. Care must be taken when applying these correlations to coals that are different from the library coals, for instance, the correlations by Genetti et al. [370] were exclusively developed on North American coals, and a significant variation can be shown between measured ^{13}C NMR parameters of a South African coal by Hattingh et al. [371] and the correlations, as illustrated in Table 3.2.

The underlying elemental chemical process of coal devolatilisation are invariably neglected, even in the more sophisticated models, and the chemical role of CO_2 is not directly accounted for. It is known that a CO_2 environment will result in higher volatile yields and altered char properties [368, 372], demonstrating that CO_2 interacts with the decomposition of the coal structure. Despite the neglect of this phenomena, the FG and CPD models have shown good agreement across a wide range of oxygen enrichments for oxyfuel combustion in a drop-tube furnace [373], although a wider range of tests for a range of fuels will be required for full confidence in the methods.

The volatile gasses themselves are often modelled by an empirical compound in CFD calculations, which maintains the parent coal's ultimate and calorific analyses, ensuring a consistent energy and mass balance with the case definition. This method to represent the volatiles requires the final volatile yield to be defined prior to the computation of the release model, so that the correct molecular and energetic portion of the fuel is accounted for, and therefore it is not straightforward to apply the sophisticated devolatilisation models in coupled CFD calculations, and empirical models are often preferred.

3.3.2.2 Char combustion

Coal char reacts through heterogeneous combustion with O_2 as well as gasification by CO_2, H_2O and CH_4. A semi-detailed kinetic mechanism for char reactivity has been proposed by Liu and Niksa [374],

$$2\,C + O_2 \longrightarrow C(O) + CO \tag{R 3.1}$$

$$C + C(O) + O_2 \longrightarrow CO_2 + C(O) \tag{R 3.2}$$

$$C(O) \longrightarrow CO \tag{R 3.3}$$

$$C + CO_2 \rightleftharpoons C(O) + CO \tag{R 3.4}$$

$$C(O) \longrightarrow CO \tag{R 3.5}$$

$$C + H_2O \rightleftharpoons C(O) + H_2 \tag{R 3.6}$$

$$C(O) \longrightarrow CO \tag{R 3.7}$$

$$C + 2\,H_2 \longrightarrow CH_4 \tag{R 3.8}$$

where C(O) represents a surface adsorbed intermediate species, which desorbs at a varying rate depending on the reagent that formed it. Conventional firing has only focussed on the char combustion rates, Reactions (R 3.1) to (R 3.3), however the gasification reactions are expected to be increasingly important under oxyfuel conditions [368, 375], although mostly in regions of low oxygen concentrations [376]. The hydrogasification reaction, Reaction (R 3.8), is not expected to occur at an appreciable rate during pulverised fuel combustion under air-fired or oxyfuel conditions, however it is treated as significant under gasifier conditions for the production of syngas [374].

The overall particle combustion rate depends on the chemical kinetics of the reactions outlined in the above mechanism, as well as the availability of the oxidising species. The particle combustion behaviour will move through the chemically limited regime, which is known as zone I, where the particle is typically at a low temperature and the combustion is limited by the reactivity of the char, to the diffusion limited regime, where bulk diffusion of the oxidising species to the particle's external surface is the limiting process, known as zone III, where the particle is at high temperatures with low availability of the oxidising species. The intermediate region between the chemically and diffusion limited combustion regimes is zone II, where porous diffusion through the particle is also important to the overall combustion rate. At temperatures greater than 1000 K, which will be typical of industrial combustion facilities, the combustion of pulverised char will most likely be burning under zone II and zone III conditions [377].

Further rate-limiting processes of char combustion include thermal annealing, where reactivity is reduced from thermal deactivation of the carbon structure, and ash inhibition, where an ash layer around the reactive carbon introduces an additional diffusional barrier for the oxidising species [378]. Thermal annealing and ash inhibition only affect the later stages of combustion, and they are often neglected in CFD calculations as the majority of char burnout can be accounted for without these processes [379].

The rate of char combustion can be expressed in terms of both the diffusion and kinetic rate with the following relation:

$$\frac{\mathrm{d}m_c}{\mathrm{d}t} = R_{d,i}A_p\left(p_{i,\infty} - p_{i,s}\right) = R_{c,i}\left(p_{i,s}\right)^n \tag{3.98}$$

where m_c is the mass of char, $p_{i,\infty}$ is the bulk partial pressure of the oxidising species, $p_{i,s}$ is the partial pressure of the oxidising species at the particle surface, A_p is the particle's external surface area, $R_{d,i}$ is the diffusion limited rate coefficient for reaction i, $R_{c,i}$ is the chemically limited rate coefficient for reaction i, and n is the apparent reaction order of the chemical rate.

The chemically limited rate of char combustion within the particle can be calculated as [380]

$$R_{c,i} = A_g k_i \tag{3.99}$$

where A_g is the internal surface area of the particle and k_i is the kinetic rate of the global reaction process. Expressions for k_i can be derived for the mechanism shown above in Reactions (R 3.1) to (R 3.8) through the assumption of the adsorbed species being in steady state [374], however it is more common to assume a global Arrhenius expression for the intrinsic reactivity, where

$$k_i = A_i \exp\left(-\frac{E_{a,i}}{RT_{\mathrm{P}}}\right) \tag{3.100}$$

where A_i is the pre-exponential factor for reaction i, $E_{a,i}$ is the activation energy for reaction i, R is the universal gas constant and T_{P} is the particle temperature. With knowledge of the internal surface area, intrinsic reactivity kinetic parameters can be derived from experiments where char particles are oxidised under zone I conditions, using methods such as thermogravimetric analysis [381].

The measurement of internal surface area is usually carried out using the Brunauer-Emmett-Teller (BET) [382] equation to relate the rate of N_2 adsorption to the surface area of the porous particle. Due to the long time-scales for the low temperatures of N_2 adsorption, typically at 77 K, the method only represents the macropores of the particle, as it is impractical to wait for N_2 to diffuse into the smallest pores. CO_2 adsorption methods are often used to represent a more complete measurement of microporous char particles as CO_2 adsorption can be conducted at higher temperatures [383]. Where measured values for the internal surface area are unavailable, correlations for the N_2 and CO_2 surface areas of char particles based on the particle's fixed carbon content have been presented by Williams et al. [384]. During combustion, the intrinsic surface area of the char particle can change by an order of magnitude [384]. Models to predict the pore evolution during burnout, such as the random pore model [385] and the pore tree model [386], are used to predict this change in the internal surface area. The morphology of char derived under oxyfuel conditions can be visibly different from conventional combustion [387], and these approaches to model pore evolution must be validated against measurements of oxyfuel derived char particles.

The diffusion limiting relation for char combustion, shown in Equation (3.98), can be expressed in terms of mass concentration as [220]

$$\frac{\mathrm{d}m_c}{\mathrm{d}t} = h_m \left(C_\infty - C_s\right) \tag{3.101}$$

where h_m is the mass diffusion coefficient, C_∞ is the bulk mass concentration of the oxidising species and C_s is the mass concentration of the oxidising species at the particle surface. By introducing the Sherwood number ($Sh = h_m d_\mathrm{P}/D_i$, where D_i is the bulk diffusion coefficient of the oxidising species), and by introducing the ideal gas law to relate mass concentration to partial pressure, $R_{d,i}$ from Equation (3.98) can be expressed as [388]

$$R_{d,i} = \frac{Sh M_\mathrm{c} \nu_\mathrm{c} D_i}{d_\mathrm{P} R T_m} \tag{3.102}$$

where M_c is the molar mass of carbon, ν_c is the molar stoichiometric coefficient (number of moles of carbon for one mole of oxidiser), D_i is the bulk diffusion coefficient of the oxidising species at the film temperature and T_m is the film temperature, which is often represented by the arithmetic average of the gas and particle temperatures. The stoichiometric coefficient is usually set to 2 for the combustion reaction, which represents the char reacting entirely to CO [388], and will be set to unity for the gasification reactions. The diffusion coefficient, D_i, can be reasonably accurately expressed from an evaluation at a reference temperature T_0 and pressure p_0 as

$$D_i(T, p) = D_i(T_0, p_0)\left(\frac{p_0}{p}\right)\left(\frac{T}{T_0}\right)^{1.75} \tag{3.103}$$

Under the assumption of spherical particles suspended in a fluid with zero slip velocity, where the Sherwood number is equal to 2 [380], and with the assumption of a constant pressure and by scaling D_i to a reference temperature of 1 K, it is possible to simplify the constants in Equation (3.102) to form the more widely used expression for the diffusion limited combustion rate,

$$R_{d,i} = \frac{D_0 T_m^{0.75}}{d_\mathrm{P}} \tag{3.104}$$

where D_0 is often used as a constant defined as

$$D_0 = \frac{2 M_\mathrm{c} \nu_\mathrm{c} D_i(T_0, p_0)}{R T_0^{1.75}} \tag{3.105}$$

Equation (3.105) differs from the form given by Chen et al. [79] in that the partial pressure of the oxidiser is calculated as $p_i = M_i C_i / RT$, where M_i is the molecular weight of the oxidiser in Equation (3.105), and where Chen et al. [79] used the mean molecular weight of the gas instead. In reality, D_0 will change for each mixture as it is dependent on the diffusion of the reactant species through the combustion environment, however the binary coefficient for O_2 in N_2 is often used for air combustion, thereby ignoring the effects of combustion products on the diffusion rate. Table 3.3 lists a series of diffusion rate constants for both air and oxyfuel combustion environments. The table illustrates that the rate constant changes most significantly when the bulk gas changes, with CO_2 reducing the diffusion reactivity rate by around one fifth, with the obvious exception of the CO_2 gasification reaction, which increases by a similar factor when considering diffusion through water vapour.

In order to model char combustion during zone II, an effectiveness factor, η_e, is introduced to Equation (3.100), so that the chemically limited combustion rate is represented as

$$R_{c,i} = \eta_e A_g k_i \tag{3.106}$$

The effectiveness factor is defined so that it is unity when there is no resistance from pore diffusion, and decreases as pore diffusion resistance increases. The effective diffusion rate through the pores can be modelled as the combination of the bulk diffusion

Diffusing species	Mixture	D_0
O_2	O_2/N_2	5.025×10^{-12}
O_2	$3\%O_2/7\%H_2O/14\%CO_2/76\%N_2$	4.939×10^{-12}
O_2	O_2/CO_2	4.031×10^{-12}
CO_2	CO_2/N_2	4.046×10^{-12}
CO_2	$3\%O_2/7\%H_2O/14\%CO_2/76\%N_2$	4.127×10^{-12}
CO_2	CO_2/H_2O	5.347×10^{-12}
H_2O	H_2O/N_2	6.610×10^{-12}
H_2O	$3\%O_2/7\%H_2O/14\%CO_2/76\%N_2$	6.386×10^{-12}
H_2O	H_2O/CO_2	5.347×10^{-12}

Table 3.3: Diffusion rate constants for different environments. The rate coefficients are calculated using the molar mixture diffusion coefficients calculated by the Cantera software library [389], using the transport properties from the GRI-3.0 mechanism [390]. Composition of the mixture is displayed as percentage by volume.

rate through the macropores and Knudsen diffusion through micropores,

$$D_{Kn} = \frac{2}{3} r_{pore} \sqrt{\frac{8RT_{\mathrm{P}}}{\pi M_i}} \tag{3.107}$$

$$D_e = \frac{\theta}{\tau^2} \left[\frac{1}{R_{d,i}} + \frac{1}{D_{Kn}} \right]^{-1} \tag{3.108}$$

where D_{Kn} is the Knudsen diffusion rate, M_i is the molecular weight of the oxidising species of reaction i, r_{pore} is the mean pore radius, θ is the porosity of the char particle, τ is the tortuosity of the pores and D_e is the effective diffusion through the pores. For the derivation of the effectiveness factor from the diffusion rate, the Thiele modulus is first introduced, which for an n-th order Arrhenius type reaction rate, as in Equation (3.100), is expressed as [380, 391]

$$\phi = r \left(\frac{(n+1)\nu_{\mathrm{C}} \rho_{\mathrm{P}} k_i A_g p_s^{n-1} R T_p}{2 M_i D_e} \right)^{\frac{1}{2}} \tag{3.109}$$

where ϕ is the Thiele modulus, r is the particle diameter and ρ_{P} is the particle density. Alternative derivations of the Thiele modulus for Langmuir-Hinshelwood mechanisms, such as in Reactions (R 3.1) to (R 3.8), have also been developed [392]. By calculating the ratio of reactivity both with and without pore diffusion resistance, and assuming an isothermal homogeneous particle, the effectiveness factor for a spherical particle is given in terms of the Thiele modulus as [393]

$$\eta_e = \frac{3}{\phi}\left(\frac{1}{\tanh\phi} - \frac{1}{\phi}\right) \tag{3.110}$$

The overall char reactivity, incorporating the effects of all three combustion zones, is calculated by rearranging Equation (3.98) to eliminate the unknown quantity $p_{i,s}$,

$$\frac{\mathrm{d}m_c}{\mathrm{d}t} = R_{c,i}\left(p_{i,\infty} - \frac{\mathrm{d}m_c}{\mathrm{d}t}\frac{1}{A_p R_{d,i}}\right)^n \tag{3.111}$$

For reaction orders of $n = 0, 0.5, 1$, analytical forms of Equation (3.111) can be derived, however an iterative method, such as Brent's method [394], must be used for other reaction orders. When the char consumption reactions are expected to compete over reactive sites, which is often the case for CO_2 and H_2O gasification mechanisms, the surface concentration of reactive species become coupled, which requires a more sophisticated numerical method such as Powell's method or the Levenberg-Marquardt method [374].

While the above derivation provides a reasonably complete description of the char combustion process, the calculation requires several parameters that are not well defined across a wide distribution of particles or throughout the combustion process. Empirical models are widely applied to describe char combustion, where kinetic parameters are fitted to Equation (3.100), with the exception that the kinetic rate is dependent on the external surface area, absorbing the role of pore diffusion into the apparent reaction order and kinetic rate. These rates are more readily developed, however the combustion measurements must match the conditions that are being modelled, and models developed in air-fired combustion are very likely to be inaccurate in an oxyfuel environment.

During char combustion, the changes to particle diameter and density are often modelled using a burnout mode parameter and the following relations [220],

$$d_{\mathrm{P}} = d_{\mathrm{P},0}\,(1 - X)^{\alpha} \tag{3.112}$$

$$\rho_{\mathrm{P}} = \rho_{\mathrm{P},0}\,(1 - X)^{1-3\alpha} \tag{3.113}$$

where d_{P} is the particle diameter, ρ_{P} is the particle density, X is the fractional degree of burnoff and $d_{\mathrm{P},0}$ and $\rho_{\mathrm{P},0}$ are the char particle diameter and density for unburned char respectively. The burnout mode α changes between the different burnout regimes. Under zone I conditions the char burns at constant diameter and reducing density, $\alpha = 0$, as the particle burns at the same rate throughout. Under zone III conditions, only the particle surface is exposed to the char consumption mechanism, and the particle shrinks while at constant density, $\alpha = 1/3$. The burnout mode α will vary throughout zone II combustion. It is most common to approximate the changes in the char size/density by using a constant value for α, and a value of 0.25 is widely used [379], however under oxyfuel combustion, where each char oxidation reaction is likely to be participating under different combustion regimes, this value may not be valid.

The heterogeneous combustion of char is a complex process, which requires numerous models to capture the various physical properties of char during the process; modelling diffusion, pore evolution and variations in the particle's size and density, as well as models for the kinetic mechanism itself. Due to the significant complexity of this process, and also due to the strong variability in many modelling parameters across coal samples, it is often preferable to use global rates that are known to perform well in the specific conditions that are being modelled. Oxyfuel environments are a relatively unfamiliar, and may not be well characterised by these modelling approaches. The high concentration of CO_2, and potentially H_2O in a wet recycle environment, will both promote enhanced oxidation, through increased gasification rates, and reduce oxidation through lower gas temperatures and lower diffusion rates [376], and therefore cannot easily be explained by intuition.

3.3.2.3 Soot formation

As mentioned in Subsection 3.2.1, soot can participate significantly in radiative transfer, and can contribute up to 60% of the total radiative emission from particulates in the flame [395]. Despite its significance, soot formation is often neglected as its production and fate is difficult to model. While accurate kinetic models exist that describe the formation and burnout of soot particles using elementary kinetics [396], these mechanisms often have several hundred reaction steps, and are clearly too large and detailed for CFD applications, particularly as the volatile gas is rarely modelled as a true species. Global soot models are often used for combustion CFD calculations, however, for coal combustion, due to the variability of the fuel and as the soot precursor volatile species are not modelled directly, it is not clear how valid these models can be.

The coal soot model derived by Brown and Fletcher [397], which is based on the global model by Brookes and Moss [398], has been applied in previous CFD studies [218]. The model has shown reasonable agreement using tar yields predicted from the CPD model, however more validation against a wide range of coal ranks is still required for confident application in general cases.

3.3.3 Turbulence-chemistry interaction

The chemical kinetics of combustion occur on very small time- and length-scales, often much smaller than the resolved scales in a LES [399]. Due to the non-linear relationship between the transported fields and the combustion kinetics, it is necessary to model the influence of unresolved turbulent structures on the chemistry of combustion in both RANS and LES calculations. The gaseous volatile matter from coal is assumed to evolve from the particle without mixing with oxygen and react as a diffusion flame, where a significant rate-limiting factor of the combustion is the displacement of the product species and the mixing of the oxidiser and the volatile gasses. Models that are used to describe the combustion of diffusion flames often rely on the assumption of the reaction being completely mixing-limited, and the combustion is modelled as the rate of turbulent mixing.

One of the most widely used methods to model turbulent combustion in coal flames is the eddy dissipation (ED) model [400]. This model approximates the averaged rate of combustion to be proportional to the slowest time-averaged dissipation rate of reactant and product species,

$$R_{\mathrm{R}} = A\rho\frac{1}{\tau}\min\left[\tilde{Y}_f, \frac{\tilde{Y}_{ox}}{\beta}, B\frac{\tilde{Y}_p}{\beta+1}\right] \tag{3.114}$$

where R_{R} is the mass rate of fuel consumption associated with the reaction, τ is the large-eddy mixing time-scale, $\tilde{Y}_f$ is the Favre-averaged mass fraction of fuel species, $\tilde{Y}_{ox}$ is the Favre-averaged mass fraction of oxidising species, usually O_2, $\tilde{Y}_p$ is the Favre-averaged mass fraction of product species, β is the mass of oxidant per unit mass of fuel stoichiometry, and A and B are model constants, which may depend on the fuel and flame structure [400]. The mixing time-scale in RANS calculations is taken as the ratio of turbulent kinetic energy to the dissipation rate, k/ϵ. For the application of this model to LES calculations, the time-averaged terms are replaced with spatially filtered values, and the mixing time-scale is calculated as the reciprocal of the rate of strain. The constants introduced in Equation (3.114) are normally assigned 4 and 0.5 for A and B respectively, which were originally suggested for methane flames [400]. Studies on swirled coal flames have identified that A should be set to 0.5 and 0.7 for volatile gas and CO oxidation respectively [206, 207], however these parameters may not necessarily translate to an oxyfuel environment or LES calculations.

The ED model is only valid in mixing-controlled regions, where temperatures are high enough to make the chemically controlled kinetics significantly faster than the physical mixing of the reactants. Due to this assumption, the ED model is only applicable with simple global reaction mechanisms that neglect intermediate species and reversible reactions that hold a balanced equilibrium. An extension of the ED method for chemically controlled regions, known as the finite-rate eddy dissipation (FR-ED) method, involves associating an Arrhenius rate expression to the reaction based on bulk thermochemical properties, and the overall reaction rate is evaluated as the minimum of this Arrhenius rate and Equation (3.114). While the FR-ED method prevents ignition in cold regions of the domain, the association of the bulk averaged quantities, or even the spatially filtered quantities in an LES, to a kinetic rate is physically unsound, and the kinetic rate only serves as an extra parameter to forcibly prevent early ignition. As with the ED method, the FR-ED method is only capable of describing global mechanisms, and cannot describe a system with a balanced equilibrium.

A more sophisticated development for the ED model, which extend its principle for systems with kinetically controlled chemistry, is the eddy dissipation concept (EDC) model. As with the ED model, the EDC model assumes that all chemical reactions take place in the fine scales, which are characterised by a length-scale, ζ^*, and time-scale, τ^*, within the EDC model [350, 401], defined as

$$\zeta^* = \left(\frac{3C_{D2}}{4C_{D1}^2}\right)^{1/4} \left(\frac{\nu\epsilon}{k^2}\right)^{1/4} \tag{3.115}$$

$$\tau^* = \left(\frac{C_{D2}}{3}\right)^{1/2} \left(\frac{\nu}{\epsilon}\right)^{1/2} \tag{3.116}$$

where ν is the kinematic viscosity of the fluid, k is the turbulent kinetic energy, ϵ is the dissipation rate of the turbulent kinetic energy, and C_{D1} and C_{D2} are model constants set to 0.134 and 0.5, respectively. The small scales can be treated as perfectly stirred reactors, with an initial condition taken from the bulk mass fractions, which react for the residence time of τ^*. The computational requirement to integrate a kinetic scheme for each control volume can be hugely significant, however this can be alleviated through tabulation techniques such as the in situ adaptive tabulation (ISAT) method [402]. The EDC model is increasingly popular in RANS calculations [77, 403] as the method is capable of applying detailed chemistry to averaged bulk fields, although most studies focus on the application of the EDC with simplified global reaction mechanisms, such as the Westbrook and Dryer [404] and Jones and Lindstedt [405] mechanisms. Some studies have applied the EDC model to LES calculations

[406, 407], however these have not been applied for LES of coal combustion.

The main benefit of the widely used ED model is its simplicity and straightforward implementation in CFD calculations. Particularly for coal combustion, where the volatile gasses are often derived empirically from the chemical analyses of the coal, the benefits of the detailed mechanisms achieved by the EDC approach is often questionable. While some methods have been developed to predict the speciation of volatile matter [408–410], these methods have not been widely validated against different coals, and the precise speciation will always depend on the chemical interactions within the coal particle during pyrolysis. However, the shortfalls of the ED method are clear; the model is incapable of representing kinetically controlled chemistry and balanced reversible reaction schemes. It has been suggested that under oxyfuel conditions the balance of the CO_2 dissociation reaction,

$$CO_2 \rightleftharpoons CO + O \tag{R 3.9}$$

is more significant than under conventional air-firing, which cannot be described by the ED model [411].

Alternatively to the models discussed above, diffusion flames are frequently modelled as the mixing of two conserved scalars, representing the fuel and the oxidiser streams. Under several simplifying assumptions, the flow field is reduced to a single transport equation for the Favre-averaged, or spatially filtered, mixture fraction that represents the composition of a location based on how well the two streams are mixed. As there are typically two fuel streams that are considered in coal combustion, one stream for gas-phase volatile species and another for the solid-phase char fuel, it is necessary to introduce the transport of a second mixture fraction.

In order to capture the distribution of the transported mixture fractions across the unresolved turbulent scales it is necessary to define a probability distribution function (PDF) that describes this variation. It is common in RANS models to assume a β-function shape, which describes the distribution as a function of the averaged mixture fraction and its variance, which is either treated as an additional transported quantity or is defined algebraically from the local levels of turbulence. In LES calculations, a small filter length will often lead to inconsistencies in applying the β-function shape, and instead a simpler top-hat function is preferred [412].

Detailed chemistry can be included in the mixture fraction approach by associating the local level of mixing to pre-computed tables. By assuming the interface between the fuel and oxidiser streams as a laminar diffusion flame, it is possible to pre-compute the representative 1D laminar flamelet for a range of local conditions, which can be used to describe the local gas composition and associated properties. In the absence of detailed kinetics, which is often the case for the unknown volatile species, it is also common to calculate an equilibrium based on the local enthalpy and elemental composition.

There are challenges associated with applying the flamelet approach to oxyfuel combustion. Under oxyfuel conditions, the oxygen concentration of the primary register is often different from the main oxidising streams, which means the oxidising stream and the transport stream must be treated separately in a flamelet approach to oxyfuel combustion. In addition to separate streams for the volatile evolution and char availability, oxyfuel will require the modelling of the mixture fractions between four separate streams, which will ideally be transported with their variance and also tabulated against fluid enthalpy, greatly increasing the complexity of the flamelet method. Despite this, the mixture fraction approach has been successfully applied to CFD calculations of a laboratory-scale oxy-coal combustion facility [413], however there was only a single inlet composition. While studies have noted a significant sensitivity on the choice of either the mixture fraction approach or the ED model for the turbulence-chemistry interaction in coal combustion [414], it was not possible to categorically suggest which model was more accurate.

Composition PDF methods have also been developed to describe the turbulence chemistry interaction [415]. In these methods the distribution of unresolved scales is discretised as a series of single-point particles that are tracked in a Lagrangian manner. Detailed chemistry can then be employed to integrate species composition as the particles are transported in time. While composition PDF methods have been employed in CFD calculations of coal combustion [212, 416], achieving good agreement to measured data, these methods are not widely available and have a considerable computational expense.

3.3.4 Turbulence-radiation interaction

As combustion largely takes place in the small unresolved eddies, temperature sources are localised to spatial regions that are not explicitly considered in spatially filtered or Favre-averaged fields. As a result of the non-linear relationship between both radiation emission and absorption with temperature and species, potentially significant features of the intensity field are neglected through the use of averaged or spatially filtered quantities in the calculation of the RTE. This dependence of accounting for the turbulent structures in the predictions of the radiation intensity field, as well as the reciprocal dependence of the temperature field on the predicted radiative transfer, is known as turbulence radiation interaction (TRI).

Methods to resolve TRI have mostly focussed on composition PDF methods [222, 417–421], on comparing DNS and LES results [422, 423], or on the influence of the resolved transient scales in LES in comparison with results obtained with averaged fields [424]. While TRI influences radiative properties including surface heat flux [222, 418, 424], the influence over the temperature field has often been shown to be less significant [417, 421, 423]. If the coal-particles are being modelled using Lagrangian particle tracking, the radiative sources from the solid-phase, which can be significantly higher than from the gas-phase, are neither averaged or spatially filtered, and so a significant portion of the TRI is being resolved.

3.4 Summary

Numerical modelling of combustion systems allows for the optimisation of the process. Applied to the oxy-coal process, modelling techniques will serve to optimise the novel combustion environment so that it can become a competitive low-carbon technology. However, models that are specific for an air-fired environment need to be re-evaluated for their applicability to predicting oxy-coal systems, specifically models for radiative heat transfer, which represents the most significant mode of energy transfer at combustion temperatures.

CFD is widely used for predicting the fluid flow within combustion systems, however the models that are widely used for radiative heat transfer are often chosen for their computational efficiency rather than their physical accuracy. This chapter has reviewed a series of models to represent the radiative properties of gaseous species and coal-derived particles.

The widely used grey WSGG method for gaseous radiative properties is fixed to predefined combustion environments and will be incapable of predicting the influence of recycle schemes on thermal radiation, and so more sophisticated models are required, which are more independent on the combustion medium. Further WSGG parameters developed for wider ranges of operating conditions have been put forward in the literature, however the grey WSGG model still relies on the poorly-defined mean beam length, and the non-grey alternative may be required for cases with higher partial pressures of participating species.

Further global methods have also been put forward, namely the ADF, SLW and FSK methods. These methods, which are independent of any predefined medium, offer a promising alternative to the WSGG methods, but require further validation and comparison before any one method can be recommended for a range of oxyfuel conditions. Each method assumes a scaled or correlated absorption coefficient across the entire spectrum, which are invalid in cases with significant thermal gradients in the medium or variations in relative species concentrations, which are both likely under oxyfuel conditions. In Chapter 5 the global models for thermal radiation are validated against narrow band and LBL calculations to identify an optimal method for representing gaseous radiative properties.

Suspended particles in a coal combustion system are responsible for significant absorption and emission of radiative energy. Despite this, the radiative properties of coal-derived particles are often assumed to be constant and grey throughout combustion. Mie theory results from optical constants measured from coal-derived particles suggest that these properties can vary across the electromagnetic spectrum, as well as varying with particle size and composition.

Further to the development of radiative property models, oxyfuel presents many challenges in the application of the heterogeneous and homogeneous combustion models. Due to the unfamiliarity of the combustion environment, additional scrutiny must be applied to all modelling assumptions used for an oxyfuel process, however this will be beyond the scope of this thesis. Consideration for the modelling assumptions and how these may influence the predictions under oxyfuel have been introduced in this chapter, however current methods will not be developed in later chapters of this work. Instead, these discussions will aid in the analysis of the later modelling results that must make use of these models to represent a real combustion environment, which will be presented in Chapter 6, where additional benchmark calculations will be compared against global model results to separate the impact of potentially inaccurate models for the other phenomena of oxy-coal combustion.

4 Modelling investigation into mercury oxidation for oxyfuel

It is possible to predict the chemical composition of a system when provided with the mechanism and kinetics of chemical reactions and the thermodynamics of the potential species that could be present. Through only the definition of the thermodynamic properties of the chemical species, namely the enthalpy and entropy of a compound, it is also possible to predict the equilibrium of a given system by calculating the species composition with a minimal Gibbs free energy [144]. The chemical equilibrium of a system can be an important consideration as it indicates the potential for a given mixture when it is not constrained by kinetic limitations, and also plays a fundamental role in the kinetics of reversible reactions.

This chapter contains fundamental investigations on thermodynamic equilibria and kinetic modelling of the gas-phase interactions of mercury under oxyfuel conditions. The purpose of the studies covered in this chapter are to question the existing data available for chemical modelling and apply these to air-fired and oxy-fired combustion environments. In Section 4.1, thermodynamic values are used to predict equilibrium distributions for mercury and the halogen species under conventional and oxyfuel flue gas conditions. A kinetic modelling study is conducted in Section 4.2, where a mechanism is constructed from published studies. The mechanism is optimised against measured values for mercury oxidation under the two flue gas conditions, and the resulting kinetic rates are analysed to provide new insight into the important reactions for mercury oxidation.

4.1 Thermodynamic modelling

Mercury does not reach an equilibrium between its elemental and oxidised states under the short residence times of the flue gas train [169]. Nevertheless, a study on the thermodynamic equilibria of mercury compounds under flue gas conditions provides a fundamental insight into the behaviour of mercury, being indicative of the dominant directions of the reversible reactions involved in a kinetic model, and the minimum temperature at which mercury will begin to oxidise. Equilibria calculations are also good at predicting high temperature gas compositions, where chemical kinetic limitations on the composition are mitigated [144]. Previous studies have analysed the equilibria shift under various halogen concentrations [94, 144, 169, 425], and for a specific chlorine concentration under oxyfuel conditions [426]. This study profiles the equilibrium distributions of gas-phase species related to coal combustion between 300 K and 2500 K. Equilibrium distributions are calculated under both air-fired and oxyfuel conditions. Additional attention is paid to fluorine and iodine species, which are often neglected. The goal of this study is to perform a preliminary investigation into the effects of oxyfuel combustion and the influence that different halogen species are likely to have.

4.1.1 Thermodynamic data and initial composition

Thermodynamic data were obtained from the NIST JANAF thermochemical tables [427]. A notable omission from these tables include the mercuric sulphide (HgS), and so thermodynamic values from Barin and Platzki [428] for this species were also included. Due to uncertainties around the thermodynamic values of HgO, mentioned in Subsection 2.1.1, the species was not included in these calculations. Previous studies have noted a very small presence of the HgO species in equilibria above 700 K [144]. Thermochemical properties were modelled by fitting a piecewise polynomial to the values in the data tables using a least-squares approximation. The piecewise polynomials were calculated as two fifth-order polynomials for each specie's heat capacity across the temperature range of 300 K to 2500 K, with a midpoint varied to suit the data. Two additional fitting coefficients were then calculated to fit the enthalpy and entropy of the substance. The polynomial coefficients were calculated as the 7-form NASA polynomials to satisfy the equations:

$$\frac{C_p}{R} = a_1 + a_2 T + a_3 T^2 + a_4 T^3 + a_5 T^4 \tag{4.1}$$

$$\frac{H}{RT} = a_1 + a_2 \frac{T}{2} + a_3 \frac{T^2}{3} + a_4 \frac{T^3}{4} + a_5 \frac{T^4}{5} + \frac{a_6}{T} \tag{4.2}$$

$$\frac{S}{R} = a_1 \ln T + a_2 T + a_3 \frac{T^2}{2} + a_4 \frac{T^3}{3} + a_5 \frac{T^4}{4} + a_7 \tag{4.3}$$

where $a_1 - a_7$ are the constant polynomial coefficients, T is the temperature, R is the universal gas constant and C_p, H and S are the heat capacity, enthalpy and entropy of the substance, respectively. The resulting thermodynamic database used in this study

Major elements	Weight %
C	70.56
H	5.96
O	16.29
N	1.47
S	4.08

Table 4.1: Major coal elements for equilibrium calculations. Values taken from Zhuang and Pavlish [33].

contained 250 species, representing 17 elements (Hg, Cl, F, Br, I, O, N, S, C, H, Be, Cr, Co, Pb, Mn, Ni, Ar). Species for arsenic, selenium, cadmium and antimony were not included as there were no data available from the thermodynamic tables.

The python interface of the Cantera [389] library was used to calculate the equilibrium values across the temperature range. The equilibrium prediction method that was used from Cantera minimises the Gibbs free energy of the system for a constant temperature and pressure. This method relies solely on the thermodynamic data and atomic composition of the species, and is independent of any reaction mechanisms. Only gaseous phase species were included in the thermodynamic calculations, as the focus on this study is on homogeneous oxidation, however it is noted that some species could form more stable solid-phase compounds at the conditions studied [144]. All calculations were undertaken for mixtures at atmospheric pressure.

The coal analysis data provided by Zhuang and Pavlish [33] was used in the thermodynamic calculations as the analysis included levels of trace elements, as well as providing an oxyfuel firing regime for the equilibria calculations. Tables 4.1 and 4.2 contain the composition values used in the calculation. Solid-phase ash species were not included in the coal composition as this analysis was based solely on gas-phase species. The only reported halogen in the analysis by Zhuang and Pavlish [33] was chlorine, so the concentrations of fluorine, bromine and iodine were estimated based on their reported Clarke value, an estimate of the average species composition across all coals, to the same ratio of the chlorine content in order to investigate their effects [86]. The fuel-to-air equivalence ratio was set to match the experimental values of 0.93 for the oxy-fired case and 0.83 for the air-fired case. The oxidant used in the oxyfuel equilibrium calculations was set to 73% CO_2 and 27% O_2 to match the experiments by Zhuang and Pavlish [33]. Unlike in the experiments, the oxidant for the oxy-fired case did not contain any pre-existing pollutants or nitrogen.

Trace elements	ppm_w
Be	0.95
Cr	14.9
Co	5.69
Pb	7.62
Mn	33.0
Hg	0.08
Ni	22.2
Cl	137
F[a]	84
Br[a]	6
I[a]	1.5

[a] Value estimated from the Clarke value and the chlorine-to-Clarke value ratio from Ketris and Yudovich [86].

Table 4.2: Trace elements for equilibrium calculations. Values taken from Zhuang and Pavlish [33].

4.1.2 Results

The results shown in Figure 4.1 illustrate that there is very little change in the equilibrium distribution of Hg species when switching from air-fired to oxy-fired coal combustion. When the halogen concentrations are increased by a factor of 100, shown in Figure 4.2, the equilibrium distributions for air and oxy-27 both demonstrate the same behaviour; shifting the point where [Hg] is equal to [$HgCl_2$] to similar higher temperatures. The results clearly show that $HgCl_2$ is the most stable form of mercury in the cooler regions of the flue gas, and is more stable than other mercuric halide compounds, and that elemental mercury will not react at temperatures above 1200 K, even with a considerable excess of halogen species. These calculations also suggests that variations between the two conditions observed in experimental studies do not arise from the thermodynamic properties of the system. This conclusion emphasises the importance of an investigation into the kinetic parameters that govern mercury interactions.

Equilibrium distributions for the halogen species were calculated for the oxyfuel and air-fired cases. As with mercury, the halogen species exhibited the same distributions for both cases, and therefore only the oxyfuel distributions have been presented in Figure 4.3. These results illustrate why the various halogens exhibit different oxidation efficiencies. Of all the atomic halogen species, only atomic fluorine is not represented at combustion temperatures, and therefore it is justified to disregard the fluoride species as an oxidiser of mercury. Reasonable levels of atomic chlorine are

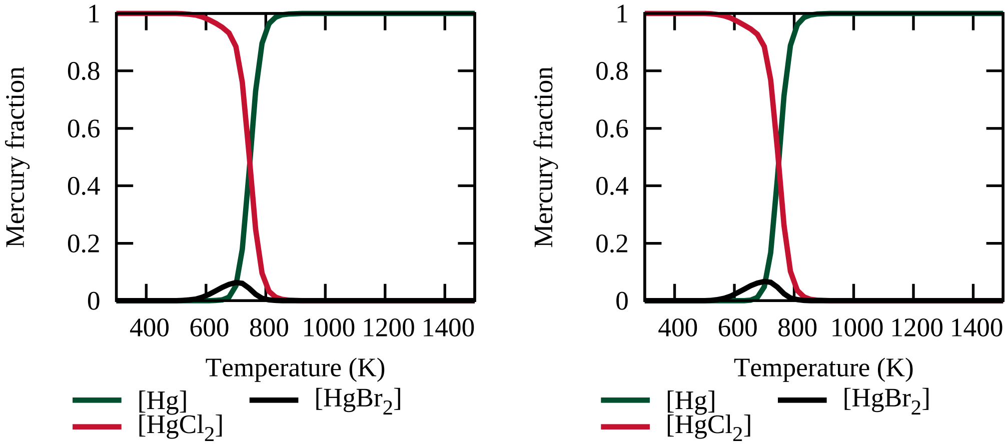

(a) Air equilibrium

(b) Oxy-27 equilibrium

Figure 4.1: Equilibrium distributions for mercury in coal derived flue gas.

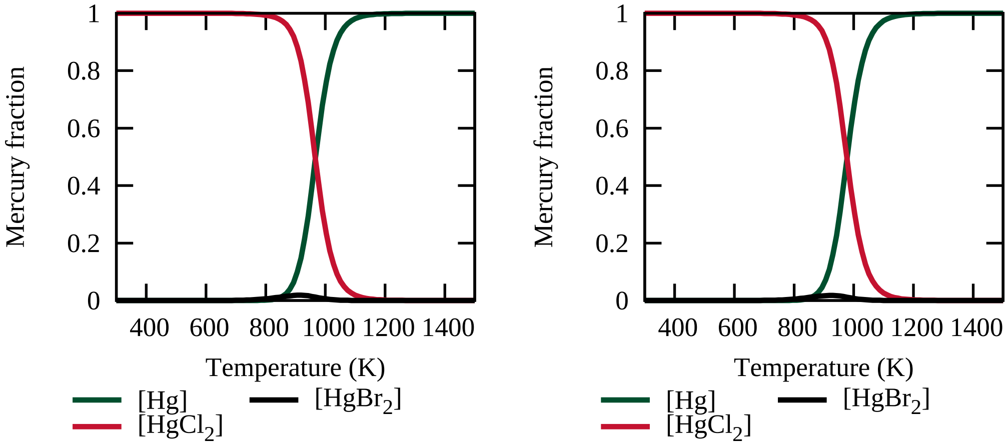

(a) Air equilibrium

(b) Oxy-27 equilibrium

Figure 4.2: Equilibrium distributions with increased halogen concentrations. Halogen species' concentrations were increased by a factor of 100 over the baseline amount in Table 4.2.

produced at the higher temperatures of combustion, which would remain in the flue gas at temperatures relevant to mercury oxidation if the kinetic rates of the reactions that consume Cl are reasonably slow. Both atomic Br and I are stable at regions close to mercury oxidation temperatures, however their low concentrations reduce the oxidising potential of these halogens. The stability of these atomic halogens may also serve to destabilise the respective mercurous halide species, which would reduce the oxidation efficiency of the halogen.

This study introduced the thermodynamic behaviour of mercury and halogen species under conventional and oxyfuel combustion conditions, for an atomic composition that is representative of coal combustion. The equilibrium distributions of both mercury and the halogen species exhibit negligible differences in response to the change in combustion environment. The equilibria calculations reaffirm that mercury will only oxidise in the lower temperature regions of the flue gas train, that atomic chlorine is only produced at higher temperatures, and that atomic bromine is well represented at far cooler temperatures than with chlorine.

4.2 Kinetic modelling investigation

A wide variety of published chemical-kinetic rate coefficients for mercury oxidation were introduced in Subsection 2.2.3. The modelling study presented in this section utilises a genetic algorithm to optimise a kinetic model so that the mechanism best approximates the experimental data by Preciado et al. [117], which were obtained for mercury oxidation under conventional and oxyfuel combustion conditions. The mechanism is then analysed to determine the processes that are responsible for the measured increase in oxidation efficiency observed under the oxyfuel conditions. The genetic algorithm is applied to both chlorine and bromine reactions, and the resulting mechanisms are investigated using a brute force sensitivity analysis to identify the most influential kinetic rates in each firing regime. This modelling investigation highlights features of the mechanism that influence mercury oxidation, and provides motivation for a wider consideration of chemical kinetics outside of the current mercury oxidation scheme.

The experimental study by Preciado et al. [117] measured mercury oxidation rates by chlorine and bromine species in both an oxyfuel and air-fired combustion environment, including measurements with varying levels of NO and SO_2 pollutants. The experiments were conducted in a 300 W laminar flow quartz reactor that was approximately 1.3 m in length. The oxyfuel experiments were conducted with an oxidant

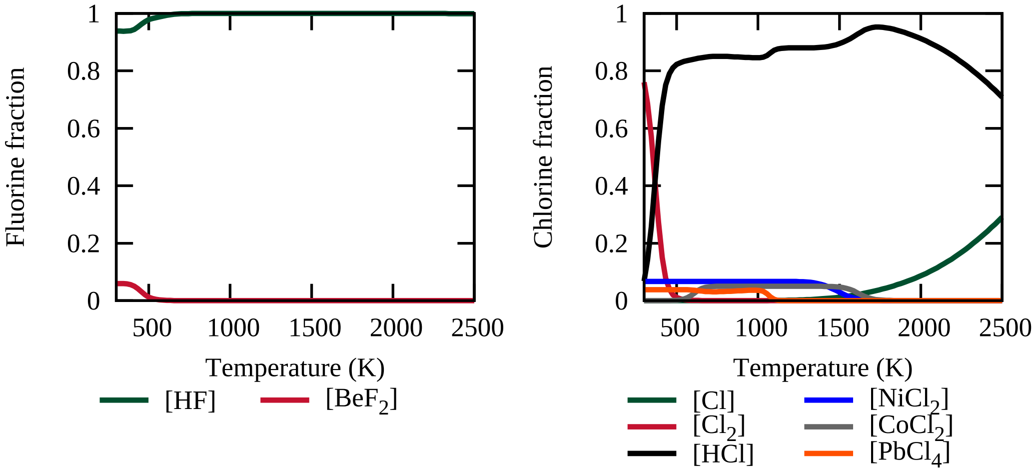

(a) Fluorine equilibrium

(b) Chlorine equilibrium

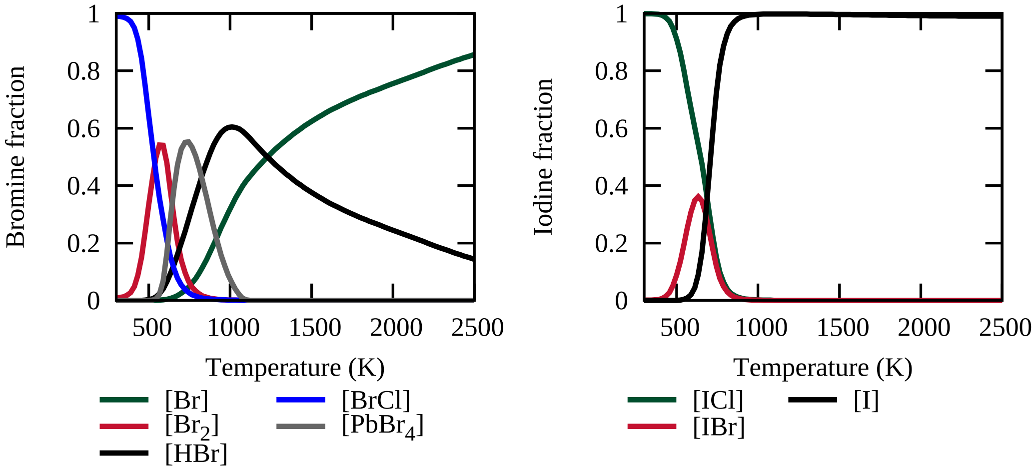

(c) Bromine equilibrium

(d) Iodine equilibrium

Figure 4.3: Equilibrium distributions for halogen species under oxy-coal flue-gas environments.

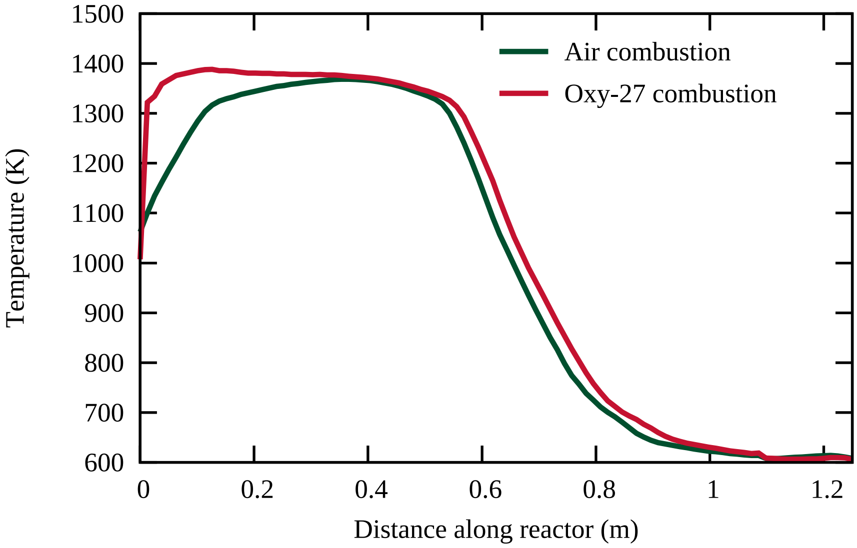

Figure 4.4: Temperature profiles for the training data from the experiments by Preciado et al. [117].

composed of 27% O_2 and 73% CO_2 supplied from gas cylinders. Chlorine concentrations were varied between 100 ppm_v to 500 ppm_v HCl, and bromine was varied between 10 ppm_v to 50 ppm_v HBr. Reactants were introduced either dilute in air or N_2, providing potentially significant sources of N_2 in the oxyfuel combustion environment. The temperature profiles across the reactor for the air-fired and oxy-fired experiments were controlled using a Thermcraft high-temperature heater within the first 0.54 m of the reactor, with the remainder being controlled with heating tapes. The resulting temperature profiles along the length of the reactor for the two firing regimes are shown in Figure 4.4. The total flow rate of the flue gas was fixed to 6 slpm, and the stoichiometric ratio was varied to achieve an exit O_2 concentration of 2% on a dry basis under both firing conditions. Mercury oxidation was detected through a scheme akin to the Ontario Hydro method, with additives to the conditioning system to overcome experimental bias introduced by Cl_2 formation or from the oxyfuel environment.

A genetic algorithm was applied to optimise the kinetic mechanism against the experimental data. Genetic algorithms are a class of optimisation techniques that are used to generate solutions that can minimise an associated arbitrary cost function. In a genetic algorithm the problem solution is encoded as a vector of numbers, allowing numerous solutions to be represented as varying strings of values. Traditionally, the

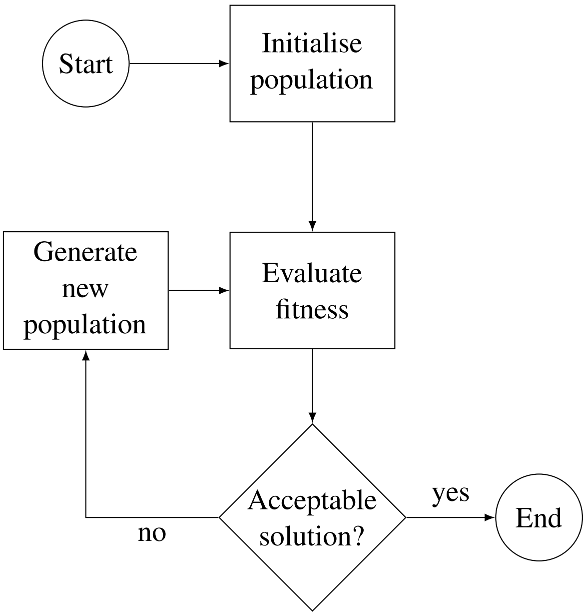

Figure 4.5: Flow chart for a genetic algorithm.

solution vector is represented by a string of binary digits, however it is also possible to use real valued numbers.

The flow diagram for an arbitrary genetic algorithm is illustrated in Figure 4.5. The algorithm starts with an initial stochastically generated population of solutions, and then each solution is evaluated against a cost function, assigning a fitness to the solutions. The best ranking solutions are mixed using cross-over operations, where new solution vectors are generated through some combination of values contained in two or more existing solutions. Mutation operations, where a new random value is introduced into a solution's vector, are also used to provide continued variance in the population. The new population that is generated from these cross-over and mutation operations is then evaluated against the cost function again, and the process continues until a satisfactory solution is produced. In this study, the optimisation process was terminated when the solution had not improved for over five generations.

A genetic algorithm is well suited for optimising a kinetic model due to the inherent parametrisation of rate coefficients in the modified Arrhenius equation, Equation (2.3) of Subsection 2.2.1. Genetic algorithms have been widely applied to successfully produce reduced kinetic mechanisms for combustion conditions [429–434]. The method in this study uses a genetic algorithm to explore the solution space described by a detailed chemical kinetic mechanism for mercury oxidation in a post-combustion flue gas. The solution vector is encoded as a three-tuple for each mercury and halogen reaction, representing the pre-exponential factor A, temperature exponent n and activation energy E_a of the modified Arrhenius equation. The solution vector omitted the parameters n or E_a for reactions where these values were equal to zero. Only the halogen and mercury reactions were allowed to change during the optimisation, as mercury oxidation is most likely to be sensitive to these sub-mechanisms, and these reactions are also associated with considerable uncertainty.

The cost function was based on the difference between measured and predicted results from the one-dimensional solver of the Cantera library [389]. Reducing the domain to a one-dimensional problem enforces assumptions that the flow has no velocity in the radial directions of the reactor and that all of the gaseous species are perfectly mixed. The C++ interface of Cantera was used to integrate the genetic algorithm implementation with the cost function evaluation. The temperature of the solution was fixed to the values presented in Figure 4.4, and the post-flame flue gas at the inlet of the domain was calculated based on an equilibrium calculation at the inlet temperature to achieve a representative radical pool, as was done in a previous study [198]. The concentration of NO was fixed after the equilibrium calculation so that the exit concentration was the same as was achieved in the experimental campaign, where the model predicted that less than 1% of the NO concentration was lost to reactions throughout the domain. The NO concentration for the oxyfuel cases was kept to the value calculated from equilibrium.

Values in the solution vectors were restricted to vary only within limits on the base mechanism. The pre-exponential factor was allowed to vary between 0.1-10, while the exponential terms, the activation energy and temperature exponent, were allowed to vary between a factor of ±0.25 from the base mechanism. The amount that the solution vector varied from the base mechanism was also included in the cost function, so that the algorithm selected solutions that are most representative of the mechanisms that were developed on alternative data sets.

The full cost function is given as

$$C(\hat{\mathbf{x}}) = \sum_{c}^{N_c} \frac{\left|M_c - P_{c\hat{\mathbf{x}}}\right|}{E_c} + \sum_{r}^{N_r} \left(\left|\log_{10} \frac{A_r}{A_{r\hat{\mathbf{x}}}}\right| + 4\left|1 - \frac{E_{ar}}{E_{ar\hat{\mathbf{x}}}}\right| + 4\left|1 - \frac{n_r}{n_{r\hat{\mathbf{x}}}}\right| \right) \tag{4.4}$$

where $C(\hat{\mathbf{x}})$ is the cost of solution vector $\hat{\mathbf{x}}$, N_c is the number of test cases, N_r is the number of variable reactions, M_c is the measured mercury oxidation ratio for case c, $P_{c\hat{\mathbf{x}}}$ is the predicted mercury oxidation ratio for case c using the mechanism described by vector $\hat{\mathbf{x}}$, E_c is the measured error bar for case c, and A_r, E_{ar} and n_r are the pre-exponential factor, activation energy and temperature exponent for reaction r, respectively, with $A_{r\hat{\mathbf{x}}}$, $E_{ar\hat{\mathbf{x}}}$ and $n_{r\hat{\mathbf{x}}}$ representing the pre-exponential factor, activation energy and temperature exponent for the mechanism described by $\hat{\mathbf{x}}$, respectively.

New generations of solution vectors were created through cross-over and mutation operations. The cross-over operation selected values between two parent solutions stochastically, providing a 50% chance of the child solution inheriting each set of rate parameters from either parent, thus avoiding any fixed relationship between the reactions. Reaction parameters were copied across as a full three-tuple, so parameters for a specific reaction were not mixed in the cross-over operation. Each generation contained a population of 128 solution vectors, where the six best performing solutions were combined through cross-over operations with the top eighteen solutions. The best performing solution was maintained across generations. Identical solutions were not combined, and any shortfall in the new generation over the last generation was regenerated with new stochastically determined solutions, as in the initiation step, to continue to promote variance in the population. Mutation operations occurred stochastically once every eighty cross-over operations.

Validation of the developed model was carried out by comparing the optimised mechanism against the measurements by van Otten et al. [97]. The validation case is very similar to the case measured by Preciado et al. [117], however the main focus on these cases was applied to different temperature profiles under air-fired conditions. The flow rates and halogen concentrations are the same between the training and validation cases, however the excess O_2 in the case by van Otten et al. [97] was kept at 0.96% dry by volume, as opposed to 2% in the case by Preciado et al. [117]. The temperature profiles used in the data by van Otten et al. [97] are shown in Figure 4.6, and represent a high quench rate of 440 K/s and a low quench rate of 210 K/s, where the temperature profile for the high quench rate is broadly similar to the temperature curves used by Preciado et al. [117]. Experimental measurements carried out after the results by van Otten et al. [97] demonstrated that the analysis of mercury oxidation by bromine species requires continual cleaning of the sampling system to provide reproducible results [435], and therefore the values for bromine oxidation efficiency presented by van Otten et al. [97] may not be reliable, and so comparisons to these data are done tentatively.

The resulting mechanisms from the genetic algorithm were analysed using a brute force sensitivity analysis. The model for the halogen run that was consistent with the measured values with pollutants, 200 ppm_v HCl or 30 ppm_v HBr, was executed separately for each of the reactions in the mechanism, with the kinetic rate scaled by 0.5

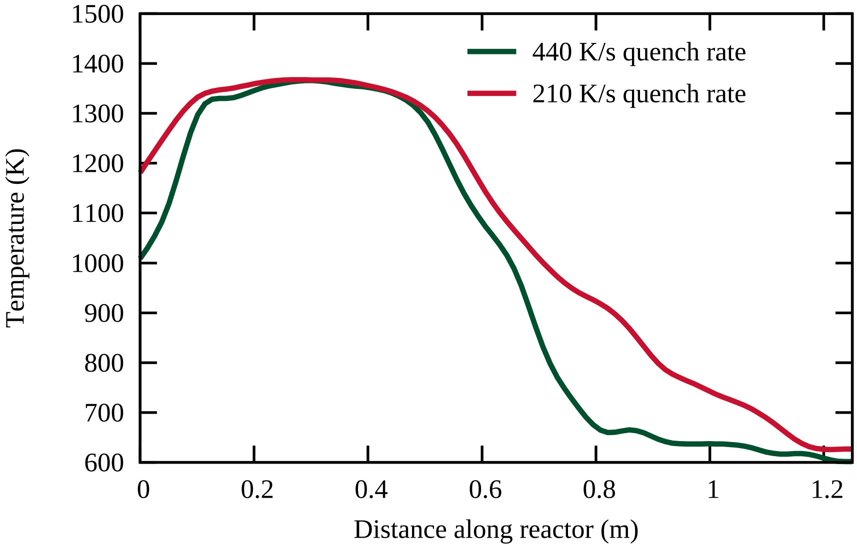

Figure 4.6: Temperature profiles for the validation data from the experiments by van Otten et al. [97].

and compared against the results without suppressing any reactions. The sensitivity of mercury oxidation towards each reaction was calculated as the logarithm of the ratio between the Hg^0 mole fraction at the outlet with the reaction suppressed and the baseline case,

$$S(r) = \log_2\left(\frac{X_{\mathrm{Hg}^0,r}}{X_{\mathrm{Hg}^0,0}}\right) \tag{4.5}$$

where $S(r)$ is the sensitivity value for reaction r, $X_{\mathrm{Hg}^0,0}$ is the baseline mole fraction for Hg^0 at the reactor outlet and $X_{\mathrm{Hg}^0,r}$ is the mole fraction for Hg^0 at the outlet when reaction r is suppressed. Intuitively a $S(r)$ value of -1 would represent twice the oxidation rate when reaction r is suppressed, thus implying that the reaction is detrimental to mercury oxidation, and a value of $+1$ would represent half of the mercury oxidation when the reaction is suppressed, implying that the reaction is a promoter of oxidation. This analysis method is simple and will allow for a quick determination of reactions that either enable or prevent mercury oxidation in isolation, however it will not highlight relationships between reactions.

This section will now continue to investigate the reaction schemes for mercury with chlorine and bromine species using the genetic algorithm. The algorithm is applied separately to the mercury-chlorine reaction scheme in Subsection 4.2.1, and the mercury-bromine scheme in Subsection 4.2.2. The conclusions to these investigations are discussed in Subsection 4.2.3.

4.2.1 Mercury chlorine reactions

The mechanism for mercury-chlorine oxidation was based on the GRI-3.0 mechanism for C/H/O/N chemistry [436]. The sub-mechanism from Pelucchi et al. [437] was used to describe the chlorine reactions, with the exception that the atomic chlorine recombination reaction was taken from the measured value by Donohoue [139]. A third body efficiency of 2.33 times that of N_2 for CO_2 was used for the recombination reaction of chlorine atoms as this has been reported previously [115]. The sub-mechanism provided by Roesler et al. [111] was used for the NO_x and Cl reactions, with the omission of the HONO reaction with atomic chlorine, as the formation of HONO is not included in the GRI-3.0 mechanism. The sulphur sub-mechanism from Giménez-López et al. [124], which has been validated for oxyfuel conditions, was used in this study for the SO_2-doped cases. Interactions between sulphur species and halogen species were neglected. The measured Arrhenius rate expression by Donohoue [139] was used for the recombination reaction of mercury and chlorine atoms, while the kinetic rates of the other reactions of the Widmer et al. [93] mechanism were taken from the theoretical study by Krishnakumar and Helble [192]. The resulting mechanism contained 86 species and 489 reactions, of which 75 reactions contained mercury or halogen species, and were allowed to change under the genetic algorithm optimisation process.

The best-performing solution was obtained by the genetic algorithm after twenty generations, and did not change after the twenty-fifth generation. The genetic algorithm took over one week to run on a 4-core 3.6 GHz CPU to optimise against the nineteen cases measured by Preciado et al. [117]. The results of the optimised mechanism against measured values of mercury oxidation are shown in Figures 4.7 to 4.10. The original mechanism was omitted from the results since less than 1% of the mercury was predicted to have been oxidised in all of the cases with the base mechanism.

The results for air and oxyfuel conditions across varying HCl concentrations without any additional pollutants is shown in Figure 4.7. The optimised mechanism demonstrates good agreement to the measured values for mercury oxidation under both firing regimes. The weakest agreement between the modelled oxidation rate and the measurements occurs at low HCl concentrations, where the oxidation efficiency under air-fired conditions is predicted to be higher than in oxyfuel, which is not the case for measured values at any HCl concentration.

The results for the mercury oxidation by chlorine under varying NO concentrations

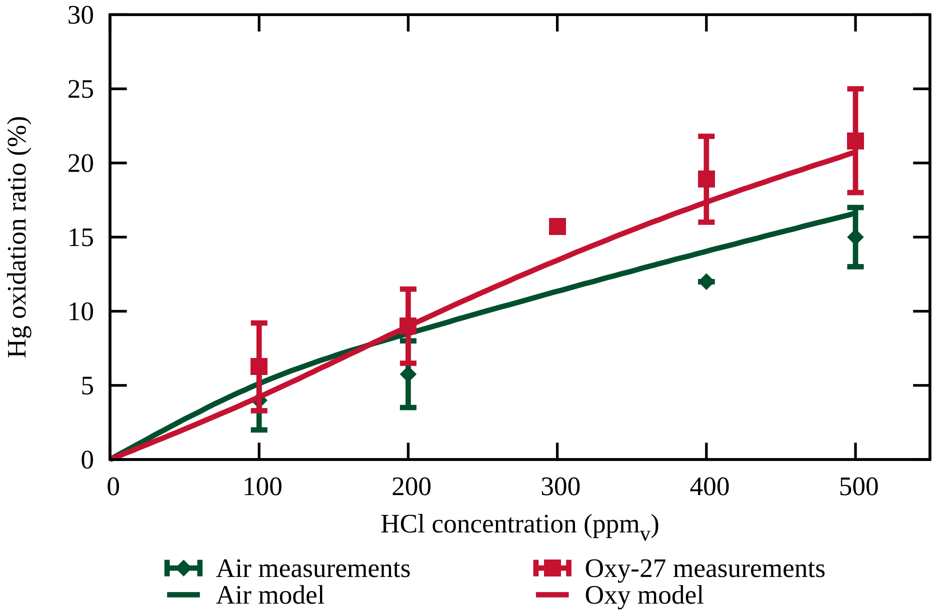

Figure 4.7: Comparison between modelled and experimental mercury chlorination across varying HCl concentrations for air-fired and oxy-fired conditions. Experimental data from Preciado et al. [116].

is shown in Figure 4.8. While there is some demonstration that increasing NO in the measurements reduces the mercury oxidation rate, although this effect can be easily masked within the error bars of the data, the model significantly over-predicts this influence. The model predicts that almost all of the mercury is present in an unoxidised state at the highest concentrations of NO, while measurements indicate less than a 50% drop in the oxidation efficiency.

The results for mercury oxidation by chlorine under conditions with SO_2 pollutants is shown in Figure 4.9. The model predicts a greater sensitivity to SO_2 concentrations under oxyfuel conditions than under air-fired conditions, however this is not reproduced in the measured data. Under both firing conditions, the mercury oxidation ratio is predicted to decrease under increasing SO_2 concentrations, although this is not demonstrated significantly in the measured data that the model was trained to.

Finally, the results for the mechanism against the validation data is shown in Figure 4.10. The mechanism shows reasonable agreement with the validation data, predicting the right relative trend between the high and low quench cases. Despite the good agreement with the low quench case, the high quench case is significantly over-predicted, however the predicted oxidation efficiencies are very similar to the air-fired

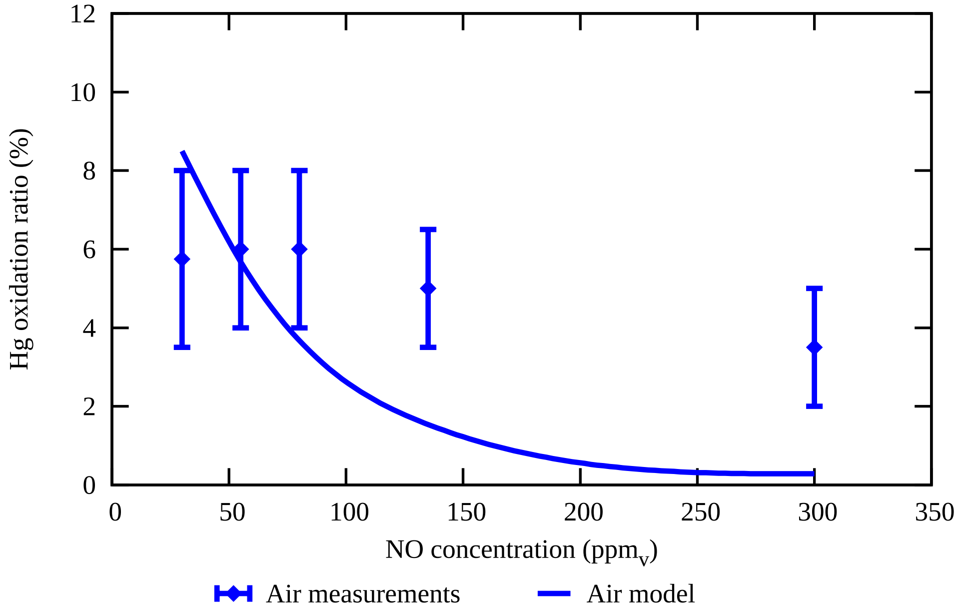

Figure 4.8: Modelled mercury chlorination with varying NO concentrations and a constant HCl concentration of 200 ppm$_v$. Experimental data from Preciado et al. [116].

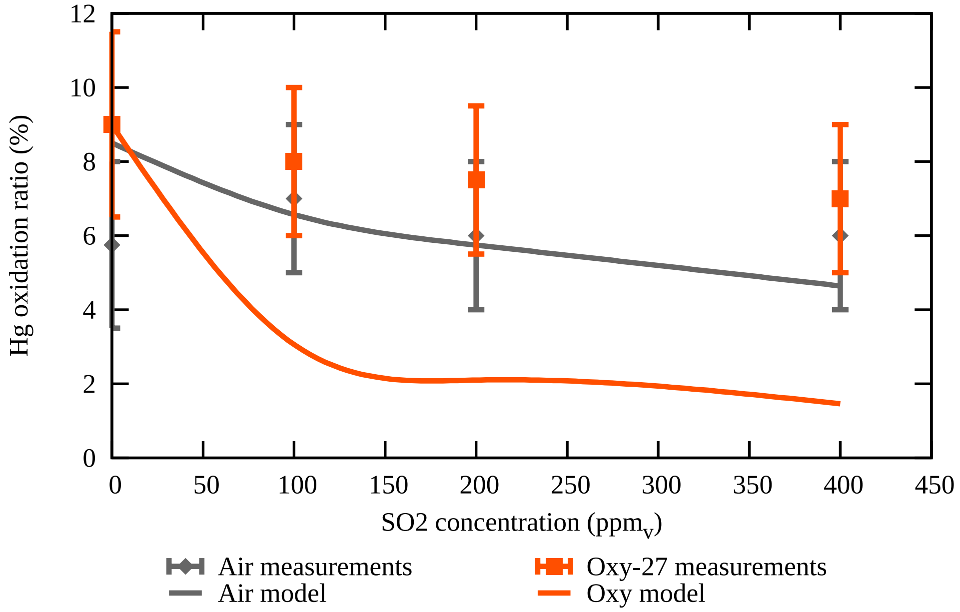

Figure 4.9: Modelled mercury chlorination with varying SO_2 concentrations and a constant HCl concentration of 200 ppm$_v$. Experimental data from Preciado et al. [116].

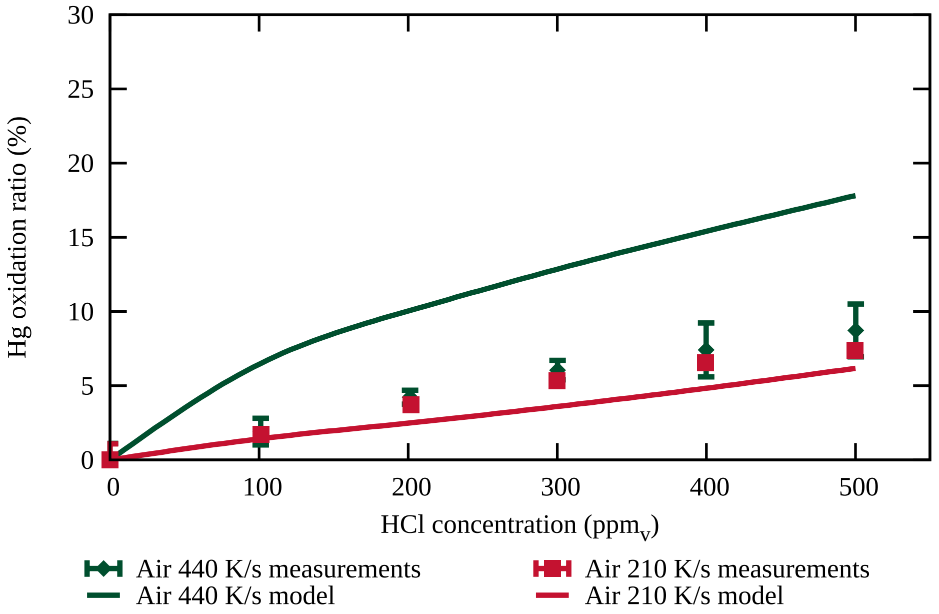

Figure 4.10: Validation of mercury chlorination model using the measurements by van Otten et al. [97].

case by Preciado et al. [117]. This similarity is unsurprising, as the high quench validation case and the air-fired case are very similar, and it is perhaps more indicative of the reproducibility of the results and the changes in the conditioning system that were developed between when the results by van Otten et al. [97] and Preciado et al. [117] were published.

A sensitivity study was carried out to analyse the trends produced by the optimised model. The sensitivity analysis was carried out on the 200 ppm$_v$ HCl air-fired and oxyfuel cases, as well as the air-fired cases with 300 ppm$_v$ NO and 400 ppm$_v$ SO_2, and the oxyfuel case with 300 ppm$_v$ NO. The results of the sensitivity analysis is presented in Figures 4.11 to 4.15, showing the ten reactions that mercury oxidation is most sensitive to. The profiles along the length of the reactor for the atomic Hg and Cl species for these cases is shown in Figure 4.16.

The results of the sensitivity study for the air-fired condition in the absence of additional pollutants is shown in Figure 4.11. The results demonstrate the main promoters of mercury oxidation in these conditions involves the atomic recombination of mercury and chlorine atoms and the further reaction of HgCl with Cl_2. The reaction between HgCl and atomic Cl is shown to be detrimental to mercury oxidation in this case, however this sensitivity is due to the reverse reaction, where atomic Cl and

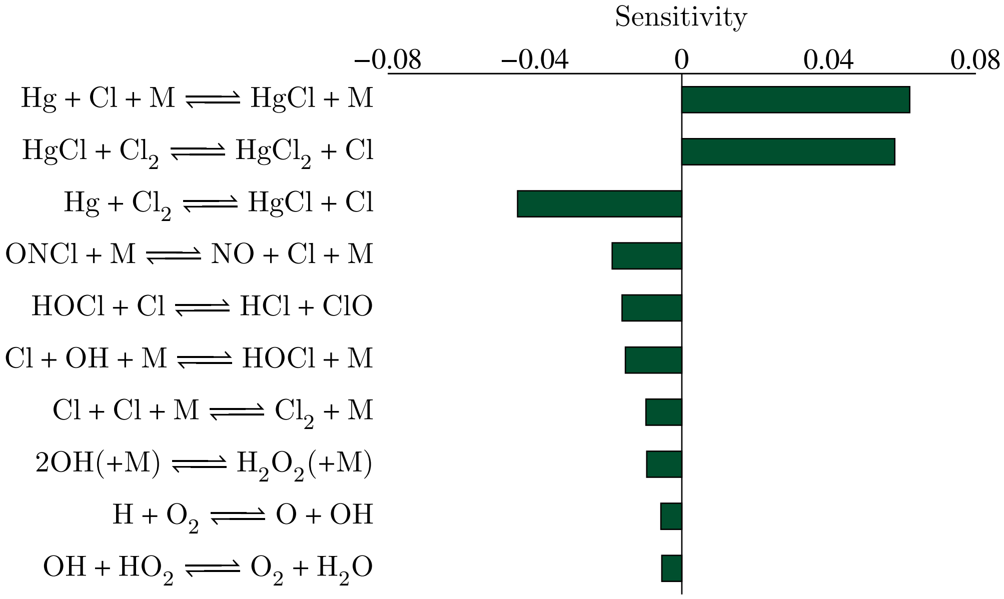

Figure 4.11: Sensitivity of mercury oxidation to mercury-chlorine reactions under the air-fired environment in the model derived from the genetic algorithm.

the monohalide species are consumed. The results also show that the formation of nitrosyl chloride, ONCl, can significantly reduce the formation of oxidised mercury species, which is due to the pathway reducing the availability of the reactive Cl species. The other reactions that control the rate of mercury oxidation are concerned with consuming atomic Cl species. The atomic Cl recombination reaction shows relatively low sensitivity, however this is likely to be due to the presence of other routes of Cl_2 production, such as using ONCl as an intermediate.

Under increased NO concentration, the sensitivity of the results to the kinetic rates of the reactions is far lower, which is shown in Figure 4.12. These low sensitivity values are due to the very low oxidation rate, something that the optimisation process was unable to rectify. The only reaction that the oxidation process shows any appreciable sensitivity to is the formation of ONCl. This process is responsible for the low oxidation rate in the cases with elevated NO concentrations. The relatively high concentration of NO compared to Hg, and the increased stability of ONCl over HgCl, are the reason why the model is incapable of predicting appreciable oxidation at higher NO concentrations, despite the reasonably liberal changes permitted under the optimisation process.

When SO_2 is present, the model shows increased sensitivity to reactions including

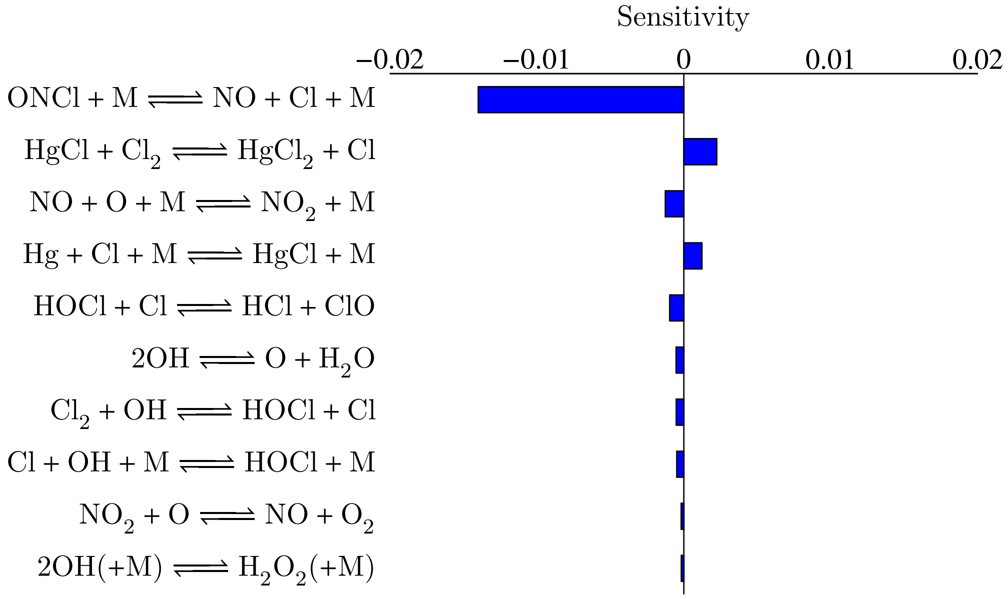

Figure 4.12: Sensitivity of mercury oxidation to mercury-chlorine reactions under the air-fired environment with 300 ppm$_v$ NO in the model derived from the genetic algorithm.

OH and HO_2. Mercury oxidation in the presence of SO_2 shows additional sensitivity to the reactions

$$SO_2 + OH(+M) \rightleftharpoons HOSO_2(+M) \tag{R 4.1}$$

$$Cl_2 + OH \rightleftharpoons HOCl + Cl \tag{R 4.2}$$

where Reaction (R 4.1) serves to mitigate mercury oxidation, and Reaction (R 4.2) promotes oxidation, but only in cases with SO_2. The presence of SO_2 serves to restrict the availability of Cl by reacting with OH species that would otherwise liberate the atomic halogen species.

The results of the sensitivity analysis for the oxyfuel combustion case is shown in Figure 4.14, with the case containing SO_2 shown in Figure 4.15. The results under oxyfuel show a similar trend as with the air-fired cases, except there is an increased sensitivity to reactions involving OH species, due to the increase in the concentration of these species under oxyfuel combustion conditions. Due to the lower concentration of NO in the oxyfuel case, there is very little sensitivity to the formation of ONCl. It is this variation in the NO levels that is responsible for the different oxidation rates

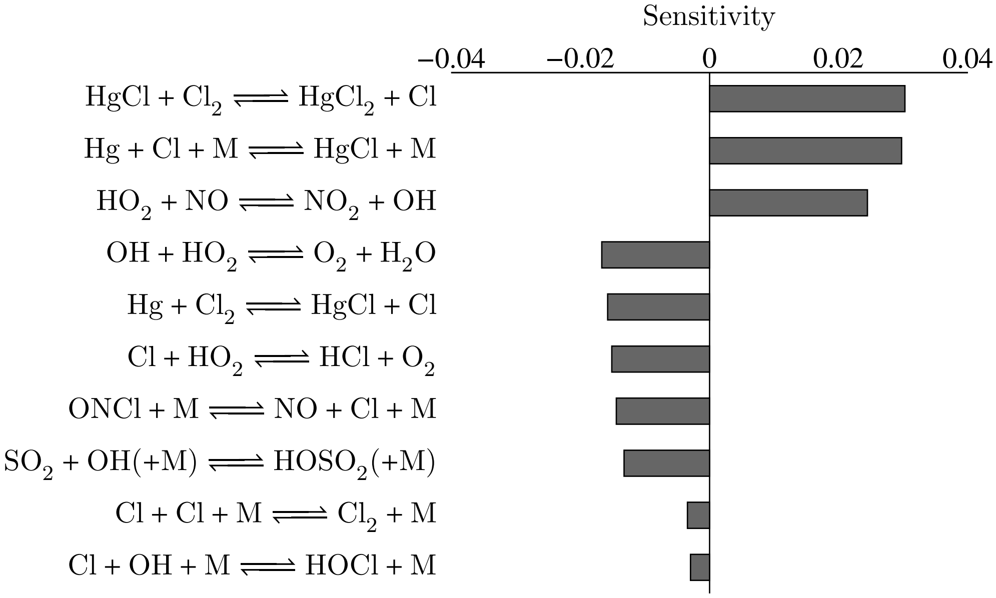

Figure 4.13: Sensitivity of mercury oxidation to mercury-chlorine reactions under the air-fired environment with 400 ppm_v SO_2 in the model derived from the genetic algorithm.

between the two firing conditions. However, as the sensitivity to the NO concentration is not adequately modelled across the air-fired conditions in Figure 4.8, it is uncertain whether this feature of the developed model is valid of real combustion systems.

The concentration profiles for the cases analysed above, shown in Figure 4.16, illustrate the dependence of mercury oxidation to the availability of atomic Cl radicals in the model. Mercury oxidation only occurs after 0.8 m from the exit of the burner, when the temperature in the domain drops below 750 K, however in the cases with NO or SO_2 added, the atomic Cl concentration has been largely consumed by this point. In both the air-fired and oxyfuel cases without added pollutants, a low but noticeable level of atomic Cl concentration persists until the exit of the domain, which causes the mercury to oxidise. In the current mechanism, the level of mercury oxidation is directly related to the availability of Cl radicals, which are sensitive to secondary chemistry with NO and SO_2.

The optimised kinetic rates for the reactions that mercury oxidation demonstrated the most sensitivity to are shown in Table 4.3. The results shown in Figures 4.7 to 4.10 can be reproduced by applying only the modifications listed in Table 4.3 to the base mechanism. The most significantly modified reaction is the formation of ONCl,

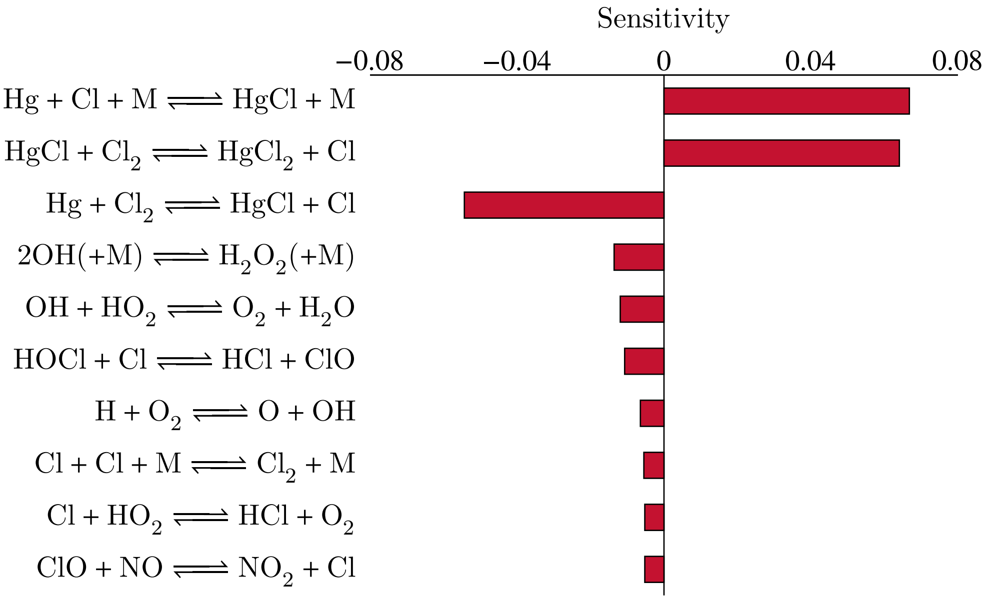

Figure 4.14: Sensitivity of mercury oxidation to mercury-chlorine reactions under the oxyfuel combustion environment in the model derived from the genetic algorithm.

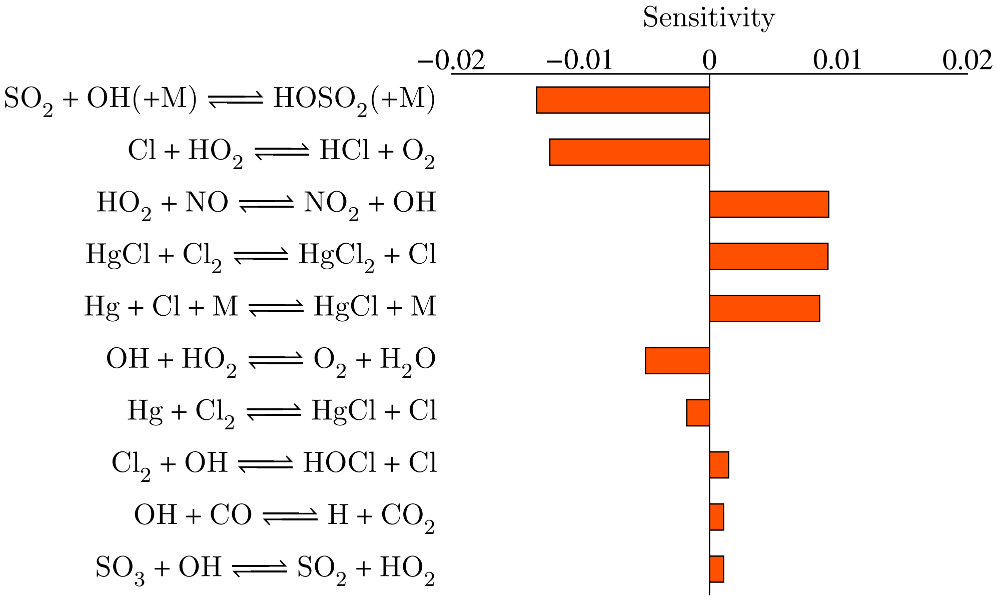

Figure 4.15: Sensitivity of mercury oxidation to mercury-chlorine reactions under the oxyfuel combustion environment with 400 ppm$_v$ SO_2 addition in the model derived from the genetic algorithm.

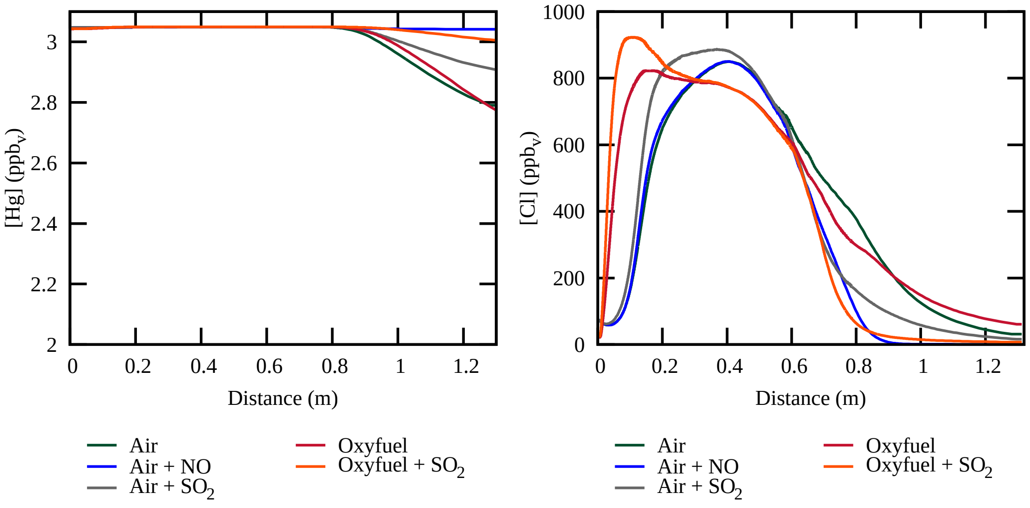

(a) Atomic mercury concentration (b) Atomic chlorine concentration

Figure 4.16: Species concentration profiles along the distance of the reactor for atomic Hg and Cl species in parts per billion by volume (ppb$_v$).

in which the pre-exponential factor is reduced by close to the limit allowed by the restrictions on the genetic algorithm, with the activation energy similarly increased by close to the maximum allowable limit. It is highly unlikely that the original kinetic rate is so significantly out of line with reality, however without these modifications to the mechanism, the predicted concentration of reactive Cl species is far too low to influence mercury oxidation. This result suggests that mercury may oxidise under alternative routes, as the currently proposed mechanisms cannot account for an adequate supply of Cl radicals without greatly reducing the formation of ONCl.

4.2.2 Mercury bromine reactions

As with the mercury-chlorine mechanism, the mechanism for mercury-bromine oxidation was based on the GRI-3.0 mechanism for C/H/O/N chemistry [436]. The mechanism from Dixon-Lewis et al. [438] was used to describe the bromine chemistry, with the rates suggested by Molina et al. [439] for the reactions between NO and bromine species. The measured rate for the atomic recombination of Hg and Br by Donohoue [139] was used in this study. The kinetic rates of mercury species with BrOH were taken from the study by Niksa et al. [197], and kinetic rates from Wilcox and Okano [191] were used for the remainder of the bromine-equivalent Widmer et al. [93] mech-

	Optimised kinetic rate			Ratio to original rate		
Reaction	A	n	E_a	A	n	E_a
$\mathrm{Hg + Cl + M \rightleftharpoons HgCl + M}$	1.74E+09	0	-5681	2.136	-	1.0
$\mathrm{Hg + Cl_2 \rightleftharpoons HgCl + Cl}$	4.90E+10	0	144755	1.085	-	0.96
$\mathrm{HgCl + Cl_2 \rightleftharpoons HgCl_2 + Cl}$	1.58E+2	2.34	-16765	2.724	0.975	1.176
$\mathrm{Cl + Cl + M \rightleftharpoons Cl_2 + M}$	4.79E+08	0	-7853	2.724	-	1.111
$\mathrm{Cl + HO_2 \rightleftharpoons HCl + O_2}$	7.18E+11	-0.676	0	0.958	1.073	-
$\mathrm{Cl + OH + M \rightleftharpoons HOCl + M}$	1.04E+14	-1.377	0	**8.647**	0.963	-
$\mathrm{HOCl + Cl \rightleftharpoons HCl + ClO}$	7.54E-4	4.54	-1207	2.093	1.115	0.856
$\mathrm{ClO + O(+M) \rightleftharpoons OClO(+M)}$	1.25E+09	0	-4784	1.535	-	0.847
$\mathrm{OClO(+M) \rightleftharpoons Cl + O_2(+M)}$	2.05E+11	0	128065	**4.540**	-	0.850
$\mathrm{ONCl + M \rightleftharpoons NO + Cl + M}$	4.55E+11	0	161128	**0.182**	-	**1.207**

Table 4.3: Optimised reaction rate parameters of the most sensitive reactions involving Hg or Cl species. The most significant deviations from the base mechanism are highlighted in bold face.

anism. The resulting mechanism contained 63 species and 369 reactions, which is far fewer than for the chlorine mechanism due to the absence of sulphur species and a less detailed mechanism for the bromine chemistry. The mechanism contained 43 reactions that involved mercury or bromine species, which were allowed to change under the genetic algorithm optimisation process.

The results of the optimised mechanism against the training data is shown in Figures 4.17 and 4.18 for the cases without added NO and with additional NO, respectively. The results for the mechanism without optimisation have been included for comparison. The genetic algorithm optimisation process was able to achieve excellent agreement with the measured values of mercury oxidation by bromine species, with all of the modelled predictions in Figure 4.17 lying between the error bars of the measurements. This agreement is likely to be due to the higher concentration of atomic Br species at equilibrium, resulting in the mercury oxidation rate being more sensitive to the kinetically limited rates involving the reactive halogen species, and less dependent on secondary chemistry that was not being modified in the optimisation.

The least agreement with the training data was found with the cases that had a higher concentration of NO, which is similar to the cases containing chlorine species. Unlike the chlorine cases, mercury oxidation by bromine is not completely suppressed at higher concentrations of NO, but a significant sensitivity is demonstrated by the model that is not present in the measurements, despite the model being optimised to these cases. Again, this suggests that there may be further routes to the mercury oxidation process that are not being considered in the current model.

Despite the shortcomings associated with the bromine cases measured by van Ot-

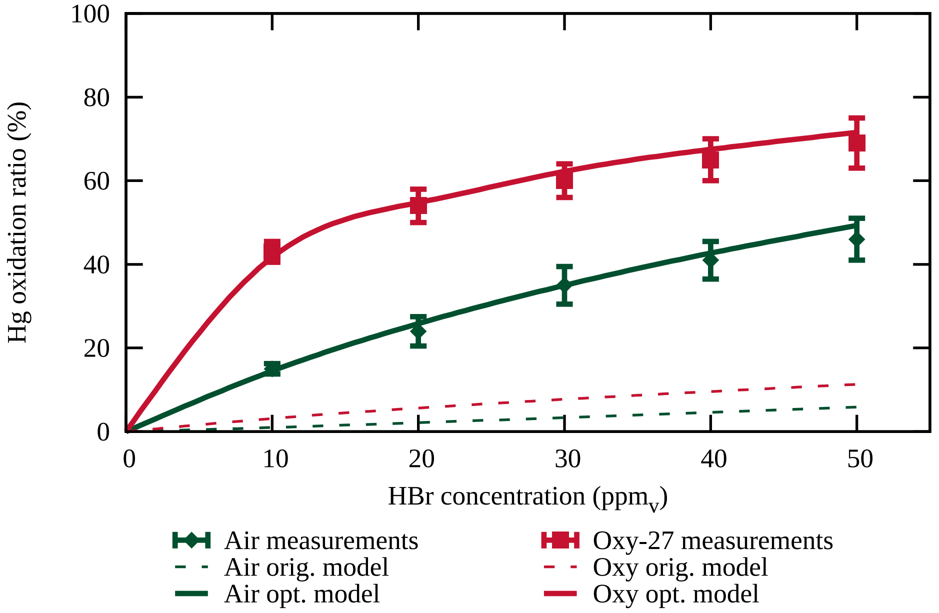

Figure 4.17: Comparison between modelled and experimental mercury bromination across varying HBr concentrations for air-fired and oxy-fired conditions. Experimental data from Preciado et al. [116].

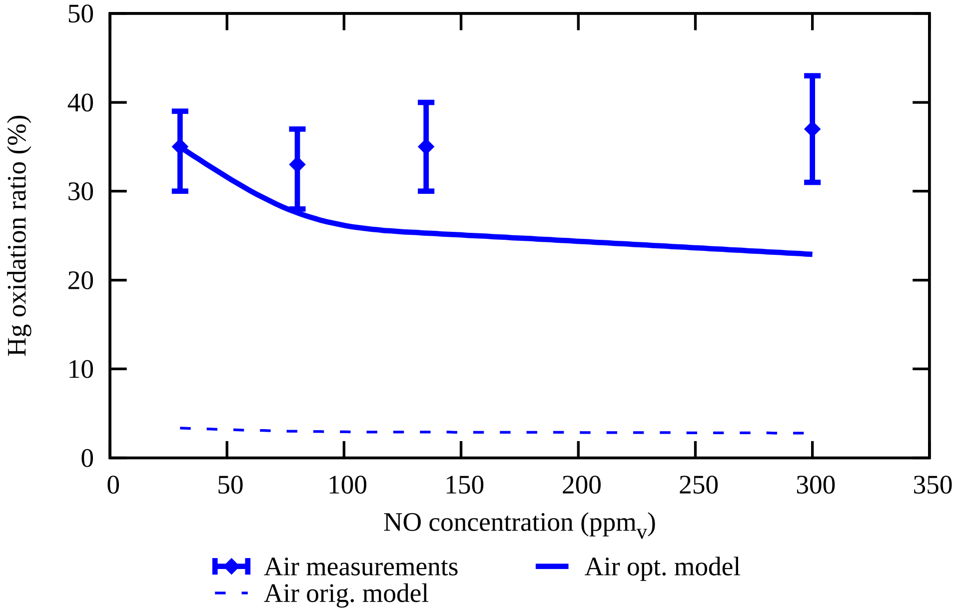

Figure 4.18: Comparison between modelled and experimental mercury bromination across varying NO concentrations with 30 ppm$_v$ HBr for air-fired and oxy-fired conditions. Experimental data from Preciado et al. [116].

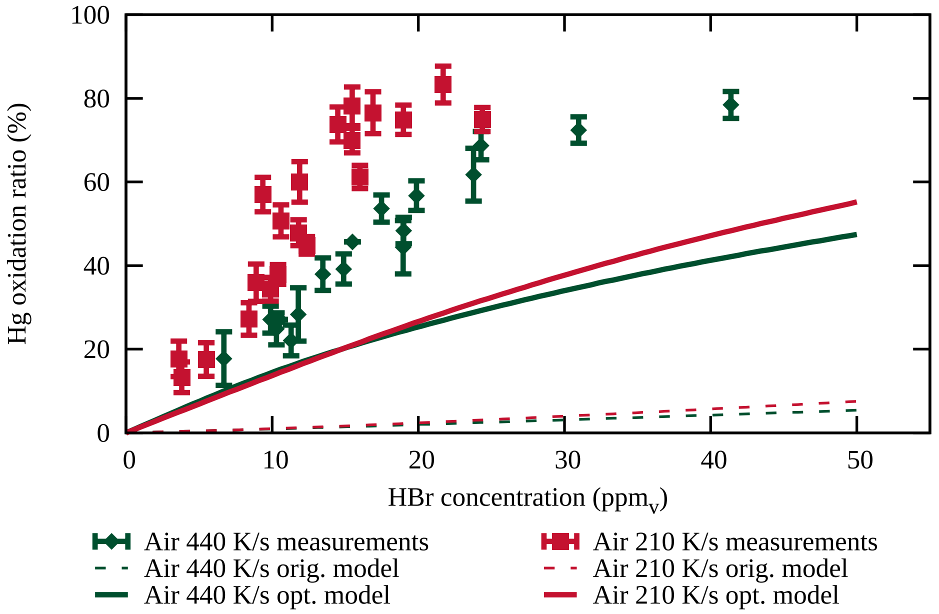

Figure 4.19: Comparison between modelled and experimental mercury bromination across varying HBr concentrations for the validation case. Experimental data from van Otten et al. [97].

ten et al. [97], the model was applied to this case for illustrative purposes, shown in Figure 4.19. While quantitatively these results show that the model fails to capture the measured mercury oxidation profile, the trend shows that the lower quench rate achieves the higher oxidation efficiency, the opposite to the results obtained for chlorine, is captured by the model.

The results for the sensitivity analysis carried out for the three experimental conditions measured by Preciado et al. [117] are shown in Figures 4.20, 4.21 and 4.22 for the air-fired, air-fired with 300 ppm$_v$ NO at the outlet and oxyfuel cases, respectively. Mercury oxidation by bromine broadly shows the same sensitivity to the analogous reactions with the chlorine mechanism. Mercury oxidation is promoted by the recombination reaction between Hg and Br, as well as the reaction between the monohalide HgBr and Br_2 species. The main inhibitory reactions involve the ONBr species, which catalyses the formation of Br_2.

At elevated NO concentrations, the oxidation of mercury by bromine species shows less sensitivity to the kinetic rates, as was also the case for mercury oxidation by chlorine species. This trend further suggests that the current mechanism is incomplete in its description of mercury and halogen chemistry, as modifying just the kinetic

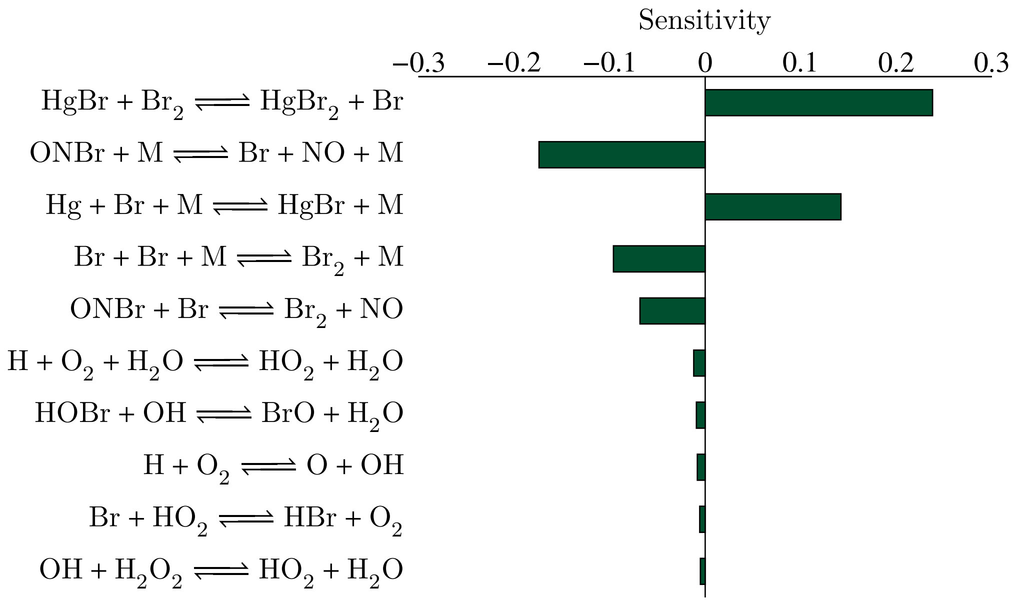

Figure 4.20: Sensitivity of mercury oxidation to mercury-bromine reactions under the air-fired environment in the model derived from the genetic algorithm.

rates will only have a small impact on the model predictions. Additional studies into further potential pathways that include reactive species that are less sensitive to NO concentrations are required to match modelling work to experimental measurements.

Under oxyfuel conditions, the reduced concentration of NO increases the importance of the direct recombination reaction of Br atoms to form Br_2 in governing the modelled rate of mercury oxidation. There is a less significant sensitivity on the OH chemistry than what was present for oxidation by chlorine species, principally due to the relative abundance of atomic Br. The differences between the mercury oxidation rates in the air-fired and oxyfuel conditions are explained by the different concentrations of NO in the model, however as the sensitivity to the NO concentration is not well predicted in air-fired environments, this may not be true in reality.

The concentration profiles for the cases analysed above, shown in Figure 4.23, again illustrate the dependence of mercury oxidation to the availability of atomic halogen radicals in the model. The concentration of Br atomic radicals is over two orders of magnitude higher than the equivalent chlorine species, however the Br species is readily consumed during the section of the reactor where mercury will oxidise, and so the model is still somewhat sensitive to the prediction of other flue gas species, most notably NO.

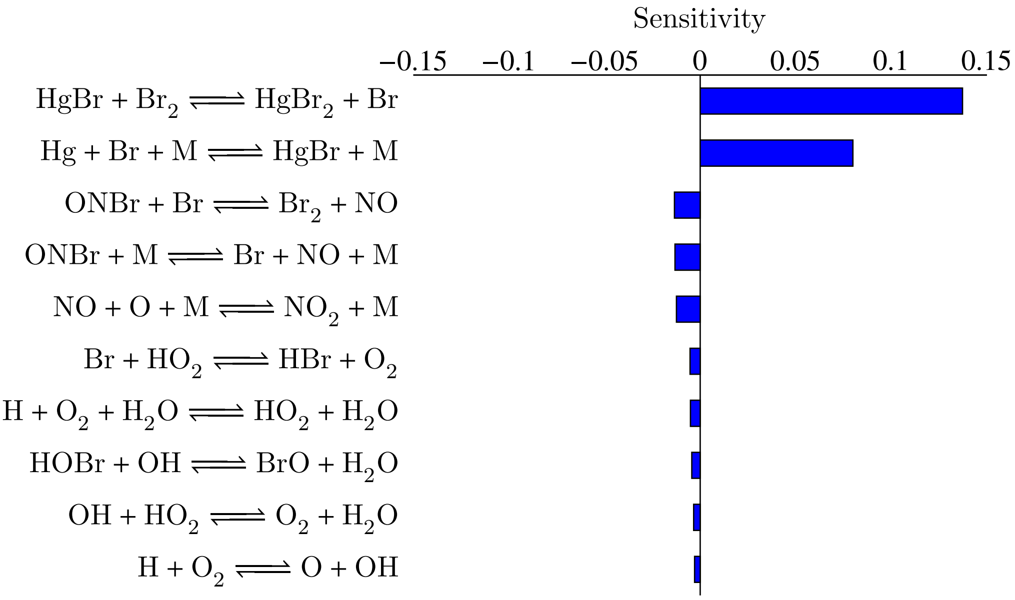

Figure 4.21: Sensitivity of mercury oxidation to mercury-bromine reactions under the air-fired environment with 300 ppm_v NO in the model derived from the genetic algorithm.

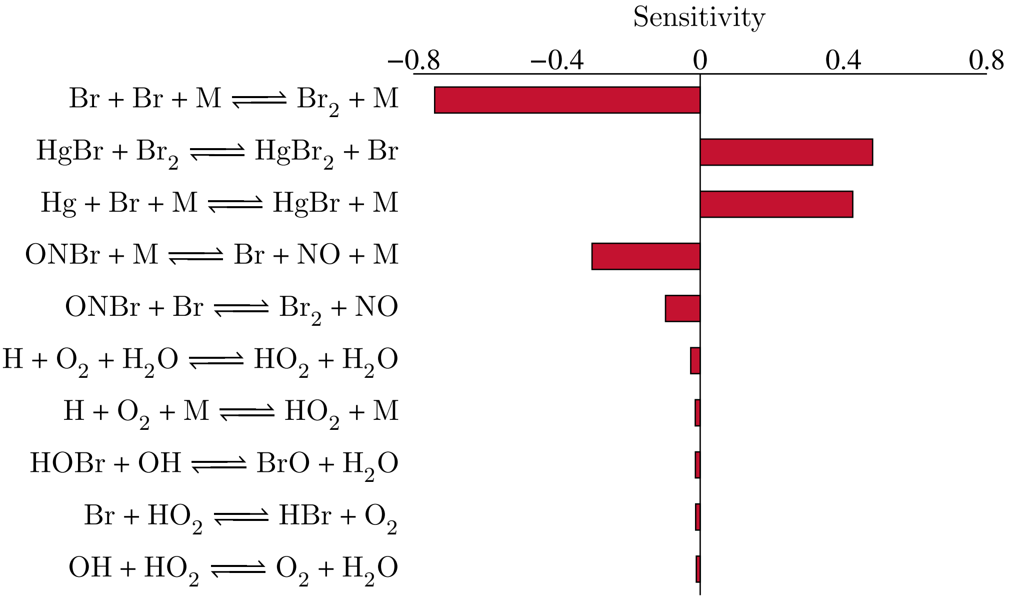

Figure 4.22: Sensitivity of mercury oxidation to mercury-bromine reactions under the oxyfuel combustion environment in the model derived from the genetic algorithm.

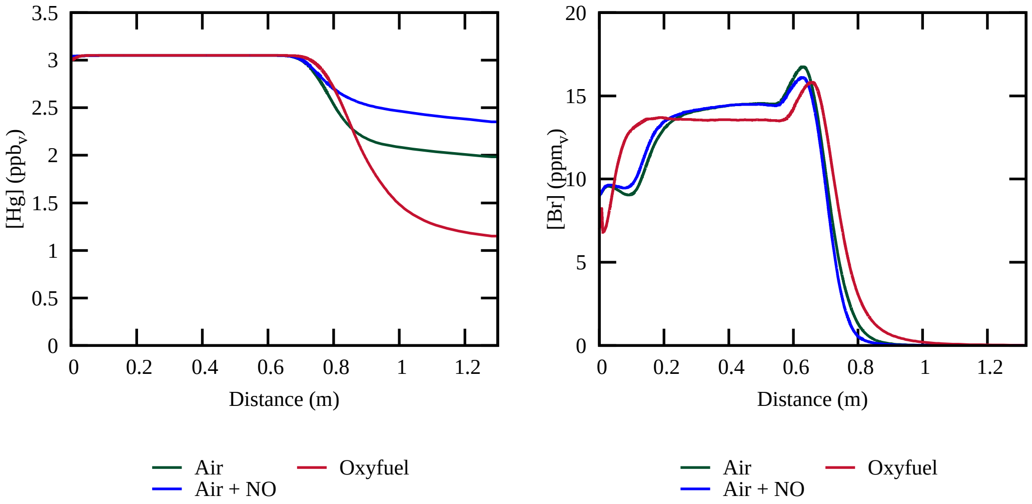

(a) Atomic mercury concentration

(b) Atomic bromine concentration

Figure 4.23: Species concentration profiles along the distance of the reactor for atomic Hg in parts per billion by volume (ppb$_v$) and Br species in parts per million by volume (ppm$_v$).

A selection of the modifications that were made in the optimisation process are shown in Table 4.4. The results shown in Figures 4.17 to 4.19 can be reproduced by only applying these modifications to the base mechanism. The three most significant modifications made by the optimisation process correspond to some of the most sensitive reactions across the studied cases. Firstly, the reaction between HgBr and Br_2 has been accelerated by close to the maximum permissible by the optimisation process. Furthermore the recombination reaction of Br atoms has been kinetically increased with a rise in the pre-exponential factor as well as very significant increase in the magnitude of the negative activation energy. The combined effect of these modifications is to push the bromine distribution close to the equilibrium values.

In the optimisied mechanism, the modification of the ONBr formation reaction is modified less significantly than what is necessary for the mercury-chlorine mechanism, however the reaction of ONBr with atomic Br has been greatly reduced by the optimisation process. This reaction is associated with considerable uncertainty, having only been represented without any temperature-dependent kinetic parameters having only been measured at 298 K [440], and must be investigated further to determine the true influence of this process. The modifications in the bromine mechanism may be feasible in reality, and therefore the current mechanism may be sufficient, however

	Optimised kinetic rate			Ratio to original rate		
Reaction	A	n	E_a	A	n	E_a
$Hg + Br + M \rightleftharpoons HgBr + M$	4.82E+14	-2.072	0	2.274	1.11	-
$HgBr + Br_2 \rightleftharpoons HgBr_2 + Br$	1.10E+12	0	517	**9.932**	-	1.035
$Br + Br + M \rightleftharpoons Br_2 + M$	6.66E+08	0	-2066	3.506	-	**1.215**
$Br + HO_2 \rightleftharpoons HBr + O_2$	7.59E+06	0.970	477	0.883	0.970	1.019
$HOBr(+M) \rightleftharpoons Br + OH(+M)$	1.73E+14	-1.581	0	0.816	0.850	-
$HOBr + OH \rightleftharpoons BrO + H_2O$	0.06213	3.036	-1345	0.327	0.973	1.076
$ONBr + M \rightleftharpoons Br + NO + M$	1.14E+12	0	27250	0.949	-	1.088
$ONBr + Br \rightleftharpoons Br_2 + NO$	3.87E+10	0	0	**0.176**	-	-

Table 4.4: Optimised Hg and Br reaction rate parameters of the most sensitive reactions. The most significant deviations from the base mechanism are highlighted in bold face.

further work is still required to identify the measured insensitivity to the NO concentration.

4.2.3 Conclusions

This study used a series of published kinetic rates to construct a model for mercury oxidation by chlorine and bromine species under the influence of NO and SO_2 pollutants. A genetic algorithm was used to optimise the model to the experimental results of Preciado et al. [117] in order to analyse the important mechanisms in the chemical process. Without optimisation, the presence of NO significantly mitigated mercury oxidation by consuming most of the reactive halogen species, and the model was incapable of predicting any of the experimentally measured oxidation rates.

While the optimised model demonstrated reasonable agreement for the baseline air and oxyfuel cases, as well as promising agreement to an alternative validation data set, the models predicted considerable sensitivity to the presence of pollutant species that was not present in the measured data. This sensitivity in the model is in spite of the optimisation process that included these cases. In particular, it was not possible for the optimisation process to mitigate the detrimental effects of NO on the consumption of reactive halogen species. Therefore, it must be concluded that there are mechanisms that are not present in the current model that need to be accounted for. This may include surface-catalysed reactions, or reactions between mercury species and nitrogen species, such as ONCl or ONBr.

4.3 Summary

This chapter presented a thermodynamic and chemical kinetic study on mercury oxidation in both air-fired and oxy-fired combustion environments. While the thermodynamic study yielded no significance in speciation between air-fired and oxy-fired conditions, the chemical kinetic study was able to capture the differences between the combustion environments, although with a heightened sensitivity to the NO concentration.

The thermodynamic study in Section 4.1 illustrates that for both air-fired and oxy-fired cases, Hg^0 is the dominant gas-phase species of mercury at higher temperatures. The equilibrium distributions also show that there is a tipping point, determined by the total halogen concentrations, at which Hg^{2+} becomes dominant. Both mercury and halogen species' equilibrium distributions are unaffected by changing the combustion environment.

The chemical kinetic investigation in Section 4.2 highlights the importance of modelling several aspects of the combustion chemistry. A genetic algorithm was employed to optimise a chemical kinetic model based on published mechanisms and kinetic rates for mercury and halogen species. The optimisation process was successful in achieving agreement across several measured values for mercury oxidation rates, however the model failed to capture some of the measured chemical behaviour.

The chemical kinetic study has demonstrated that the observed variations in mercury oxidation rates under air-fired and oxy-fired combustion can be somewhat explained by variations in NO concentrations. However, the study has also demonstrated that the currently published mechanisms for mercury oxidation are incapable of replicating the insensitivity to the NO concentration in air-fired combustion, even with a fairly liberal optimisation process. Further work should investigate the importance of additional routes to mercury oxidation, which may include surface catalysed reactions or interactions with other halogen species, such as the nitrosyl halides.

5 Radiation model validation for oxyfuel conditions

This chapter presents calculations of idealised environments that represent potential oxyfuel conditions to provide validation of modelling approaches for the spectral absorption coefficient. Firstly, in Section 5.1, the LBL and narrow band models are validated against the high resolution measurements of gas transmissivity by Alberti et al. [256] for $CO_2/H_2O/N_2$ mixtures. In Section 5.2, the LBL and narrow band models are used to calculate radiative transfer through a one-dimensional inhomogeneous medium to test the inherent approximations introduced by the narrow band models against LBL calculations. In Section 5.3, the global models that were introduced in Subsection 3.1.2 are compared against narrow band calculations of radiative transfer within a three-dimensional enclosure, which represents conditions that are relevant to CFD calculations of oxy-coal combustion environments. Conclusions from these studies are presented in Section 5.4.

The methods that are considered in this chapter are the LBL method using the HITEMP-2010 [224] and CDSD-4000 [253] spectral databases, the SNB and CK narrow band models with the parameters provided by Rivière and Soufiani [263], the SLW model using the ALBDF provided by Pearson et al. [309], the WSGG model with the coefficients suggested by Smith et al. [220], Yin et al. [286], Johansson et al. [291], Krishnamoorthy [293] and Kangwanpongpan et al. [292], and the FSK models using the narrow band k-g distributions from Cai and Modest [441]. The SLW method uses the multiplicative approach to generate the ALBDF from the single-specie lookup tables, and the CK and FSK models both employ the mixing scheme of Modest and Riazzi [282] to calculate the mixture k-g distributions. This study aims to validate these various approaches and suggest a method for modelling the spectral component of radiation that is suitable for CFD calculations of oxyfuel combustion.

5.1 Validation of spectral models

Measurements by Alberti et al. [256] provide high resolution transmissivity values for mixtures of CO_2, H_2O and N_2 at elevated temperatures, and at concentrations that are relevant for oxyfuel conditions. These fundamental measurements of homogeneous paths allow for the validation of the computationally expensive LBL and narrow band models, which are used as benchmark solutions to validate more expensive methods in complex cases, such as the studies in Sections 5.2 and 5.3.

5.1.1 Case definitions

The LBL and narrow band models are validated against the measurements by Alberti et al. [256] through the comparison of total emissivity. The measurements were conducted using a high temperature ceramic flow gas cell, which has been used in other previous measurements of gas spectra [259, 442]. Gas transmissivity was measured using a blackbody power source at one end of the gas cell and an FTIR spectrometer at the other end, separated by a column of radiatively participating gas species. It is expected that uncertainties in the measurements using this technique are below 0.5% for the majority of spectral lines [256].

The calculations in this study compare model results against the experimental measurements of all 22 cases from Alberti et al. [256], which are outlined in Table 5.1. These cases are grouped into cases that contain only CO_2 and N_2, labelled as the C# cases, containing only H_2O and N_2, labelled as the W# cases, and containing mixtures of the two participating species in N_2, labelled as M# cases. The LBL calculations in this study were evaluated using the HITEMP-2010 [224] spectral database for CO_2 and H_2O, which is also compared against the CDSD-4000 [253] database for the cases that contain CO_2. All of the LBL calculations assume a Voigt line profile, which is calculated using the algorithm by Humlíček [255]. The modelled spectrum in the LBL method was divided into uniform discrete intervals that were 0.001 cm^{-1} wide, and was bound between 450 cm^{-1} and 7600 cm^{-1}, representing the measured portion of the spectrum and resulting in 7.15×10^6 spectral intervals for the absorption coefficient. The contribution of each spectral line was truncated when the line strength fell below a cutoff of 10^{-9} cm^{-1}. The HITEMP-2010 database was used with the omission of the spectral lines that were identified by Rivière and Soufiani [263] as being anomalous, which have been similarly noted by other studies [256, 259].

Case	Length (m)	Temp. (K)	X_{CO_2}	X_{H_2O}	X_{N_2}
C1	0.5339	500.15	1.0	0.0	0.0
C2	0.5371	1202.75	0.4314	0.0	0.5686
C3	0.54	1770.75	0.1726	0.0	0.8274
C4	0.54	1770.75	0.4314	0.0	0.5686
C5	0.54	1770.75	0.6903	0.0	0.3097
C6	0.54	1770.75	1.0	0.0	0.0
W1	0.5339	500.15	0.0	0.9811	0.0189
W2	0.5371	1202.75	0.0	0.1726	0.8274
W3	0.5371	1202.75	0.0	0.4314	0.5686
W4	0.5376	1302.15	0.0	0.9811	0.0189
W5	0.5389	1552.15	0.0	0.9811	0.0189
W6	0.54	1770.15	0.0	0.4314	0.5686
W7	0.54	1770.15	0.0	0.9811	0.0189
M1	0.5352	801.95	0.4314	0.4314	0.1372
M2	0.5352	801.95	0.6903	0.1726	0.1371
M3	0.5352	801.95	0.1726	0.6903	0.1371
M4	0.5371	1202.75	0.4314	0.4314	0.1372
M5	0.5371	1202.75	0.6903	0.1726	0.1371
M6	0.5371	1202.75	0.1726	0.6903	0.1371
M7	0.54	1770.75	0.4314	0.4314	0.1372
M8	0.54	1770.75	0.6903	0.1726	0.1371
M9	0.54	1770.75	0.1726	0.6903	0.1371

Table 5.1: Cases for the calculations of spectral transmissivity, taken from the experimental cases defined by Alberti et al. [256]. Cases are defined by path length, temperature and mole fractions of CO_2, H_2O and N_2.

The total gas emissivity for a path, $\epsilon_{s\rightarrow s'}$, is calculated as

$$\epsilon_{s\rightarrow s'}(T) = \frac{\int_{\eta^-}^{\eta^+} I_{b\eta}(T)\left(1 - \exp\left[-\kappa_\eta L\right]\right) \mathrm{d}\eta}{I_b(T)} \tag{5.1}$$

where η denotes wavenumber, $I_{b\eta}$ is the Planck function, I_b is the total blackbody emissivity, T is the temperature of the gas, L is the length of the gas column, and η^- and η^+ are the minimum and maximum bounds over the spectral dimension that the measurements were taken over, set to be 450 cm^{-1} and 7600 cm^{-1} respectively. The relative percentage error in this study is expressed in the same terms as in the study by Alberti et al. [256], and is given by

$$Error = \frac{\epsilon_p - \epsilon_m}{\epsilon_m} \times 100\% \tag{5.2}$$

where ϵ_p is the predicted emissivity from the model calculations and ϵ_m is the measured emissivity from the gas cell experiment, which was calculated using Equation (5.1) with the measured spectral transmissivity data.

5.1.2 Results and discussion

The results of this study are shown in Figures 5.1 to 5.3. The results for the emissivity calculations for CO_2, Figure 5.1, demonstrate good agreement between the models and the measured data, with the CDSD-4000 database achieving the greatest agreement with the measured results for total emissivity across the majority of the CO_2 cases. The two narrow band models, which are based on the data from the CDSD-4000 database, show the most deviation from the measured values of total emissivity, however this disagreement is still below 5% for all of the cases.

The disagreement with the measured spectral data is greater for the cases containing H_2O, shown in Figure 5.2. The spectral absorption for water vapour extends past the measured range in the experiments by Alberti et al. [256], which causes some inaccuracy in applying the narrow band CK model, as the model parameters by Rivière and Soufiani [263] are not aligned with the boundaries of the measured spectrum. The SNB model, however, is aligned to a spectral resolution of 25 cm^{-1}, and demonstrates better agreement with the LBL data that the SNB parameters are based upon, however the LBL data itself shows the worst agreement to the measured data across most of the cases, and the greater agreement achieved by the narrow band models may be assumed to be coincidental.

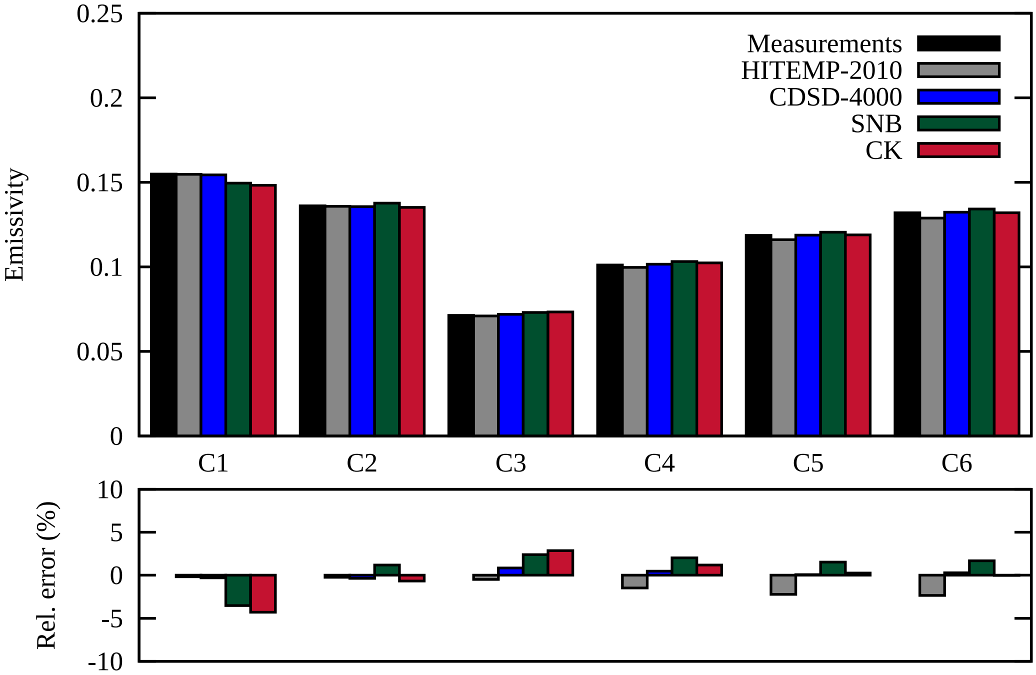

Figure 5.1: Results for the total emissivity calculated for the cases C1–C6 against the measurements by Alberti et al. [256].

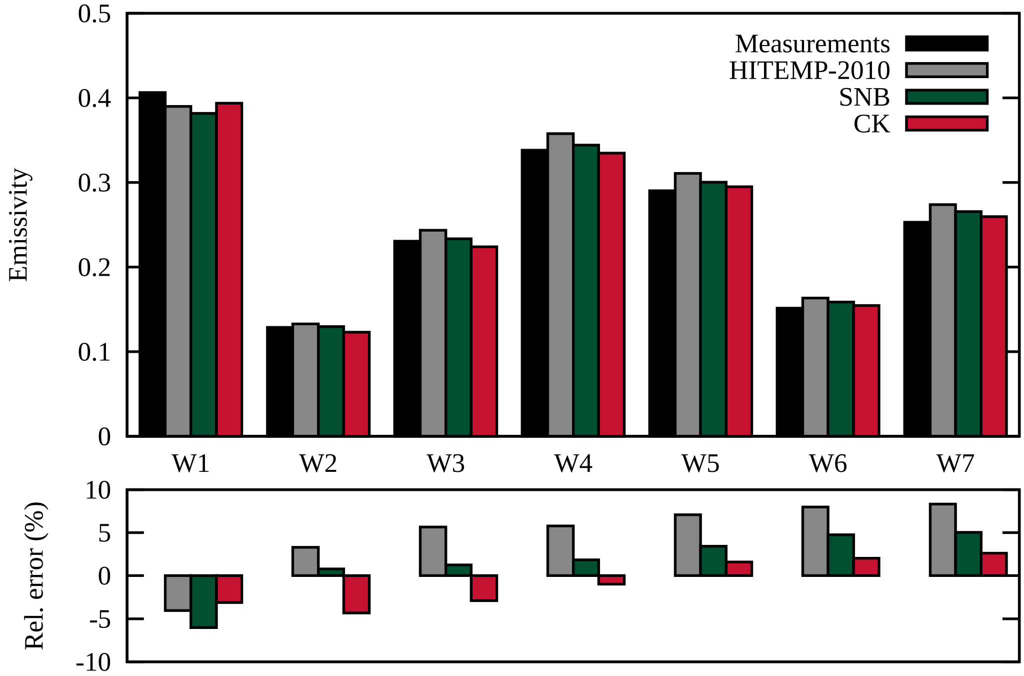

Figure 5.2: Results for the total emissivity calculated for the cases W1–W7 against the measurements by Alberti et al. [256].

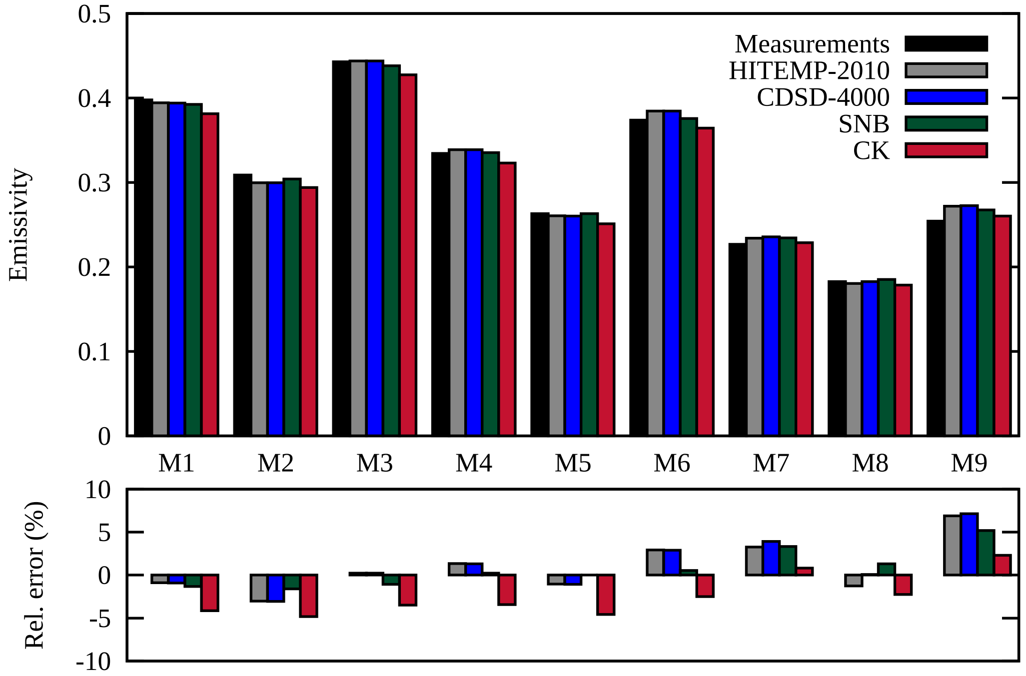

Figure 5.3: Results for the total emissivity calculated for the cases M1–M9 against the measurements by Alberti et al. [256].

The total emissivity values for the cases that contain a mixture of CO_2 and H_2O are shown in Figure 5.3. The level of relative error in the mixture cases are consistent with the error in the H_2O cases, and are least significant in cases with a high concentration of CO_2. The errors associated with the two LBL methods are broadly similar across all of the cases, thus indicating that the largest source of inaccuracy is in the treatment of the H_2O spectral absorption coefficient.

In general, the results of the calculations shown in Figures 5.1 to 5.3 demonstrate good agreement between measured emissivity and model predictions across all of the 22 cases. Errors in the calculations are most significant for the higher temperature emissivity of H_2O, however all errors are below 7% of the measured emissivity value, and the models accurately follow the relative trends across the cases. It is not possible to use measured values for the following test cases used in this chapter, and therefore the results of the spectral models are taken as an analogue for reality. While these methods are reasonably accurate, it is important to acknowledge that these methods will still have inaccuracies when compared against the true radiative properties of gasses.

5.2 Calculations of one-dimensional radiative transfer

The cases defined by Alberti et al. [256], which were used in Section 5.1 for validating the spectral models, describe the transmissivity across a homogeneous path, where the narrow band models are very close representations of the LBL data, and inaccuracies are mostly incurred from numerical considerations associated with the implementation. It is necessary to define cases that describe radiative transfer through inhomogeneous media to test the inherent approximations in the models for practical cases, namely the assumptions of a scaled or correlated absorption coefficient. Both the scaled and correlated approximations break down in cases with strong temperature gradients [283], or in cases with variations in the relative composition of the participating species [284]. Additional hypothetical cases are introduced to compare the predictions of LBL and narrow band models across a one-dimensional path. For brevity, the global models are not included in this study, however these models are validated in Section 5.3 against the narrow band models that are included in this study.

The radiative transfer in the hypothetical cases of inhomogeneous media is calculated using the DO method for a one-dimensional slab and solving for the integral form of the RTE, which is presented for a non-scattering medium as [270]

$$I_{i,n+1} = \tau_{i,n\to n+1} I_{i,n} + (1 - \tau_{i,n\to n+1}) I_{b,n+1/2} \tag{5.3}$$

where $I_{i,n}$ is the radiative intensity at nodal point n and direction i, $\tau_{i,n\to n+1}$ is the monochromatic transmissivity between nodal point n and $n+1$ in direction i, and $I_{b,n+1/2}$ is the blackbody intensity evaluated at the temperature between the nodal points n and $n+1$. The path length between nodal point n and $n+1$ along direction i, which is used to calculate $\tau_{i,n\to n+1}$, is evaluated as $|x_n \to x_{n+1}|/|\mu_i|$, where x_n is the position of node n and μ_i is the directional cosine associated with direction i, which is defined by the angular quadrature scheme. The results for the CK model were evaluated in the same way, where each interval in the spectral dimension was replaced by a term for each quadrature point within each narrow band. The RTE for the SNB model is modified to account for the additional correlation terms that arise from applying the narrow-band averaged transmissivity, so that the averaged intensity at a node n in direction i, $\bar{I}_{i,n}$, is given by [270]

$$\bar{I}_{i,n+1} = \bar{I}_{i,n} + (1 - \bar{\tau}_{i,n\to n+1}) \bar{I}_{b,n+1/2} + \bar{C}_{i,n+1/2} \tag{5.4}$$

where

$$\bar{C}_{i,n+1/2} = \bar{I}_{i,1}(\bar{\tau}_{i,1\to n+1} - \bar{\tau}_{i,1\to n}) + \sum_{k=1}^{n-1} \left[(\bar{\tau}_{i,k+1\to n+1} - \bar{\tau}_{i,k+1\to n}) - (\bar{\tau}_{i,k\to n+1} - \bar{\tau}_{i,k\to n}) \right] \bar{I}_{b,k+1/2} \quad (5.5)$$

where the nodal point 1 corresponds to the boundary. All of the models assume that the medium is constant between nodal points.

Once the intensity has been calculated for each directional position, the radiative heat flux at each nodal point is calculated as

$$q_n = \sum_{i}^{N_i} w_i \mu_i I_{i,n} \quad (5.6)$$

where q_n is the nodal radiative heat flux, w_i is the quadrature weight associated with the directional cosine μ_i and N_i is the number of ordinates. The results from the different models are compared against their prediction of the radiative source term, $-\,\mathrm{d}q/\,\mathrm{d}x$, which is calculated from the nodal heat flux using a finite difference scheme. The S_8 quadrature scheme was used to describe the ordinates in this study, resulting in a total of eight directional cosines for the one-dimensional cases.

The LBL calculations in this study are calculated using the HITEMP-2010 and CDSD-4000 databases. The LBL spectral data is calculated using Voigt line profiles with a line cut-off intensity of 10^{-9} cm^{-1} and omitting the lines that were identified by Rivière and Soufiani [263] as being anomalous, in the same way as was calculated in Section 5.1. The spectral range was increased in this study to cover 50 cm^{-1} to 15000 cm^{-1}, with the same resolution of 0.001 cm^{-1}, resulting in 1.495×10^7 discrete intervals across the spectral dimension.

The percentage relative error in this study was calculated as

$$Error = \frac{\nabla q_{nb} - \nabla q_{\text{CDSD}}}{\max\left|\nabla q_{\text{CDSD}}\right|} \times 100\% \quad (5.7)$$

where ∇q_{nb} is the radiative source term calculated from the narrow band models, ∇q_{CDSD} is the radiative source term calculated from the LBL calculation using the CDSD-4000 database for the spectral lines of CO_2. The LBL results using the CDSD-4000 database was chosen for the benchmark in the error calculation as both sets of narrow band model parameters are based on the spectral data in the CDSD-4000 database.

5.2.1 Case definitions

Three test cases are introduced in this study to validate the assumptions of a scaled or correlated absorption coefficient in an oxyfuel combustion environment. The first hypothetical test case, which will be referred to as H1, is based on the three-dimensional case introduced by Liu [272], and updated by Porter et al. [299] to represent oxyfuel conditions. The test case has a fixed gas composition, with the mole fractions of CO_2, H_2O and N_2 set to 0.85, 0.1, and 0.05 respectively, which loosely represents the flue gas of an oxyfuel process with a dry recycle. The case is defined with variable temperature along the path, which is defined as the centreline temperature in the original case [272]; a piecewise linear profile across a 4 m domain is defined as

$$T(x) = \begin{cases} 400 + 1400x/0.375 & x \leq 0.375 \text{ m} \\ 1800 - 1000(x - 0.375)/3.625 & x > 0.375 \text{ m} \end{cases} \tag{5.8}$$

where $T(x)$ is the temperature, in Kelvin, at position x, in metres. The boundary conditions of the case, where $x = 0$ m and $x = 4$ m, is set to the blackbody intensity evaluated at 300 K, and neither boundary is treated as reflective with an emissivity of 1. The RTE is calculated over 24 grid points, which are most finely spaced across the high temperature region, as defined in the case by Liu [272].

The second hypothetical case, H2, represents a similar 4 m path length with variable species concentrations with a fixed temperature. The species concentration was chosen to vary so that the relative partial pressures of CO_2 and H_2O obeyed the relationship $0.125 \leq H_2O/CO_2 \leq 2$, so that the conditions span the range of the ratios specified by the oxyfuel WSGG coefficients that are employed in the Section 5.3 where this distribution is also applied. The species concentrations are defined according to the following distribution

$$X_{H_2O}(x) = 2\left(\frac{x}{4}\right)\left(1 - \frac{x}{4}\right) + 0.1 \tag{5.9}$$

$$X_{CO_2}(x) = 0.9 - X_{H_2O}(x) \tag{5.10}$$

$$X_{N_2}(x) = 0.1 \tag{5.11}$$

where X_{sp} denotes mole fraction of species sp, and again, x is the position in metres. The boundary to this case is set to the blackbody intensity at 500 K to comply with the limits of the WSGG coefficients that are used in the latter study.

The final case, denoted H3, is similar to the oxyfuel case put forward by Chu et al.

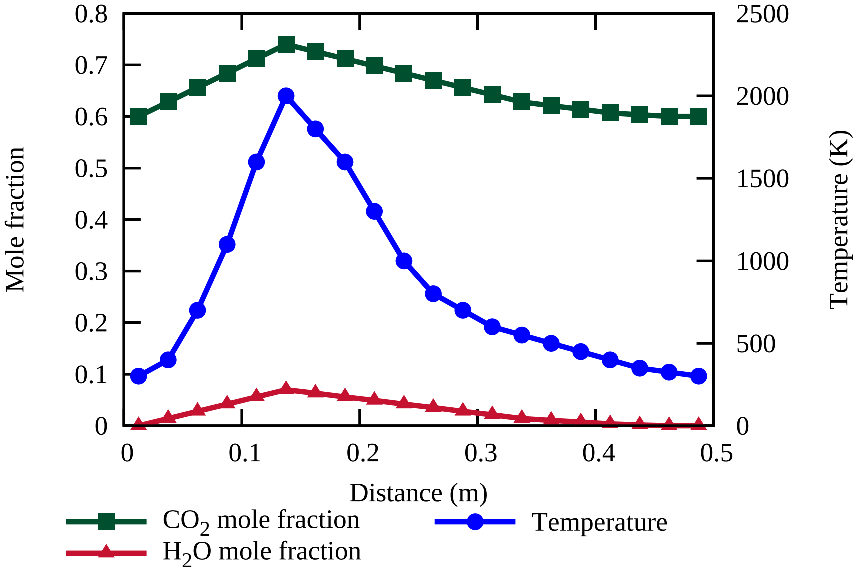

Figure 5.4: Temperature and species distribution for the third one-dimensional test case, H3. Points indicate the location of the node centres used in the calculation.

[265], which was used to compare LBL databases and narrow band predictions for oxyfuel conditions, and was based on the initial case by Liu et al. [271] to represent a counterflow diffusion methane-flame. In the previous study by Chu et al. [265], the LBL method with the HITEMP2010 database was compared with the SNB model using parameters based on earlier spectral data databases, and was shown to have good agreement. In this study the narrow band CK model and more recently developed SNB parameters are compared against the HITEMP-2010 and CDSD-4000 databases. The composition of the domain is also modified to represent an oxy-coal combustion environment with a dry recycle. The advantages of testing with a dry recycle ensures that the molar ratio of CO_2 and H_2O varies across the domain, which will test one of the noted causes of inaccuracies in the application of the correlated or scaled assumption for oxyfuel combustion. The temperature and species distribution is listed in Table 5.2 and shown graphically in Figure 5.4. The inlet and outlet points are set to the same values, which are 300 K for the temperature and 0.6 and 0 for the mole fractions of CO_2 and H_2O, respectively. All values peak at a distance of 0.1375 m, with values of 2000 K for temperature, and mole fractions of 0.74 and 0.07 for CO_2 and H_2O respectively. Twenty evenly spaced nodes were used for the solutions of case H3.

Distance (m)	**Temp. (K)**	$\mathbf{X_{CO_2}}$	$\mathbf{X_{H_2O}}$
0.0125	300	0.600	0.000
0.0375	400	0.628	0.014
0.0625	700	0.656	0.028
0.0875	1100	0.684	0.042
0.1125	1600	0.712	0.056
0.1375	2000	0.740	0.070
0.1625	1800	0.726	0.063
0.1875	1600	0.712	0.056
0.2125	1300	0.698	0.049
0.2375	1000	0.684	0.042
0.2625	800	0.670	0.035
0.2875	700	0.656	0.028
0.3125	600	0.642	0.021
0.3375	550	0.628	0.014
0.3625	500	0.621	0.011
0.3875	450	0.614	0.007
0.4125	400	0.607	0.004
0.4375	350	0.604	0.002
0.4625	325	0.600	0.000
0.4875	300	0.600	0.000

Table 5.2: Temperature and species distribution for the third one-dimensional test case, H3. Locations are represented at the location between nodes used in the calculation.

5.2.2 Results and discussion

The results for cases H1, H2 and H3 are shown in Figures 5.5, 5.6 and 5.7, respectively. Within all three of the test cases, the LBL method demonstrated excellent agreement between the two databases, with the only visual disagreements occurring around the peak temperatures in the cases H1 and H3.

The results for the case H1, shown in Figure 5.5, demonstrate a less than ±2% disagreement between the benchmark data and the narrow band models across the entire domain. The results show a similar profile that is present in the three-dimensional case by Liu [272], where the source term is positive in the low temperature regions, reduces to a sharp negative peak where the gas temperature is at its maximum, and then reduces to a value close to zero in the region where the temperature is more uniform. The majority of the error is associated with the region close to $x = 0$ m, where the temperature gradient is most significant. The error is significantly reduced in the low-gradient region past $x = 0.5$ m. Between the two narrow band models, the SNB model shows the most smooth and consistent error that follows the magnitude of the source term, thus indicating that the induced error is likely to be a systematic error associated with the specific implementation of the model, and which is likely to be case independent.

The results for the case with variable species composition across the path length, case H2, is shown in Figure 5.6. The error in all but two of the nodal locations is less than ±1%, however the error next to the boundaries of the domain are significantly higher at over 8%. Within this region there is a sharp temperature gradient between the walls at 500 K and the medium at 1500 K, which explains the disagreement being localised to the edge nodal locations. The predicted radiative source term from the narrow band models across the path with variable species concentrations is in excellent agreement with the benchmark data, and so the variations in species distributions appear to be captured well by the narrow band models, while errors are still induced by strong temperature gradients.

The results of the radiative source term calculation for the case with variable species concentrations and gas temperature, case H3, is shown in Figure 5.7. As with the H1 case, the source term shows a sharp negative peak at the maximum temperature, which also coincides with the maximum species concentration as well. The shape of the source term plot generally follows the same trend as the gas temperature across the domain. As with the case in H1, the errors for the SNB model smoothly follow the magnitude of the source term calculation, further indicating that the SNB model demonstrates a very good approximation of the LBL data. While the CK model

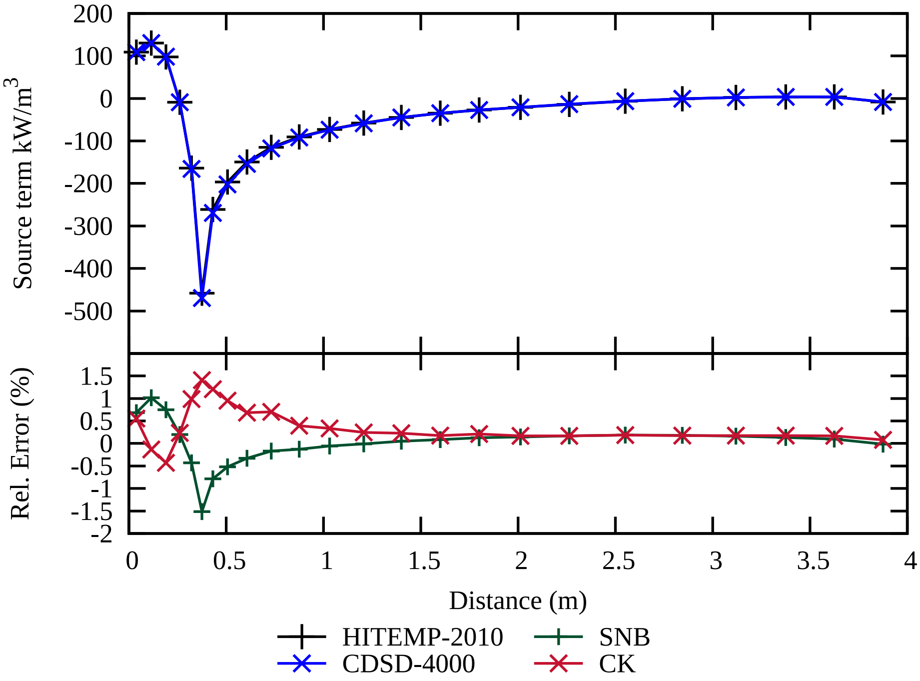

Figure 5.5: Radiative source term across the one-dimensional slab for case H1.

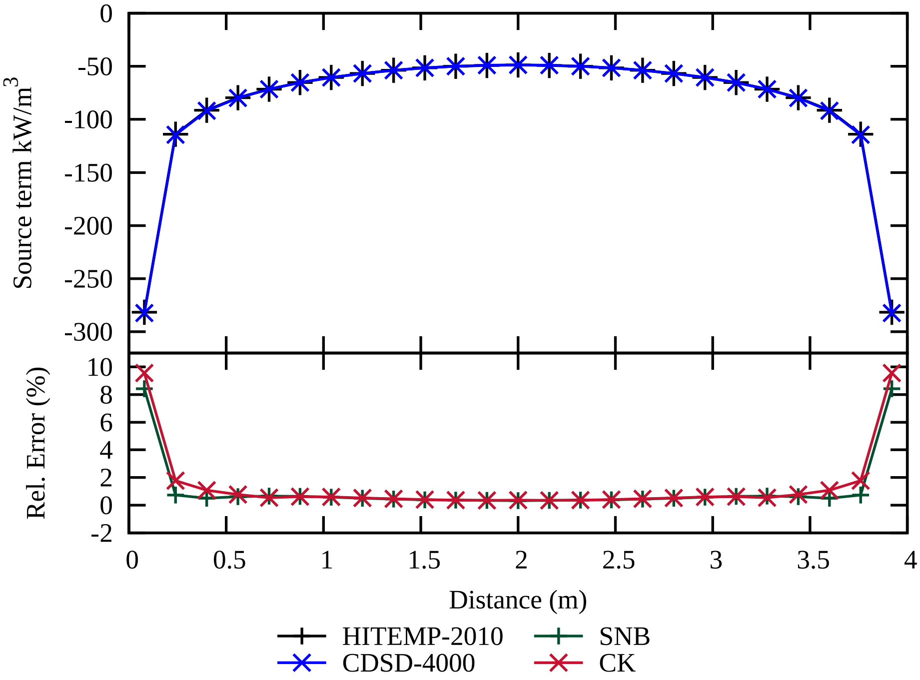

Figure 5.6: Radiative source term across the one-dimensional slab for case H2.

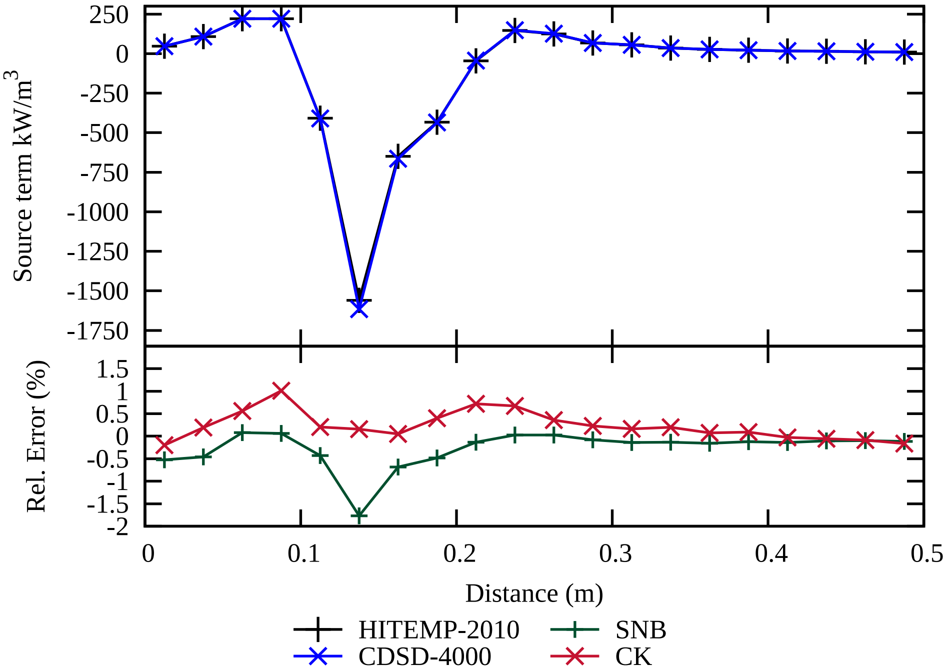

Figure 5.7: Radiative source term across the one-dimensional slab for case H3.

demonstrates more variable error relative to the LBL data, specifically across the peak temperature region of the domain, all errors are below 2% of the maximum source term value.

The narrow band models demonstrated excellent agreement with the LBL method for the calculation of the radiative source term, with all relative errors being less than 2%, with the exception of the near-boundary locations in case H2. The relative errors induced in the calculation of the radiative source term are significantly lower than the errors encountered for the calculation of the total emissivity presented in Section 5.1. While the SNB model was shown to agree better with the LBL data, both narrow band models are applicable to calculating benchmark results for oxyfuel environments in more complex cases.

5.3 Calculations of radiative transfer within a three-dimensional enclosure

The studies in Sections 5.1 and 5.2 identified the narrow band methods as being accurate in the calculation of radiative transfer through media relevant for an oxyfuel environment. This study applies narrow band and global methods to a three-dimensional enclosure, calculating the radiation energy source term and radiative heat flux within the framework of the commercial CFD code ANSYS Fluent v15. The conclusions from this study are directly applicable to CFD calculations of oxyfuel combustion.

The two narrow band models that were validated in the previous sections are used to generate benchmark data to validate the global methods. The benchmark data are generated for two cases within a three-dimensional geometry with fixed temperature and species compositions. Both the SNB and the CK methods are used to generate benchmark data. The CK model and the global methods are solved using the FVM in Fluent, with user-defined functions to customise how the RTE is solved. The FVM is used due to its accuracy at the boundary for evaluating the radiative heat flux. The large computational cells used in this study result in a significant optical thickness for the control volumes, so the second order upwind scheme was used for the FVM spatial discretisation. The results for varying the number of quadrature points in the FSK methods, and the number of grey gasses in the SLW method, are compared, as well as comparing the grey and non-grey WSGG approaches and the SLW-1 method. Validation is carried out by comparing the calculation of the radiation energy source term and the radiative heat flux, the two quantities that have a direct impact on the energy and temperature fields in the solutions of CFD calculations.

The SNB model cannot be used with the RTE solvers that are available in Fluent, and so the model is applied to the cases by implementing a ray tracing method similar to the DTM to solve the RTE, as described in the study by Liu [272]. The narrow band averaged integral form of the RTE, Equation (5.4), is solved for a number of rays, which are prescribed by the T_N quadrature set [443], originating from the faces of each cell in the domain. The radiative source term for the centre of a cell is calculated by a finite difference between the values of the radiative heat flux at the cell faces. This method is implemented with a user-defined function within Fluent to ensure that the case specifications between the SNB and CK benchmark calculations and the global methods are identical.

As discussed in Chapter 3, the application of the non-grey WSGG method cannot be applied to non-homogeneous cases without further development, specifically for the parameters defined by Johansson et al. [291] and Kangwanpongpan et al. [292], as these methods directly base the emissivity weighting function on the local gas composition, which is not defined for radiation emitting from the boundary. In the current study, two approaches are proposed. In the first method, the gas composition used for the emissivity weighting of the boundary is derived from the adjacent fluid cell. In the second method the gas composition for all spectral quantities is derived from the volume averaged mole fractions, and is applied to the fluid absorption coefficient as well as the emissivity weighting function. The WSGG parameters defined by Yin et al. [286] and Krishnamoorthy [293], which are defined across discontinuous intervals of the gas composition, are also compared in a similar manner, whereby either the local composition or the volume-averaged composition is used to select the discrete interval for the radiative properties. This treatment is not considered for the grey WSGG method, which has been widely implemented by only considering local gas compositions.

The FSK models were implemented using the narrow band k-g distribution databases from Cai and Modest [441]. The full-spectrum k-g distributions for mixtures were generated by applying the mixing scheme by Modest and Riazzi [282] to the narrow band distributions first, and then constructing the full-spectrum k-g distribution from the narrow band mixture distribution. As the construction of these k-g distributions can be relatively computationally expensive, and would therefore be inappropriate for CFD calculations, full-spectrum k-g distributions are tabulated in a pre-processing step for a range of thermodynamic states and linear interpolation is used to calculate the local k-g distribution. The tabulation uses temperature spacing of 100 K, and the species tabulation is done across intervals in the mole fraction of 0.1. As the benchmark cases are at a constant atmospheric pressure, the k-g distributions are only calculated for the one pressure value.

The reference state in the FSK models was calculated as a volume averaged species composition and using a reference temperature T_0 that satisfies the implicit relation [284]

$$\kappa_{\text{PL}}(\underline{\phi}_0)T_0^4 = \frac{1}{V}\int_V \kappa_{\text{PL}}(\underline{\phi})T^4 \, \mathrm{d}V \tag{5.12}$$

where $\kappa_{\text{PL}}(\underline{\phi})$ is the Planck averaged absorption coefficient at the thermodynamic state $\underline{\phi}$, V denotes volume and $\underline{\phi}_0$ is the reference state, which is composed of the volume averaged gas species composition, the reference temperature and the pressure at 1 atm.

The SLW and SLW-1 methods are implemented using the ALBDF lookup tables from Pearson et al. [309]. The mixture ALBDF is generated using the multiplicative approach in the SLW method. The SLW-1 parameters are generated by using a Newton-Raphson method to fit the emissivity over two lengths to the predicted value from the SLW method using the direct integration method to calculate the mixture ALBDF. The two lengths were calculated as factors of 0.5 and 2 of the mean beam length [306], where the mean beam length is approximated as [223]

$$s = \frac{3.6V}{A} \tag{5.13}$$

where s is the mean beam length, V is the internal volume and A is the surface area of the box. The mean beam length in these cases was 1.44 m. The reference approach was employed for both the SLW and SLW-1 to extend the methods to a non-homogeneous medium [303].

5.3.1 Case definitions

The two cases used in this study are similar to two of the cases originally proposed by Liu [272], and are defined on a cuboid geometry that is 2 m × 2 m × 4 m and bounded by black walls and at a constant atmospheric pressure. The predictions from the global methods are compared against the narrow band calculations of the radiative source term along the centreline of the domain parallel to the z-axis and the radiative heat flux half way up the wall, along the line (0 m, 1 m, z).

The first case has a non-uniform temperature distribution that is symmetrical around the z-axis, and is identical to the oxyfuel case proposed by Porter et al. [299]. The centreline temperature parallel to the z-axis is defined by a piecewise linear temperature profile, as described for case H1 in Subsection 5.2.1, with the radial temperature distribution defined as

$$T = \begin{cases} (T_c - 800)f(r) + 800 & r \leq 1 \\ 800 & r > 1 \end{cases} \tag{5.14}$$

where T_c is the centreline temperature, defined by Equation (5.8), r is the distance of the location from the centreline and where $f(r) = 1 - 3r^2 + 2r^3$. The walls of the geometry are set to 300 K with an emissivity of 1. The temperature distribution in this case is shown in Figure 5.8. The gas composition is constant throughout the medium, with the mole fractions of CO_2 and H_2O are set to 0.85 and 0.1 respectively, with the balance made up from N_2, which is assumed to be transparent. The case is solved on a 17×17×24 cell grid, with a higher density of cells in the high temperature region; identical to the original case proposed by Liu [272]. Both the SNB benchmark data and the FSCK results for this case have been updated to the more recent parameters used in this study. The T_6 quadrature scheme was used to generate the SNB benchmark data, as increasing the number of rays to the T_8 scheme did not significantly affect the

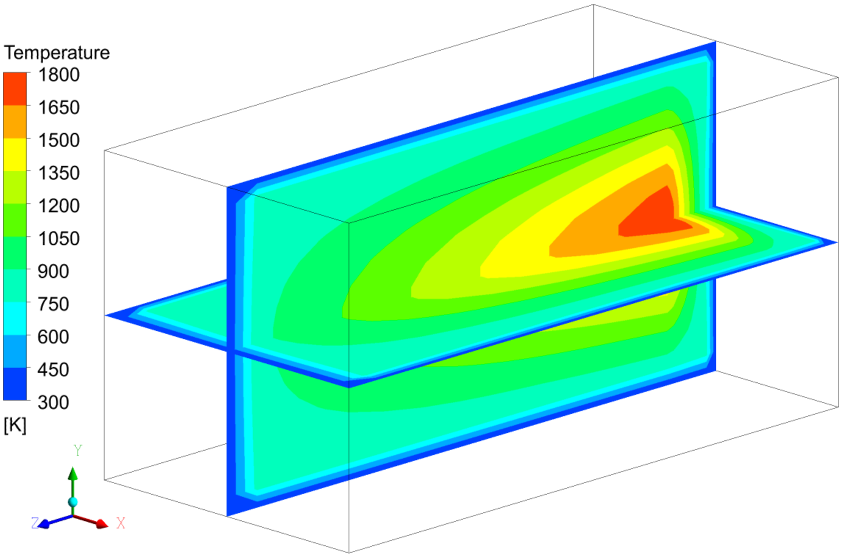

Figure 5.8: Temperature distribution for case 1.

solution. A 3×3 angular discretisation was used in the FVM method, where increasing to a 4 × 4 discretisation did not affect the solution.

The second case has a variable species concentration and a uniform temperature. The species distribution along the z-axis is the same as the distribution in case H2, which is defined in Equations (5.9) to (5.11), and did not vary along the x and y directions. The distribution of H_2O is shown in Figure 5.9. The geometry is divided into a uniform 11×11×25 cell grid, as was done for the second case in Liu [272]. The temperature of the medium in the second case is 1500 K and the walls are fixed to 500 K to adhere to the limits of the WSGG methods. The T_8 quadrature scheme was used for the SNB results on the second case as there were noticeable differences between the T_6 and T_8 schemes, but not between the T_8 and T_{10} schemes. As with the first case, a 3×3 angular discretisation was used in the FVM method, where increasing to a 4 × 4 discretisation did not affect the solution.

5.3.2 Results and discussion

All global methods were calculated in serial on a 3 GHz CPU, and took less than a few minutes to reach a converged solution. The time required to reach the converged solution was directly related to the number of RTEs required, regardless of the model, with the addition that the FSK models also required a preprocessing step to generate

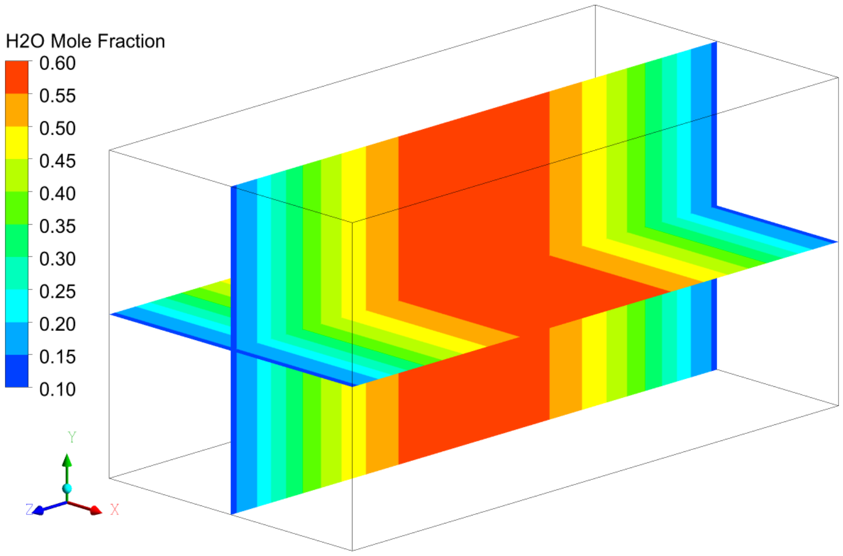

Figure 5.9: H_2O mole fraction distribution for case 2.

the k-distributions. The results are given in Figures 5.10 to 5.21. The two narrow band models show good agreement in both of the cases, and variations between the two are assumed to be due to the different RTE solver as these differences are more significant than in the errors in the study shown in Section 5.2.

The calculated values for the radiative source term and heat flux for the widely used grey WSGG are shown in Figures 5.10 and 5.11. The calculated values for the radiative source term in the non-isothermal case, Figure 5.10(a), demonstrate the unsuitability of the widely used parameters by Smith et al. [220] for oxyfuel environments, as these parameters significantly under-predict the magnitude of the source term across the whole domain. The parameters developed for oxyfuel conditions produce results that are much closer to the benchmark data. However these results show the same qualitative trend as the results from the parameters by Smith et al. [220], and do not capture the peaks in gas absorption and emission at z=0 m and z=0.375 m respectively.

The heat flux calculations from the grey WSGG methods are shown in Figure 5.10(b). The parameters that were developed for oxyfuel conditions all significantly over-predict the heat flux compared to the benchmark data. The only calculation that is close to the benchmark data is from the parameters by Smith et al. [220], however, due to the significant under prediction of the magnitude of the radiative source term, this is likely to be a coincidental result, and the parameters by Smith et al. [220] are not recommended for CFD calculations of oxyfuel combustion.

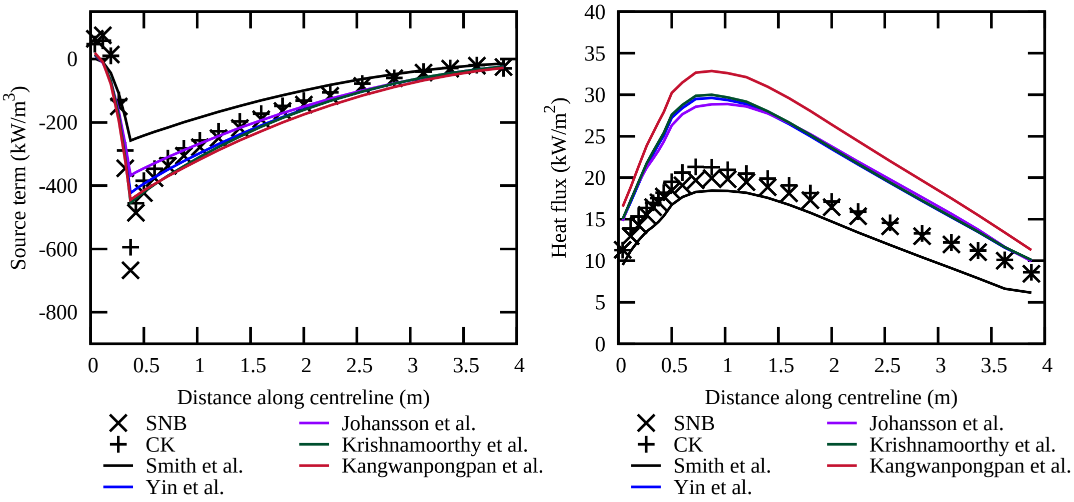

(a) Radiation energy source term

(b) Radiative heat flux

Figure 5.10: Results from applying the grey WSGG model in case 1 for calculating the radiation source term along the centreline parallel to the z-axis and the radiative heat flux at the wall line (0 m, 1 m, z).

The calculations on the case with a variable gas composition highlight significant deficiencies in the grey WSGG methods, shown in Figure 5.11. The calculation of the radiation source term, Figure 5.11(a), shows neither qualitative or quantitative agreement with the benchmark data. Furthermore, discontinuities in the WSGG model parameters by Smith et al. [220], Yin et al. [286] and Krishnamoorthy [293] are clearly visible in the derived quantities. The prediction of the radiative heat flux in Figure 5.11(b) shows better agreement with the benchmark data, however the misrepresentation of the radiation source term is likely to cause significant errors in coupled CFD calculations.

The results for the non-grey WSGG method are shown in Figures 5.12 and 5.13. In comparison to the grey formulation discussed above, the non-grey WSGG shows much better agreement with the benchmark data in the non-isothermal case. The calculation of the radiative source term, Figure 5.12(a), correctly captures the peaks at z=0 m and z=0.375 m, and the calculations of radiative heat flux, Figure 5.12(b), are in close agreement with the benchmark data.

The non-grey WSGG model was applied using two approaches on the second case, the first approach applied the radiative properties calculated from the gas composition of the nearest cell, and the second approach applied the volume averaged species

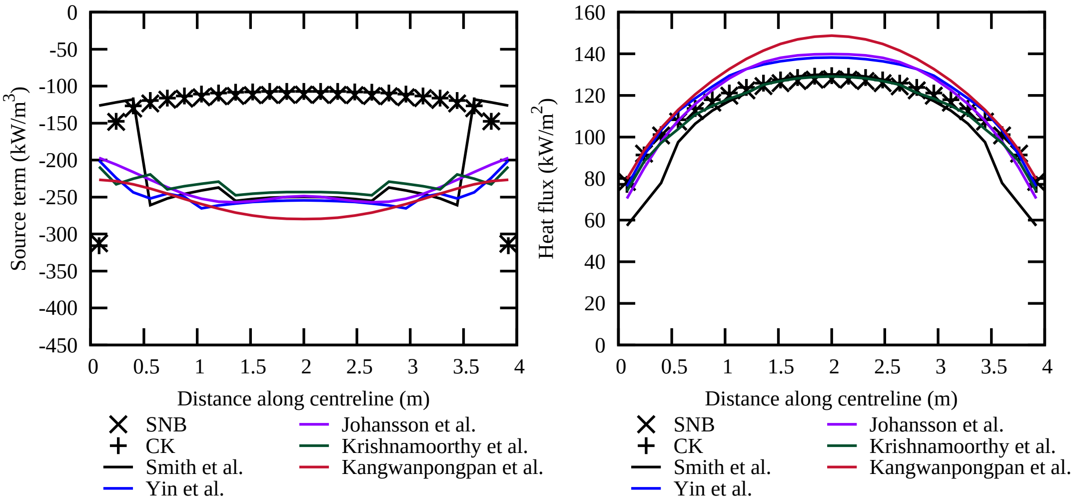

(a) Radiation energy source term (b) Radiative heat flux

Figure 5.11: Results from applying the grey WSGG model in case 2 for calculating the radiation source term along the centreline parallel to the z-axis and the radiative heat flux at the wall line (0 m, 1 m, z).

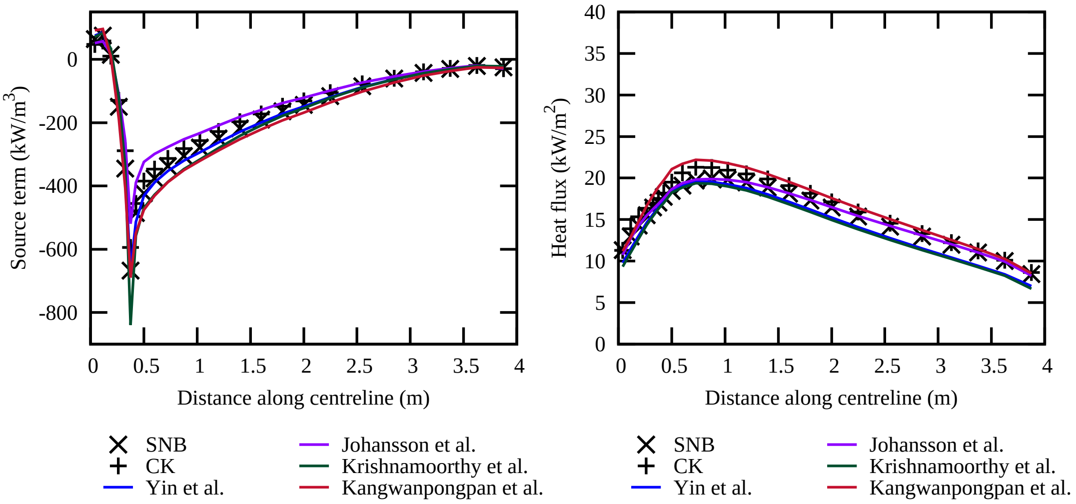

(a) Radiation energy source term (b) Radiative heat flux

Figure 5.12: Results from applying the non-grey WSGG model in case 1 for calculating the radiation source term along the centreline parallel to the z-axis and the radiative heat flux at the wall line (0 m, 1 m, z).

concentrations. The results for both approaches is shown in Figure 5.13. The results for the application of the nearest cell's composition shows the same errors associated with discontinuities in the radiative source term that were apparent for the grey WSGG model, shown in Figure 5.13(a). The source term appears much smoother when the global species composition is taken instead of the values at the nearest local cell and there is better agreement with the benchmark data, as shown in Figure 5.13(c). Despite this agreement in the radiative source term, without accounting for the local variations in the gas composition the heat flux predictions produce a flat profile along the wall, which does not match the benchmark data, as shown in Figure 5.13(d). The best agreement with the heat flux is achieved by using the parameters by Kangwanpongpan et al. [292] based on the local cell composition, however the source term predictions for these values demonstrates significant variability across the centreline that is not present in the benchmark data.

The calculated results using the SLW method are shown in Figures 5.14 and 5.15 for a range of values for the number of grey gasses, N_j. The results across the two test cases show a reasonable approximation of the benchmark results, however the method demonstrates noticeable inaccuracies In the second case that are not resolved through the refinement of the total number of grey gasses. The optimal number of grey gasses in the two benchmark cases is around 10, which is twice as high as the requirement for the non-grey WSGG methods.

The results for the more computationally efficient SLW-1 method are shown in Figures 5.16 and 5.17. The trends in the results from the SLW-1 model are very similar to the trends shown by the SLW method in the first case, however with a significantly reduced computational requirement. However, unlike the grey WSGG model and the SLW model with few grey gas components, the SLW-1 method under-predicts the heat flux in the first case, shown in Figure 5.16(b). The results for the calculation of the radiative source term from the SLW-1 method in the second case are also show a similar, but more exaggerated, curvature in the centre of the domain to the non-grey WSGG method, illustrated in Figure 5.17(a). In contrast with the first case, the SLW-1 over-predicts the heat flux in the second case, however there is a good agreement in the corners of the domain.

Finally, the results for the FSK models are shown in Figures 5.18 to 5.21. Both the FSCK and FSSK models were calculated with a variation of the number of Gaussian quadrature points, N_q, between 2 and 9, but only the values for 3, 5 and 7 are presented. There was very little change in the calculated results for the FSK models beyond $N_q = 5$, as can be seen in the results for $N_q = 5$ and $N_q = 7$.

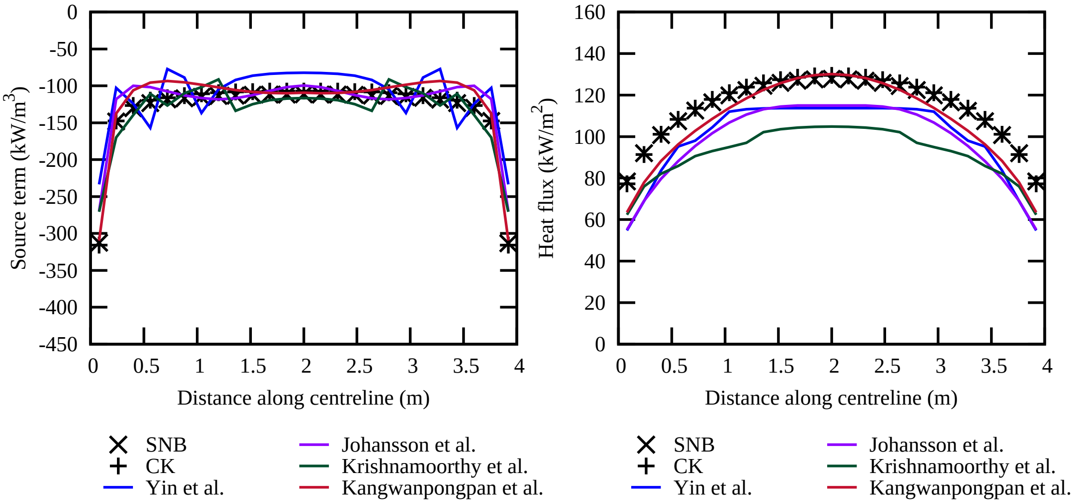

(a) Radiation energy source term with local gas composition used to evaluate radiative parameters

(b) Radiative heat flux with local gas composition used to evaluate radiative parameters

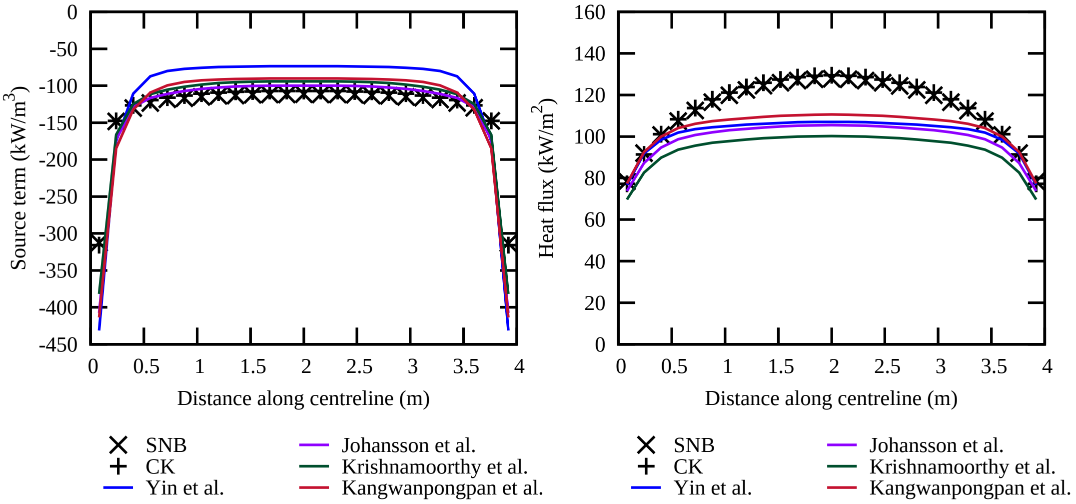

(c) Radiation energy source term with global gas compoistion used to evaluate radiative parameters

(d) Radiative heat flux with global gas composition used to evaluate radiative parameters

Figure 5.13: Results from applying the grey WSGG model in case 2 for calculating the radiation source term along the centreline parallel to the z-axis and the radiative heat flux at the wall line (0 m, 1 m, z) for two approaches of applying the species composition dependency on the radiative properties.

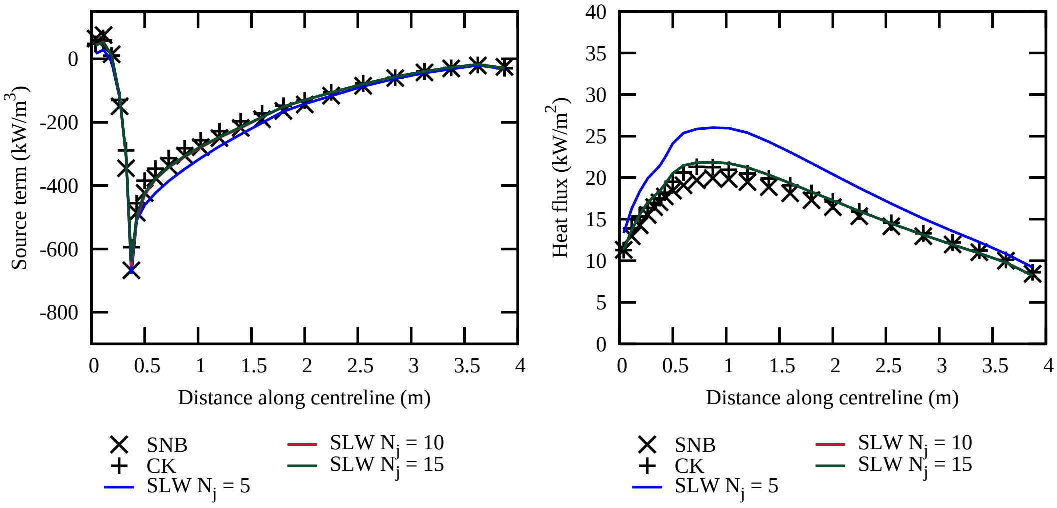

(a) Radiation energy source term

(b) Radiative heat flux

Figure 5.14: Results from applying the SLW model in case 1 for calculating the radiation source term along the centreline parallel to the z-axis and the radiative heat flux at the wall line (0 m, 1 m, z).

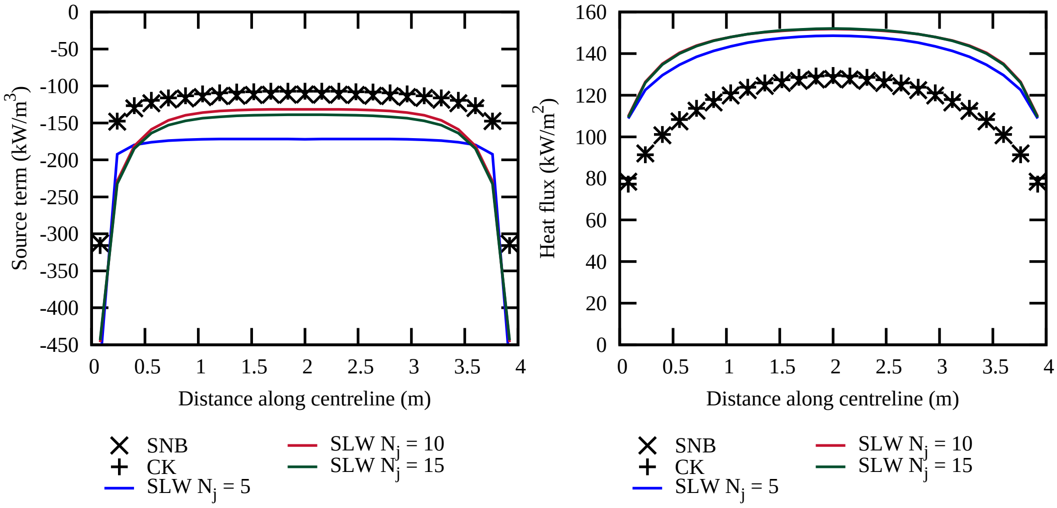

(a) Radiation energy source term

(b) Radiative heat flux

Figure 5.15: Results from applying the SLW model in case 2 for calculating the radiation source term along the centreline parallel to the z-axis and the radiative heat flux at the wall line (0 m, 1 m, z).

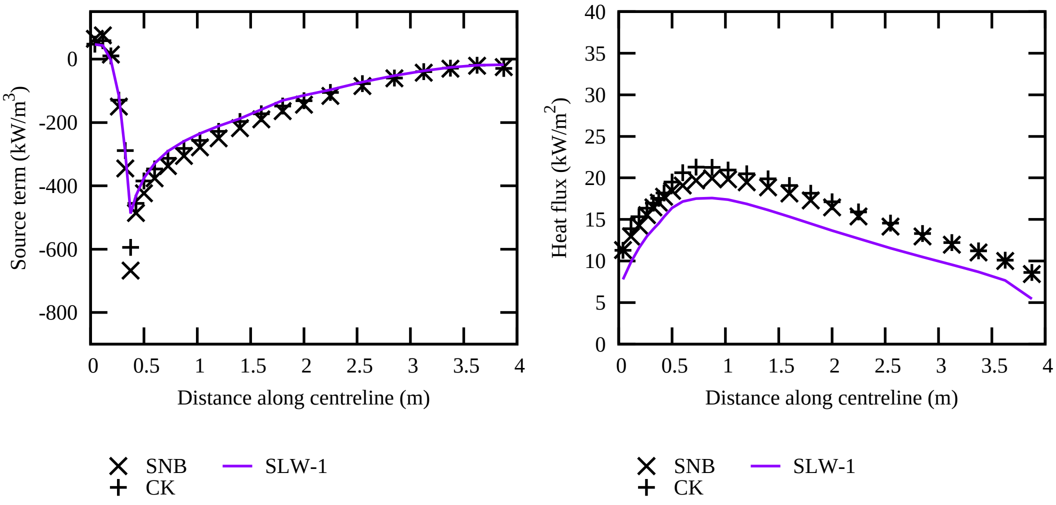

(a) Radiation energy source term

(b) Radiative heat flux

Figure 5.16: Results from applying the SLW-1 model in case 1 for calculating the radiation source term along the centreline parallel to the z-axis and the radiative heat flux at the wall line (0 m, 1 m, z).

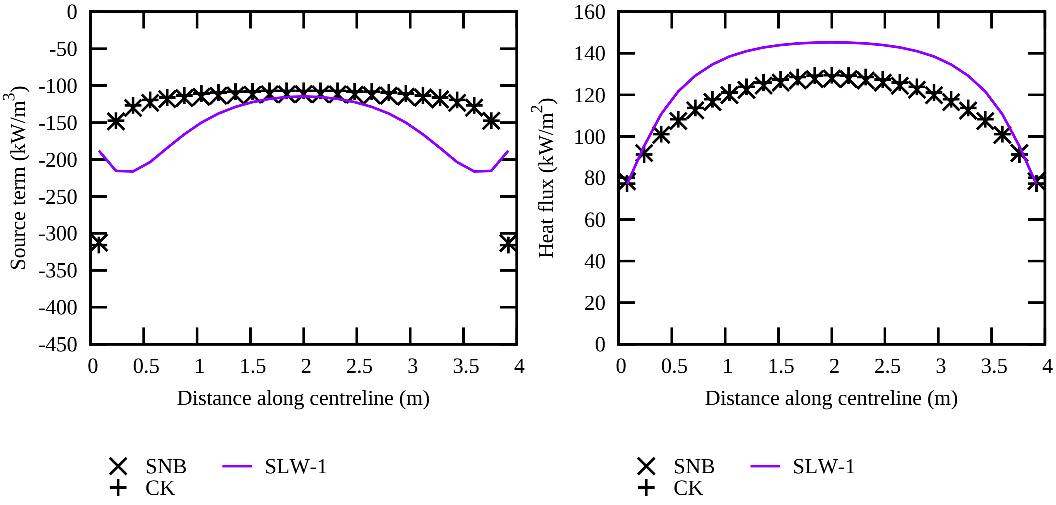

(a) Radiation energy source term

(b) Radiative heat flux

Figure 5.17: Results from applying the SLW-1 model in case 2 for calculating the radiation source term along the centreline parallel to the z-axis and the radiative heat flux at the wall line (0 m, 1 m, z).

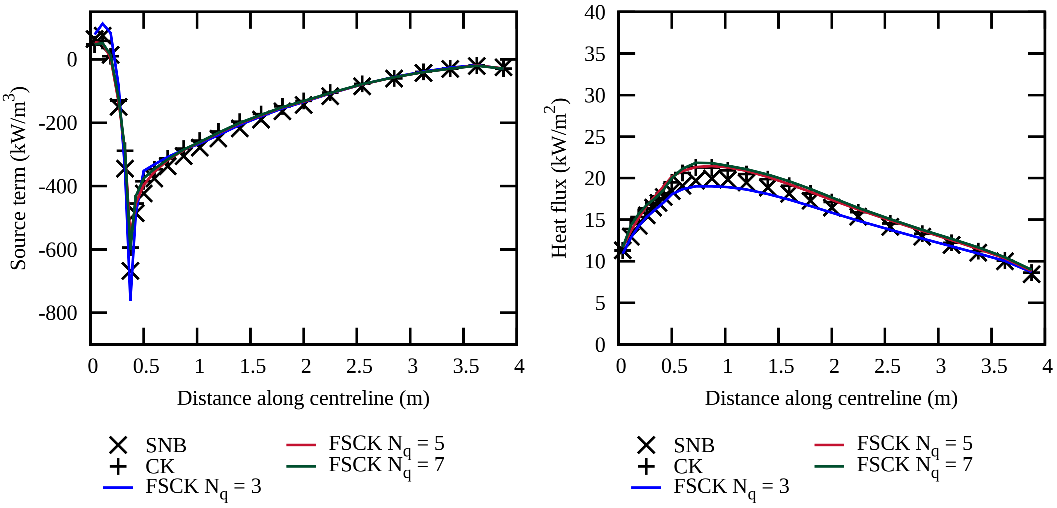

(a) Radiation energy source term

(b) Radiative heat flux

Figure 5.18: Results from applying the FSCK model in case 1 for calculating the radiation source term along the centreline parallel to the z-axis and the radiative heat flux at the wall line (0 m, 1 m, z).

Both the FSCK and the FSSK model demonstrate excellent agreement to the benchmark solutions for the first case, with very little difference between the predicted values from the two models. For both of the FSK models the optimal number of quadrature points, N_q, is shown to be around five points. Across both the radiative source term and the heat flux calculations the FSK models show greater agreement with the CK model. This agreement is most likely attributable to the shared RTE solver between the CK and global methods, as the assumption of a scaled or correlated absorption coefficient between the SNB and CK models respectively is shared with the two FSK models, however the disagreement is only apparent for the narrow-band models.

The second case shows some small differences between the two FSK models, with the FSCK model showing better agreement with the benchmark data for the radiative source term near to the boundary of the domain. The FSSK model does not fully capture the sharp gradient in the radiative source term across the first few nodes, however the prediction of the FSCK model is almost in complete agreement with the benchmark data. Both FSK models show a slightly higher calculated radiative heat flux than the narrow band models in the second case, however this error is significantly lower than any of the other global models tested in this study.

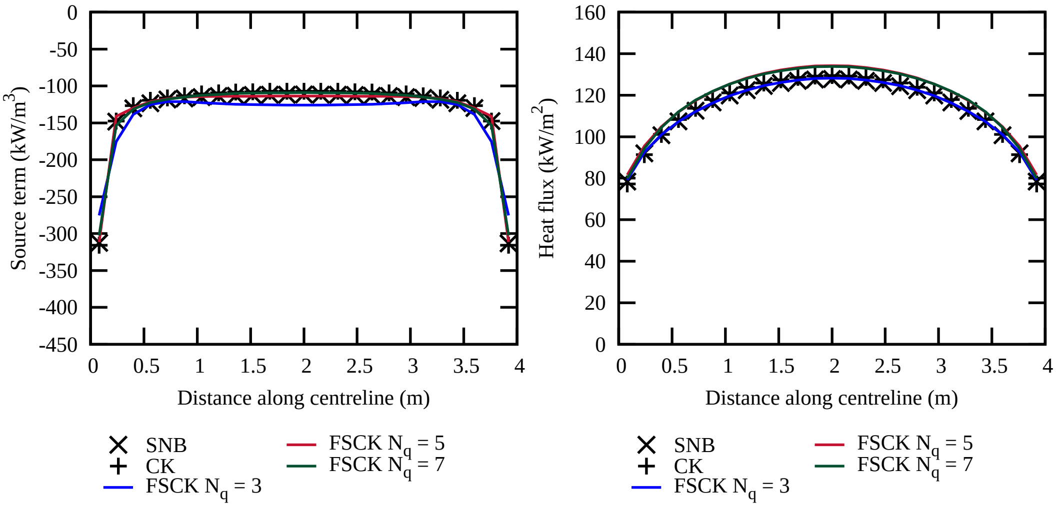

(a) Radiation energy source term

(b) Radiative heat flux

Figure 5.19: Results from applying the FSCK model in case 2 for calculating the radiation source term along the centreline parallel to the z-axis and the radiative heat flux at the wall line (0 m, 1 m, z).

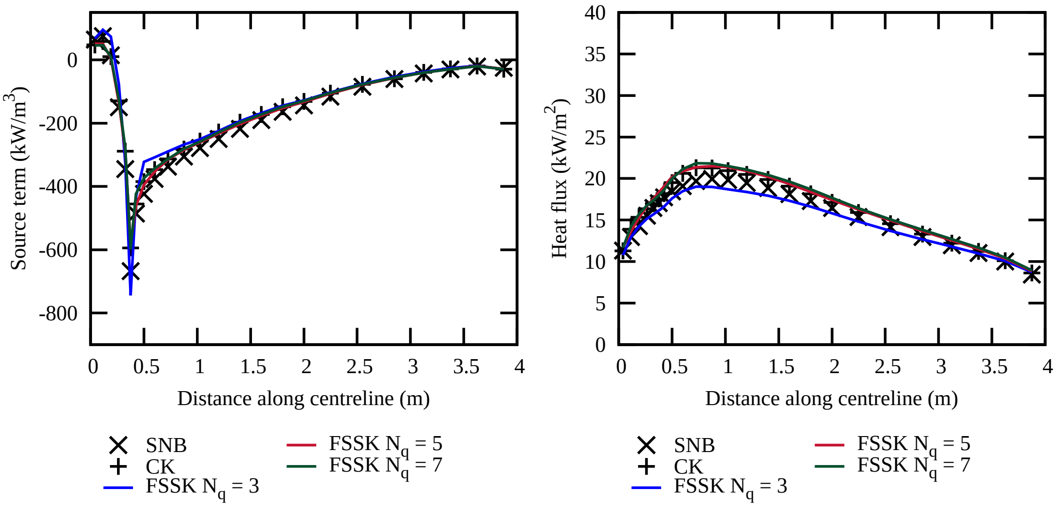

(a) Radiation energy source term

(b) Radiative heat flux

Figure 5.20: Results from applying the FSSK model in case 1 for calculating the radiation source term along the centreline parallel to the z-axis and the radiative heat flux at the wall line (0 m, 1 m, z).

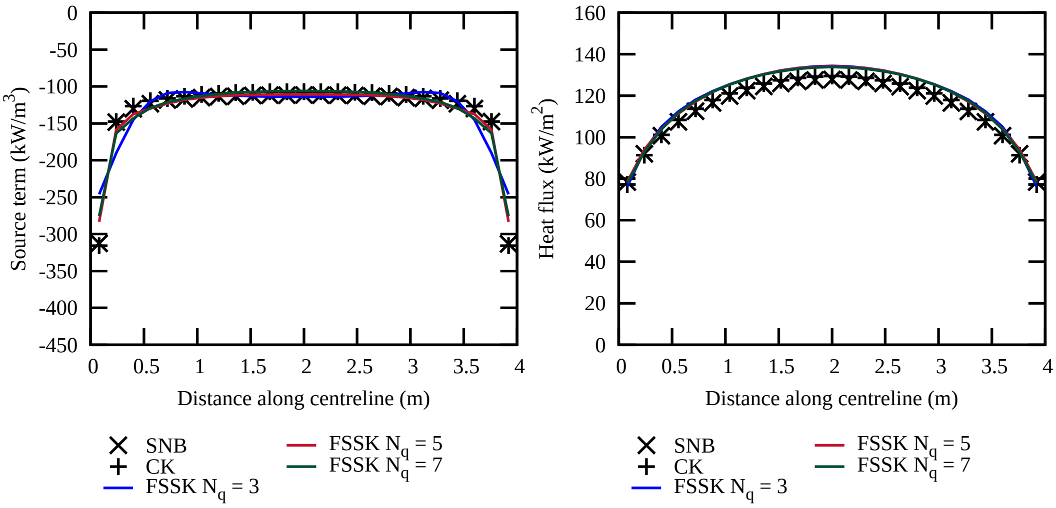

(a) Radiation energy source term (b) Radiative heat flux

Figure 5.21: Results from applying the FSSK model in case 2 for calculating the radiation source term along the centreline parallel to the z-axis and the radiative heat flux at the wall line (0 m, 1 m, z).

5.4 Conclusions

The study in this chapter aimed to validate a range of methods for modelling spectral radiation in an oxyfuel combustion environment. This aim was achieved using three approaches. Firstly, high resolution spectral measurements were used to validate the LBL and narrow band methods, which are often used in place of real values for the absorption coefficients of participating gas species. Secondly, the approximations of a scaled or correlated absorption coefficient in the narrow band models was challenged by comparing calculated results with LBL calculations of radiative transfer in a one-dimensional domain. Finally, global models were validated against the narrow band models in a three-dimensional enclosure, using implementations that are directly applicable to CFD calculations of oxyfuel combustion.

The LBL and narrow band calculations of total emissivity were shown to achieve good agreement across all 22 cases measured by Alberti et al. [256], with maximum errors of less than 10% when compared to the measured emissivity. While the LBL method introduces very few approximations regarding the underlying physical phenomena of radiative transfer, it must be recognised that this approach still induces some errors, and inaccuracies in more approximate models will propagate these errors further.

Comparisons of the narrow band models with LBL calculations under conditions relevant for oxyfuel combustion demonstrated good agreement between the spectral models. While the narrow band models showed similar disagreement towards the LBL calculations and the measurements for total emissivity, less than 7% error, the calculations of the radiation energy source term showed much better agreement, with less than 2% error across the cases studied, with the exception of the locations with a hot gas juxtaposed to a significantly cooler wall. These results indicate that for problems of practical interest, the narrow band models agree very closely with the LBL results and can be used as benchmark data for oxyfuel combustion cases.

The global methods were implemented in ANSYS Fluent v15, a commercial CFD software code, and were validated against the narrow band models that were previously validated for one-dimensional cases. It was found that the grey WSGG method, which is widely used in CFD calculations, is inaccurate for both the radiation source term and heat flux, failing to capture large gradients in the source term and significantly over-predicting the heat flux. It was also found that discontinuous WSGG parameters induce significant errors in the resulting predicted radiation fields when thermodynamic properties crossed the defined boundaries. The non-grey WSGG model showed significantly better agreement with the benchmark data, however the method is not directly applicable to media containing variable species distributions. While it was shown that taking a global species distribution for calculating the radiative parameters achieved reasonable agreement for the radiation source term, the prediction of radiative heat flux reduced in accuracy.

The SLW, SLW-1, FSSK and FSCK models were also validated against the narrow band benchmark data. The SLW-1 method demonstrated significant inaccuracies for the variable species case, and the SLW method required a significant number of grey gasses to achieve a solution that was invariable to the introduction of further grey gasses. The results showed that the FSK models achieved the best agreement to the benchmark data. The FSCK model, using five quadrature points, is recommended as an accurate radiation model for oxyfuel conditions, as this method demonstrates the greatest agreement with the benchmark data, and has a similar computational cost as the non-grey WSGG methods.

6 Modelling of oxy-coal combustion systems

The work in this chapter applies the radiation models that were introduced in Chapter 3 and validated in Chapter 5 to CFD calculations of a coal-fired test facility. The facility that has been modelled is the 500 kW_{th} Pulverised Fuel Combustion Rig (KSVA) operated by the Institute of Combustion and Power Plant Technology at the University of Stuttgart. The cases that are modelled include one air-fired case and one oxy-coal case, with modelling results validated against experimental measurements of gas temperature, gas species composition and radiative heat flux to the furnace walls. As the furnace can be approximated as a two-dimensional axis-symmetric geometry, it is also possible to apply the narrow-band CK model that was used to validate the global models in Chapter 5. Applying the CK model allows for the approximations in the global radiation models applied in this study to be assessed separately from the assumptions introduced by other approximate sub-models, such as turbulence and combustion models, that were necessary to model the entire combustion process.

Section 6.1 introduces the cases to be modelled, including a description of the furnace. Studies into the influence of radiation models and particle radiation treatment on the KSVA facility are discussed in Section 6.2, and the conclusions from these studies are discussed in Section 6.3.

6.1 Case description

The KSVA is a 500 kW_{th} down fired single-burner combustion facility. The facility is equipped with pollutant control devices, such as a selective catalytic converter (SCR) and ESP, and a flue gas recycle line, thus allowing the furnace to be operated in an oxyfuel mode that would be typical for a utility power station operating with oxyfuel combustion for CCS [211, 444]. A process flow diagram of the KSVA facility is shown in Figure 6.1. The furnace is cylindrical in shape, and is approximately 7 m high with an internal diameter of 0.8 m. The furnace is equipped with numerous access ports to facilitate the measurement of wall heat fluxes and in-flame species concentrations

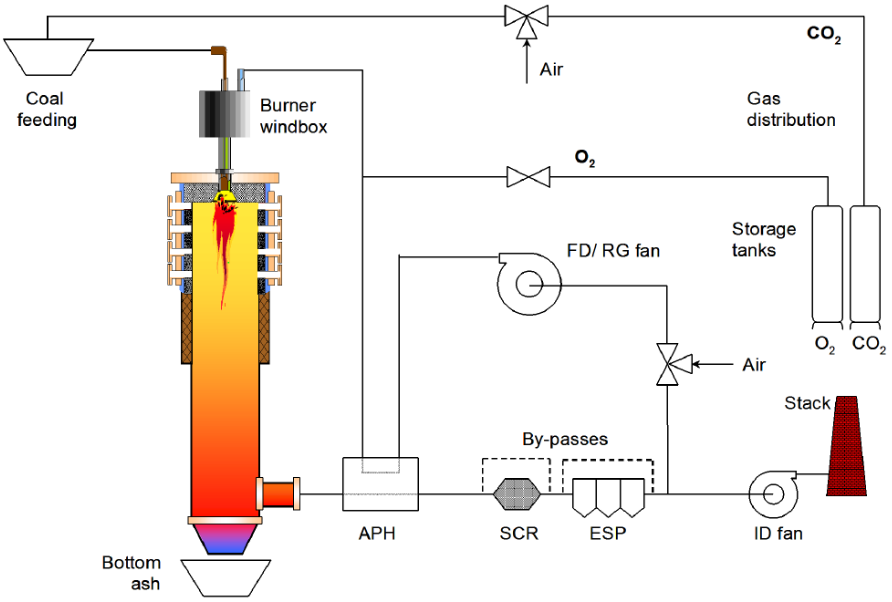

Figure 6.1: The KSVA test facility. Figure taken from Grathwohl et al. [444].

and gas temperatures. The top 4 m of the furnace is lined with a refractory material that is 0.12 m thick and has a low thermal conductivity of 2.4 W/mK, so that the gas temperature and residence times are comparable to a full-scale boiler. The outside of the refractory wall is water-cooled to control the refractory temperature. Storage tanks are used for the O_2 supply when the facility is running in oxyfuel mode. Additionally, CO_2 storage tanks are used during oxyfuel firing to transport the coal into the combustion chamber.

Two cases have been calculated in this study; a baseline air-fired case and an oxy-coal case, which are reported in detail by Grathwohl et al. [444]. The two cases were operated at the same thermal input and with the same South African coal. The calorific, proximate and ultimate analyses of the coal are shown in Table 6.1, and the particle size distribution is shown in Figure 6.2. A Rosin-Rammler distribution was used to model the range of particle sizes, which defines the mass fraction of particles with a diameter greater than diameter d as

$$Y_d = \exp\left[-\left(\frac{d}{\bar{d}}\right)^n\right] \tag{6.1}$$

where Y_d is the mass fraction of particles with a diameter greater than d, $\bar{d}$ is the mean particle diameter and n is the spread parameter. The particle size distribution provided by Grathwohl et al. [444] is defined based on the volume fraction of particles, however

Calorific Value (kJ/kg, ar[a]):	
Net	24,316
Gross	25,444
Proximate Analysis (weight%, ar[a]):	
Moisture	8.94
Volatile Matter	25.20
Fixed Carbon	52.56
Ash	13.30
Ultimate Analysis (weight%, dab[b]):	
C	80.76
H	5.47
O	11.13
N	2.11
S	0.53

[a] As received.
[b] Dry, ash-free basis.

Table 6.1: Coal properties from the KSVA experiments. Coal analysis from Grathwohl et al. [444].

in the model each particle is assumed to have the same density, so Equation (6.1) is used without modification. The Rosin-Rammler distribution parameters were chosen by fitting Equation (6.1) to the measured distribution, which resulted in a mean diameter of 41 μm and a spread parameter of 1.2, which is also shown in Figure 6.2. The operating parameters of the two cases are outlined in Table 6.2. The oxyfuel case was operated with a total inlet oxygen concentration of 29.5% by volume so that the adiabatic flame temperature between the oxyfuel case and the air-fired case were the same.

The KSVA furnace was fitted with a burner that was based on a scaled IFRF aerodynamically air staged burner (AASB) design during the test campaigns. The dimensions of the burner and the quarl are shown in Figure 6.3. The burner consists of an inner primary annulus, which carries the pulverised coal particles into the furnace, and an outer secondary annulus that carries the majority of the oxidant for combustion. The core that is internal to the primary annulus consists of a perforated plate that is used to introduce a methane flame at start-up, but is not in use under steady conditions of solid fuel combustion. The secondary register is swirled using four fixed blades at a 45° angle to ensure a well-defined inlet boundary condition. Due to the fixed thermal load and stoichiometric ratio between the two cases, while the total O_2 concentration varied, the velocity of the secondary register in the oxyfuel case is significantly re-

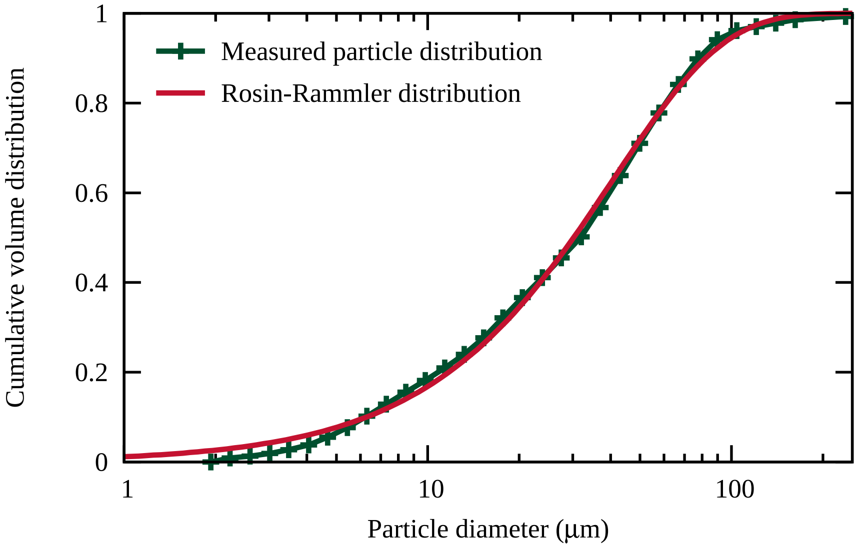

Figure 6.2: Coal particle size distribution compared with a fitted Rosin-Rammler distribution. Measured particle size distribution from Grathwohl et al. [444].

Operating parameters	**Air**	**Oxy**
Thermal input (kW)	305	305
Primary inlet gas	Air	CO_2
Primary gas mass flow (kg/h)	43	67
Primary velocity magnitude (m/s)	22.2	22.8
Fuel feed rate (kg/h)	41.5	41.5
Secondary gas mass flow (kg/h)	371	309
Secondary velocity magnitude (m/s)	55.0	37.0
Secondary gas composition (vol %, wet):		
O_2	20.84	36.04
N_2	77.71	5.8
CO_2	0.04	47.25
H_2O	0.49	10.91
Total O_2 (vol%, wet)	20.9	29.5
Recycle ratio (%)	–	76.9
Stoichiometric ratio	1.15	1.15

Table 6.2: Operating parameters for the KSVA experiments.

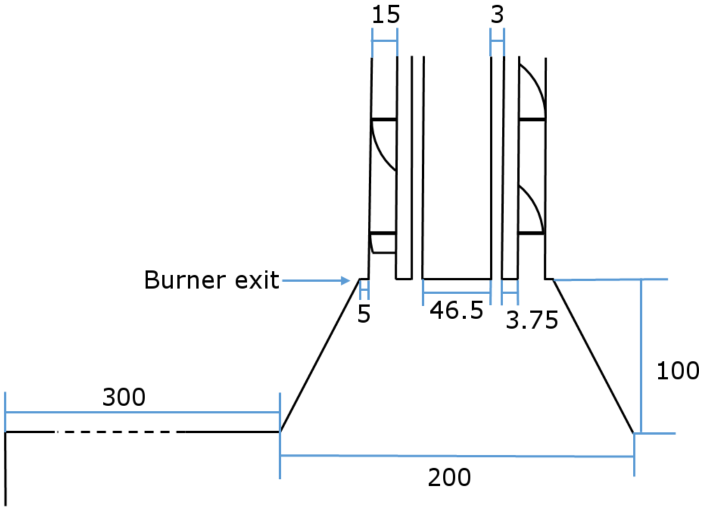

Figure 6.3: Schematic of the burner fitted to the KSVA facility. Measurements are given in mm. Locations within the furnace are given relative to the ‘Burner exit’ point in this figure.

duced from the air-fired case, which may have an impact on the burner aerodynamics.

6.2 Radiation models for oxy-coal combustion

The objective of this study is to validate global radiation models for CFD modelling of oxy-coal combustion. The work in this chapter will first define a baseline modelling approach, which will be tested for grid dependency and validated against experimental measurements. Following the definition of the baseline case, the results are then compared against different approaches for modelling gas and particle radiation.

6.2.1 Baseline model specifications

The KSVA furnace was modelled as a two-dimensional axis-symmetric cylinder using the commercial CFD code ANSYS Fluent v15. Only the first 4 m from the exit of the burner was modelled, as the refractory material changes past 4 m and this region contained all of the measurements made in the experimental campaign. The flows used to cool the diagnostic flame-scanning equipment were neglected in order to model the furnace as a two-dimensional geometry. The two flame scanners were positioned in the ceiling of the furnace, angled 30° towards the flame, and at port 5, 0.63 m from the exit of the burner. The cooling flow from the two flame scanners were each metered to the same value at 8.5 kg/h and 9 kg/h under air and oxyfuel conditions, respectively.

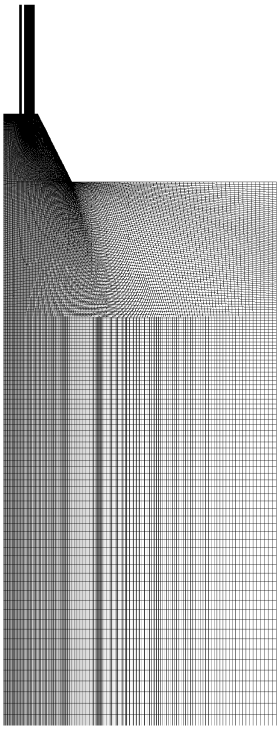

Figure 6.4: Computational mesh that was developed for the CFD calculations of the KSVA test facility.

The total mass flow from the two scanners accounted for less than 5% of the overall mass flow.

The computational mesh that was developed for the CFD calculations of the KSVA furnace, shown in Figure 6.4, contained 59,990 quadrilateral cells. The mesh was developed so that the y^+ value, a non-dimensional wall distance related to the thickness of the laminar boundary layer, is greater than 11 inside the furnace, so that the standard wall functions of Launder and Spalding [445] can be used. Scalable wall functions were selected so that in regions where the value of y^+ falls below a minimum value it is clamped, so that the wall functions do not deteriorate under grid refinement. Grid dependency was tested by calculating the results on a new mesh that was generated by reducing the lengths of the cells by a factor of 0.5, thus dividing each quadrilateral cell into four smaller cells, resulting in a total cell count of 239,960 cells. The mesh is refined so that there is a high density of cells inside the quarl to resolve the mixing between the two inlet registers and capture the combustion behaviour in the near-quarl region.

The baseline modelling approach is outlined in Table 6.3. A RANS model was used for predicting the turbulent flow, utilising the Launder et al. [446] Reynolds stress model. The constants in the Reynolds stress model were kept to the same values as those used by Launder et al. [446]. The Reynolds stress model has been chosen as this method has been shown to work reasonably well in similar combusting flows [351, 447]. The dispersed phase was modelled with Lagrangian tracking of discrete particles, using the discrete random walk model [359] to include the effect of turbulence on the particle motion. The two phases were coupled by introducing source terms into the appropriate equations for the continuous phase.

The ED combustion model [400] was applied for the gaseous combustion, with a two-step mechanism for volatile combustion. The volatile gasses were modelled as an empirical species based on the ultimate analysis of the fuel, assuming a molecular weight of 30 g/mol. The ratio between the volatile gas yield at high temperatures and the measured value in the proximate analysis was also taken to be the same as the value measured by Backreedy et al. [448] for a similar South African coal, which were based on drop-tube furnace measurements. This high temperature volatile yield resulted in a total yield of 26.8% by weight of the 'as received' coal particle, with the increased yield is offset by a reduced fixed carbon content. The resulting two-step mechanism that was used to model the gas-phase combustion reactions is given as

$$\mathrm{C_{1.10}H_{4.72}O_{0.61}N_{0.13}S_{0.01} + 1.44O_2 \longrightarrow} \tag{R 6.1}$$

$$\mathrm{1.10CO + 2.36H_2O + 0.065N_2 + 0.01SO_2}$$

$$\mathrm{CO + 0.5O_2 \longrightarrow CO_2} \tag{R 6.2}$$

The standard mixing parameters defined by Magnussen and Hjertager [400] were used in this study, where $A = 4$ and $B = 0.5$ for both reactions, and where A and B are the mixing parameters defined in Equation (3.114) in Subsection 3.3.3.

The single Arrhenius rate devolatilisation model and apparent char kinetics were used to model the coal conversion. The same devolatilisation rate that was used by Backreedy et al. [448] for a similar South African coal was used in this study, which was based on FG-DVC [366] calculations at a high heating rate of 10^5 K/s. The particle swelling coefficient, the ratio between the raw and devolatilised coal particle diameter, was set to 1.1 [208].

The char combustion kinetics were modelled using an n-th order Arrhenius expression based on apparent kinetics from the study by Karlström et al. [379], that measured the combustion rate for a similar South African coal char in a drop-tube furnace under

	Model	**Details**
Turbulence	Reynolds stress model	Model constants from [446]
Coal particles	Lagrangian tracking	$N_{diameters} = 30$
Particle dispersion	Discrete random walk	$N_{tries} = 10$
Spectral radiation	FSCK	$N_q = 5$
Particle Q_{abs}	Mie theory	
Particle Q_{sca}	Mie theory	
RTE solver	Finite volume method	3×3 angle
Combustion model	Eddy-dissipation	
Devolatilisation	Single kinetic rate [448]	$A = 4.68 \times 10^{11}$ s^{-1} $E_a = 155.9$ kJ/mol
Char combustion	Apparent kinetics [379]	$A = 1.9 \times 10^{-4}$ kg/(m^{2}sPa^n) $E_a = 70$ kJ/mol $n = 1.08$ $\alpha = 0.25$

Table 6.3: Models employed for calculating the baseline case for the KSVA facility.

air-fired combustion conditions. The rate of char consumption is calculated as

$$\frac{\mathrm{d}m_c}{\mathrm{d}t} = k_i A_{\mathrm{P}} p^n_{\mathrm{O}_2,s} \tag{6.2}$$

where $k_i = A\exp(-E_a/RT)$ is the kinetic rate of combustion in Arrhenius form, m_c is the mass of char, t denotes time, A_{P} is the external surface area of the particle ($A_{\mathrm{P}} = \pi d_{\mathrm{P}}^2$ with particle diameter d_{P}), $p_{\mathrm{O}_2,s}$ is the partial pressure of O_2 at the particle surface and n is the apparent reaction order. The values for A, E_a and n are parameters that are taken from the study by Karlström et al. [379]. The partial pressure at the particle surface is eliminated, and the overall rate of char combustion is calculated as [379]

$$\frac{\mathrm{d}m_c}{\mathrm{d}t} = k_i A_{\mathrm{P}} \left(p_{\mathrm{O}_2,\infty} - \frac{\mathrm{d}m_c}{\mathrm{d}t} \frac{1}{A_{\mathrm{P}} R_{d,i}} \right)^n \tag{6.3}$$

where $R_{d,i}$ is the diffusion limited rate, which is calculated using the expression in Equation (3.102). Equation (6.3) is solved using Brent's method [394]. The bulk diffusion of O_2 to the particle surface, used in evaluating $R_{d,i}$, is calculated using the binary diffusion coefficients calculated by ANSYS Fluent that are based on kinetic theory, in order to account for the difference in diffusion between air- and oxy-coal combustion environments. The size of the char particle during combustion is modelled with a burning mode $\alpha = 0.25$, as in the study by Karlström et al. [379].

The recommended radiation property model from Chapter 5, the FSCK model with a five-point Gaussian quadrature, was applied in the baseline case due to its computational efficiency and accuracy in the validation cases. The FSCK model is implemented so that full-spectrum mixture k-g distributions are assembled from the single-specie narrow band k-g distributions tabulated by Cai and Modest [441], using the mixing scheme by Modest and Riazzi [282]. In order to improve computational efficiency, the full-spectrum k-g distributions are tabulated for a range of temperatures and gas concentrations that span the computational domain, and the local k-g distributions are calculated using linear interpolation. As with the study in Chapter 5, the tabulation is implemented with a constant step size of 100 K in temperature and a value of 0.1 in gas specie mole fraction. The reference state in the FSCK model was calculated as a volume averaged species composition and using a reference temperature T_0 that satisfies the implicit relation [284]

$$\kappa_{\text{PL}}(\underline{\phi}_0)T_0^4 = \frac{1}{V}\int_V \kappa_{\text{PL}}(\underline{\phi})T^4 \,\mathrm{d}V \tag{6.4}$$

where $\kappa_{\text{PL}}(\underline{\phi})$ is the Planck averaged absorption coefficient at the thermodynamic state $\underline{\phi}$, V denotes volume and $\underline{\phi}_0$ is the reference state, which is composed of the volume averaged gas species composition, the reference temperature and the pressure at 1 atm. The tabulated k-g distributions were recalculated regularly, every 2000 iterations, to ensure that the reference condition was representative of the solution.

The particle radiation properties were calculated from the Mie theory, using the method of Bohren and Huffman [333]. The optical constants that were used for coal particles were taken from the measured values by Manickavasagam and Mengüç [337] for a constant real index of $n = 1.8$ for the Kentucky No. 9 coal. The measured optical constants by Goodwin and Mitchner [322] were used for fly ash particles, using the tabulation from Liu and Swithenbank [347]. Planck averaged Mie theory values were tabulated in a pre-processing step for a range of temperature and particle sizes, and were linearly interpolated at run-time. The optical properties for burning char particles were calculated as a linear interpolation between the optical properties of char and ash particles based on the fractional burnoff of the particle. A zero-order delta-Eddington scattering phase function was used, where the scattering efficiency of the particle, Q_{sca}, was modified by the asymmetry factor to remove forward scattering directions, $Q^*_{sca} = Q_{sca}(1 - g)$, where g is the asymmetry factor [245]. Efficiency values for the mean particle diameter, 41 μm, for the absorption efficiency, Q_{abs}, and the modified scattering efficiency are shown in Figure 6.5.

One of the main deficiencies in the modelling approach outlined in this subsection

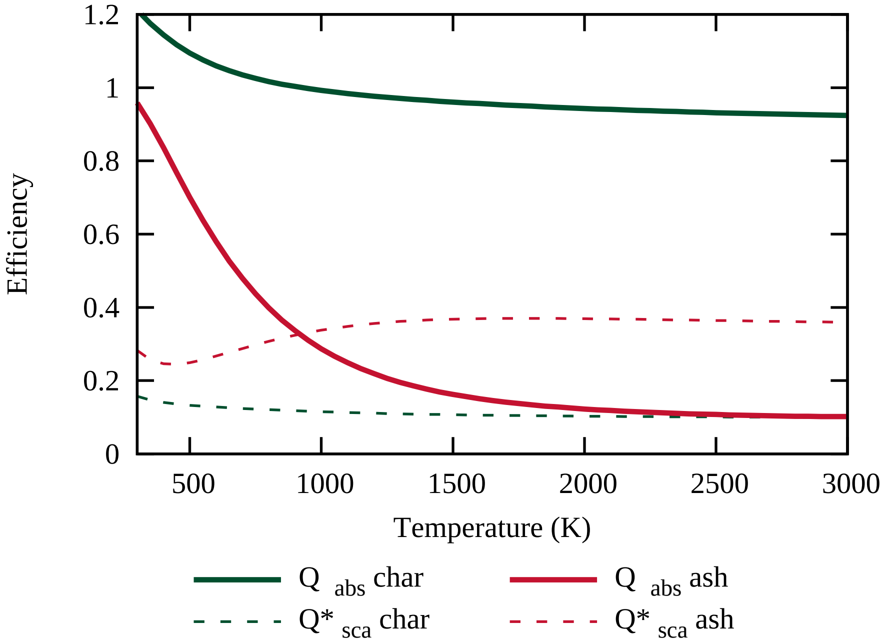

Figure 6.5: Particle scattering and absorption efficiency for the particle size with the mean diameter as a function of particle temperature.

is that the effect of the oxyfuel environment on the coal conversion and combustion processes is largely neglected. Devolatilisation kinetics and the devolatilisation yield is constant between the two combustion environments, and neither CO_2 or H_2O gasification is considered. Furthermore, a simple two-step volatile combustion mechanism is used, neglecting the potential equilibrium balance in CO_2 dissociation. As the focus of this thesis is on radiation models, only standard modelling approaches have been considered for other phenomena, however it is acknowledged that the simplifications in these models could lead to significant errors in the resulting predictions.

Two thermal boundary conditions were applied in the modelling work. The vertical section of the furnace wall was modelled with an outside temperature of 350 K and a thermal thickness based on the conductivity of the wall. The surfaces inside the burner and the ceiling of the furnace, which make the remainder of the other walled surfaces of the case, were modelled as adiabatic walls, where it was assumed that no heat was lost through these surfaces at steady conditions. The furnace walls, namely the vertical wall, the ceiling and the quarl, were modelled with an internal emissivity of 0.8, which has been used in other studies on similar furnace refractory materials [216], while the internal burner surfaces were modelled with an emissivity of 1.

The primary and secondary gas inlets were both specified as constant velocity profiles across the surfaces, however the domain was extended so that a fully developed velocity profile was produced before the primary and secondary gasses were introduced into the combustion furnace. The swirl in the secondary gas register was modelled by imposing an initial constant swirl velocity to represent a 45° swirl angle. An outflow boundary condition, which assumes a zero diffusive flux at the exit of the domain, was used to model the boundary at 4 m from the burner. Both the inlets and outlets are treated as blackbody surfaces at the boundary temperatures for the radiation boundary conditions.

6.2.2 Baseline results

Three cases were run with the baseline case approach; the ‘baseline’ case as outlined above, the ‘refined space’ case, which is calculated on the finer 239,960 cell mesh, and the ‘refined angle’ case, which is calculated on the original mesh but with a 4×4 angular discretisation in the FVM RTE solver. Results are presented for the air-fired and oxyfuel cases, comparing against in-flame temperature and species profiles and surface radiative heat flux. The results for the air-fired case are presented in Figures 6.6 to 6.8, and the oxyfuel case results are presented in Figures 6.9 to 6.11 for the baseline modelling approach.

Comparisons of the CFD results for air-fired combustion against in-flame temperature and O_2 concentration are shown in Figure 6.6(a) and 6.6(b), respectively. In both plots it is shown that refining the mesh or the angular discretisation has only a minor impact on the results. The results show that the for the z=0.33 m to z=0.99 m lines, the combustion rate is being significantly under-predicted, as the gas temperature is far lower than the measured value while the O_2 concentration is being over-predicted in the central region.

It is unlikely that the homogeneous combustion model is under-predicting the rate of combustion, as the ED model neglects any kinetic limitations of the combustion mechanism. Additionally, the devolatilisation process has largely finished by this region, with the ignition of the flame falling behind the first measurement line. It is most likely that the char combustion process is being inadequately modelled. This could be due to many reasons, such as the aerodynamics incorrectly tracking the particles, resulting in a shorter residence times, the char conversion model incorrectly predicting the correct rate of combustion, or that the particle radiative properties are not accurately affecting the particle temperature. Only the latter of these is tested in this chapter, however it is likely that a combination of these factors, and more besides, could be contributing to

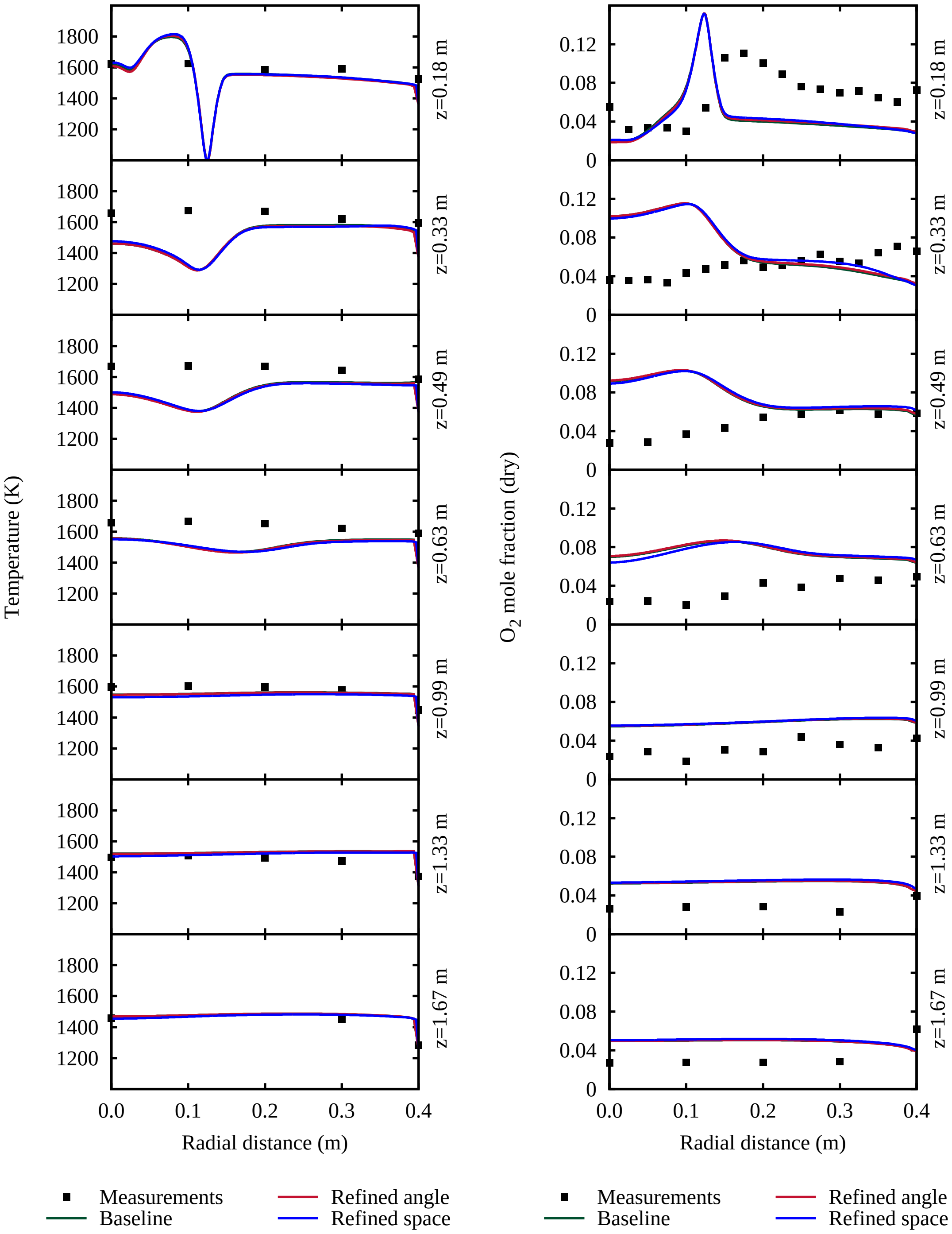

(a) Temperature

(b) O_2 concentration

Figure 6.6: Baseline CFD calculations against in-flame measurements in the air-fired case for (a) temperature and (b) O_2 concentration.

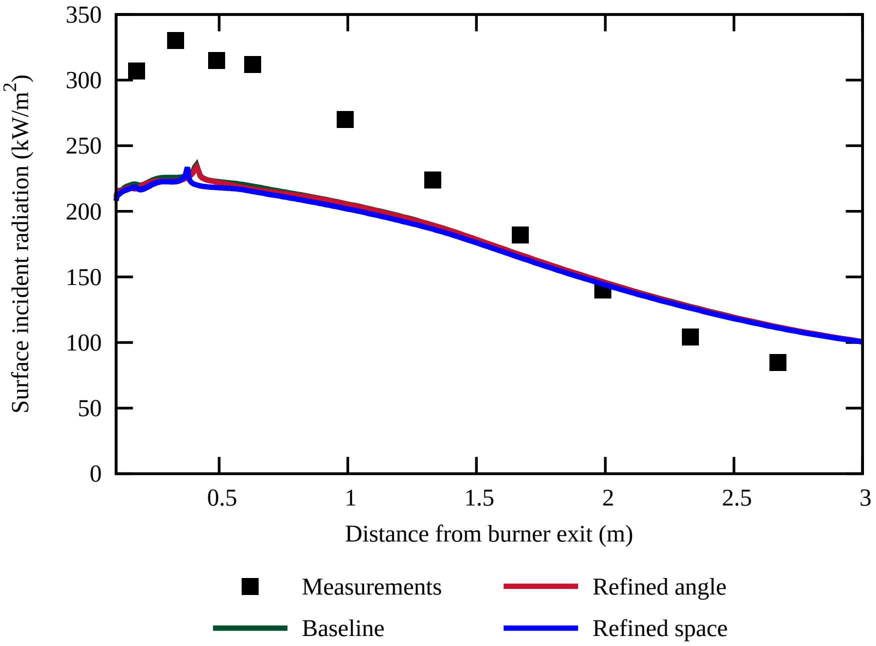

Figure 6.7: Baseline results for radiative heat flux in air.

these results.

The results for the radiative heat flux to the furnace wall is shown in Figure 6.7. As with the in-flame predictions, there is no significant deviation between the baseline, refined space, or refined angle calculations. The greatest disagreement between the measured values and the predictions from CFD calculations occurs in the top 1 m of the furnace, which corresponds to the region where the combustion rate is being under-predicted. Further downstream, the radiative heat flux starts to become over-predicted, presumably due to the combustion process being deferred to the later stages in the furnace.

The results in the radiative heat flux also demonstrate a sharp spike near to the location 0.5 m from the burner exit, which does not change under grid refinement. This spike corresponds to a region where the particle tracking model predicts an accumulation of particles undergoing char combustion. This region is noticeable in the O_2 distribution shown in Figure 6.8(b) between the second and third measuring line and against the furnace wall. The level of turbulent kinetic energy is small in this region, so the discrete random walk model does not predict any sizeable perturbations from the continuous velocity in this region. Furthermore, the axial velocity, shown in Figure 6.8(c), is essentially zero, which causes long residence times. The discrete random walk model is known to perform poorly in wall bounded flows [357], and models that

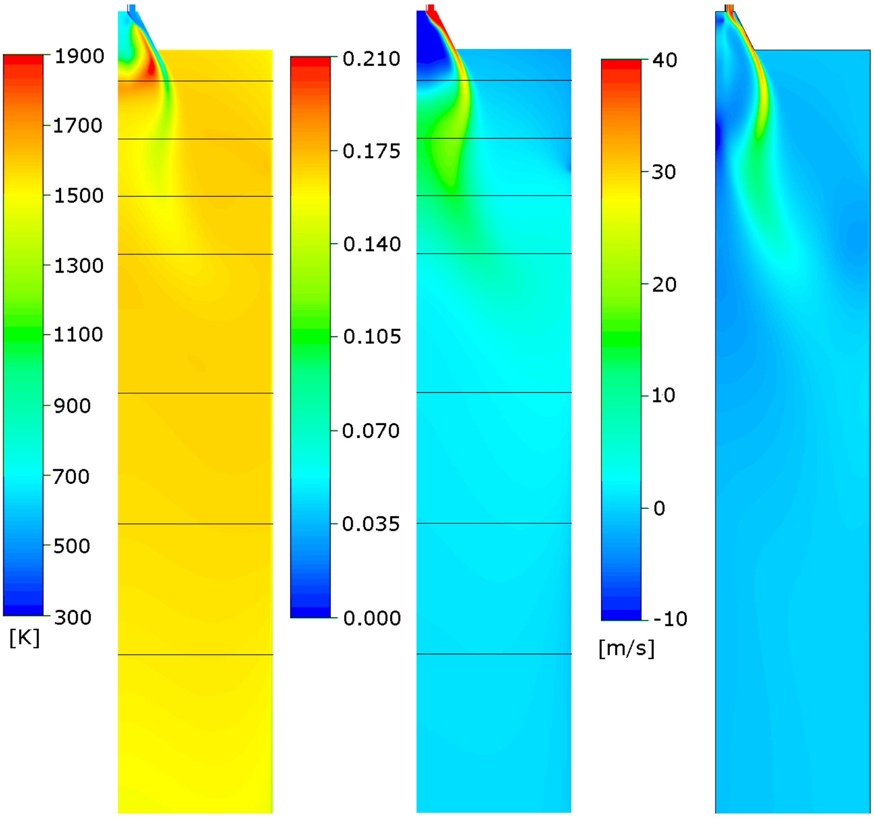

(a) Temperature (b) O_2 mole fraction (dry) (c) Axial velocity

Figure 6.8: Distributions of baseline CFD calculations in air for (a) temperature, (b) O_2 distribution and (c) axial velocity. Lines indicate the position of the measurement ports.

account for the boundary layer may improve these predictions [449]. This sharp spike in the radiative heat flux is an artefact of the particle tracking method; however, even with this somewhat artificial influence, the results are still significantly lower than the measured values for the surface incident radiation.

Comparisons between CFD predictions and measured gas temperatures and O_2 concentrations are shown in Figures 6.9(a) and 6.9(b), respectively. As with the air-fired case, the results with a refined angular discretisation and the case with the refined spatial mesh demonstrate the same results as the baseline case. Generally, the results for temperature and O_2 show a greater agreement between CFD and measurements than was found for the air-fired case, although the region that is closest to the burner is still not well predicted.

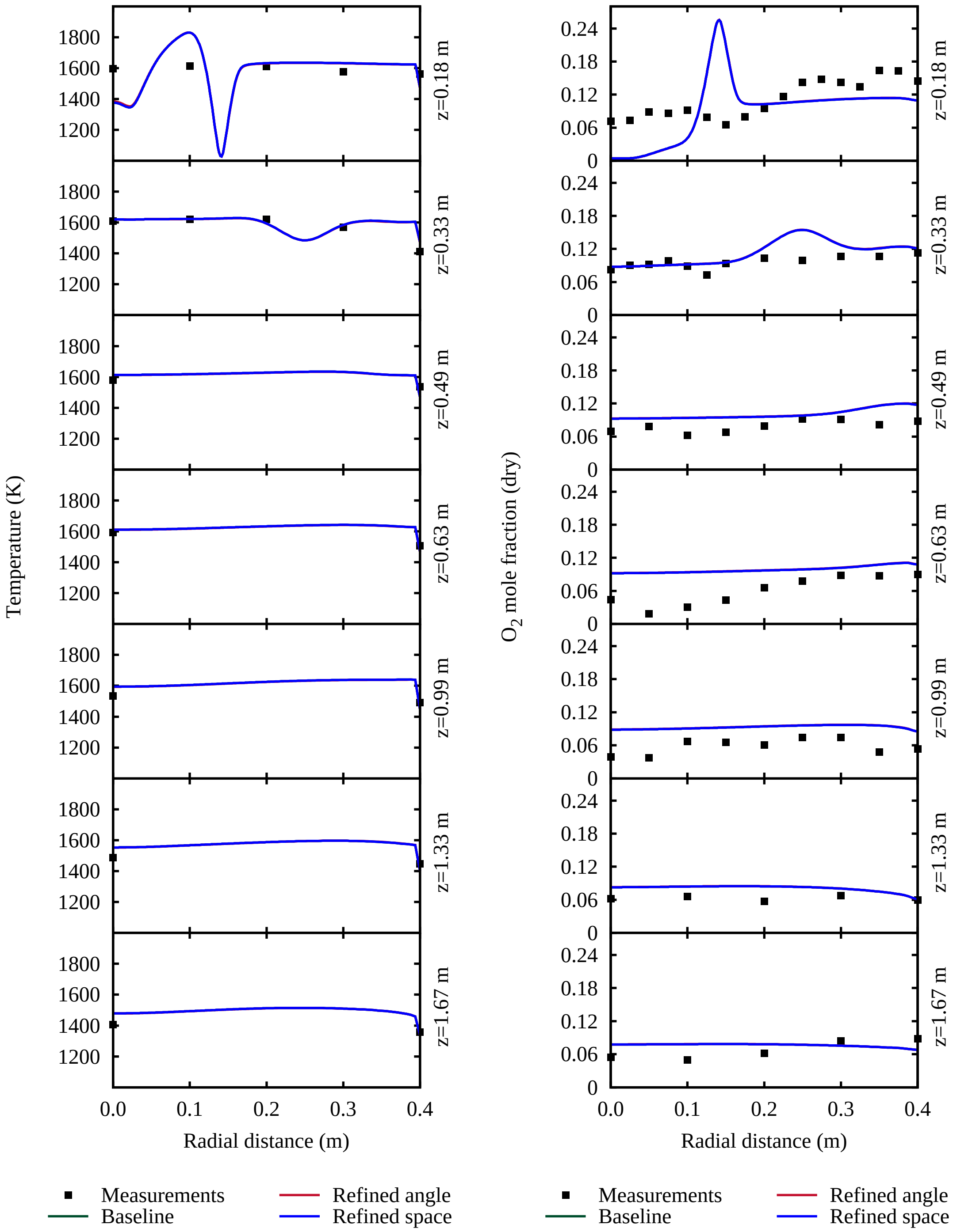

(a) Temperature

(b) O_2 concentration

Figure 6.9: Baseline CFD calculations against in-flame measurements in the oxyfuel case for (a) temperature and (b) O_2 concentration.

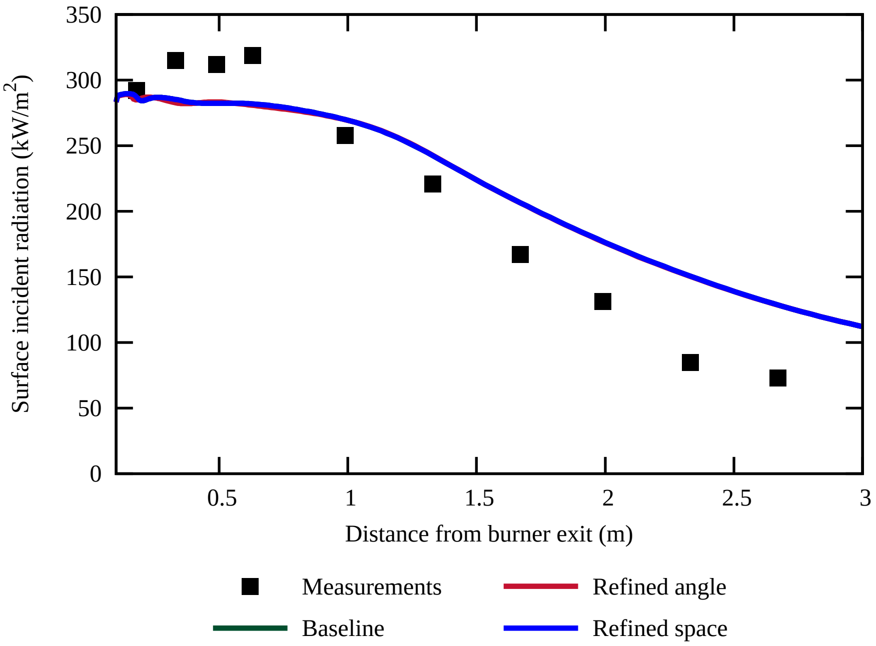

Figure 6.10: Baseline results for radiative heat flux in the oxyfuel case.

The radiative heat flux predictions against measured values in the oxyfuel case is shown in Figure 6.10. Again, the refined cases show little deviation from the baseline modelling approach. The radiative heat flux is captured better by the CFD calculations of the oxyfuel case, however the heat flux is still over-predicted in the downstream regions of the domain.

The distributions of temperature, O_2 concentration and axial velocity are shown in Figure 6.11 for the oxyfuel case. These results show that the flame shape is different to the air-fired case. This is due to the lower velocity in the secondary register, which causes a weaker recirculation zone in the centre of the domain, and causes the secondary stream to directly impinge on the furnace wall.

The results shown in this subsection provide a baseline calculation for further comparisons. The results demonstrate that the mesh containing 59,990 cells and a 3×3 angular discretisation is adequate for these calculations. The results also show some significant deviations from measured values. The narrow band calculations that are undertaken in Subsection 6.2.3 are important in separating the influence of other modelling assumptions, and allow for the assessment of radiation models in isolation.

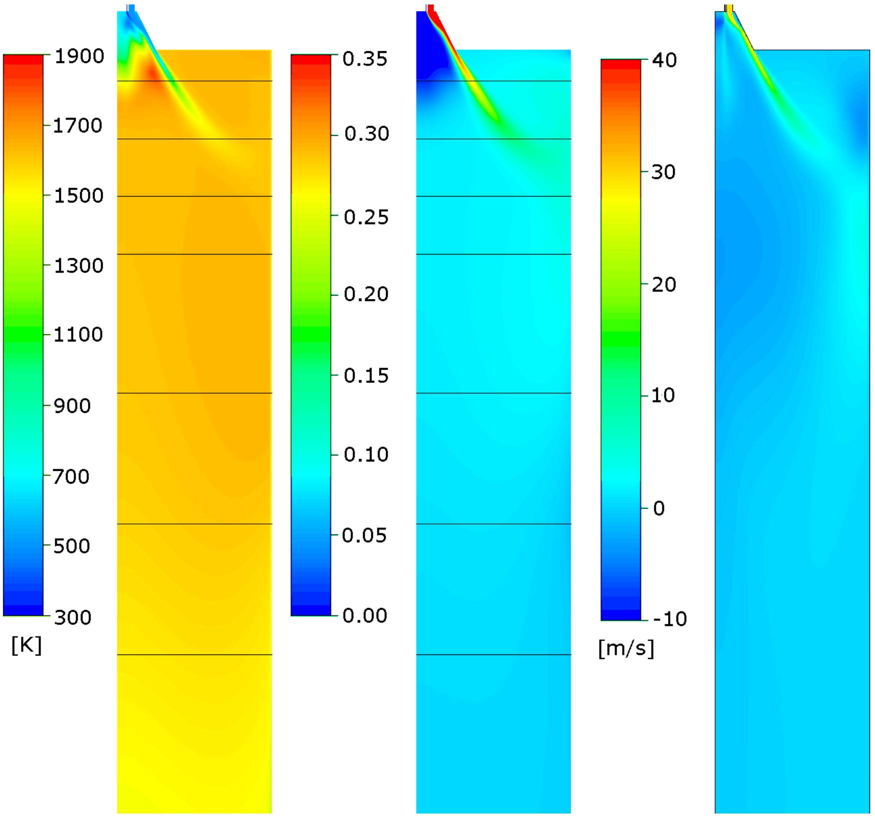

(a) Temperature (b) O_2 mole fraction (dry) (c) Axial velocity

Figure 6.11: Distributions of baseline CFD calculations in the oxyfuel case for (a) temperature, (b) O_2 distribution and (c) axial velocity. Lines indicate the position of the measurement ports.

6.2.3 Gas radiative property models

To analyse the sensitivity of the gas property model on the prediction of the radiative heat flux and in-flame gas temperatures and compositions, the CFD calculations of the KSVA facility are repeated with different gas property models. Furthermore, the narrow band CK method is also applied, which, due to its close agreement to the LBL calculations presented in Chapter 5, is expected to be highly accurate. The narrow band CK model serves as additional validation data so that the radiation models can be compared without the additional uncertainties introduced by other modelling assumptions of the combustion process. Due to the significantly increased computational requirements of the CK model, this method was only validated by solving the RTE with a fixed temperature and gas composition, which was taken from the baseline case results. The other gas property models were evaluated by undertaking fully coupled calculations.

The gas property models that are compared in this study include the grey WSGG method with the parameters by Smith et al. [220], which is the most widely applied method for modelling radiative properties of combustion gasses, the grey and non-grey WSGG method using the parameters of Kangwanpongpan et al. [292], the FSCK baseline case and the narrow band CK model, which was applied using the parameters by Rivière and Soufiani [263]. The non-grey WSGG method was implemented using the volume averaged gas composition to evaluate the local radiative properties. The results for in-flame temperature and O_2 predictions from applying the spectral models are shown in Figures 6.12 and 6.13 for the air-fired and oxyfuel cases, respectively.

The air-fired case and the oxyfuel case show a small sensitivity of in-flame properties towards the choice of radiation model, with gas temperatures at the final measurement port differing by around 50 K. As radiation is a long-distance thermal transport mechanism, this sensitivity is expected to increase for larger combustion systems. In the refractory lined KSVA facility, the hot walls and particles act as significant sources of radiative energy, and the treatment of the participating medium becomes less significant than would be the case under large-scale industrial combustion systems.

The radiative heat flux values, shown in Figures 6.14 and 6.15 for air and oxyfuel respectively, demonstrate some sensitivity to the choice of radiation model in the upstream region of the furnace. The results demonstrate that the grey WSGG methods predict a higher radiative heat flux to the wall, in a very similar fashion to what was found in the study in Chapter 5. Changing to a non-grey method, such as the non-grey WSGG or FSCK methods, lowers the prediction of radiative heat flux. The non-grey methods also show excellent agreement to the narrow band CK method, further sug-

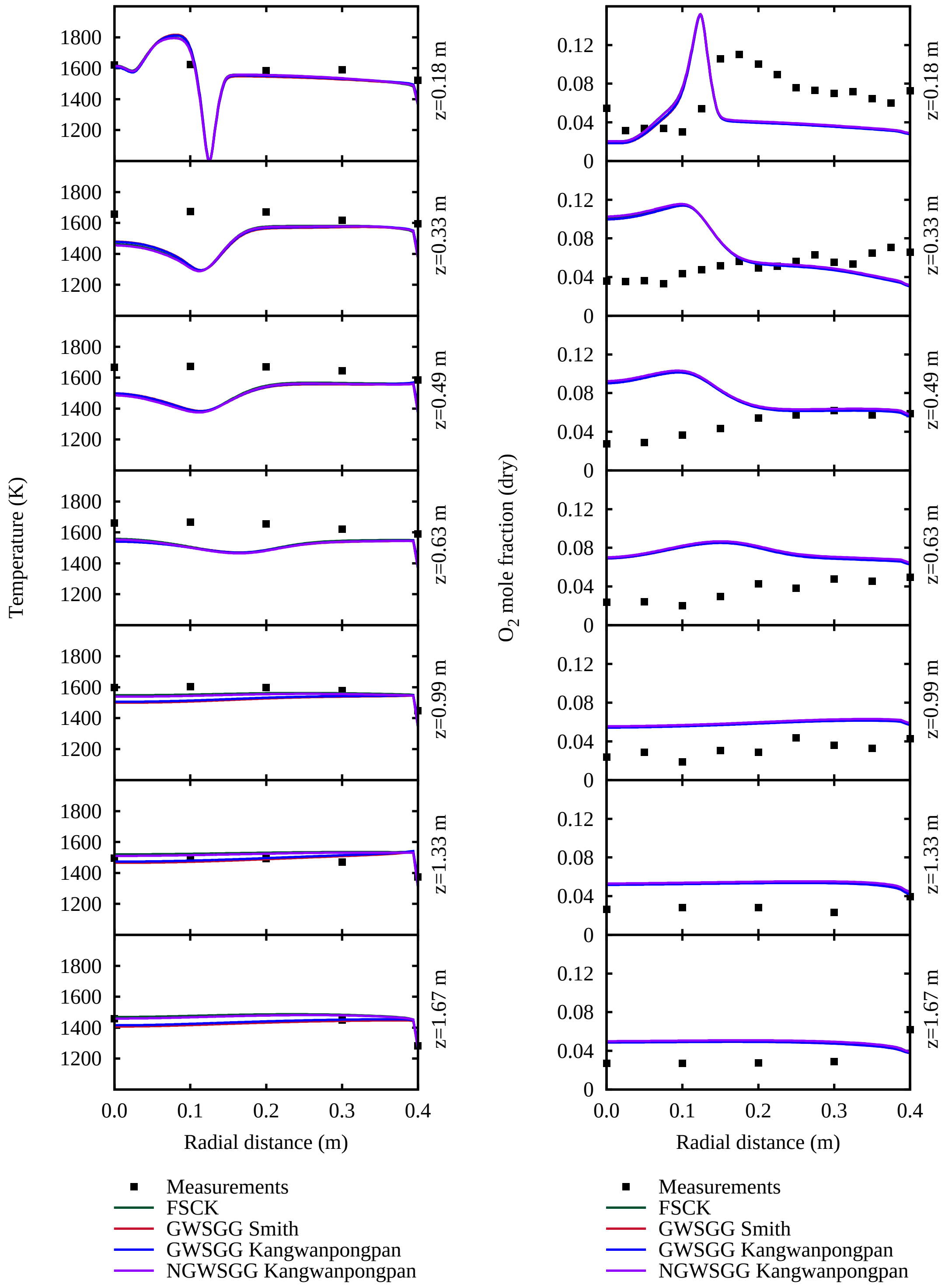

(a) Temperature

(b) O_2 concentration

Figure 6.12: Different radiation models against in-flame measurements in the air-fired case for (a) temperature and (b) O_2 concentration.

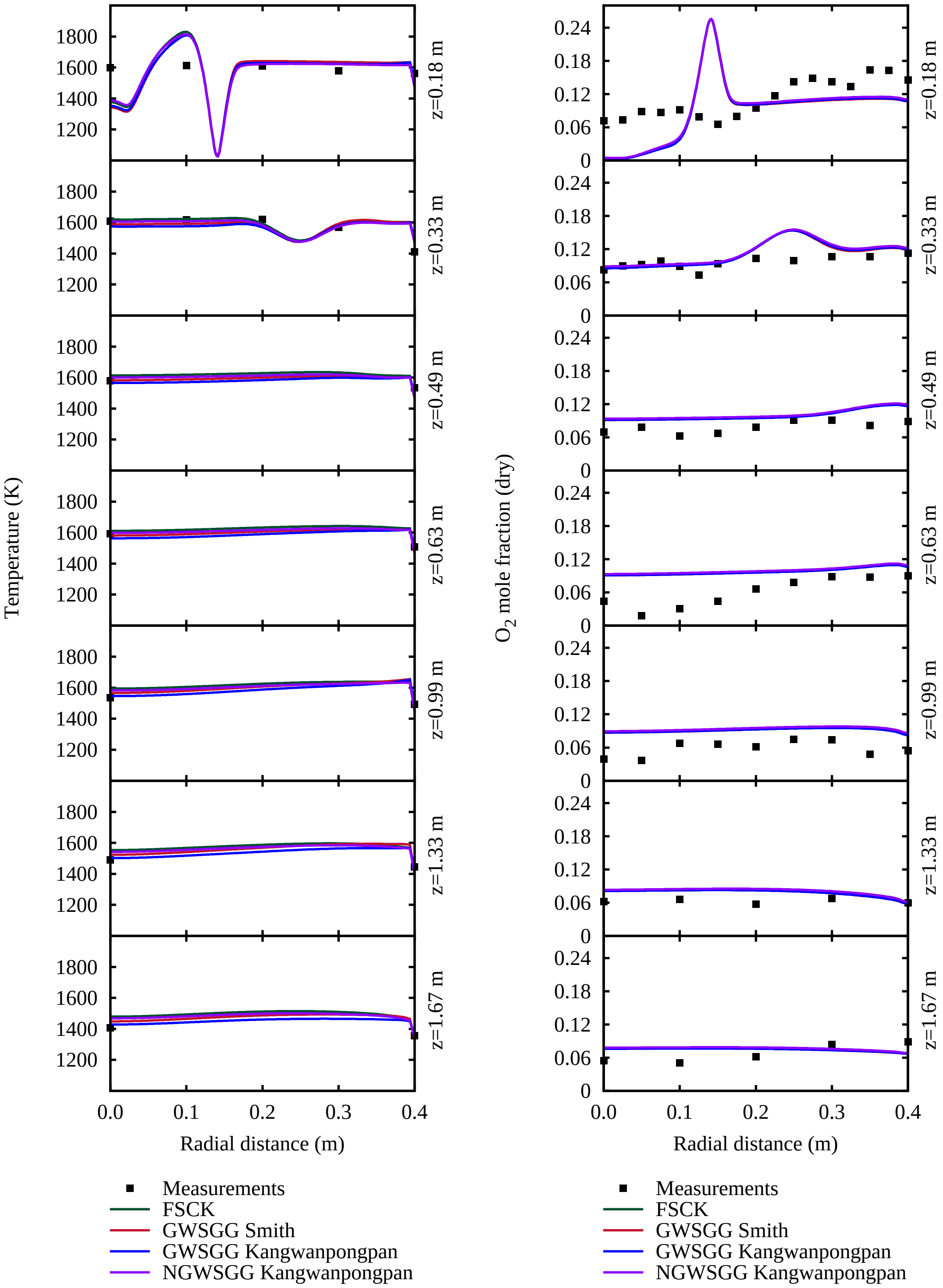

(a) Temperature

(b) O_2 concentration

Figure 6.13: Different radiation models against in-flame measurements in the oxyfuel case for (a) temperature and (b) O_2 concentration.

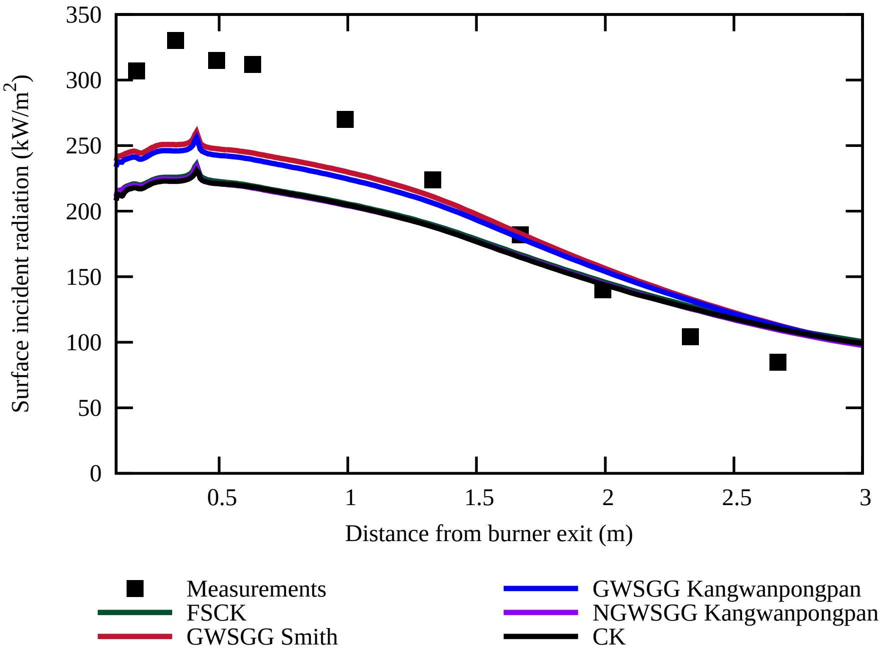

Figure 6.14: Radiative heat flux for the air-fired case with different radiation models.

gesting that these methods are accurate.

Under oxyfuel combustion, only the grey WSGG method using the parameters by Kangwanpongpan et al. [292] predicts a higher radiative flux to the wall, with the model by Smith et al. [220] showing similar predictions to the non-grey methods. However, as with the benchmark cases in Chapter 5, this is most likely to be a compensation of errors due to the model not accounting for the high levels of CO_2. Again, the non-grey WSGG method and the FSCK method show excellent agreement to the narrow band CK method in the oxyfuel case.

The study in this subsection applied a selection of gas radiative property models to the CFD calculations of the KSVA facility operating under air-fired and oxyfuel coal combustion. Both the air-fired and oxyfuel cases demonstrated the same relative behaviour when the radiation model was changed. The results demonstrated that the prediction of in-flame temperature had a small sensitivity to the choice of radiation property model. The prediction of heat flux was over-predicted in the grey radiation models, which caused extra heat to be lost through the boundaries of the domain, and lowered the gas temperatures. The results of the non-grey radiation models, namely the FSCK and non-grey WSGG method, showed excellent agreement to a narrow band radiation model, and are recommended for CFD calculations of coal combustion environments.

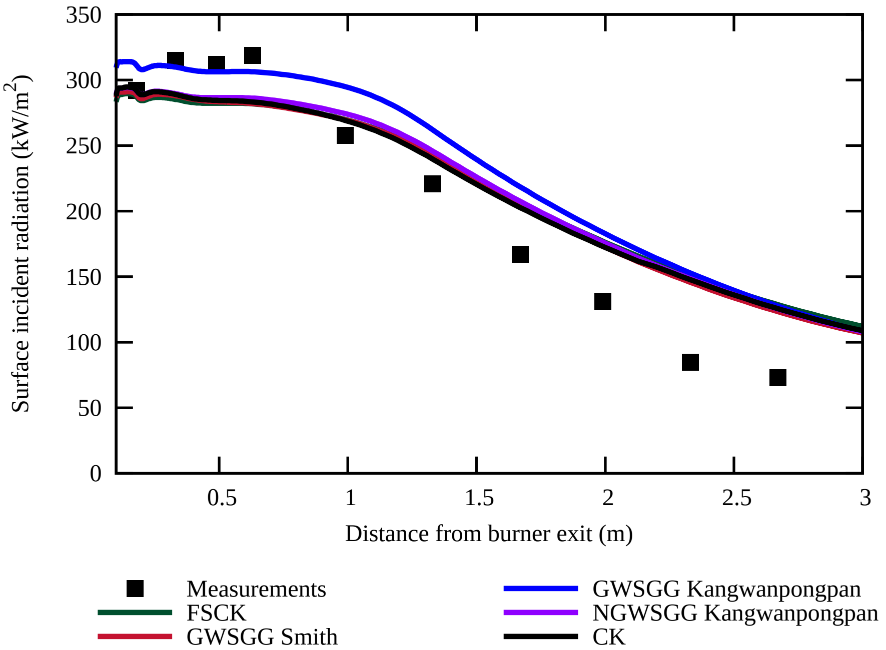

Figure 6.15: Radiative heat flux for the oxyfuel case with different radiation models.

6.2.4 Particle radiation treatment

The particles in the medium participate significantly in radiation. Planck averaged values from Mie theory calculations have been used in the baseline case to describe the particle absorption and scattering efficiencies. The study in this subsection also investigates the impact of using more conventional methods to model the particle radiative properties, namely using a constant value. The constants that have been chosen have been $Q_{abs} = 0.9$ and $Q_{sca} = 0.01$, which correspond to the default values implemented in ANSYS Fluent.

One of the most strict constraints of using global radiation models is the requirement that all radiative quantities other than the absorption coefficient are treated as grey. This study will validate this assumption by using the CK method with non-grey particle radiative properties. The value of Q_{abs} and Q_{sca} were calculated for each of the spectral interval as an arithmetic average across each narrow band. As with the narrow band model calculations introduced in the last subsection, these calculations are done in an uncoupled fashion, where heat transfer to the particle is still calculated with grey particle values, and only the radiative source terms to the medium are non-grey.

The non-grey particle radiative properties for the particle with the mean diameter,

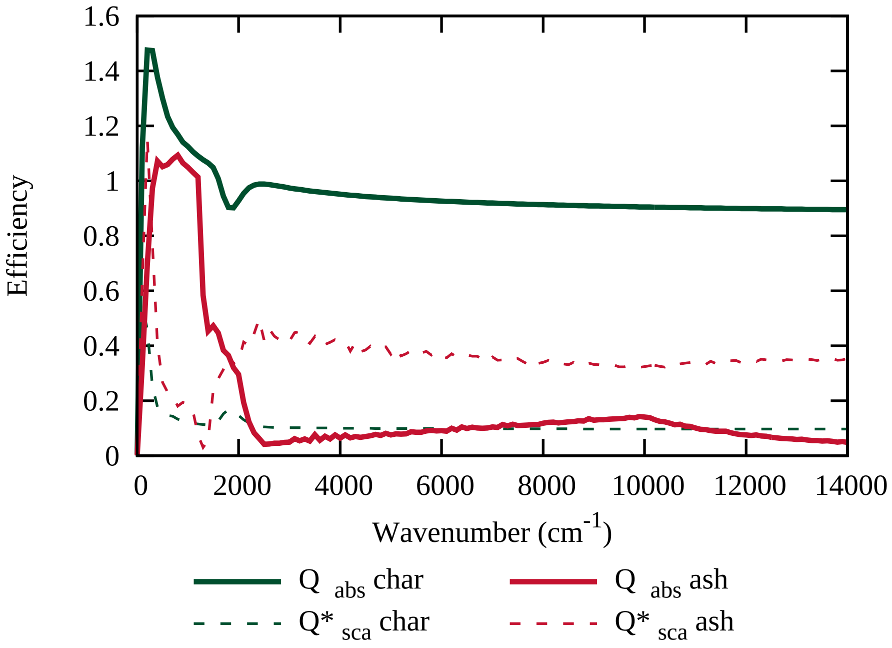

Figure 6.16: Non-grey particle scattering and absorption efficiency for the particle size with the mean diameter as a function of wavenumber.

41µm, is shown in Figure 6.16. Both particle materials, coal and fly-ash, demonstrate a peak absorption efficiency in the wavenumber range between 0 cm^{-1} and 2000 cm^{-1}, which correspond to significant absorption bands for both CO_2 and H_2O [256]. While the absorption of the char particle is fairly constant for the remainder of the spectrum, the fly-ash particle changes from being opaque to practically transparent, which may cause inaccuracies when the properties are applied as spectrally averaged quantities.

The impact that particle radiative properties have on the in-flame predictions is shown in Figures 6.17 and 6.18. A greater sensitivity in the prediction of gas temperatures is shown over what was demonstrated by the choice over radiative property model, with in-flame temperature predictions changing by up to 70 K near the exit of the domain. There are no changes in the prediction of the O_2 concentration, which indicates that the radiative properties are not affecting the combustion of the particles, and only affect the rate that heat is lost from the system.

The influence that the particle radiative properties have over the radiative heat flux is shown in Figures 6.19 and 6.20 for the air-fired and oxyfuel cases, respectively. The results show a similar dependency on the particle radiative properties as there exists on the gas radiative properties. The higher surface incident radiation using constant

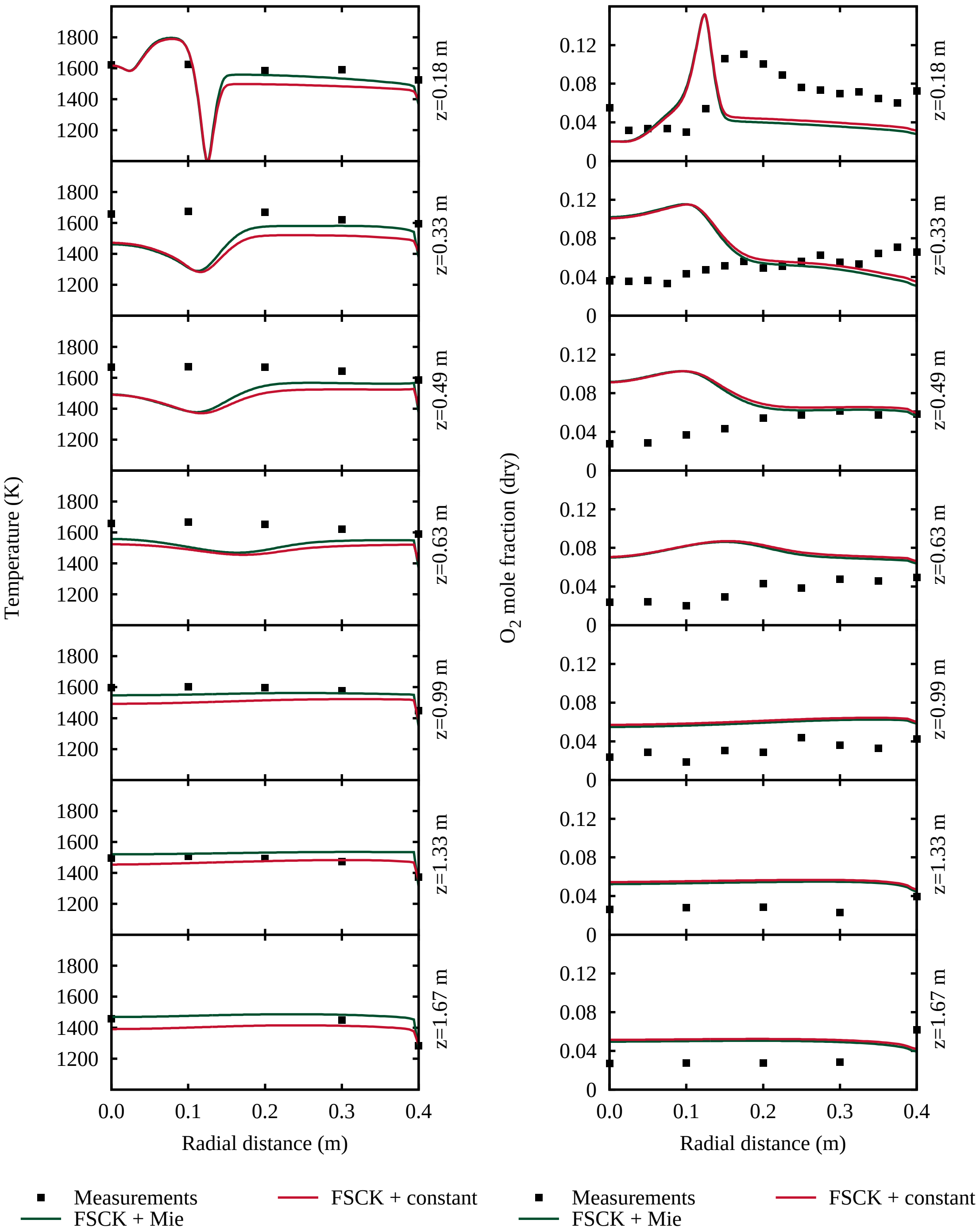

(a) Temperature

(b) O_2 concentration

Figure 6.17: Different treatment of particle radiative properties against in-flame measurements in the air-fired case for (a) temperature and (b) O_2 concentration.

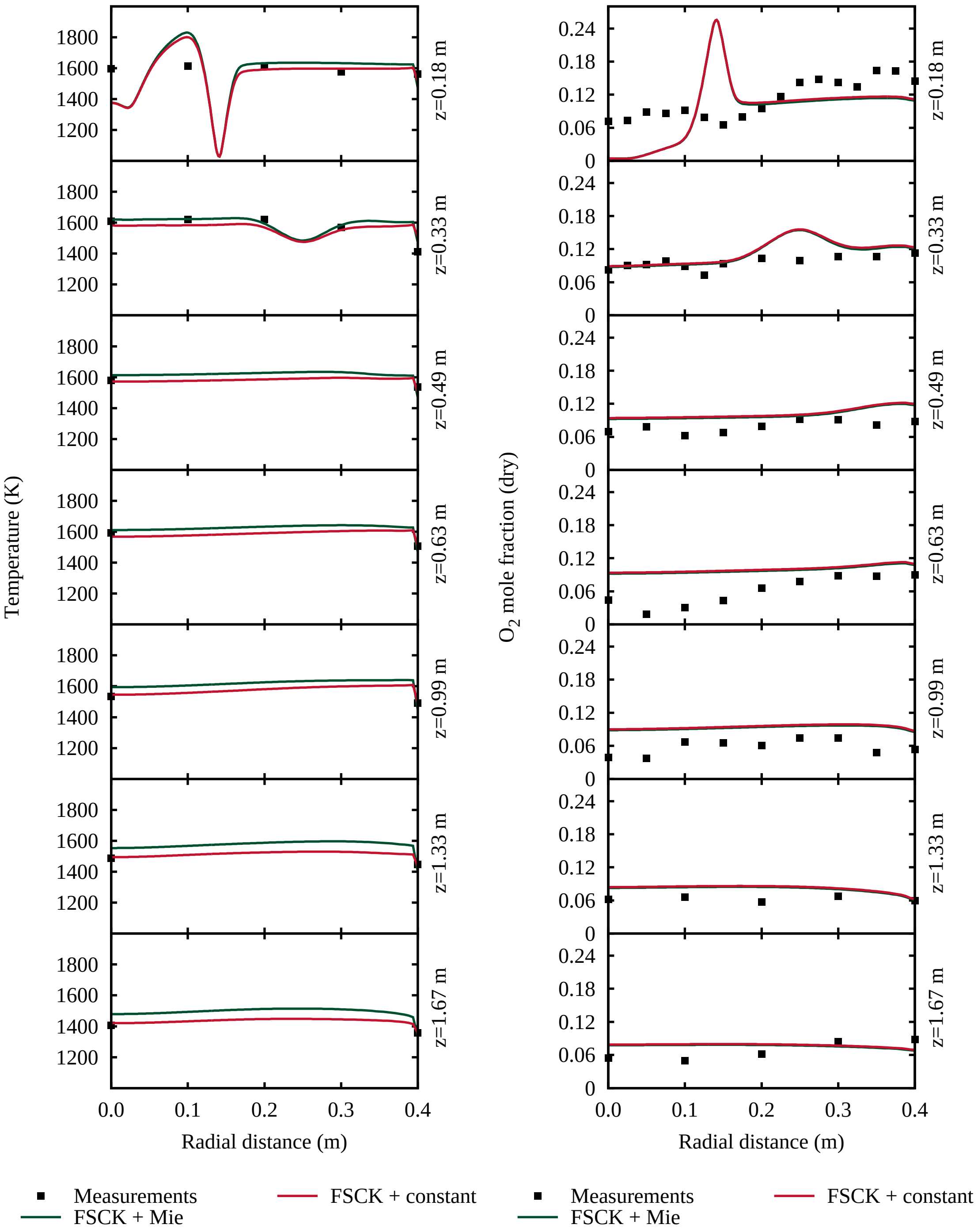

(a) Temperature

(b) O_2 concentration

Figure 6.18: Different treatment of particle radiative properties against in-flame measurements in the oxyfuel case for (a) temperature and (b) O_2 concentration.

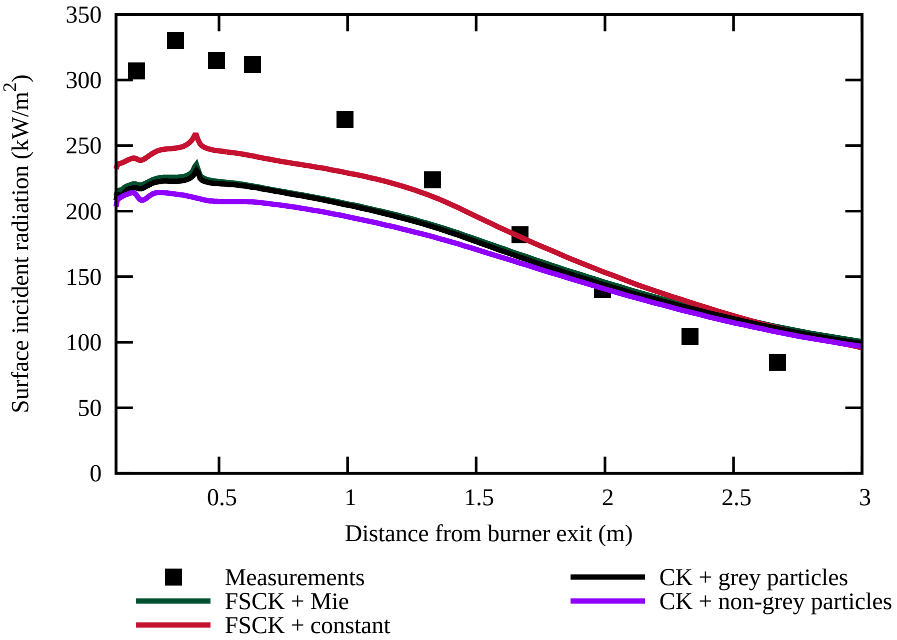

Figure 6.19: Radiative heat flux for different particle radiative properties in the air-fired case.

particle radiative properties causes more heat loss from the domain, and results in the lower gas temperature predictions. The influence of non-grey particle properties demonstrated only a small impact on the overall results, which was most significant under air-fired conditions.

6.3 Summary & conclusions

The study in this chapter applied the radiation models developed and validated in Chapter 5 to CFD calculations of the KSVA combustion test facility operating in air and oxyfuel combustion modes. The results showed some departure from the measured values for in-flame temperature and species composition, particularly for air-fired combustion, however this was due to inaccuracies incurred through modelling assumptions in the combustion process and flow calculations. Comparisons of the non-grey radiation models against the narrow band CK method showed very good agreement, and the non-grey radiation models, namely the FSCK model with a five-point Gaussian quadrature and non-grey WSGG model, are recommended for modelling radiation in combustion environments.

The radiative properties for the particulate phase are also important in the accurate

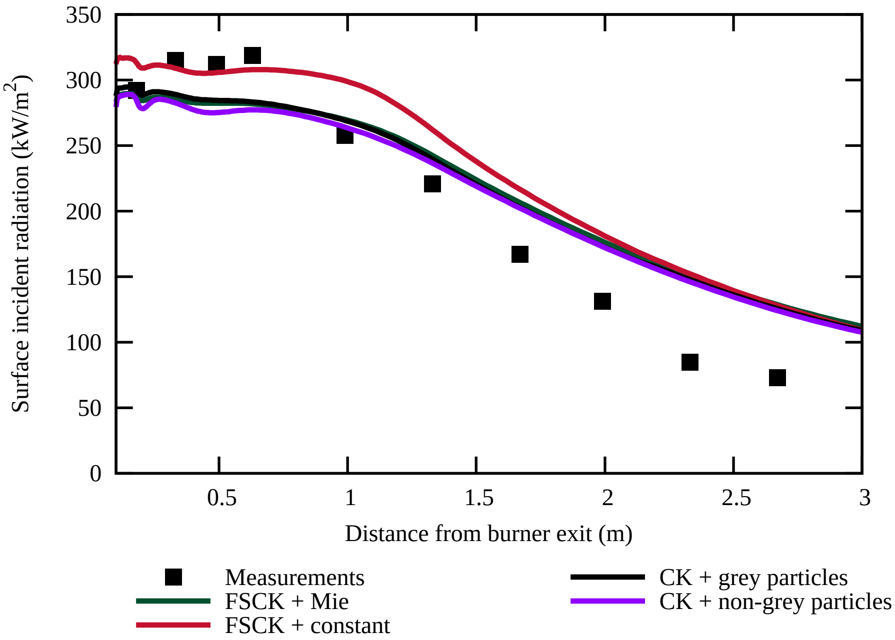

Figure 6.20: Radiative heat flux for different particle radiative properties in the oxyfuel case.

prediction of heat fluxes and gas temperatures. This study used three approaches for the particle properties; firstly, the Planck function weighted average values from Mie theory calculations, constant values and spectrally variable Mie theory values. It was found that non-grey particle radiative properties had little impact on the narrow band calculations. However these calculations were undertaken with band-averaged properties in uncoupled calculations, and further calculations without any spectral averaging or with fully coupled calculations may identify different results.

Finally, it was noticed with increased fidelity in the calculations, the results for the radiative heat flux move further away from the measured values. These results suggest the importance of improving the accuracy of all aspects of modelling combustion systems. Furthermore, the particle radiative properties used in this study were not measured for the coal that was fired in the experimental campaign, and there is a need for more measured values for the radiative properties of coal particles. This is particularly true of fly ash particles, which may be chemically altered for different combustion regimes [322].

7 Conclusions and future work

The work in this thesis has focussed on the development of sub-models for mercury oxidation and radiative heat transfer under oxyfuel conditions. Modelling can be a valuable tool for designing and understanding combustion systems, however the current models require further development and validation before they can be used with confidence to predict the behaviour of unfamiliar combustion environments, such as the conditions that are present under oxyfuel combustion. This thesis provides new insights and new guidance on how to model some aspects of oxy-coal combustion. The main conclusions of this thesis are outlined in Section 7.1, and suggestions for further work are discussed in Section 7.2.

7.1 Conclusions

Mercury, a toxic pollutant released from coal combustion, is being targeted for stricter controls over emissions, and current control technologies are dependent upon the metal's oxidation chemistry. The study presented in Chapter 4 provided a detailed modelling investigation into the oxidation of mercury under air-fired and oxy-fired combustion conditions. The study identified negligible differences in equilibrium distributions between the two firing regimes, however, through an optimised chemical kinetic mechanism, it was possible to replicate the experimentally observed trends using a chemical kinetic model. The study demonstrated that the genetic algorithm method is well suited to optimising chemical kinetic schemes. Analysis of the model provided new insight into the role of the nitrosyl halide species in preventing mercury oxidation.

The formation of both nitrosyl chloride and nitrosyl bromide were responsible for reducing the concentration of the reactive atomic halogen species in the cooler regions of the reactor. These results demonstrated that mercury oxidation is highly sensitive to secondary chemistry. It is necessary to correctly predict the concentration of halogen species in order to reasonably predict mercury oxidation. However, there is still significant uncertainties in correctly predicting the distribution of halogen species under combustion conditions.

While it was possible to achieve a good agreement with measured values of mercury oxidation, the optimisation method was required to significantly reduce the kinetic rate of nitrosyl chloride formation in order to predict any mercury oxidation. The degree that the kinetic rate of this reaction was reduced by was so severe that this may not bear out in reality, and therefore it must be considered that the current mechanisms for mercury oxidation by chlorine species may be incomplete. Modelling of mercury oxidation by bromine species achieved through less severe kinetic restrictions, and it may be feasible to describe the oxidation chemistry with the currently available mechanisms, however there exists greater uncertainties associated with bromine reactions.

Accurate calculation of heat transfer at combustion temperatures is dependent upon the thermal radiation mechanism. For the complete description of radiative heat transfer, it is necessary to account for the spectral variation in the radiative absorbency of participating gas species, such as CO_2 and H_2O, which are present under significantly higher concentrations under oxyfuel environments than conventional firing conditions. A complete description of this spectral variation is computationally prohibitive, and approximate models must be used when considering fully coupled calculations of the combustion process.

The validation study in Chapter 5 compared a series of spectral radiation models against idealised environments that were relevant to oxyfuel combustion conditions. The study demonstrated that the LBL and narrow band methods show reasonable accuracy in predicting gas emissivity against experimental measurements, particularly for the CO_2 molecule. The study went on to show that the narrow band models show excellent agreement with the more expensive LBL methods for a wide range of conditions that are relevant for oxyfuel combustion. Finally, through a comparison between the validated narrow band models, global methods implemented on a three-dimensional enclosure were validated. This validation work demonstrated that the FSK methods, particularly the FSCK method using a five-point Gaussian quadrature, achieve very good accuracy, while still being sufficiently computationally efficient to be applied to CFD calculations.

A range of WSGG methods were also applied to the cases in the three-dimensional enclosure in Chapter 5. These methods represent the most widely used approach to modelling spectral radiative properties in CFD calculations, and included parameters that were developed specifically for oxyfuel conditions. It was shown that discontinuous WSGG parameters, such as the parameters by Smith et al. [220], Yin et al. [286] and Krishnamoorthy [293], induce discontinuous results in derived properties, and therefore should be avoided in CFD calculations where the gas properties in the domain cross the boundaries in the WSGG parameters. Two methods were also introduced to apply the non-grey WSGG method to non-homogeneous gas mixtures, where either the volume averaged values of the domain's gas composition were used to evaluate the radiative properties, or the local conditions of the nearest cell were used. It was found that the former approach achieved the greatest agreement for the radiative source term in the case that was tested, although the method was not able to predict the radiative heat flux accurately.

Some of the radiation models that were validated in Chapter 5 were then applied to the CFD calculation of a coal-fired combustion test facility under air and oxyfuel combustion modes in Chapter 6. Generally, both the air-fired and oxyfuel conditions demonstrated the same level of sensitivity to the radiative properties of the combustion medium in the case that was modelled. The study demonstrated that the FSCK method is very accurate under a broad range of conditions through comparisons with the narrow band CK model. Comparisons against measured data proved to be less straightforward due to significant uncertainties and assumptions associated with the modelling approaches for other combustion phenomena.

The CFD calculations of the coal combustion facility also demonstrated significant sensitivity to the gas temperatures and surface heat flux associated with the radiative properties of particulates. Narrow band calculations using grey and non-grey particle radiative properties were conducted for the first time for a coal combustion case, and demonstrated that grey particle radiative properties are a reasonable assumption with the parameters that were tested. There is a significant need for accurate spectrally variable particle radiative properties before the assumption of grey properties can be fully justified.

The results in this thesis have shown that the FSCK method represents an accurate description of gaseous radiative properties across a wide range of combustion conditions. A five-point Gaussian quadrature, which represents at least the same computational complexity as other accurate non-grey methods, was found to produce the best results, and is therefore strongly recommended for CFD calculations of combustion in air and oxyfuel conditions. Mie theory values were introduced for modelling the radiative properties of particulates, however this approach could not be validated in the current work.

7.2 Topics for future work

Further work is required in the development of a predictive chemical kinetic model of mercury oxidation. Despite the modelling investigation undertaken in Chapter 4 being able to achieve good agreement across several trends in mercury oxidation, one of the most significant outcomes was that the model is incapable of capturing the measured insensitivity to NO concentration. The incapability of the model to capture this trend, despite subjecting the mechanism to a reasonably liberal optimisation approach, hints strongly that the mechanism for mercury oxidation is incomplete. In order to provide predictive modelling capabilities for mercury oxidation under combustion conditions, either conventional or oxyfuel conditions, it is necessary to further investigate alternative routes for mercury oxidation. These additional routes may include reactions with halogen species that have not yet been investigated, such as the nitrosyl halides.

The kinetic parameters used to describe a reactive system, such as the mercury oxidation process studied in this work, are inherently subject to significant uncertainties. A significant number of principle reactions, such as the reactions that directly concern mercury and halogen species, are subject to considerable uncertainties, and have yet to be validated against detailed measurements under combustion conditions. It is necessary to develop detailed halogen sub-mechanisms, that are validated against a range of conventional and oxyfuel combustion conditions. The development of these mechanisms will include further theoretical and experimental determination of key kinetic rates, including investigations into the impact of CO_2 as a third body species in gas-phase reactions.

Further to a more complete gas-phase description of mercury oxidation, insights into how mercury binds and reacts with particulate matter would be important in developing a comprehensive model. The work in this thesis only focussed on gas-phase interactions, however surface catalysed reactions and mercury adsorption mechanisms must be considered if a predictive model is to be used for large scale combustion systems. Further laboratory scale experiments to isolate these phenomena and provide a model validation data set would be hugely beneficial to the understanding of mercury oxidation mechanisms.

The studies in Chapters 5 and 6 demonstrated that the FSCK model is a highly accurate method for representing gas radiative absorptivity in the cases that were studied. However the cases also highlighted that the representation of particle radiative properties can have a similar impact on the predictions of the combustion process. It has been several decades since spectrally variable optical properties of coal particles have been published, and studies on more modernly available fuels would be beneficial to reducing uncertainties in applying these properties. Furthermore, the optical properties of fly-ash can change based on the oxidation level of the mineral content contained in the particle [322], and experimental measurements of the optical properties of a wide range of fly-ash particles is necessary for the development of accurate models for coal combustion.

One of the main deficiencies in applying the FSCK method in coal combustion systems is the requirement to treat all particle radiative properties as spectrally constant. This assumption was challenged in Chapter 6, and it was found that the use of grey particles was an accurate assumption based on narrow-band averaged particle properties. In order to fully assert that this assumption is not detrimental to numerical results, it is necessary to measure high resolution particle optical properties and validate this approach on a LBL basis.

In addition to further improvements in the modelling of thermal radiation, developments into combustion chemistry and char reactivity would also go a long way to improving predictions of coal combustion systems. The rate of combustion in both the homogeneous gas-phase and the heterogeneous gas-solid reactions are both known to change under oxyfuel conditions [375, 411], and without accounting these changes, it will be impossible to predict the influence of operating an oxyfuel combustion environment on an existing system with confidence.

Furthermore, the results in Chapter 6 also highlighted a shortcoming in the widely used discrete random walk model for predicting turbulent dispersions in bounded flows. While it is known that this model performs poorly in bounded flows [357], alternative models are not widely available. Validated particle trajectory modelling would improve confidence in RANS modelling of coal combustion systems.

The pathway to widespread adoption of CCS will require great efficiency savings in order to make the technology economically viable. Computational modelling will be part of the design process to reduce the energy penalty associated with separating the CO_2 stream, however greater confidence in the modelling approaches is required. Following the validation work in this thesis, the FSCK method can be used with confidence for predicting gas radiative properties, however application of a combined advanced modelling approach for turbulence, combustion, radiative heat transfer and pollutant formation for oxy-coal combustion still needs further developments. Mercury oxidation, in particular, is still subject to considerable uncertainties. More detailed pilot-scale measurements and demonstration scale experience of oxy-coal facilities will aid in the validation and development of these modelling capabilities, as well as improve the general experience of oxyfuel conditions, and will be crucial in the large-scale deployment of CCS.

Bibliography

[1] E. Pacyna, J. Pacyna, K. Sundseth, J. Munthe, K. Kindbom, S. Wilson, F. Steenhuisen, and P. Maxson, “Global emission of mercury to the atmosphere from anthropogenic sources in 2005 and projections to 2020,” *Atmospheric Environment*, vol. 44, no. 20, pp. 2487 – 2499, 2010.

[2] United Nations Environmental Program, “Study on mercury sources and emissions, and analysis of cost and effectiveness of control measures “UNEP paragraph 29 study”,” Division of Technology, Industry and Economics (DTIE) Chemicals Branch, Tech. Rep., November 2010.

[3] D. McAlpine and S. Araki, “Minimata disease an unusual neurological disorder caused by contaminated fish,” *The Lancet*, vol. 272, no. 7047, pp. 629 – 631, 1958.

[4] E. Guallar, M. I. Sanz-Gallardo, P. van’t Veer, P. Bode, A. Aro, J. Gómez-Aracena, J. D. Kark, R. A. Riemersma, J. M. Martín-Moreno, and F. J. Kok, “Mercury, fish oils, and the risk of myocardial infarction,” *New England Journal of Medicine*, vol. 347, no. 22, pp. 1747–1754, 2002.

[5] T. W. Clarkson, L. Magos, and G. J. Myers, “The toxicology of mercury – current exposures and clinical manifestations,” *New England Journal of Medicine*, vol. 349, no. 18, pp. 1731–1737, 2003.

[6] M. R. Pinnel and J. E. Bennett, “Voluminous oxidation of aluminium by continuous dissolution in a wetting mercury film,” *Journal of Materials Science*, vol. 7, pp. 1016–1026, 1972.

[7] M. Subir, P. A. Ariya, and A. P. Dastoor, “A review of uncertainties in atmospheric modeling of mercury chemistry i. uncertainties in existing kinetic parameters – fundamental limitations and the importance of heterogeneous chemistry,” *Atmospheric Environment*, vol. 45, no. 32, pp. 5664 – 5676, 2011.

[8] R. Viskanta and M. P. Mengüc, “Radiation heat transfer in combustion systems,” *Progress in Energy and Combustion Science*, vol. 13, no. 2, pp. 97 – 160, 1987.

[9] L. Bernstein, P. Bosch, O. Canziani, Z. Chen, R. Christ, O. Davidson, W. Hare, S. Huq, D. Karoly, V. Kattsov, Z. Kundzewicz, J. Liu, U. Lohmann, M. Manning, T. Matsuno, B. Menne, B. Metz, M. Mirza, N. Nicholls, L. Nurse, R. Pachauri, J. Palutikof, M. Parry, D. Qin, N. Ravindranath, A. Reisinger, J. Ren, K. Riahi, C. Rosenzweig, M. Rusticucci, S. Schneider, Y. Sokona, S. Solomon, P. Stott, R. Stouffer, T. Sugiyama, R. Swart, D. Tirpak, C. Vogel, G. Yohe, and T. Barker, “Fourth assessment report,” Intergovernmental panel on climate change, Tech. Rep., 2007.

[10] J. Hansen, M. Sato, R. Ruedy, L. Nazarenko, A. Lacis, G. A. Schmidt, G. Russell, I. Aleinov, M. Bauer, S. Bauer, N. Bell, B. Cairns, V. Canuto, M. Chandler, Y. Cheng, A. D. Genio, G. Faluvegi, E. Fleming, A. Friend, T. Hall, C. Jackman, M. Kelley,

N. Kiang, D. Koch, J. Lean, J. Lerner, K. Lo, S. Menon, R. Miller, P. Minnis, T. Novakov, V. Oinas, J. Perlwitz, J. Perlwitz, D. Rind, A. Romanou, D. Shindell, P. Stone, S. Sun, N. Tausnev, D. Thresher, B. Wielicki, T. Wong, M. Yao, and S. Zhang, "Efficacy of climate forcings," *Journal of Geophysical Research*, vol. 110, no. D18, p. D18104, 2005.

[11] (2005, March) Presidency conclusions. The Council of the European Union. Accessed 08/10/2012. [Online]. Available: http://www.consilium.europa.eu/uedocs/cms_data/docs/pressdata/en/ec/84335.pdf

[12] (2009, October) Presidency conclusions. The Council of the European Union. Accessed 08/10/2012. [Online]. Available: http://register.consilium.europa.eu/pdf/en/09/st15/st15265-re01.en09.pdf

[13] P. Tans and R. Keeling. (2015) Trends in atmospheric carbon dioxide. NOAA/ESRL. Accessed 16th November 2015. [Online]. Available: http://www.esrl.noaa.gov/gmd/ccgg/trends/

[14] B. Metz, O. Davidson, H. de Coninck, M. Loos, and L. Meyer, "IPCC special report on carbon dioxide capture and storage," Working Group III of the Intergovernmental Panel on Climate Change, Tech. Rep., 2005.

[15] O. Eiken, P. Ringrose, C. Hermanrud, B. Nazarian, T. A. Torp, and L. Høier, "Lessons learned from 14 years of CCS operations: Sleipner, in salah and snhvit," *Energy Procedia*, vol. 4, pp. 5541 – 5548, 2011, 10th International Conference on Greenhouse Gas Control Technologies.

[16] L. Strömberg, G. Lindgren, J. Jacoby, R. Giering, M. Anheden, U. Burchhardt, H. Altmann, F. Kluger, and G.-N. Stamatelopoulos, "Update on Vattenfalls 30 MWth oxyfuel pilot plant in Schwarze Pumpe," *Energy Procedia*, vol. 1, no. 1, pp. 581 – 589, 2009.

[17] D. N. Veritas, "Recommended practice DNV-RP-J202 design and operation of CO_2 pipelines," April 2010.

[18] X. Li, Y. Liu, R. Stanger, L. Belo, T. Ting, and T. Wall, "Gas quality control in oxy-pf technology for carbon capture and storage," Chemical Engineering, University of Newcastle, Australia, 2308, Tech. Rep., February 2012.

[19] (1999, November) ChemicaLogic Corporation. Accessed 02/11/2012. [Online]. Available: http://www.chemicalogic.com/download/phase_diagram.html

[20] N. MacDowell, N. Florin, A. Buchard, J. Hallett, A. Galindo, G. Jackson, C. S. Adjiman, C. K. Williams, N. Shah, and P. Fennell, "An overview of CO_2 capture technologies," *Energy & Environmental Science*, vol. 3, pp. 1645–1669, 2010.

[21] L. J. Kaplan, "Cost-saving process recovers CO_2 from power-plant flue gas," *Chem. Eng.(NY);(United States)*, vol. 89, no. 24, pp. 30–31, 1982.

[22] R. A. Gardiner, S. Bowden, and F. D. Fitzgerald, "Demonstration and verification of post combustion capture using solvent scrubbing," *Energy Procedia*, vol. 4, pp. 5623 – 5630, 2011.

[23] Z. Cui, A. Aroonwilas, and A. Veawab, “Simultaneous capture of mercury and CO_2 in amine-based CO_2 absorption process,” *Industrial & Engineering Chemistry Research*, vol. 49, no. 24, pp. 12 576–12 586, 2010.

[24] T. Andersen, H. M. Kvamsdal, and O. Bolland, “Gas turbine combined cycle with co2 capture using auto-thermal reforming of natural gas,” in *Proceedings of ASME Turbo Expo*, 2000.

[25] P. Chiesa, S. Consonni, T. Kreutz, and R. Williams, “Co-production of hydrogen, electricity and CO_2 from coal with commercially ready technology. Part A: performance and emissions,” *International Journal of Hydrogen Energy*, vol. 30, no. 7, pp. 747 – 767, 2005.

[26] E. Catalanotti, K. J. Hughes, R. T. J. Porter, J. Price, and M. Pourkashanian, “Evaluation of performance and cost of combustion-based power plants with CO_2 capture in the united kingdom,” *Environmental Progress & Sustainable Energy*, vol. 33, no. 4, pp. 1425–1431, 2013.

[27] J. H. Pavlish, L. L. Hamre, and Y. Zhuang, “Mercury control technologies for coal combustion and gasification systems,” *Fuel*, vol. 89, no. 4, pp. 838 – 847, 2010.

[28] M. Anheden, U. Burchhardt, H. Ecke, R. Faber, O. Jidinger, R. Giering, H. Kass, S. Lysk, E. Ramstrm, and J. Yan, “Overview of operational experience and results from test activities in vattenfalls 30 mwth oxyfuel pilot plant in schwarze pumpe,” *Energy Procedia*, vol. 4, pp. 941 – 950, 2011.

[29] R. Stanger, T. Ting, C. Spero, and T. Wall, “Oxyfuel derived CO_2 compression experiments with nox, SOx and mercury removal – experiments involving compression of slip-streams from the callide oxyfuel project (COP),” *International Journal of Greenhouse Gas Control*, vol. 41, pp. 50 – 59, 2015.

[30] R. Stanger, T. Ting, L. Belo, C. Spero, and T. Wall, “Field measurements of NOx and mercury from oxy-fuel compression condensates at the callide oxyfuel project,” *International Journal of Greenhouse Gas Control*, vol. 42, pp. 485 – 493, 2015.

[31] E. Croiset and K. Thambimuthu, “NOx and SO_2 emissions from O_2/CO_2 recycle coal combustion,” *Fuel*, vol. 80, no. 14, pp. 2117 – 2121, 2001.

[32] E. G. Eddings, R. Okerlund, and L. E. Bool, “Pilot-scale evaluation of oxycoal firing in circulating fluidized bed and pulverized coal-fired test facilities,” in *1st Oxyfuel combustion conference*, 2009.

[33] Y. Zhuang and J. H. Pavlish, “Fate of hazardous air pollutants in oxygen-fired coal combustion with different flue gas recycling,” *Environmental Science & Technology*, vol. 46, no. 8, pp. 4657–4665, 2012.

[34] L. Torrente-Murciano, V. White, F. Petrocelli, and D. Chadwick, “Study of individual reactions of the sour compression process for the purification of oxyfuel-derived CO_2,” *International Journal of Greenhouse Gas Control*, vol. 5, Supplement 1, pp. S224 – S230, 2011, oxyfuel Combustion Technology - Working Toward Demonstration and Commercialisation.

[35] J. P. Smart and G. S. Riley, "On the effects of firing semi-anthracite and bituminous coal under oxy-fuel firing conditions," *Fuel*, vol. 90, no. 8, pp. 2812 – 2816, 2011.

[36] S. M. Hashim, A. R. Mohamed, and S. Bhatia, "Current status of ceramic-based membranes for oxygen separation from air," *Advances in Colloid and Interface Science*, vol. 160, no. 12, pp. 88 – 100, 2010.

[37] J. Adanez, A. Abad, F. Garcia-Labiano, P. Gayan, and L. F. de Diego, "Progress in chemical-looping combustion and reforming technologies," *Progress in Energy and Combustion Science*, vol. 38, no. 2, pp. 215 – 282, 2012.

[38] M. Kanniche, R. Gros-Bonnivard, P. Jaud, J. Valle-Marcos, J.-M. Amann, and C. Bouallou, "Pre-combustion, post-combustion and oxy-combustion in thermal power plant for co2 capture," *Applied Thermal Engineering*, vol. 30, no. 1, pp. 53 – 62, 2010.

[39] M. Corsten, A. Ramírez, L. Shen, J. Koornneef, and A. Faaij, "Environmental impact assessment of CCS chains – lessons learned and limitations from LCA literature," *International Journal of Greenhouse Gas Control*, vol. 13, pp. 59 – 71, 2013.

[40] T. Wall, R. Stanger, and Y. Liu, "Gas cleaning challenges for coal-fired oxy-fuel technology with carbon capture and storage," *Fuel*, vol. 108, pp. 85–90, 2011.

[41] M. Subir, P. A. Ariya, and A. P. Dastoor, "A review of the sources of uncertainties in atmospheric mercury modeling ii. mercury surface and heterogeneous chemistry – a missing link," *Atmospheric Environment*, vol. 46, pp. 1 – 10, 2012.

[42] Y. E. Yudovich and M. Ketris, "Mercury in coal: a review: Part 1. geochemistry," *International Journal of Coal Geology*, vol. 62, no. 3, pp. 107 – 134, 2005.

[43] T. W. Clarkson, "The toxicology of mercury," *Critical Reviews in Clinical Laboratory Sciences*, vol. 34, no. 4, pp. 369–403, 1997.

[44] AMAP/UNEP, "Technical background report to the global atmospheric mercury assessment," Arctic Monitoring and Assessment Programme / UNEP Chemicals Branch, Tech. Rep., 2008.

[45] F. Slemr, E.-G. Brunke, R. Ebinghaus, and J. Kuss, "Worldwide trend of atmospheric mercury since 1995," *Atmospheric Chemistry & Physics*, vol. 11, pp. 4779–4787, May 2011.

[46] S. Lindberg, R. Bullock, R. Ebinghaus, D. Engstrom, X. Feng, W. Fitzgerald, N. Pirrone, E. Prestbo, and C. Seigneur, "A synthesis of progress and uncertainties in attributing the sources of mercury in deposition," *Ambio*, vol. 36, no. 1, pp. 19–33, 2007.

[47] O. Travnikov, "Contribution of the intercontinental atmospheric transport to mercury pollution in the northern hemisphere," *Atmospheric Environment*, vol. 39, no. 39, pp. 7541 – 7548, 2005.

[48] S. Jensen and A. Jernelöv, "Biological methylation of mercury in aquatic organisms," *Nature*, vol. 223, pp. 753–754, Aug. 1969.

[49] H. Nagase, Y. Ose, T. Sato, and T. Ishikawa, "Mercury methylation by compounds in humic material," *Science of The Total Environment*, vol. 32, no. 2, pp. 147 – 156, 1984.

[50] S. T. Kolev and N. Bates. (1996, March) Mercury. [Online]. Available: http://www.inchem.org/documents/ukpids/ukpids/ukpid27.htm

[51] L. Friberg. (1991) Inorganic mercury (environmental health criteria 118). World Health Orgnization. [Online]. Available: http://www.inchem.org/documents/ehc/ehc/ehc118.htm

[52] T. W. Clarkson, J. B. Vyas, and N. Ballatori, "Mechanisms of mercury disposition in the body," *American Journal of Industrial Medicine*, vol. 50, no. 10, pp. 757–764, 2007.

[53] M. Nylander, L. Friberg, and B. Lind, "Mercury concentrations in the human brain and kidneys in relation to exposure from dental amalgam fillings," *Swedish dental journal*, vol. 11, no. 5, pp. 179–87, 1987.

[54] A. Franzblau, H. dArcy, M. B. Ishak, R. A. Werner, B. W. Gillespie, J. W. Albers, C. Hamann, S. E. Gruninger, H.-N. Chou, and D. M. Meyer, "Low-level mercury exposure and peripheral nerve function," *NeuroToxicology*, vol. 33, no. 3, pp. 299 – 306, 2012.

[55] F. M. M. Morel, A. M. L. Kraepiel, and M. Amyot, "The chemical cycle and bioaccumulation of mercury," *Annual Review of Ecology and Systematics*, vol. 29, pp. 543–566, 1998.

[56] G. Compeau and R. Bartha, "Sulfate-reducing bacteria: Principal methylators of mercury in anoxic estuarine sediment," *Applied and Environmental Microbiology*, vol. 50, no. 2, pp. 498–502, 1985.

[57] C. J. Watras and N. S. Bloom, "Mercury and methylmercury in individual zooplankton: Implications for bioaccumulation," *Limnology and Oceanography*, vol. 37, no. 6, pp. 1313–1318, 1992.

[58] K. R. Mahaffey, R. P. Clickner, and C. C. Bodurow, "Blood organic mercury and dietary mercury intake: National health and nutrition examination survey, 1999 and 2000." *Environmental Health Perspectives*, vol. 112, no. 5, p. 562, 2004.

[59] L. E. Kerper, N. Ballatori, and T. W. Clarkson, "Methylmercury transport across the blood-brain barrier by an amino acid carrier," *American Journal of Physiology - Regulatory, Integrative and Comparative Physiology*, vol. 262, no. 5, pp. R761–R765, 1992.

[60] Y. Kajiwara, A. Yasutake, T. Adachi, and K. Hirayama, "Methylmercury transport across the placenta via neutral amino acid carrier," *Archives of Toxicology*, vol. 70, pp. 310–314, 1996.

[61] M. Aschner, "Possible mechanisms of methylmercury cytotoxicity," *Molecular Biology Today*, vol. 1, no. 2, pp. 43–48, 2000.

[62] M. Harada, "Minamata disease: Methylmercury poisoning in japan caused by environmental pollution," *Critical Reviews in Toxicology*, vol. 25, no. 1, pp. 1–24, 1995.

[63] P. Grandjean, P. Weihe, R. F. White, F. Debes, S. Araki, K. Yokoyama, K. Murata, N. Sørensen, R. Dahl, and P. J. Jørgensen, “Cognitive deficit in 7-year-old children with prenatal exposure to methylmercury,” *Neurotoxicology and Teratology*, vol. 19, no. 6, pp. 417 – 428, 1997.

[64] G. J. Myers, P. W. Davidson, C. Cox, C. F. Shamlaye, D. Palumbo, E. Cernichiari, J. Sloane-Reeves, G. E. Wilding, J. Kost, L.-S. Huang, and T. W. Clarkson, “Prenatal methylmercury exposure from ocean fish consumption in the seychelles child development study,” *The Lancet*, vol. 361, no. 9370, pp. 1686 – 1692, 2003.

[65] M. C. Houston, “The role of mercury and cadmium heavy metals in vascular disease, hypertension, coronary heart disease, and myocardial infarction,” *Alternative Therapies In Health And Medicine*, vol. 13, no. 2, pp. S128–S133, 2007.

[66] N. Bocharova, G. Treu, G. A. Czirják, O. Krone, V. Stefanski, G. Wibbelt, E. R. Unnsteinsdóttir, P. Hersteinsson, G. Schares, L. Doronina, M. Goltsman, and A. D. Greenwood, “Correlates between feeding ecology and mercury levels in historical and modern arctic foxes (vulpes lagopus),” *PLoS ONE*, vol. 8, no. 5, p. e60879, 2013.

[67] (2012, April) Mercury. European Union. Accessed 02/08/2012. [Online]. Available: http://ec.europa.eu/environment/chemicals/mercury/

[68] (2008) Regulation (ec) no 1102/2008 of the european parliament and of the council of 22 october 2008 on the banning of exports of metallic mercury and certain mercury compounds and mixtures and the safe storage of metallic mercury. European Union.

[69] (2010) Directive 2010/75/eu of the european parliament and of the council of 24 november 2010 on industrial emissions (integrated pollution prevention and control). European Union.

[70] (2009, January) Thirteenth ordinance on the implementation of the federal immission control act (ordinance on large combustion plants and gas turbine plants - 13. bimschv). Federal Ministry for the Environment, Nature Conservation and Nuclear Safety. [Online]. Available: http://www.bmu.de/english/air_pollution_control/downloads/doc/47237.php

[71] United States Environmental Protection Agency. (2011, December) Regulatory impact analysis. Accessed 06/08/2012. [Online]. Available: http://www.epa.gov/mats/actions.html

[72] United States Environmental Protection Agency. (2015, January) Intergovermental negotiating committee 5. Accessed 16/11/2015. [Online]. Available: http://www.unep.org/chemicalsandwaste/Mercury/GlobalMercuryPartnership/tabid/1253/

[73] P. J. Edge, P. J. Heggs, M. Pourkashanian, and A. Williams, “An integrated computational fluid dynamics-process model of natural circulation steam generation in a coal-fired power plant,” *Computers & Chemical Engineering*, vol. 35, no. 12, pp. 2618 – 2631, 2011.

[74] P. Edge, P. Heggs, M. Pourkashanian, P. Stephenson, and A. Williams, “A reduced order full plant model for oxyfuel combustion,” *Fuel*, vol. 101, pp. 234 – 243, 2012.

[75] Y. Fei, S. Black, J. Szuhnszki, L. Ma, D. Ingham, P. Stanger, and M. Pourkashanian, "Evaluation of the potential of retrofitting a coal power plant to oxy-firing using {CFD} and process co-simulation," *Fuel Processing Technology*, vol. 131, no. 0, pp. 45 – 58, 2015.

[76] R. Porter, "Theoretical modelling and design tools for oxy-coal combustion technology," Ph.D. dissertation, School of Process, Environmental and Materials Engineering, University of Leeds, January 2011.

[77] C. Yin, L. A. Rosendahl, and S. K. Kr, "Chemistry and radiation in oxy-fuel combustion: A computational fluid dynamics modeling study," *Fuel*, vol. 90, no. 7, pp. 2519 – 2529, 2011.

[78] P. Edge, M. Gharebaghi, R. Irons, R. Porter, R. Porter, M. Pourkashanian, D. Smith, P. Stephenson, and A. Williams, "Combustion modelling opportunities and challenges for oxy-coal carbon capture technology," *Chemical Engineering Research and Design*, vol. 89, no. 9, pp. 1470 – 1493, 2011.

[79] L. Chen, S. Z. Yong, and A. F. Ghoniem, "Oxy-fuel combustion of pulverized coal: Characterization, fundamentals, stabilization and cfd modeling," *Progress in Energy and Combustion Science*, vol. 38, no. 2, pp. 156 – 214, 2012.

[80] G. Scheffknecht, L. Al-Makhadmeh, U. Schnell, and J. Maier, "Oxy-fuel coal combustion – a review of the current state-of-the-art," *International Journal of Greenhouse Gas Control*, vol. 5, Supplement 1, no. 0, pp. S16 – S35, 2011.

[81] R. Meij, L. H. J. Vredenbregt, and H. te Winkel, "The fate and behavior of mercury in coal-fired power plants," *Journal of the Air & Waste Management Association*, vol. 52, no. 8, pp. 912–917, 2002.

[82] J. H. Pavlish, E. A. Sondreal, M. D. Mann, E. S. Olson, K. C. Galbreath, D. L. Laudal, and S. A. Benson, "Status review of mercury control options for coal-fired power plants," *Fuel Processing Technology*, vol. 82, no. 2-3, pp. 89 – 165, 2003.

[83] D. Cremer, E. Kraka, and M. Filatov, "Bonding in mercury molecules described by the normalized elimination of the small component and coupled cluster theory," *ChemPhysChem*, vol. 9, no. 17, pp. 2510–2521, 2008.

[84] N. Noda and S. Ito, "The release and behavior of mercury, selenium, and boron in coal combustion," *Powder Technology*, vol. 180, no. 1-2, pp. 227 – 231, 2008.

[85] S. Guo, J. Yang, and Z. Liu, "Characterization of Hg in coals by temperature-programmed decomposition–atomic fluorescence spectroscopy and acid-leaching techniques," *Energy & Fuels*, vol. 26, no. 6, pp. 3388–3392, 2012.

[86] M. Ketris and Y. Yudovich, "Estimations of clarkes for carbonaceous biolithes: World averages for trace element contents in black shales and coals," *International Journal of Coal Geology*, vol. 78, no. 2, pp. 135 – 148, 2009.

[87] S. Vassilev, G. Eskenazy, and C. Vassileva, "Contents, modes of occurrence and origin of chlorine and bromine in coal," *Fuel*, vol. 79, no. 8, pp. 903 – 921, 2000.

[88] D. Spears and Y. Zheng, "Geochemistry and origin of elements in some UK coals," *International Journal of Coal Geology*, vol. 38, no. 3-4, pp. 161 – 179, 1999.

[89] United States Environmental Protection Agency. (2011, December) Air toxics standards for utilities. Online. Accessed 06/08/2012. [Online]. Available: http://www.epa.gov/ttn/atw/utility/egu_hg_speciation_data_camr.xls

[90] J. L. Ticknor, H. Hsu-Kim, and M. A. Deshusses, "A robust framework to predict mercury speciation in combustion flue gases," *Journal of Hazardous Materials*, vol. 264, pp. 380 – 385, 2014.

[91] E. M. Prestbo and N. S. Bloom, "Mercury speciation adsorption (mesa) method for combustion flue gas: Methodology, artifacts, intercomparison, and atmospheric implications," *Water, Air, & Soil Pollution*, vol. 80, pp. 145–158, 1995.

[92] A. Carpi, "Mercury from combustion sources: A review of the chemical species emitted and their transport in the atmosphere," *Water, Air, & Soil Pollution*, vol. 98, pp. 241–254, 1997.

[93] N. C. Widmer, J. West, and J. A. Cole, "Thermochemical study of mercury oxidation in utility boiler flue gases," in *Proceedings of the Air & Waste Management Association Annual Conference*, Salt Lake City, Pittsburgh, 2000.

[94] R. N. Sliger, J. C. Kramlich, and N. M. Marinov, "Towards the development of a chemical kinetic model for the homogeneous oxidation of mercury by chlorine species," *Fuel Processing Technology*, vol. 65 & 66, pp. 423 – 438, 2000.

[95] K. Schofield, "Let them eat fish: hold the mercury," *Chemical Physics Letters*, vol. 386, no. 1-3, pp. 65 – 69, 2004.

[96] R. Yan, D. Gauthier, and G. Flamant, "Volatility and chemistry of trace elements in a coal combustor," *Fuel*, vol. 80, no. 15, pp. 2217 – 2226, 2001.

[97] B. van Otten, P. A. Buitrago, C. L. Senior, and G. D. Silcox, "Gas-phase oxidation of mercury by bromine and chlorine in flue gas," *Energy & Fuels*, vol. 25, no. 8, pp. 3530–3536, 2011.

[98] M. Berry, K. Dombrowski, C. Richardson, R. Chang, E. Borders, and B. Vosteen, "Mercury control evaluation of calcium bromide injection into a prb-fired furnace with an scr," in *Air Quality VI*, September 2007.

[99] S. Derenne, P. Sartorelli, J. Bustard, R. Stewart, S. Sjostrom, P. Johnson, M. McMillian, F. Sudhoff, and R. Chang, "TOXECON clean coal demonstration for mercury and multi-pollutant control at the presque isle power plant," *Fuel Processing Technology*, vol. 90, no. 11, pp. 1400 – 1405, 2009.

[100] F. E. Huggins, G. P. Huffman, G. E. Dunham, and C. L. Senior, "XAFS examination of mercury sorption on three activated carbons," *Energy & Fuels*, vol. 13, no. 1, pp. 114–121, 1999.

[101] Y. Li, M. Daukoru, A. Suriyawong, and P. Biswas, "Mercury emissions control in coal combustion systems using potassium iodide: Bench-scale and pilot-scale studies," *Energy & Fuels*, vol. 23, no. 1, pp. 236–243, 2009.

[102] Z. Qu, N. Yan, P. Liu, J. Jia, and S. Yang, "The role of iodine monochloride for the oxidation of elemental mercury," *Journal of Hazardous Materials*, vol. 183, no. 13, pp. 132 – 137, 2010.

[103] K. Schofield, "Mercury emission control from coal combustion systems: A modified air preheater solution," *Combustion and Flame*, vol. 159, no. 4, pp. 1741 – 1747, 2012.

[104] A. K. Medhekar, M. Rokni, D. W. Trainor, and J. Jacob, "Surface catalyzed reaction of Hg + Cl_2," *Chemical Physics Letters*, vol. 65, no. 3, pp. 600 – 604, 1979.

[105] K. Schofield, "Fuel-mercury combustion emissions: An important heterogeneous mechanism and an overall review of its implications," *Environmental Science & Technology*, vol. 42, no. 24, pp. 9014–9030, 2008.

[106] S. J. Lee, Y.-C. Seo, H.-N. Jang, K.-S. Park, J.-I. Baek, H.-S. An, and K.-C. Song, "Speciation and mass distribution of mercury in a bituminous coal-fired power plant," *Atmospheric Environment*, vol. 40, no. 12, pp. 2215 – 2224, 2006.

[107] E. S. Olson, A. Azenkeng, J. D. Laumb, R. R. Jensen, S. A. Benson, and M. R. Hoffmann, "New developments in the theory and modeling of mercury oxidation and binding on activated carbons in flue gas," *Fuel Processing Technology*, vol. 90, no. 11, pp. 1360 – 1363, 2009.

[108] J. Hranisavljevic and A. Fontijn, "Kinetics of ground-state Cd reactions with Cl_2, O_2, and HCl over wide temperature ranges," *The Journal of Physical Chemistry A*, vol. 101, no. 12, pp. 2323–2326, 1997.

[109] J. Wilcox, "A kinetic investigation of high-temperature mercury oxidation by chlorine," *Journal of Physical Chemistry A*, vol. 113, no. 24, pp. 6633–6639, 2009.

[110] J. Wilcox, "On the path to elucidating the speciation of mercury in the flue gasses of coal combustion," Ph.D. dissertation, Department of Chemical and Environmental Engineering, The University of Arizona, 2004.

[111] J. F. Roesler, R. A. Yetter, and F. L. Dryer, "Kinetic interactions of CO, NOx, and HCl emissions in postcombustion gases," *Combustion and Flame*, vol. 100, no. 3, pp. 495 – 504, 1995.

[112] A. Suriyawong, "Oxy-coal combustion: Submicrometer particle formation, mercury speciation, and their capture," Ph.D. dissertation, School of Engineering and Applied Science, Washington University, August 2009.

[113] S. Niksa, J. Helble, and N. Fujiwara, "Kinetic modeling of homogeneous mercury/oxidation: The importance of no and h2o in predicting oxidation in coal-derived systems," *Environmental Science and Technology*, vol. 35, no. 18, pp. 3701–3706, 2001.

[114] I. A. Murua and J. W. Bozzelli, "Gas-phase mercury conversion in H_2, O_2, chloro C_1-hydrocarbon, and NOx combustion effluent from use of an elementary kinetic mechanism," *Combustion Science and Technology*, vol. 182, no. 4-6, pp. 529–543, 2010.

[115] H. Hippler and J. Troe, “Flash photolysis study of the recombination of chlorine atoms in the presence of various inert gases and no,” *International Journal of Chemical Kinetics*, vol. 8, no. 4, pp. 501–510, 1976.

[116] I. Preciado, T. Young, G. Silcox, J. Wendt, B. van Otten, and A. Fry, “Mercury oxidation by halogens under air-fired and oxy-fuel conditions,” in *American Flame Research Committee Annual Meeting*, Officers Club, University of Utah, Salt Lake City, Utah, September 2012.

[117] I. Preciado, T. Young, and G. Silcox, “Mercury oxidation by halogens under air- and oxygen-fired conditions,” *Energy & Fuels*, vol. 28, no. 2, pp. 1255–1261, 2014.

[118] R. Spörl, L. Belo, K. Shah, R. Stanger, R. Giniyatullin, J. Maier, T. Wall, and G. Scheffknecht, “Mercury emissions and removal by ash in coal-fired oxy-fuel combustion,” *Energy & Fuels*, vol. 28, no. 1, pp. 123–135, 2014.

[119] R. Spörl, J. Maier, L. Belo, K. Shah, R. Stanger, T. Wall, and G. Scheffknecht, “Mercury and SO_3 emissions in oxy-fuel combustion,” *Energy Procedia*, vol. 63, pp. 386 – 402, 2014, 12th International Conference on Greenhouse Gas Control Technologies, GHGT-12.

[120] W. P. Linak, J. V. Ryan, B. S. Ghorishi, and J. O. L. Wendt, “Issues related to solution chemistry in mercury sampling impingers,” *Journal of the Air & Waste Management Association*, vol. 51, no. 5, pp. 688–698, 2001.

[121] B. Cauch, G. D. Silcox, J. S. Lighty, J. O. L. Wendt, A. Fry, and C. L. Senior, “Confounding effects of aqueous-phase impinger chemistry on apparent oxidation of mercury in flue gases,” *Environmental Science & Technology*, vol. 42, no. 7, pp. 2594–2599, 2008.

[122] C. A. Smith, B. Krishnakumar, and J. J. Helble, “Homo- and heterogeneous mercury oxidation in a bench-scale flame-based flow reactor,” *Energy & Fuels*, vol. 25, no. 10, pp. 4367–4376, 2011.

[123] M. U. Alzueta, R. Bilbao, and P. Glarborg, “Inhibition and sensitization of fuel oxidation by SO_2,” *Combustion and Flame*, vol. 127, no. 4, pp. 2234 – 2251, 2001.

[124] J. Giménez-López, M. Martínez, A. Millera, R. Bilbao, and M. U. Alzueta, “SO_2 effects on CO oxidation in a CO_2 atmosphere, characteristic of oxy-fuel conditions,” *Combustion and Flame*, vol. 158, no. 1, pp. 48 – 56, 2011.

[125] P. A. Buitrago, “Gas-phase mercury oxidation: effects of bromine, chlorine and SO_2 under air firing and oxy-fuel conditions, experimental and modeling study,” Ph.D. dissertation, The University of Utah, August 2011.

[126] S. Niksa, C. V. Naik, M. S. Berry, and L. Monroe, “Interpreting enhanced hg oxidation with br addition at plant miller,” *Fuel Processing Technology*, vol. 90, no. 11, pp. 1372 – 1377, 2009.

[127] K. J. Hughes, L. Ma, R. T. Porter, and M. Pourkashanian, “Mercury transformation modelling with bromine addition in coal derived flue gases,” in *21st European Symposium on Computer Aided Process Engineering*, ser. Computer Aided Chemical Engineering, M. G. E.N. Pistikopoulos and A. Kokossis, Eds. Elsevier, 2011, vol. 29, pp. 171 – 175.

[128] M. S. Germani and W. H. Zoller, “Vapor-phase concentrations of arsenic, selenium, bromine, iodine, and mercury in the stack of a coal-fired power plant,” *Environmental Science & Technology*, vol. 22, no. 9, pp. 1079–1085, 1988.

[129] R. Meij, “Trace element behavior in coal-fired power plants,” *Fuel Processing Technology*, vol. 39, no. 1 - 3, pp. 199 – 217, 1994.

[130] M. Xu, Y. Qiao, C. Zheng, L. Li, and J. Liu, “Modeling of homogeneous mercury speciation using detailed chemical kinetics,” *Combustion and Flame*, vol. 132, no. 1 - 2, pp. 208 – 218, 2003.

[131] B. C. Shepler and K. A. Peterson, “Mercury monoxide: A systematic investigation of its ground electronic state,” *The Journal of Physical Chemistry A*, vol. 107, no. 11, pp. 1783–1787, 2003.

[132] W. Chase, *JANAF thermochemical tables*, ser. Journal of Physical and Chemical Reference data. American Chemical Society, 1986.

[133] N. B. Balabanov and K. A. Peterson, “Mercury and reactive halogens: The thermochemistry of Hg + {Cl_2, Br_2, BrCl, ClO, and BrO},” *The Journal of Physical Chemistry A*, vol. 107, no. 38, pp. 7465–7470, 2003.

[134] J. A. Tossell, “Calculation of the energetics for oxidation of gas-phase elemental Hg by Br and BrO,” *The Journal of Physical Chemistry A*, vol. 107, no. 39, pp. 7804–7808, 2003.

[135] N. B. Balabanov and K. A. Peterson, “Accurate theoretical near-equilibrium potential energy and dipole moment surfaces of HgClO and HgBrO,” *The Journal of Chemical Physics*, vol. 120, no. 14, pp. 6585–6592, 2004.

[136] B. C. Shepler, “Ab initio investigation of the thermochemistry, spectroscopy and dynamics of reactions between mercury and reactive halogen species,” Ph.D. dissertation, Department of Chemistry, Washington State University, August 2006.

[137] N. B. Balabanov, B. C. Shepler, and K. A. Peterson, “Accurate global potential energy surface and reaction dynamics for the ground state of $HgBr_2$,” *The Journal of Physical Chemistry A*, vol. 109, no. 39, pp. 8765–8773, 2005.

[138] F. Raofie and P. A. Ariya, “Product study of the gas-phase BrO-initiated oxidation of Hg^0: Evidence for stable Hg^{1+} compounds,” *Environmental Science & Technology*, vol. 38, no. 16, pp. 4319–4326, 2004.

[139] D. L. Donohoue, “Kinetic studies of the oxidation pathways of gaseous elemental mercury,” Ph.D. dissertation, University of Miami, June 2008.

[140] Y. Byun, M. Cho, W. Namkung, K. Lee, D. J. Koh, and D. N. Shin, “Insight into the unique oxidation chemistry of elemental mercury by chlorine-containing species: Experiment and simulation,” *Environmental Science & Technology*, vol. 44, no. 5, pp. 1624–1629, 2010.

[141] L. Andrews, X. Wang, Y. Gong, T. Schlöder, S. Riedel, and M. J. Franger, “Spectroscopic observation of a group 12 oxyfluoride: A matrix-isolation and quantum-chemical investigation of mercury oxyfluorides,” *Angewandte Chemie International Edition*, vol. 51, no. 33, pp. 8235–8238, 2012.

[142] I. Skare and R. Johansson, “Reactions between mercury vapor and chlorine gas at occupational exposure levels,” *Chemosphere*, vol. 24, no. 11, pp. 1633 – 1644, 1992.

[143] P. A. Ariya, A. Khalizov, and A. Gidas, “Reactions of gaseous mercury with atomic and molecular halogens: Kinetics, product studies, and atmospheric implications,” *The Journal of Physical Chemistry A*, vol. 106, no. 32, pp. 7310–7320, 2002.

[144] F. Frandsen, K. Dam-Johansen, and P. Rasmussen, “Trace elements from combustion and gasification of coal – an equilibrium approach,” *Progress in Energy and Combustion Science*, vol. 20, no. 2, pp. 115 – 138, 1994.

[145] D. Yu, W. J. Morris, R. Erickson, J. O. L. Wendt, A. Fry, and C. L. Senior, “Ash and deposit formation from oxy-coal combustion in a 100 kw test furnace,” *International Journal of Greenhouse Gas Control*, vol. 5, Supplement 1, pp. S159 – S167, 2011, oxyfuel Combustion Technology - Working Toward Demonstration and Commercialisation.

[146] W. P. Linak and J. O. Wendt, “Trace metal transformation mechanisms during coal combustion,” *Fuel Processing Technology*, vol. 39, no. 13, pp. 173 – 198, 1994.

[147] D. J. Hassett and K. E. Eylands, “Mercury capture on coal combustion fly ash,” *Fuel*, vol. 78, no. 2, pp. 243 – 248, 1999.

[148] M. A. López-Antón, M. Díaz-Somoano, and M. R. Martínez-Tarazona, “Mercury retention by fly ashes from coal combustion: Influence of the unburned carbon content,” *Industrial & Engineering Chemistry Research*, vol. 46, no. 3, pp. 927–931, 2007.

[149] P. Abad-Valle, M. Lopez-Anton, M. Diaz-Somoano, and M. Martinez-Tarazona, “The role of unburned carbon concentrates from fly ashes in the oxidation and retention of mercury,” *Chemical Engineering Journal*, vol. 174, no. 1, pp. 86 – 92, 2011.

[150] F. Wang, S. Wang, Y. Meng, L. Zhang, Q. Wu, and J. Hao, “Mechanisms and roles of fly ash compositions on the adsorption and oxidation of mercury in flue gas from coal combustion,” *Fuel*, vol. 163, pp. 232 – 239, 2016.

[151] J.-E. Jung, D. Geatches, K. Lee, S. Aboud, J. Gordon E. Brown, and J. Wilcox, “First-principles investigation of mercury adsorption on the α-Fe_2O_3-(1102) surface,” *The Journal of Physical Chemistry C*, vol. 119, no. 47, pp. 26 512–26 518, 2015.

[152] T. Sakulpitakphon, J. C. Hower, A. S. Trimble, W. H. Schram, and G. A. Thomas, “Mercury capture by fly ash: Study of the combustion of a high-mercury coal at a utility boiler,” *Energy & Fuels*, vol. 14, no. 3, pp. 727–733, 2000.

[153] S. D. Serre and G. D. Silcox, “Adsorption of elemental mercury on the residual carbon in coal fly ash,” *Industrial & Engineering Chemistry Research*, vol. 39, no. 6, pp. 1723–1730, 2000.

[154] T. Brown and V. Lissianski, “First full-scale demonstration of mercury control in alberta,” *Fuel Processing Technology*, vol. 90, no. 11, pp. 1412 – 1418, 2009.

[155] J. C. Hower, C. L. Senior, E. M. Suuberg, R. H. Hurt, J. L. Wilcox, and E. S. Olson, “Mercury capture by native fly ash carbons in coal-fired power plants,” *Progress in Energy and Combustion Science*, vol. 36, no. 4, pp. 510 – 529, 2010.

[156] T. R. Carey, O. W. H. Jr., C. F. Richardson, R. Chang, and F. B. Meserole, "Factors affecting mercury control in utility flue gas using activated carbon," *Journal of the Air & Waste Management Association*, vol. 48, no. 12, pp. 1166–1174, 1998.

[157] S. J. Miller, G. E. Dunham, E. S. Olson, and T. D. Brown, "Flue gas effects on a carbon-based mercury sorbent," *Fuel Processing Technology*, vol. 6566, pp. 343 – 363, 2000.

[158] R. Ochiai, M. A. Uddin, E. Sasaoka, and S. Wu, "Effects of hcl and so2 concentration on mercury removal by activated carbon sorbents in coal-derived flue gas," *Energy & Fuels*, vol. 23, no. 10, pp. 4734–4739, 2009.

[159] I. Diamantopoulou, G. Skodras, and G. Sakellaropoulos, "Sorption of mercury by activated carbon in the presence of flue gas components," *Fuel Processing Technology*, vol. 91, no. 2, pp. 158 – 163, 2010.

[160] H.-C. Hsi and C.-T. Chen, "Influences of acidic/oxidizing gases on elemental mercury adsorption equilibrium and kinetics of sulfur-impregnated activated carbon," *Fuel*, vol. 98, pp. 229 – 235, 2012.

[161] N. D. Hutson, B. C. Attwood, and K. G. Scheckel, "Xas and xps characterization of mercury binding on brominated activated carbon," *Environmental Science & Technology*, vol. 41, no. 5, pp. 1747–1752, 2007.

[162] E. Sasmaz, A. Kirchofer, A. D. Jew, A. Saha, D. Abram, T. F. Jaramillo, and J. Wilcox, "Mercury chemistry on brominated activated carbon," *Fuel*, vol. 99, pp. 188 – 196, 2012.

[163] A. Azenkeng, J. D. Laumb, R. R. Jensen, E. S. Olson, S. A. Benson, and M. R. Hoffmann, "Carbene proton attachment energies: Theoretical study," *The Journal of Physical Chemistry A*, vol. 112, no. 23, pp. 5269–5277, 2008.

[164] E. Freeman, Y.-M. Gao, R. Hurt, and E. Suuberg, "Interactions of carbon-containing fly ash with commercial air-entraining admixtures for concrete," *Fuel*, vol. 76, no. 8, pp. 761 – 765, 1997.

[165] Y.-M. Gao, H.-S. Shim, R. H. Hurt, E. M. Suuberg, and N. Y. C. Yang, "Effects of carbon on air entrainment in fly ash concrete: The role of soot and carbon black," *Energy & Fuels*, vol. 11, no. 2, pp. 457–462, 1997.

[166] K. Pedersen, A. Jensen, M. Berg, L. Olsen, and K. Dam-Johansen, "The effect of combustion conditions in a full-scale low-nox coal fired unit on fly ash properties for its application in concrete mixtures," *Fuel Processing Technology*, vol. 90, no. 2, pp. 180 – 185, 2009.

[167] W. J. Morris, D. Yu, and J. O. Wendt, "Soot, unburned carbon and ultrafine particle emissions from air- and oxy-coal flames," *Proceedings of the Combustion Institute*, vol. 33, no. 2, pp. 3415 – 3421, 2011.

[168] W. J. Morris, D. Yu, and J. O. Wendt, "A comparison of soot, fine particle and sodium emissions for air- and oxy-coal flames, with recycled flue gases of various compositions," *Proceedings of the Combustion Institute*, vol. 34, no. 2, pp. 3453 – 3461, 2013.

[169] C. L. Senior, A. F. Sarofim, T. Zeng, J. J. Helble, and R. Mamani-Paco, "Gas-phase transformations of mercury in coal-fired power plants," *Fuel Processing Technology*, vol. 63, no. 23, pp. 197 – 213, 2000.

[170] K. J. Laidler, "The development of the arrhenius equation," *Journal of Chemical Education*, vol. 61, no. 6, p. 494, 1984.

[171] W. C. Gardiner, "Temperature dependence of bimolecular gas reaction rates," *Accounts of Chemical Research*, vol. 10, no. 9, pp. 326–331, 1977.

[172] J. Troe, "Atom and radical recombination reactions," *Annual Review of Physical Chemistry*, vol. 29, no. 1, pp. 223–250, 1978.

[173] M. J. Pilling and P. W. Seakins, *Reaction Kinetics*. Oxford University Press, 1995.

[174] J. E. Morgan and H. I. Schiff, "Recombination of oxygen atoms in the presence of inert gases," *The Journal of Chemical Physics*, vol. 38, no. 7, pp. 1495–1500, 1963.

[175] M. F. R. Mulcahy and D. J. Williams, "Kinetics of combination of oxygen atoms with oxygen molecules," *Trans. Faraday Soc.*, vol. 64, pp. 59–70, 1968.

[176] H. Hippler, J. Troe, and H. J. Wendelken, "Collisional deactivation of vibrationally highly excited polyatomic molecules. II. direct observations for excited toluene," *The Journal of Chemical Physics*, vol. 78, no. 11, pp. 6709–6717, 1983.

[177] C. J. Weng, T. I. Ho, and T. M. Su, "Laser photolysis study of the recombination reactions of atomic chlorine in inert gases," *The Journal of Physical Chemistry*, vol. 91, no. 20, pp. 5235–5238, 1987.

[178] R. P. Widman and B. A. DeGraff, "Gas-phase recombination of chlorine atoms," *The Journal of Physical Chemistry*, vol. 77, no. 11, pp. 1325–1328, 1973.

[179] J. Wilcox, D. C. Marsden, and P. Blowers, "Evaluation of basis sets and theoretical methods for estimating rate constants of mercury oxidation reactions involving chlorine," *Fuel Processing Technology*, vol. 85, no. 5, pp. 391 – 400, 2004.

[180] P. H. Taylor, R. Mallipeddi, and T. Yamada, "LP/LIF study of the formation and consumption of mercury (I) chloride: Kinetics of mercury chlorination," *Chemosphere*, vol. 61, no. 5, pp. 685 – 692, 2005.

[181] D. L. Donohoue, D. Bauer, and A. J. Hynes, "Temperature and pressure dependent rate coefficients for the reaction of Hg with Cl and the reaction of Cl with Cl: A pulsed laser photolysis-pulsed laser induced fluorescence study," *The Journal of Physical Chemistry A*, vol. 109, no. 34, pp. 7732–7741, 2005.

[182] D. L. Donohoue, D. Bauer, B. Cossairt, and A. J. Hynes, "Temperature and pressure dependent rate coefficients for the reaction of Hg with Br and the reaction of Br with Br: A pulsed laser photolysis-pulsed laser induced fluorescence study," *The Journal of Physical Chemistry A*, vol. 110, no. 21, pp. 6623–6632, 2006.

[183] J. R. Edwards, R. K. Srivastava, and J. D. Kilgroe, "A study of gas-phase mercury speciation using detailed chemical kinetics," *Journal of the Air & Waste Management Association*, vol. 51, no. 6, pp. 869–877, 2001.

[184] A. F. Khalizov, B. Viswanathan, P. Larregaray, and P. A. Ariya, "A theoretical study on the reactions of hg with halogens: Atmospheric implications," *The Journal of Physical Chemistry A*, vol. 107, no. 33, pp. 6360–6365, 2003.

[185] J. Wilcox, J. Robles, D. C. J. Marsden, and P. Blowers, "Theoretically predicted rate constants for mercury oxidation by hydrogen chloride in coal combustion flue gases," *Environmental Science & Technology*, vol. 37, no. 18, pp. 4199–4204, 2003.

[186] J. Qiu, R. O. Sterling, and J. J. Helble, "Development of an improved model for determining the effects of SO_2 on homogeneous mercury oxidation," in *28th International Technical Conference on Coal Utilization and Fuel Systems*, Clearwater, FL, USA, 2003.

[187] M. E. Goodsite, J. M. C. Plane, and H. Skov, "A theoretical study of the oxidation of Hg^0 to $HgBr_2$ in the troposphere," *Environmental Science & Technology*, vol. 38, no. 6, pp. 1772–1776, 2004.

[188] B. C. Shepler, N. B. Balabanov, and K. A. Peterson, "Hg + Br $\longrightarrow$ HgBr recombination and collision-induced dissociation dynamics," *The Journal of Chemical Physics*, vol. 127, no. 16, p. 164304, 2007.

[189] B. Cauch, "Experimental investigation and kinetic modeling of homogeneous mercury oxidation by halogens," Master's thesis, The University of Utah, 2008.

[190] J. Liu, W. Qu, J. Yuan, S. Wang, J. Qiu, and C. Zheng, "Theoretical studies of properties and reactions involving mercury species present in combustion flue gases," *Energy & Fuels*, vol. 24, no. 1, pp. 117–122, 2010.

[191] J. Wilcox and T. Okano, "Ab initio-based mercury oxidation kinetics via bromine at postcombustion flue gas conditions," *Energy & Fuels*, vol. 25, no. 4, pp. 1348–1356, 2011.

[192] B. Krishnakumar and J. J. Helble, "Determination of transition state theory rate constants to describe mercury oxidation in combustion systems mediated by cl, cl2, hcl and hocl," *Fuel Processing Technology*, vol. 94, no. 1, pp. 1 – 9, 2012.

[193] W. Qing, Y. Bowen, and B. Jingru, "Rate constant computation on some chlorination reactions of hg in combustion flue gas," *Energy Procedia*, vol. 14, no. 0, pp. 66 – 72, 2012.

[194] R. A. Ogg, H. C. Martin, and P. A. Leighton, "Kinetics of the vapor phase reaction of mercury and halogens," *Journal of the American Chemical Society*, vol. 58, no. 10, pp. 1922–1924, 1936.

[195] D. G. Horne, R. Gosavi, and O. P. Strausz, "Reactions of metal atoms. i. the combination of mercury and chlorine atoms and the dimerization of hgcl," *The Journal of Chemical Physics*, vol. 48, no. 10, pp. 4758–4764, 1968.

[196] G. Greig, H. E. Gunning, and O. P. Strausz, "Reactions of metal atoms. ii. the combination of mercury and bromine atoms and the dimerization of hgbr," *The Journal of Chemical Physics*, vol. 52, no. 7, pp. 3684–3690, 1970.

[197] S. Niksa, B. Padak, B. Krishnakumar, and C. V. Naik, "Process chemistry of Br addition to utility flue gas for Hg emissions control," *Energy & Fuels*, vol. 24, no. 2, pp. 1020–1029, 2010.

[198] M. Gharebaghi, K. Hughes, R. Porter, M. Pourkashanian, and A. Williams, "Mercury speciation in air-coal and oxy-coal combustion: A modelling approach," *Proceedings of the Combustion Institute*, vol. 33, no. 2, pp. 1779 – 1786, 2011.

[199] A. Fry, B. Cauch, G. D. Silcox, J. S. Lighty, and C. L. Senior, "Experimental evaluation of the effects of quench rate and quartz surface area on homogeneous mercury oxidation," *Proceedings of the Combustion Institute*, vol. 31, no. 2, pp. 2855 – 2861, 2007.

[200] S. Niksa and N. Fujiwara, "Estimating Hg emissions from coal-fired power stations in China," *Fuel*, vol. 88, no. 1, pp. 214 – 217, 2009.

[201] T. Okano, "High temperature mercury oxidation kinetics via bromine mechanisms," Master's thesis, Worcester Polytechnic Institute, May 2009.

[202] R. Jovanović, B. Rašuo, P. Stefanović, D. Cvetinović, and B. Swiatkowski, "Numerical investigation of pulverized coal jet flame characteristics under different oxy-fuel conditions," *International Journal of Heat and Mass Transfer*, vol. 58, no. 1-2, pp. 654 – 662, 2013.

[203] B. M. Franchetti, F. C. Marincola, S. Navarro-Martinez, and A. M. Kempf, "Large eddy simulation of a pulverised coal jet flame," *Proceedings of the Combustion Institute*, vol. 34, no. 2, pp. 2419 – 2426, 2013.

[204] J. Cai, M. Handa, and M. F. Modest, "Eulerian-eulerian multi-fluid methods for pulverized coal flames with nongray radiation," *Combustion and Flame*, vol. 162, no. 4, pp. 1550 – 1565, 2014.

[205] F. Lockwood and A. Salooja, "The prediction of some pulverized bituminous coal flames in a furnace," *Combustion and Flame*, vol. 54, no. 13, pp. 23 – 32, 1983.

[206] B. M. Visser, J. P. Smart, W. L. van de Kamp, and R. Weber, "Measurements and predictions of quarl zone properties of swirling pulverised coal flames," *Symposium (International) on Combustion*, vol. 23, no. 1, pp. 949 – 955, 1991.

[207] A. A. F. Peters and R. Weber, "Mathematical modeling of a 2.4 mw swirling pulverized coal flame," *Combustion Science and Technology*, vol. 122, no. 1-6, pp. 131–182, 1997.

[208] R. I. Backreedy, L. M. Fletcher, L. Ma, M. Pourkashanian, and A. Williams, "Modelling pulverised coal combustion using a detailed coal combustion model," *Combustion Science and Technology*, vol. 178, no. 4, pp. 763–787, 2006.

[209] M. Gharebaghi, R. Irons, L. Ma, M. Pourkashanian, and A. Pranzitelli, "Large eddy simulation of oxy-coal combustion in an industrial combustion test facility," *International Journal of Greenhouse Gas Control*, vol. 5, Supplement 1, pp. S100 – S110, 2011.

[210] P. Edge, S. Gubba, L. Ma, R. Porter, M. Pourkashanian, and A. Williams, “LES modelling of air and oxy-fuel pulverised coal combustion–impact on flame properties,” *Proceedings of the Combustion Institute*, vol. 33, no. 2, pp. 2709 – 2716, 2011.

[211] M. Müller, U. Schnell, S. Grathwohl, J. Maier, and G. Scheffknecht, “Evaluation of oxy-coal combustion modelling at semi-industrial scale,” *Energy Procedia*, vol. 23, pp. 197 – 206, 2012.

[212] M. Stöllinger, B. Naud, D. Roekaerts, N. Beishuizen, and S. Heinz, “PDF modeling and simulations of pulverized coal combustion – part 2: Application,” *Combustion and Flame*, vol. 160, no. 2, pp. 396 – 410, 2013.

[213] G. Olenik, O. Stein, and A. Kronenburg, “LES of swirl-stabilised pulverised coal combustion in IFRF furnace no. 1,” *Proceedings of the Combustion Institute*, vol. 35, no. 3, pp. 2819–2828, 2015.

[214] M. Rabaçal, B. M. Franchetti, F. C. Marincola, F. Proch, M. Costa, C. Hasse, and A. M. Kempf, “Large eddy simulation of coal combustion in a large-scale laboratory furnace,” *Proceedings of the Combustion Institute*, vol. 35, no. 3, pp. 3609–3617, 2015.

[215] C. Galletti, G. Coraggio, and L. Tognotti, “Modelling oxy-coal flames in a semi-industrial furnace,” *Journal of the International Flame Research Foundation*, 2014.

[216] A. J. Black, “Oxy-fuel combustion for carbon capture using computational fluid dynamics,” Ph.D. dissertation, Energy Technology and Innovation Innitiative, University of Leeds, May 2014.

[217] P. J. Edge, P. J. Heggs, M. Pourkashanian, and P. L. Stephenson, “Integrated fluid dynamics-process modelling of a coal-fired power plant with carbon capture,” *Applied Thermal Engineering*, vol. 60, no. 12, pp. 242 – 250, 2013.

[218] S. Black, J. Szuhánszki, A. Pranzitelli, L. Ma, P. J. Stanger, D. B. Ingham, and M. Pourkashanian, “Effects of firing coal and biomass under oxy-fuel conditions in a power plant boiler using CFD modelling,” *Fuel*, vol. 113, pp. 780 – 786, 2013.

[219] J.-E. A. Kim, C. Ryu, W. Yang, Y. J. Kim, H.-Y. Park, and H.-P. Kim, “Assessment of combustion and heat transfer in youngdong 100 MWe retrofit boiler for demonstration of oxy-coal combustion,” *International Journal of Greenhouse Gas Control*, vol. 17, pp. 250 – 258, 2013.

[220] T. F. Smith, Z. F. Shen, and J. N. Friedman, “Evaluation of coefficients for the weighted sum of gray gases model,” *Journal of Heat Transfer*, vol. 104, no. 4, pp. 602–608, 1982.

[221] J. P. Smart, P. O’Nions, and G. S. Riley, “Radiation and convective heat transfer, and burnout in oxy-coal combustion,” *Fuel*, vol. 89, no. 9, pp. 2468 – 2476, 2010.

[222] A. Gupta, D. Haworth, and M. Modest, “Turbulence-radiation interactions in large-eddy simulations of luminous and nonluminous nonpremixed flames,” *Proceedings of the Combustion Institute*, vol. 34, no. 1, pp. 1281 – 1288, 2013.

[223] M. F. Modest, *Radiative heat transfer*, 2nd ed. Academic Press, 2003.

[224] L. Rothman, I. Gordon, R. Barber, H. Dothe, R. Gamache, A. Goldman, V. Perevalov, S. Tashkun, and J. Tennyson, "HITEMP, the high-temperature molecular spectroscopic database," *Journal of Quantitative Spectroscopy and Radiative Transfer*, vol. 111, no. 15, pp. 2139 – 2150, 2010.

[225] M. F. Modest, "Further development of the elliptic PDE formulation of the P_N approximation and its Marshak boundary conditions," *Numerical Heat Transfer, Part B: Fundamentals*, vol. 62, no. 2-3, pp. 181–202, 2012.

[226] M. F. Modest and J. Yang, "Elliptic PDE formulation and boundary conditions of the spherical harmonics method of arbitrary order for general three-dimensional geometries," *Journal of Quantitative Spectroscopy and Radiative Transfer*, vol. 109, no. 9, pp. 1641 – 1666, 2008.

[227] J. Yang and M. F. Modest, "Elliptic PDE formulation of general, three-dimensional high-order -approximations for radiative transfer," *Journal of Quantitative Spectroscopy and Radiative Transfer*, vol. 104, no. 2, pp. 217 – 227, 2007.

[228] R. Marquez and M. Modest, "Implementation of the Pn-approximation for radiative heat transfer on openfoam," in *ASME 2013 Heat Transfer Summer Conference collocated with the ASME 2013 7th International Conference on Energy Sustainability and the ASME 2013 11th International Conference on Fuel Cell Science, Engineering and Technology*. American Society of Mechanical Engineers, 2013.

[229] W. Ge, R. Marquez, M. F. Modest, and S. P. Roy, "Implementation of high-order spherical harmonics methods for radiative heat transfer on openfoam," *Journal of Heat Transfer*, vol. 137, no. 5, p. 052701, 2015.

[230] W. Ge, M. F. Modest, and R. Marquez, "Two-dimensional axisymmetric formulation of high order spherical harmonics methods for radiative heat transfer," *Journal of Quantitative Spectroscopy and Radiative Transfer*, vol. 156, pp. 58–66, 2015.

[231] F. Liu, E. S. Garbett, and J. Swithenbank, "Effects of anisotropic scattering on radiative heat transfer using the p1-approximation," *International Journal of Heat and Mass Transfer*, vol. 35, no. 10, pp. 2491 – 2499, 1992.

[232] R. Yadav, A. Kushari, A. K. Verma, and V. Eswaran, "Weighted sum of gray gas modeling for nongray radiation in combusting environment using the hybrid solution methodology," *Numerical Heat Transfer, Part B: Fundamentals*, vol. 64, no. 2, pp. 174–197, 2013.

[233] D. B. Olfe, "A modification of the differential approximation for radiative transfer." *AIAA Journal*, vol. 5, no. 4, pp. 638–643, 1967.

[234] M. F. Modest, "Two-dimensional radiative equilibrium of a gray medium in a plane layer bounded by gray nonisothermal walls," *Journal of Heat Transfer*, vol. 96, no. 4, pp. 483–488, 1974.

[235] F. Lockwood and N. G. Shah, "A new radiation solution method for incorporation in general combustion prediction procedures," *Symposium (International) on Combustion*, vol. 18, no. 1, pp. 1405 – 1414, 1981.

[236] J. C. Henson and W. M. G. Malalasekera, “Comparison of the discrete transfer and monte carlo methods for radiative heat transfer in three-dimensional nonhomogeneous scattering media,” *Numerical Heat Transfer, Part A: Applications*, vol. 32, no. 1, pp. 19–36, 1997.

[237] N. Selçuk and N. Kayakol, “Evaluation of discrete ordinates method for radiative transfer in rectangular furnaces,” *International Journal of Heat and Mass Transfer*, vol. 40, no. 2, pp. 213 – 222, 1997.

[238] P. J. Coelho, J. M. Gonçalves, M. G. Carvalho, and D. N. Trivic, “Modelling of radiative heat transfer in enclosures with obstacles,” *International Journal of Heat and Mass Transfer*, vol. 41, no. 4–5, pp. 745 – 756, 1998.

[239] W. A. Fiveland, “Discrete-ordinates solutions of the radiative transport equation for rectangular enclosures,” *Journal of Heat Transfer*, vol. 106, p. 699, 1984.

[240] G. D. Raithby, “Discussion of the finite-volume method for radiation, and its application using 3d unstructured meshes,” *Numerical Heat Transfer, Part B: Fundamentals*, vol. 35, no. 4, pp. 389–405, 1999.

[241] P. J. Coelho, “The role of ray effects and false scattering on the accuracy of the standard and modified discrete ordinates methods,” *Journal of Quantitative Spectroscopy and Radiative Transfer*, vol. 73, no. 2–5, pp. 231 – 238, 2002, third International Symposium on Radiative Transfer.

[242] P. J. Coelho, “Advances in the discrete ordinates and finite volume methods for the solution of radiative heat transfer problems in participating media,” *Journal of Quantitative Spectroscopy and Radiative Transfer*, vol. 145, pp. 121 – 146, 2014.

[243] T.-K. Kim and H. S. Lee, “Radiative transfer in two-dimensional anisotropic scattering media with collimated incidence,” *Journal of Quantitative Spectroscopy and Radiative Transfer*, vol. 42, no. 3, pp. 225 – 238, 1989.

[244] W. J. Wiscombe, “On initialization, error and flux conservation in the doubling method,” *Journal of Quantitative Spectroscopy and Radiative Transfer*, vol. 16, no. 8, pp. 637 – 658, 1976.

[245] P. Boulet, A. Collin, and J. L. Consalvi, “On the finite volume method and the discrete ordinates method regarding radiative heat transfer in acute forward anisotropic scattering media,” *Journal of Quantitative Spectroscopy and Radiative Transfer*, vol. 104, no. 3, pp. 460 – 473, 2007.

[246] T.-K. Kim and H. Lee, “Effect of anisotropic scattering on radiative heat transfer in two-dimensional rectangular enclosures,” *International Journal of Heat and Mass Transfer*, vol. 31, no. 8, pp. 1711 – 1721, 1988.

[247] E. H. Chui and G. D. Raithby, “Computation of radiant heat transfer on a nonorthogonal mesh using the finite-volume method,” *Numerical Heat Transfer, Part B: Fundamentals*, vol. 23, no. 3, pp. 269–288, 1993.

[248] H. C. Hottel and E. S. Cohen, “Radiant heat exchange in a gas-filled enclosure: Allowance for nonuniformity of gas temperature,” *AIChE Journal*, vol. 4, no. 1, pp. 3–14, 1958.

[249] H. C. Hottel and A. F. Sarofim, *Radiative transfer*, ser. McGraw-Hill series in mechanical engineering. McGraw-Hill, 1967.

[250] M. G. Carvalho and T. L. Farias, "Modelling of heat transfer in radiating and combusting systems," *Chemical Engineering Research and Design*, vol. 76, no. 2, pp. 175 – 184, 1998, 5th UK National Heat Transfer Conference.

[251] M. H. Bordbar, K. Myöhänen, and T. Hyppänen, "Coupling of a radiative heat transfer model and a three-dimensional combustion model for a circulating fluidized bed furnace," *Applied Thermal Engineering*, vol. 76, pp. 344 – 356, 2015.

[252] L. Rothman, I. Gordon, Y. Babikov, A. Barbe, D. C. Benner, P. Bernath, M. Birk, L. Bizzocchi, V. Boudon, L. Brown, A. Campargue, K. Chance, E. Cohen, L. Coudert, V. Devi, B. Drouin, A. Fayt, J.-M. Flaud, R. Gamache, J. Harrison, J.-M. Hartmann, C. Hill, J. Hodges, D. Jacquemart, A. Jolly, J. Lamouroux, R. L. Roy, G. Li, D. Long, O. Lyulin, C. Mackie, S. Massie, S. Mikhailenko, H. Mller, O. Naumenko, A. Nikitin, J. Orphal, V. Perevalov, A. Perrin, E. Polovtseva, C. Richard, M. Smith, E. Starikova, K. Sung, S. Tashkun, J. Tennyson, G. Toon, V. Tyuterev, and G. Wagner, "The HITRAN2012 molecular spectroscopic database," *Journal of Quantitative Spectroscopy and Radiative Transfer*, vol. 130, pp. 4 – 50, 2013.

[253] S. A. Tashkun and V. I. Perevalov, "CDSD-4000: High-resolution, high-temperature carbon dioxide spectroscopic databank," *Journal of Quantitative Spectroscopy and Radiative Transfer*, vol. 112, no. 9, pp. 1403 – 1410, 2011.

[254] L. ROTHMAN, C. RINSLAND, A. GOLDMAN, S. MASSIE, D. EDWARDS, J.-M. FLAUD, A. PERRIN, C. CAMY-PEYRET, V. DANA, J.-Y. MANDIN, J. SCHROEDER, A. MCCANN, R. GAMACHE, R. WATTSON, K. YOSHINO, K. CHANCE, K. JUCKS, L. BROWN, V. NEMTCHINOV, and P. VARANASI, "The HITRAN molecular spectroscopic database and HAWKS (HITRAN atmospheric workstation): 1996 edition," *Journal of Quantitative Spectroscopy and Radiative Transfer*, vol. 60, no. 5, pp. 665 – 710, 1998.

[255] J. Humlíček, "Optimized computation of the voigt and complex probability functions," *Journal of Quantitative Spectroscopy and Radiative Transfer*, vol. 27, no. 4, pp. 437 – 444, 1982.

[256] M. Alberti, R. Weber, M. Mancini, A. Fateev, and S. Clausen, "Validation of HITEMP-2010 for carbon dioxide and water vapour at high temperatures and atmospheric pressures in 450–7600cm$^-$1 spectral range," *Journal of Quantitative Spectroscopy and Radiative Transfer*, vol. 157, pp. 14 – 33, 2015.

[257] F. R. Centeno, R. Brittes, F. H. França, and O. A. Ezekoye, "Evaluation of gas radiation heat transfer in a 2D axisymmetric geometry using the line-by-line integration and WSGG models," *Journal of Quantitative Spectroscopy and Radiative Transfer*, vol. 156, pp. 1 – 11, 2015.

[258] S. P. Bharadwaj and M. F. Modest, "Medium resolution transmission measurements of at high temperature–an update," *Journal of Quantitative Spectroscopy and Radiative Transfer*, vol. 103, no. 1, pp. 146 – 155, 2007.

[259] V. Becher, S. Clausen, A. Fateev, and H. Spliethoff, “Validation of spectral gas radiation models under oxyfuel conditions. part a: Gas cell experiments,” *International Journal of Greenhouse Gas Control*, vol. 5, Supplement 1, pp. S76 – S99, 2011.

[260] A. Soufiani, J. Hartmann, and J. Taine, “Validity of band-model calculations for CO_2 and H_2O applied to radiative properties and conductive-radiative transfer,” *Journal of Quantitative Spectroscopy and Radiative Transfer*, vol. 33, no. 3, pp. 243–257, 1985.

[261] A. Soufiani and J. Taine, “Experimental and theoretical studies of combined radiative and convective transfer in CO_2 and H_2O laminar flows,” *International Journal of Heat and Mass Transfer*, vol. 32, no. 3, pp. 477 – 486, 1989.

[262] A. Soufiani and J. Taine, “High temperature gas radiative property parameters of statistical narrow-band model for H_2O, CO_2 and CO, and correlated-k model for H_2O and CO_2,” *International Journal of Heat and Mass Transfer*, vol. 40, no. 4, pp. 987 – 991, 1997.

[263] P. Rivière and A. Soufiani, “Updated band model parameters for H_2O, CO_2, CH_4 and CO radiation at high temperature,” *International Journal of Heat and Mass Transfer*, vol. 55, pp. 3349 – 3358, 2012.

[264] V. Becher, J.-P. Bohn, P. Dias, and H. Spliethoff, “Validation of spectral gas radiation models under oxyfuel conditions–part b: Natural gas flame experiments,” *International Journal of Greenhouse Gas Control*, vol. 5, Supplement 1, pp. S66 – S75, 2011.

[265] H. Chu, F. Liu, and H. Zhou, “Calculations of gas thermal radiation transfer in one-dimensional planar enclosure using LBL and SNB models,” *International Journal of Heat and Mass Transfer*, vol. 54, pp. 4736 – 4745, 2011.

[266] R. M. Goody, “A statistical model for water-vapour absorption,” *Quarterly Journal of the Royal Meteorological Society*, vol. 78, no. 336, pp. 165–169, 1952.

[267] W. Malkmus, “Random lorentz band model with exponential-tailed S^{-1} line-intensity distribution function,” *Journal of the Optical Society of America*, vol. 57, no. 3, pp. 323–329, Mar 1967.

[268] V. Becher, A. Goanta, and H. Spliethoff, “Validation of spectral gas radiation models under oxyfuel conditions–part c: Validation of simplified models,” *International Journal of Greenhouse Gas Control*, vol. 11, pp. 34 – 51, 2012.

[269] W. L. Godson, “The evaluation of infra-red radiative fluxes due to atmospheric water vapour,” *Quarterly Journal of the Royal Meteorological Society*, vol. 79, no. 341, pp. 367–379, 1953.

[270] T. K. Kim, J. A. Menart, and H. S. Lee, “Nongray radiative gas analyses using the S-N discrete ordinates method,” *Journal of Heat Transfer*, vol. 113, no. 4, pp. 946–952, November 1991.

[271] F. Liu, O. L. Gülder, G. J. Smallwood, and Y. Ju, “Non-grey gas radiative transfer analyses using the statistical narrow-band model,” *International Journal of Heat and Mass Transfer*, vol. 41, no. 14, pp. 2227 – 2236, 1998.

[272] F. Liu, "Numerical solutions of three-dimensional non-grey gas radiative transfer using the statistical narrow-band model," *Journal of heat transfer*, vol. 121, no. 1, pp. 200–203, 1999.

[273] S. J. Young, "Nonisothermal band model theory," *Journal of Quantitative Spectroscopy and Radiative Transfer*, vol. 18, no. 1, pp. 1 – 28, 1977.

[274] L. Pierrot, A. Soufiani, and J. Taine, "Accuracy of narrow-band and global models for radiative transfer in H_2O, CO_2, and H_2O-CO_2 mixtures at high temperature," *Journal of Quantitative Spectroscopy and Radiative Transfer*, vol. 62, no. 5, pp. 523 – 548, 1999.

[275] J. A. Menart, H. S. Lee, and T.-K. Kim, "Discrete ordinates solutions of nongray radiative transfer with diffusely reflecting walls," *Journal of heat transfer*, vol. 115, no. 1, pp. 184–193, 1993.

[276] R. Goody, R. West, L. Chen, and D. Crisp, "The correlated-k method for radiation calculations in nonhomogeneous atmospheres," *Journal of Quantitative Spectroscopy and Radiative Transfer*, vol. 42, no. 6, pp. 539 – 550, 1989.

[277] K. C. Tang and M. Q. Brewster, "K-distribution analysis of gas radiation with nongray, emitting, absorbing, and anisotropic scattering particles," *Journal of heat transfer*, vol. 116, no. 4, pp. 980–985, 1994.

[278] V. Goutiere, F. Liu, and A. Charette, "An assessment of real-gas modelling in 2d enclosures," *Journal of Quantitative Spectroscopy and Radiative Transfer*, vol. 64, no. 3, pp. 299 – 326, 2000.

[279] M. F. Modest, "Narrow-band and full-spectrum k-distributions for radiative heat transfer–correlated-k vs. scaling approximation," *Journal of Quantitative Spectroscopy and Radiative Transfer*, vol. 76, no. 1, pp. 69 – 83, 2003.

[280] A. A. Lacis and V. Oinas, "A description of the correlated k distribution method for modeling nongray gaseous absorption, thermal emission, and multiple scattering in vertically inhomogeneous atmospheres," *Journal of Geophysical Research*, vol. 96, no. 15, pp. 9027–9064, 1991.

[281] F. Liu and G. J. Smallwood, "An efficient approach for the implementation of the SNB based correlated-k method and its evaluation," *Journal of Quantitative Spectroscopy and Radiative Transfer*, vol. 84, no. 4, pp. 465 – 475, 2004.

[282] M. F. Modest and R. J. Riazzi, "Assembly of full-spectrum k-distributions from a narrow-band database; effects of mixing gases, gases and nongray absorbing particles, and mixtures with nongray scatterers in nongray enclosures," *Journal of Quantitative Spectroscopy and Radiative Transfer*, vol. 90, no. 2, pp. 169 – 189, 2005.

[283] P. Rivière, A. Soufiani, and J. Taine, "Correlated-k and fictitious gas methods for H_2O near 2.7 μm," *Journal of Quantitative Spectroscopy and Radiative Transfer*, vol. 48, no. 2, pp. 187 – 203, 1992.

[284] M. F. Modest and H. Zhang, "The full-spectrum correlated-k distribution for thermal radiation from molecular gas-particulate mixtures," *Journal of Heat Transfer*, vol. 124, no. 1, pp. 30–38, 2002.

[285] D. K. Edwards and W. A. Menard, "Comparison of models for correlation of total band absorption," *Applied Optics*, vol. 3, no. 5, pp. 621–625, May 1964.

[286] C. Yin, L. C. R. Johansen, L. A. Rosendahl, and S. K. Kær, "New weighted sum of gray gases model applicable to computational fluid dynamics (CFD) modeling of oxy-fuel combustion: Derivation, validation, and implementation," *Energy & Fuels*, vol. 24, no. 12, pp. 6275–6282, 2010.

[287] M. F. Modest, "The weighted-sum-of-gray-gases model for arbitrary solution methods in radiative transfer," *Journal of Heat Transfer (Transactions of the ASME (American Society of Mechanical Engineers), Series C);(United States)*, vol. 113, no. 3, pp. 650–656, 1991.

[288] C. Galletti, G. Coraggio, and L. Tognotti, "Numerical investigation of oxy-natural-gas combustion in a semi-industrial furnace: Validation of CFD sub-models," *Fuel*, vol. 109, pp. 445 – 460, 2013.

[289] G. Krishnamoorthy, "A comparison of gray and non-gray modeling approaches to radiative transfer in pool fire simulations," *Journal of Hazardous Materials*, vol. 182, no. 1–3, pp. 570 – 580, 2010.

[290] P. Nakod, G. Krishnamoorthy, M. Sami, and S. Orsino, "A comparative evaluation of gray and non-gray radiation modeling strategies in oxy-coal combustion simulations," *Applied Thermal Engineering*, vol. 54, no. 2, pp. 422 – 432, 2013.

[291] R. Johansson, B. Leckner, K. Andersson, and F. Johnsson, "Account for variations in the H_2O to CO_2 molar ratio when modelling gaseous radiative heat transfer with the weighted-sum-of-grey-gases model," *Combustion and Flame*, vol. 158, no. 5, pp. 893 – 901, 2011.

[292] T. Kangwanpongpan, F. H. França, R. C. da Silva, P. S. Schneider, and H. J. Krautz, "New correlations for the weighted-sum-of-gray-gases model in oxy-fuel conditions based on hitemp 2010 database," *International Journal of Heat and Mass Transfer*, vol. 55, no. 25-26, pp. 7419 – 7433, 2012.

[293] G. Krishnamoorthy, "A new weighted-sum-of-gray-gases model for oxy-combustion scenarios," *International Journal of Energy Research*, vol. 37, no. 14, pp. 1752–1763, 2012.

[294] M. H. Bordbar, G. Węcel, and T. Hyppänen, "A line by line based weighted sum of gray gases model for inhomogeneous CO_2-H_2O mixture in oxy-fired combustion," *Combustion and Flame*, vol. 161, no. 9, pp. 2435 – 2445, 2014.

[295] C. Yin, "Refined weighted sum of gray gases model for air-fuel combustion and its impacts," *Energy & Fuels*, vol. 27, no. 10, pp. 6287–6294, 2013.

[296] L. J. Dorigon, G. Duciak, R. Brittes, F. Cassol, M. Galara, and F. H. Frana, "WSGG correlations based on HITEMP2010 for computation of thermal radiation in non-isothermal, non-homogeneous H_2O/CO_2 mixtures," *International Journal of Heat and Mass Transfer*, vol. 64, pp. 863 – 873, 2013.

[297] M. Alberti, R. Weber, M. Mancini, and M. Modest, "Comparison of models for predicting band emissivity of carbon dioxide and water vapour at high temperatures," *International Journal of Heat and Mass Transfer*, vol. 64, no. 0, pp. 910 – 925, 2013.

[298] A. Soufiani and E. Djavdan, "A comparison between weighted sum of gray gases and statistical narrow-band radiation models for combustion applications," *Combustion and Flame*, vol. 97, no. 2, pp. 240 – 250, 1994.

[299] R. Porter, F. Liu, M. Pourkashanian, A. Williams, and D. Smith, "Evaluation of solution methods for radiative heat transfer in gaseous oxy-fuel combustion environments," *Journal of Quantitative Spectroscopy and Radiative Transfer*, vol. 111, no. 14, pp. 2084 – 2094, 2010.

[300] M. K. Denison and B. W. Webb, "An absorption-line blackbody distribution function for efficient calculation of total gas radiative transfer," *Journal of Quantitative Spectroscopy and Radiative Transfer*, vol. 50, no. 5, pp. 499 – 510, 1993.

[301] M. K. Denison and B. W. Webb, "The spectral-line weighted-sum-of-gray-gases model for H_2O/CO_2 mixtures," *Journal of heat transfer*, vol. 117, no. 3, pp. 788–792, 1995.

[302] V. P. Solovjov and B. W. Webb, "SLW modeling of radiative transfer in multicomponent gas mixtures," *Journal of Quantitative Spectroscopy and Radiative Transfer*, vol. 65, no. 4, pp. 655 – 672, 2000.

[303] M. K. Denison and B. W. Webb, "The spectral line-based weighted-sum-of-gray-gases model in nonisothermal nonhomogeneous media," *Journal of Heat Transfer*, vol. 117, no. 2, pp. 359–365, 1995.

[304] L. Pierrot, P. Rivière, A. Soufiani, and J. Taine, "A fictitious-gas-based absorption distribution function global model for radiative transfer in hot gases," *Journal of Quantitative Spectroscopy and Radiative Transfer*, vol. 62, no. 5, pp. 609 – 624, 1999.

[305] V. P. Solovjov and B. W. Webb, "Global spectral methods in gas radiation: The exact limit of the SLW model and its relationship to the ADF and FSK methods," *Journal of Heat Transfer*, vol. 133, no. 4, p. 042701, 2011.

[306] V. P. Solovjov, D. Lemonnier, and B. W. Webb, "The SLW-1 model for efficient prediction of radiative transfer in high temperature gases," *Journal of Quantitative Spectroscopy and Radiative Transfer*, vol. 112, no. 7, pp. 1205–1212, 2011.

[307] V. P. Solovjov, D. Lemonnier, and B. W. Webb, "SLW-1 modeling of radiative heat transfer in nonisothermal nonhomogeneous gas mixtures with soot," *Journal of Heat Transfer*, vol. 133, no. 10, p. 102701, 2011.

[308] H. Chu, F. Liu, and J.-L. Consalvi, "Relationship between the spectral line based weighted-sum-of-gray-gases model and the full spectrum k-distribution model," *Journal of Quantitative Spectroscopy and Radiative Transfer*, vol. 143, pp. 111 – 120, 2014, special Issue: The Seventh International Symposium on Radiative Transfer.

[309] J. T. Pearson, B. W. Webb, V. P. Solovjov, and J. Ma, "Efficient representation of the absorption line blackbody distribution function for H_2O, CO_2, and CO at variable temperature, mole fraction, and total pressure," *Journal of Quantitative Spectroscopy and Radiative Transfer*, vol. 138, pp. 82 – 96, 2014.

[310] L. Wang, D. C. Haworth, S. R. Turns, and M. F. Modest, "Interactions among soot, thermal radiation, and NO_x emissions in oxygen-enriched turbulent nonpremixed flames: a computational fluid dynamics modeling study," *Combustion and Flame*, vol. 141, pp. 170 – 179, 2005.

[311] J. L. Consalvi, R. Demarco, A. Fuentes, S. Melis, and J. P. Vantelon, "On the modeling of radiative heat transfer in laboratory-scale pool fires," *Fire Safety Journal*, vol. 60, no. 0, pp. 73 – 81, 2013.

[312] S. Mazumder and M. F. Modest, "Application of the full spectrum correlated-k distribution approach to modeling non-gray radiation in combustion gases," *Combustion and Flame*, vol. 129, no. 4, pp. 416 – 438, 2002.

[313] R. Demarco, J. L. Consalvi, A. Fuentes, and S. Melis, "Assessment of radiative property models in non-gray sooting media," *International Journal of Thermal Sciences*, vol. 50, no. 9, pp. 1672 – 1684, 2011.

[314] T. F. Wall, A. Lowe, L. J. Wibberley, T. Mai-Viet, and R. P. Gupta, "Fly ash characteristics and radiative heat transfer in pulverized-coal-fired furnaces," *Combustion Science and Technology*, vol. 26, no. 3-4, pp. 107–121, 1981.

[315] R. Gupta and T. Wall, "The optical properties of fly ash in coal fired furnaces," *Combustion and Flame*, vol. 61, no. 2, pp. 145 – 151, 1985.

[316] D. G. Goodwin and M. Mitchner, "Flyash radiative properties and effects on radiative heat transfer in coal-fired systems," *International Journal of Heat and Mass Transfer*, vol. 32, no. 4, pp. 627 – 638, 1989.

[317] B. W. Butler, M. K. Denison, and B. W. Webb, "Radiation heat transfer in a laboratory-scale, pulverized coal-fired reactor," *Experimental Thermal and Fluid Science*, vol. 9, no. 1, pp. 69 – 79, 1994.

[318] K. Andersson and F. Johnsson, "Flame and radiation characteristics of gas-fired O_2/CO_2 combustion," *Fuel*, vol. 86, no. 5-6, pp. 656 – 668, 2007.

[319] K. Andersson, R. Johansson, and F. Johnsson, "Thermal radiation in oxy-fuel flames," *International Journal of Greenhouse Gas Control*, vol. 5, Supplement 1, pp. S58 – S65, 2011.

[320] R. Johansson, B. Leckner, K. Andersson, and F. Johnsson, "Influence of particle and gas radiation in oxy-fuel combustion," *International Journal of Heat and Mass Transfer*, vol. 65, pp. 143 – 152, 2013.

[321] S. Hjärtstam, R. Johansson, K. Andersson, and F. Johnsson, "Computational fluid dynamics modeling of oxy-fuel flames: The role of soot and gas radiation," *Energy & Fuels*, vol. 26, no. 5, pp. 2786–2797, 2012.

[322] D. G. Goodwin and M. Mitchner, "Measuremnts of the near infrared optical properties of coal slags," *Chemical Engineering Communications*, vol. 44, no. 1-6, pp. 241–255, 1986.

[323] S. M. Godoy and F. C. Lockwood, "Development of a two-colour infrared pyrometer for coal particle temperature measurements during devolatilisation," *Fuel*, vol. 77, no. 9-10, pp. 995 – 999, 1998.

[324] J. J. Murphy and C. R. Shaddix, "Combustion kinetics of coal chars in oxygen-enriched environments," *Combustion and Flame*, vol. 144, no. 4, pp. 710 – 729, 2006.

[325] T. Maffei, R. Khatami, S. Pierucci, T. Faravelli, E. Ranzi, and Y. A. Levendis, "Experimental and modeling study of single coal particle combustion in O_2/N_2 and oxy-fuel (O_2/CO_2) atmospheres," *Combustion and Flame*, vol. 160, no. 11, pp. 2559 – 2572, 2013.

[326] H. Tolvanen and R. Raiko, "An experimental study and numerical modeling of combusting two coal chars in a drop-tube reactor: A comparison between N_2/O_2, CO_2/O_2, and $N_2/CO_2/O_2$ atmospheres," *Fuel*, vol. 124, pp. 190 – 201, 2014.

[327] D. Kim, S. Choi, C. R. Shaddix, and M. Geier, "Effect of CO_2 gasification reaction on char particle combustion in oxy-fuel conditions," *Fuel*, vol. 120, pp. 130 – 140, 2014.

[328] P. Foster and C. Howarth, "Optical constants of carbons and coals in the infrared," *Carbon*, vol. 6, no. 5, pp. 719 – 729, 1968.

[329] W. H. Dalzell and A. F. Sarofim, "Optical constants of soot and their application to heat-flux calculations," *Journal of Heat Transfer*, vol. 91, no. 1, pp. 100–104, 1969.

[330] S. Lee and C. Tien, "Optical constants of soot in hydrocarbon flames," *Symposium (International) on Combustion*, vol. 18, no. 1, pp. 1159 – 1166, 1981.

[331] H. Chang and T. T. Charalampopoulos, "Determination of the wavelength dependence of refractive indices of flame soot," *Proceedings of the Royal Society of London. Series A: Mathematical and Physical Sciences*, vol. 430, no. 1880, pp. 577–591, 1990.

[332] T. H. Fletcher, J. Ma, J. R. Rigby, A. L. Brown, and B. W. Webb, "Soot in coal combustion systems," *Progress in Energy and Combustion Science*, vol. 23, no. 3, pp. 283 – 301, 1997.

[333] C. F. Bohren and D. R. Huffman, *Absorption and scattering of light by small particles*, ser. Wiley science paperback series. Wiley, 1983.

[334] M. P. Mengüç and R. Viskanta, "On the radiative properties of polydispersions : A simplified approach," *Combustion Science and Technology*, vol. 44, no. 3-4, pp. 143–159, 1985.

[335] M. F. Modest and J. Cai, "Spectral photon monte carlo with energy splitting across phases for gas–particle mixtures," *Journal of Heat Transfer*, vol. 137, pp. 121 012–1 – 121 012–10, 2015.

[336] J. G. Marakis, C. Papapavlou, and E. Kakaras, "A parametric study of radiative heat transfer in pulverised coal furnaces," *International Journal of Heat and Mass Transfer*, vol. 43, no. 16, pp. 2961 – 2971, 2000.

[337] S. Manickavasagam and M. P. Mengüç, "Effective optical properties of pulverized coal particles determined from ft-ir spectrometer experiments," *Energy & Fuels*, vol. 7, no. 6, pp. 860–869, 1993.

[338] L. G. Henyey and J. L. Greenstein, "Diffuse radiation in the galaxy," *The Astrophysical Journal*, vol. 93, pp. 70–83, 1941.

[339] J. H. Joseph, W. J. Wiscombe, and J. A. Weinman, "The delta-eddington approximation for radiative flux transfer," *Journal of the Atmospheric Sciences*, vol. 33, no. 12, pp. 2452–2459, 1976.

[340] P. Chýlek, G. W. Grams, and R. G. Pinnick, “Light scattering by irregular randomly oriented particles,” *Science*, vol. 193, no. 4252, pp. 480–482, 1976.

[341] M. I. Mishchenko and L. D. Travis, “Capabilities and limitations of a current FORTRAN implementation of the T-matrix method for randomly oriented, rotationally symmetric scatterers,” *Journal of Quantitative Spectroscopy and Radiative Transfer*, vol. 60, no. 3, pp. 309 – 324, 1998.

[342] M. I. Mishchenko, “Electromagnetic scattering by nonspherical particles: A tutorial review,” *Journal of Quantitative Spectroscopy and Radiative Transfer*, vol. 110, no. 11, pp. 808 – 832, 2009, light Scattering: Mie and More Commemorating 100 years of Mie’s 1908 publication.

[343] P. R. Solomon, R. M. Carangelo, P. E. Best, J. R. Markham, and D. G. Hamblen, “Analysis of particle emittance, composition, size and temperature by FT-i.r. emission/transmission spectroscopy,” *Fuel*, vol. 66, no. 7, pp. 897 – 908, 1987.

[344] J. R. Markham, P. E. Best, P. R. Solomon, and Z. Z. Yu, “Measurement of radiative properties of ash and slag by FT-IR emission and reflection spectroscopy,” *Journal of heat transfer*, vol. 114, no. 2, pp. 458–464, 1992.

[345] E. H. Chui, P. M. J. Hughes, and G. D. Raithby, “Implementation of the finite volume method for calculating radiative transfer in a pulverized fuel flame,” *Combustion Science and Technology*, vol. 92, no. 4-6, pp. 225–242, 1993.

[346] A. G. Blokh, *Heat transfer in steam boiler furnaces*, R. Viskanta, Ed. Springer-Verlag, 1988.

[347] F. Liu and J. Swithenbank, “The effects of particle size distribution and refractive index on fly-ash radiative properties using a simplified approach,” *International Journal of Heat and Mass Transfer*, vol. 36, no. 7, pp. 1905 – 1912, 1993.

[348] K. Onda, “Prediction of scattering effect by ash polydispersion on spectral emission from coal-fired MHD combustion gas,” *Journal of Quantitative Spectroscopy and Radiative Transfer*, vol. 53, no. 4, pp. 381 – 395, 1995.

[349] M. Bahador and B. Sundén, “Investigation on the effects of fly ash particles on the thermal radiation in biomass fired boilers,” *International Journal of Heat and Mass Transfer*, vol. 51, no. 910, pp. 2411 – 2417, 2008.

[350] I. R. Gran and B. F. Magnussen, “A numerical study of a bluff-body stabilized diffusion flame. Part 2. Influence of combustion modeling and finite-rate chemistry,” *Combustion Science and Technology*, vol. 119, no. 1-6, pp. 191–217, 1996.

[351] F. Breussin, F. Pigari, and R. Weber, “Predicting the near-burner-zone flow field and chemistry of swirl-stabilied low-NOx flames of pulveried coal using the RNG-k-ε, RSM and k-ε turbulence models,” *Symposium (International) on Combustion*, vol. 26, no. 1, pp. 211 – 217, 1996.

[352] A. E. German and T. Mahmud, “Modelling of non-premixed swirl burner flows using a reynolds-stress turbulence closure,” *Fuel*, vol. 84, no. 5, pp. 583 – 594, 2005.

[353] U. Schumann and R. A. Sweet, “A direct method for the solution of poisson’s equation with neumann boundary conditions on a staggered grid of arbitrary size,” *Journal of Computational Physics*, vol. 20, no. 2, pp. 171 – 182, 1976.

[354] P. Warzecha and A. Boguslawski, “LES and RANS modeling of pulverized coal combustion in swirl burner for air and oxy-combustion technologies,” *Energy*, vol. 66, pp. 732 – 743, 2014.

[355] J. Pedel, “Large eddy simulations of coal jet flame ignition using the direct quadrature method of moments,” Ph.D. dissertation, The University of Utah, 2012.

[356] J. Pedel, J. N. Thornock, and P. J. Smith, “Ignition of co-axial turbulent diffusion oxy-coal jet flames: Experiments and simulations collaboration,” *Combustion and Flame*, vol. 160, no. 6, pp. 1112 – 1128, 2013.

[357] A. Dehbi, “A CFD model for particle dispersion in turbulent boundary layer flows,” *Nuclear Engineering and Design*, vol. 238, no. 3, pp. 707 – 715, 2008.

[358] W. E. Ranz and W. R. Marshall, “Evaporation from drops,” *Chem. Eng. Prog*, vol. 48, no. 3, pp. 141–146, 1952.

[359] A. D. Gosman and E. Loannides, “Aspects of computer simulation of liquid-fueled combustors,” *Journal of Energy*, vol. 7, no. 6, pp. 482–490, 1983.

[360] M. Bini and W. P. Jones, “Large-eddy simulation of particle-laden turbulent flows,” *Journal of Fluid Mechanics*, vol. 614, pp. 207–252, 2008.

[361] R. Khatami, C. Stivers, K. Joshi, Y. A. Levendis, and A. F. Sarofim, “Combustion behavior of single particles from three different coal ranks and from sugar cane bagasse in o2/n2 and o2/co2 atmospheres,” *Combustion and Flame*, vol. 159, no. 3, pp. 1253 – 1271, 2012.

[362] M. M. Baum and P. J. Street, “Predicting the combustion behaviour of coal particles,” *Combustion Science and Technology*, vol. 3, no. 5, pp. 231–243, 1971.

[363] H. Kobayashi, J. B. Howard, and A. F. Sarofim, “Coal devolatilization at high temperatures,” *Symposium (International) on Combustion*, vol. 16, no. 1, pp. 411 – 425, 1977.

[364] S. Niksa and A. R. Kerstein, “FLASHCHAIN theory for rapid coal devolatilization kinetics. 1. Formulation,” *Energy & Fuels*, vol. 5, no. 5, pp. 647–665, 1991.

[365] P. Solomon and M. Colket, “Coal devolatilization,” *Symposium (International) on Combustion*, vol. 17, no. 1, pp. 131 – 143, 1979, seventeenth Symposium (International) on Combustion.

[366] P. R. Solomon, D. G. Hamblen, R. M. Carangelo, M. A. Serio, and G. V. Deshpande, “General model of coal devolatilization,” *Energy & Fuels*, vol. 2, no. 4, pp. 405–422, 1988.

[367] T. H. Fletcher, A. R. Kerstein, R. J. Pugmire, M. S. Solum, and D. M. Grant, “Chemical percolation model for devolatilization. 3. direct use of carbon-13 nmr data to predict effects of coal type,” *Energy & Fuels*, vol. 6, no. 4, pp. 414–431, 1992.

[368] R. K. Rathnam, L. K. Elliott, T. F. Wall, Y. Liu, and B. Moghtaderi, "Differences in reactivity of pulverised coal in air (O_2/N_2) and oxy-fuel (O_2/CO_2) conditions," *Fuel Processing Technology*, vol. 90, no. 6, pp. 797 – 802, 2009.

[369] J. Ballester and S. Jiménez, "Kinetic parameters for the oxidation of pulverised coal as measured from drop tube tests," *Combustion and Flame*, vol. 142, no. 3, pp. 210 – 222, 2005.

[370] D. Genetti, T. H. Fletcher, and R. J. Pugmire, "Development and application of a correlation of ^{13}C NMR chemical structural analyses of coal based on elemental composition and volatile matter content," *Energy & Fuels*, vol. 13, no. 1, pp. 60–68, 1999.

[371] B. B. Hattingh, R. C. Everson, H. W. J. P. Neomagus, J. R. Bunt, D. van Niekerk, J. H. L. Jordaan, and J. P. Mathews, "Elucidation of the structural and molecular properties of typical south african coals," *Energy & Fuels*, vol. 27, no. 6, pp. 3161–3172, 2013.

[372] A. G. Borrego and D. Alvarez, "Comparison of chars obtained under oxy-fuel and conventional pulverized coal combustion atmospheres," *Energy & Fuels*, vol. 21, no. 6, pp. 3171–3179, 2007.

[373] R. Jovanovic, A. Milewska, B. Swiatkowski, A. Goanta, and H. Spliethoff, "Sensitivity analysis of different devolatilisation models on predicting ignition point position during pulverized coal combustion in O_2/N_2 and O_2/CO_2 atmospheres," *Fuel*, vol. 101, pp. 23 – 37, 2012.

[374] G.-S. Liu and S. Niksa, "Coal conversion submodels for design applications at elevated pressures. part ii. char gasification," *Progress in Energy and Combustion Science*, vol. 30, no. 6, pp. 679 – 717, 2004.

[375] O. Senneca and L. Cortese, "Kinetics of coal oxy-combustion by means of different experimental techniques," *Fuel*, vol. 102, pp. 751 – 759, 2012.

[376] J. Brix, P. A. Jensen, and A. D. Jensen, "Modeling char conversion under suspension fired conditions in O_2/N_2 and O_2/CO_2 atmospheres," *Fuel*, vol. 90, no. 6, pp. 2224 – 2239, 2011.

[377] R. E. Mitchell, L. Ma, and B. Kim, "On the burning behavior of pulverized coal chars," *Combustion and Flame*, vol. 151, no. 3, pp. 426 – 436, 2007.

[378] R. Hurt, J.-K. Sun, and M. Lunden, "A kinetic model of carbon burnout in pulverized coal combustion," *Combustion and Flame*, vol. 113, no. 1 - 2, pp. 181 – 197, 1998.

[379] O. Karlström, A. Brink, M. Hupa, and L. Tognotti, "Multivariable optimization of reaction order and kinetic parameters for high temperature oxidation of 10 bituminous coal chars," *Combustion and Flame*, vol. 158, no. 10, pp. 2056 – 2063, 2011.

[380] N. M. Laurendeau, "Heterogeneous kinetics of coal char gasification and combustion," *Progress in Energy and Combustion Science*, vol. 4, no. 4, pp. 221 – 270, 1978.

[381] A. Tremel, "Reaction kinetics of solid fuel during entrained flow gasification," Ph.D. dissertation, Technical University of Munich, 2012.

[382] S. Brunauer, P. H. Emmett, and E. Teller, “Adsorption of gases in multimolecular layers,” *Journal of the American Chemical Society*, vol. 60, no. 2, pp. 309–319, 1938.

[383] R. E. Mitchell, R. H. Hurt, L. L. Baxter, and D. R. Hardesty, *Compilation of Sandia coal char combustion data and kinetic analyses*. Sandia National Laboratories, 1992.

[384] A. Williams, M. Pourkashanian, and J. Jones, “The combustion of coal and some other solid fuels,” *Proceedings of the Combustion Institute*, vol. 28, no. 2, pp. 2141 – 2162, 2000.

[385] G. R. Gavalas, “A random capillary model with application to char gasification at chemically controlled rates,” *AIChE Journal*, vol. 26, no. 4, pp. 577–585, 1980.

[386] G. A. Simons, “The pore tree structure of porous char,” *Symposium (International) on Combustion*, vol. 19, no. 1, pp. 1067 – 1076, 1982, nineteenth Symposium (International) on Combustion.

[387] M. V. Gil, J. Riaza, L. Álvarez, C. Pevida, J. J. Pis, and F. Rubiera, “Oxy-fuel combustion kinetics and morphology of coal chars obtained in N_2 and CO_2 atmospheres in an entrained flow reactor,” *Applied Energy*, vol. 91, no. 1, pp. 67 – 74, 2012.

[388] M. A. Field, “Rate of combustion of size-graded fractions of char from a low-rank coal between 1 200k and 2 000k,” *Combustion and Flame*, vol. 13, no. 3, pp. 237 – 252, 1969.

[389] D. G. Goodwin, H. K. Moffat, and R. L. Speth, “Cantera: An object-oriented software toolkit for chemical kinetics, thermodynamics, and transport processes,” http://www.cantera.org, 2015, version 2.2.0.

[390] G. P. Smith, D. M. Golden, M. Frenklach, N. W. Moriarty, B. Eiteneer, M. Goldenberg, C. T. Bowman, R. K. Hanson, S. Song, W. C. G. Jr., V. V. Lissianski, and Z. Qin. (2015) Gri-mech 3.0. [Online]. Available: http://www.me.berkeley.edu/gri_mech/

[391] B. N. Mehta and R. Aris, “Communications on the theory of diffusion and reaction–VII the isothermal pth order reaction,” *Chemical Engineering Science*, vol. 26, no. 10, pp. 1699 – 1712, 1971.

[392] J. Hong, “Modeling char oxidation as a function of pressure using an intrinsic Langmuir rate equation,” Ph.D. dissertation, Brigham Young University, 2000.

[393] R. Aris, “On shape factors for irregular particles–I: the steady state problem. diffusion and reaction,” *Chemical Engineering Science*, vol. 6, no. 6, pp. 262 – 268, 1957.

[394] R. P. Brent, “Algorithms for minimizing without derivatives,” 1973.

[395] T. F. Wall and I. M. Stewart, “The measurement and prediction of solids- and soot-absorption coefficients in the flame region of an industrial P.F. chamber,” *Symposium (International) on Combustion*, vol. 14, no. 1, pp. 689 – 697, 1973, fourteenth Symposium (International) on Combustion.

[396] A. T. Wijayanta, M. S. Alam, K. Nakaso, and J. Fukai, “Numerical investigation on combustion of coal volatiles under various o2/co2 mixtures using a detailed mechanism with soot formation,” *Fuel*, vol. 93, pp. 670 – 676, 2012.

[397] A. L. Brown and T. H. Fletcher, "Modeling soot derived from pulverized coal," *Energy & Fuels*, vol. 12, no. 4, pp. 745–757, 1998.

[398] S. J. Brookes and J. B. Moss, "Predictions of soot and thermal radiation properties in confined turbulent jet diffusion flames," *Combustion and Flame*, vol. 116, no. 4, pp. 486 – 503, 1999.

[399] L. Y. M. Gicquel, G. Staffelbach, and T. Poinsot, "Large eddy simulations of gaseous flames in gas turbine combustion chambers," *Progress in Energy and Combustion Science*, vol. 38, no. 6, pp. 782 – 817, 2012.

[400] B. F. Magnussen and B. H. Hjertager, "On mathematical modeling of turbulent combustion with special emphasis on soot formation and combustion," *Symposium (International) on Combustion*, vol. 16, no. 1, pp. 719 – 729, 1977.

[401] B. F. Magnussen and B. W. Hjertager, "On the structure of turbulence and a generalized eddy dissipation concept for chemical reaction in turbulent flow," in *19th AIAA Aerospace Meeting, St. Louis, USA*, 1981.

[402] S. B. Pope, "Computationally efficient implementation of combustion chemistry using in situ adaptive tabulation," *Combustion Theory and Modelling*, vol. 1, no. 1, pp. 41–63, 1997.

[403] J. P. Kim, U. Schnell, and G. Scheffknecht, "Comparison of different global reaction mechanisms for MILD combustion of natural gas," *Combustion Science and Technology*, vol. 180, no. 4, pp. 565–592, 2008.

[404] C. K. Westbrook and F. L. Dryer, "Simplified reaction mechanisms for the oxidation of hydrocarbon fuels in flames," *Combustion Science and Technology*, vol. 27, no. 1-2, pp. 31–43, 1981.

[405] W. P. Jones and R. P. Lindstedt, "Global reaction schemes for hydrocarbon combustion," *Combustion and Flame*, vol. 73, no. 3, pp. 233 – 249, 1988.

[406] L. Zhou, L. Hu, and F. Wang, "Large-eddy simulation of turbulent combustion using different combustion models," *Fuel*, vol. 87, no. 1314, pp. 3123 – 3131, 2008.

[407] C. Fureby, "Large eddy simulation modelling of combustion for propulsion applications," *Philosophical Transactions of the Royal Society of London A: Mathematical, Physical and Engineering Sciences*, vol. 367, no. 1899, pp. 2957–2969, 2009.

[408] D. Merrick, "Mathematical models of the thermal decomposition of coal: 1. the evolution of volatile matter," *Fuel*, vol. 62, no. 5, pp. 534 – 539, 1983.

[409] T. K. Das, "Evolution characteristics of gases during pyrolysis of maceral concentrates of russian coking coals," *Fuel*, vol. 80, no. 4, pp. 489 – 500, 2001.

[410] R. S. Jupudi, V. Zamansky, and T. H. Fletcher, "Prediction of light gas composition in coal devolatilization," *Energy & Fuels*, vol. 23, no. 6, pp. 3063–3067, 2009.

[411] J. Andersen, C. L. Rasmussen, T. Giselsson, and P. Glarborg, "Global combustion mechanisms for use in CFD modeling under oxy-fuel conditions," *Energy & Fuels*, vol. 23, no. 3, pp. 1379–1389, 2009.

[412] J. Floyd, A. M. Kempf, A. Kronenburg, and R. H. Ram, "A simple model for the filtered density function for passive scalar combustion LES," *Combustion Theory and Modelling*, vol. 13, no. 4, pp. 559–588, 2009.

[413] L. Álvarez, M. Gharebaghi, J. Jones, M. Pourkashanian, A. Williams, J. Riaza, C. Pevida, J. J. Pis, and F. Rubiera, "CFD modeling of oxy-coal combustion: Prediction of burnout, volatile and NO precursors release," *Applied Energy*, vol. 104, pp. 653 – 665, 2013.

[414] P. J. Smith and T. H. Fletcher, "A study of two chemical reaction models in turbulent coal combustion," *Combustion Science and Technology*, vol. 58, no. 1-3, pp. 59–76, 1988.

[415] S. B. Pope, "PDF methods for turbulent reactive flows," *Progress in Energy and Combustion Science*, vol. 11, no. 2, pp. 119 – 192, 1985.

[416] M. Stöllinger, B. Naud, D. Roekaerts, N. Beishuizen, and S. Heinz, "PDF modeling and simulations of pulverized coal combustion – part 1: Theory and modeling," *Combustion and Flame*, vol. 160, no. 2, pp. 384 – 395, 2013.

[417] B. R. Adams and P. J. Smith, "Modeling effects of soot and turbulence-radiation coupling on radiative transfer in turbulent gaseous combustion," *Combustion Science and Technology*, vol. 109, no. 1-6, pp. 121–140, 1995.

[418] S. Mazumder and M. F. Modest, "A probability density function approach to modeling turbulence-radiation interactions in nonluminous flames," *International Journal of Heat and Mass Transfer*, vol. 42, no. 6, pp. 971 – 991, 1999.

[419] G. Li and M. F. Modest, "Importance of turbulence-radiation interactions in turbulent diffusion jet flames," *Journal of heat transfer*, vol. 125, no. 5, pp. 831–838, 2003.

[420] A. J. Chandy, D. J. Glaze, and S. H. Frankel, "A hybrid large eddy simulation/filtered mass density function for the calculation of strongly radiating turbulent flames," *Journal of heat transfer*, vol. 131, no. 5, pp. 051 201–1 – 051 201–9, 2009.

[421] A. Gupta, "Large-eddy simulation of turbulent flames with radiation heat transfer," Ph.D. dissertation, The Pennsylvania State University, 2011.

[422] M. Roger, P. J. Coelho, and C. B. da Silva, "The influence of the non-resolved scales of thermal radiation in large eddy simulation of turbulent flows: A fundamental study," *International Journal of Heat and Mass Transfer*, vol. 53, pp. 2897 – 2907, 2010.

[423] M. Roger, P. J. Coelho, and C. B. da Silva, "Relevance of the subgrid-scales for large eddy simulations of turbulence-radiation interactions in a turbulent plane jet," *Journal of Quantitative Spectroscopy and Radiative Transfer*, vol. 112, no. 7, pp. 1250 – 1256, 2011.

[424] D. Poitou, J. Amaya, M. E. Hafi, and B. Cuénot, "Analysis of the interaction between turbulent combustion and thermal radiation using unsteady coupled LES/DOM simulations," *Combustion and Flame*, vol. 159, no. 4, pp. 1605 – 1618, 2012.

[425] Y. Cao, Q. Wang, C. wei Chen, B. Chen, M. Cohron, Y. chuan Tseng, C. chung Chiu, P. Chu, and W.-P. Pan, “Investigation of mercury transformation by HBr addition in a slipstream facility with real flue gas atmospheres of bituminous coal and powder river basin coal,” *Energy & Fuels*, vol. 21, no. 5, pp. 2719–2730, 2007.

[426] L. Zheng and E. Furimsky, “Assessment of coal combustion in O_2+CO_2 by equilibrium calculations,” *Fuel Processing Technology*, vol. 81, no. 1, pp. 23 – 34, 2003.

[427] M. W. Chase, C. A. Davies, J. R. Downey, D. J. Frurip, R. A. McDonald, and A. N. Syverud. (1985) NIST JANAF thermochemical tables. Distributed by Standard Reference Data Program National Institute of Standards and Technology Gaithersburg, MD 20899. Accessed 3/10/2012. [Online]. Available: http://kinetics.nist.gov/janaf/

[428] I. Barin and G. Platzki, *Thermochemical data of pure substances*, 3rd ed., ser. Thermochemical Data of Pure Substances. VCH, 1995, vol. 1.

[429] W. Polifke, W. Geng, and K. Döbbeling, “Optimization of rate coefficients for simplified reaction mechanisms with genetic algorithms,” *Combustion and Flame*, vol. 113, no. 1-2, pp. 119 – 134, 1998.

[430] S. D. Harris, L. Elliott, D. B. Ingham, M. Pourkashanian, and C. W. Wilson, “The optimisation of reaction rate parameters for chemical kinetic modelling of combustion using genetic algorithms,” *Computer Methods in Applied Mechanics and Engineering*, vol. 190, no. 8-10, pp. 1065 – 1090, 2000.

[431] M. Tsuchiya and J. Ross, “Application of genetic algorithm to chemical kinetics: Systematic determination of reaction mechanism and rate coefficients for a complex reaction network,” *The Journal of Physical Chemistry A*, vol. 105, no. 16, pp. 4052–4058, 2001.

[432] L. Elliott, D. B. Ingham, A. G. Kyne, N. S. Mera, M. Pourkashanian, and C. W. Wilson, “Genetic algorithms for optimisation of chemical kinetics reaction mechanisms,” *Progress in Energy and Combustion Science*, vol. 30, no. 3, pp. 297 – 328, 2004.

[433] F. Perini, J. L. Brakora, R. D. Reitz, and G. Cantore, “Development of reduced and optimized reaction mechanisms based on genetic algorithms and element flux analysis,” *Combustion and Flame*, vol. 159, no. 1, pp. 103 – 119, 2012.

[434] N. Sikalo, O. Hasemann, C. Schulz, A. Kempf, and I. Wlokas, “A genetic algorithm-based method for the automatic reduction of reaction mechanisms,” *International Journal of Chemical Kinetics*, vol. 46, no. 1, pp. 41–59, 2014.

[435] P. A. Buitrago, B. V. Otten, C. L. Senior, and G. D. Silcox, “Impinger-based mercury speciation methods and gas-phase mercury oxidation by bromine in combustion systems,” *Energy & Fuels*, vol. 27, no. 10, pp. 6255–6261, 2013.

[436] G. P. Smith, D. M. Golden, M. Frenklach, N. W. Moriarty, B. Eiteneer, M. Goldenberg, C. T. Bowman, R. K. Hanson, S. Song, W. C. G. Jr., V. V. Lissianski, and Z. Qin. GRI-MECH 3.0. [Online]. Available: http://combustion.berkeley.edu/gri-mech/version30/text30.html

[437] M. Pelucchi, A. Frassoldati, T. Faravelli, B. Ruscic, and P. Glarborg, “High-temperature chemistry of HCl and Cl_2,” *Combustion and Flame*, vol. 162, no. 6, pp. 2693–2704, 2015.

[438] G. Dixon-Lewis, P. Marshall, B. Ruscic, A. Burcat, E. Goos, A. Cuoci, A. Frassoldati, T. Faravelli, and P. Glarborg, “Inhibition of hydrogen oxidation by HBr and Br_2,” *Combustion and Flame*, vol. 159, no. 2, pp. 528 – 540, 2012.

[439] A. Molina, J. J. Murphy, C. R. Shaddix, and L. G. Blevins, “The effect of potassium bromide and sodium carbonate on coal char combustion reactivity,” *Proceedings of the Combustion Institute*, vol. 30, no. 2, pp. 2187 – 2195, 2005.

[440] H. Hippler, S. H. Luu, H. Teitelbaum, and J. Troe, “Flash photolysis study of the no-catalyzed recombination of bromine atoms,” *International Journal of Chemical Kinetics*, vol. 10, no. 2, pp. 155–169, 1978.

[441] J. Cai and M. F. Modest, “Improved full-spectrum k-distribution implementation for inhomogeneous media using a narrow-band database,” *Journal of Quantitative Spectroscopy and Radiative Transfer*, vol. 141, pp. 65 – 72, 2014.

[442] V. Evseev, A. Fateev, and S. Clausen, “High-resolution transmission measurements of CO_2 at high temperatures for industrial applications,” *Journal of Quantitative Spectroscopy and Radiative Transfer*, vol. 113, no. 17, pp. 2222 – 2233, 2012.

[443] C. P. Thurgood, A. Pollard, and H. A. Becker, “The T_{N} quadrature set for the discrete ordinates method,” *Journal of heat transfer*, vol. 117, no. 4, pp. 1068–1070, 1995.

[444] S. Grathwohl, M. E. de Tejada, J. Maier, A. Baumgartner, M. Blume, and P. Dias, “AASB burner tests,” Reliable and Efficient Combustion of Oxygen/Coal/Recycled Flue Gas Mixtures, Tech. Rep., 2013.

[445] B. E. Launder and D. B. Spalding, “The numerical computation of turbulent flows,” *Computer Methods in Applied Mechanics and Engineering*, vol. 3, no. 2, pp. 269 – 289, 1974.

[446] B. E. Launder, G. J. Reece, and W. Rodi, “Progress in the development of a reynolds-stress turbulence closure,” *Journal of fluid mechanics*, vol. 68, no. 3, pp. 537–566, 1975.

[447] R. Weber, B. M. Visser, and F. Boysan, “Assessment of turbulence modeling for engineering prediction of swirling vortices in the near burner zone,” *International Journal of Heat and Fluid Flow*, vol. 11, no. 3, pp. 225 – 235, 1990.

[448] R. I. Backreedy, J. M. Jones, L. Ma, M. Pourkashanian, A. Williams, A. Arenillas, B. Arias, J. J. Pis, and F. Rubiera, “Prediction of unburned carbon and NOx in a tangentially fired power station using single coals and blends,” *Fuel*, vol. 84, no. 17, pp. 2196 – 2203, 2005, special Issue: The 5th European Conference on Coal Research and its Applications.

[449] A. Dehbi and F. de Crécy, “Validation of the langevin particle dispersion model against experiments on turbulent mixing in a t-junction,” *Powder Technology*, vol. 206, no. 3, pp. 312 – 321, 2011.